Synthesis of organometallic coordination polymers for thermoelectric applications

by

Zilu Liu

A thesis submitted in partial fulfilment of the requirement for the degree of

Doctor of Philosophy

Department of Chemistry

University College London

DECLARATION

The work described in this thesis is the work of the author and has not previously been submitted to this or any other university for any other degree.

Signed: Zilu Liu

Date: August 2020

Abstract

As an intriguing class of thermoelectric (TE) candidates, organometallic coordination polymers (OMCPs) have become a new research focus in this area, regardless of the extensive research on inorganic and organic thermoelectric materials. This thesis showcases the synthesis and comprehensive characterization of a series of linear OMCPs based on metal-bis(dithiolato) coordination, **Ni-ett**, **Ni-diett** and **Ni-btt** (Chapter 2). The studies proved that changing organic ligands is a successful strategy to tune the thermoelectric properties of OMCPs, including electrical conductivity, Seebeck coefficient and power factor. By developing complex model for analogous spectroscopic study, we proved the polymer frames of three OMCPs are radial involving. Moreover, alternative synthetic route was also developed for polymer Ni-btt.

Meanwhile, a couple of structural isomeric ligands OMCPs (Chapter 3), benzene-1,2,3,4-tetrakis(thiolate) and benzene-1,2,4,5-tetrakis(thiolate), were employed to synthesize mono-ligand OMCPs (**Ni-ibtt** and **Ni-btt**) and dual-ligand OMCPs **Ni(ibtt)$_x$(btt)$_{1-x}$**. The comparative study upon their thermoelectric properties was correlated with their structural difference in both intrachain and interchain characters.

Regardless of organic bridging ligand, the metal center is the other most important role on the thermoelectric properties of OMCPs. Systematic comparison among OMCPs with different metal centers cross reports is usually unfeasible, as chemical composition and properties for a certain OMCP formula usually (like **Ni-ett**) differ from

report to report and involve multiple reaction and measurement factors. In this study, OMCPs with various metal cations were synthesized in the M-ett and M-btt system to conduct a parallel comparison in their thermoelectric performance (Chapter 4). Preliminary molecular design and synthesis work were also carried out to experimentally obtain the OMCPs based on benzenetetrathiolate backbone with different sidechains, to examine the effect of sidechains on thermoelectric properties in this system.

.

Statement of impact

Many organometallic coordination polymers are evaluated as promising thermoelectric materials in recent computational work, while the experimental synthesis and studies of stable and durable OMCPs for thermoelectric application are still laggard, confined to very few systems like poly(Ni-ett). Meanwhile, compositional understanding on this system has long hold divided ideas due to its insoluble nature. This thesis developed a series of organic ligands as scaffolding for new metal-bis(dithiolato) polymers and highlighted the radical-involving features of these OMCPs, via an extensive purification, comprehensive characterization and parallel comparison with complex models. For specific bridging ligands, alternative synthetic routes were developed. These OMCPs demonstrate the tunable thermoelectric properties by ligand design. On the other hand, to exemplify the effect of various metal centers on the resulting OMCPs, comparative experiments were conducted to two systems. The synthetic routes and thermoelectric measurement elucidate key factors for good thermoelectric properties in metal-bis(dithiolato) based OMCPs and inspire more discovery to thermoelectric candidates.

Publications

1. **Liu, Z.**; Liu, T.; Savory, C. N.; Jurado, J. P.; Reparaz, J. S.; Li, J.; Pan, L.; Faul, C. F. J.; Parkin, I. P.; Sankar, G.; Matsuishi, S.; Campoy‐Quiles, M.; Scanlon, D. O.; Zwijnenburg, M. A.; Fenwick, O.; Schroeder, B. C., Controlling the Thermoelectric Properties of Organometallic Coordination Polymers via Ligand Design. Advanced Functional Materials **2020**, *30* (32), 2003106

2. Liu, T.; Zhao, X.; Li, J.; **Liu, Z.**; Liscio, F.; Milita, S.; Schroeder, B. C.; Fenwick, D. Enhanced control of self-doping in halide perovskites for improved thermoelectric performance. *Nature Communications* **2019**, *10* (1), 5750

3. Pan, L.; **Liu, Z.**; Tian, M.; Schroeder, B. C.; Faul, C. F. J. Luminescent and Swellable Conjugated Microporous Polymers for Detecting Nitroaromatic Explosives and Removing Harmful Organic Vapors. *Applied Material & Interfaces* **2019**, *11*, 48352−48362

4. Wan, K.; Junior, P. T.; **Liu, Z.**; Liu, Y.; Tu, Y.; Santagiuliana, J.; Hsia, I. C.; Zhang, H.; Fenwick, O.; Krause, S.; Baxendale, M.; Schroeder, B. C.; Bilotti, E. Flexible and Stretchable Self-Powered Multi-Sensors Based on the N-Type Thermoelectric Response of Polyurethane/Na_x(Ni-ett)$_n$ Composites. *Advanced Electronic Materials* **2019**, *5*, 1900582.

5. Bilotti, E.; Fenwick, O.; Schroeder, B. C.; Baxendale, M.; Junior, P. T.; Degousée, T.; **Liu, Z.** 6.14 Organic Thermoelectric Composites Materials. In: Comprehensive Composite Materials II; Beaumont, P. W. R.; Zweben, C. H.; *Oxford Academic Press* 2018; pp 408-430.

Acknowledgements

I would like to thank my supervisor, Dr. Bob C. Schroeder, for his guidance and help in my research during the past four years. This research was full of challenges and would never have been done without his mentorship and encouragement.

Special thanks go to my husband, Long Pan, who always calmed me down upon the countless experimental failures and discussed new synthetic strategies with me, even when we were on a date. I would like to thank my family for their strong support through all the time.

I appreciate the invaluable help from all the collaborators for measurement, computational work and research discussion: Dr. M. A. Zwijnenburg, Prof. D. O. Scanlon and Dr. C. N. Savory at UCL for their contribution to the DFT calculations; Dr. S. Matsuishi at Tokyo Institute of Technology for solid EPR and SQUID; Dr. M. Campoy-Quiles, Dr. J. S. Reparaz and J. P. Jurado at Institute of Materials Science of Barcelona for thermal conductivity; Prof. G. Sankar for XANES; Dr. T. Liu at QMUL (Chapter 2) and Prof. D. Baran, Dr. A. Mohammed and Dr. Y. Liu at King Abdullah University of Science and Technology (Chapter 3 and 4) for Seebeck coefficient and electrical conductivity; Dr. L Pan at University of Bristol for the TGA and single crystallography and Jianwei Li at UCL for powder XRD. I also want to thank the support from Dr. Abil Aliev for NMR, Dr. Kersti Karu for mass spectroscopy and Steve Firth for many equipment trainings.

I would also like to thank the members of our group and colleagues in other groups. In particular, a big thank you goes to Tianjun for his continuous support and contribution to the thermoelectric measurement and idea exchange; Yasmin, my dearest workmate, deserves special recognition for lab work discussion and precious friendship. It also involves many friends whose superb research assistance, wonderful encouragement or idea exchange often go unnoticed, especially Divya, Fangqing, Jingyuan, Leren, Lewis, Mona, Xueyan, Xiaoming, Xiangyu, Yuqiao, and Zach.

At last, I greatly appreciate this funding by *UCL-Chinese Scholarship Council (CSC) joint scholarship* for this chance to do my PhD research at UCL.

List of abbreviations

1D	= One dimensional
2D	= Two dimensional
DCM	= Dichloromethane
DFT	= Density functional theory
DMA	= Dimethylacetamide
DMF	= *N*,*N*-Dimethylformamide
DMSO	= Dimethyl sulfoxide
EDS	= Energy-dispersive X-ray spectroscopy
EPR	= Electron paramagnetic resonance
ESI	= Electrospray ionization
FC	= Field cooling
FTIR	= Fourier-transform infrared spectra
HER	= Hydrogen evolution reaction
HOMOs	= Highest occupied orbitals
iPr	= Isopropyl
LUMOs	= Lowest unoccupied orbitals
MS	= Mass spectrometry
MS_4	= Metal-tetrathiolate
NMR	= Nuclear magnetic resonance

NBu_4	= Tetra-*n*-butylammonium
OMCP	= Organometallic coordination polymer
OTE	= Organic thermoelectric
PEDOT	= Poly(3,4-ethylenedioxythiophene)
Per	= Perylene
PF	= Power factor
PSS	= Poly-styrene sulfonate
PVDF	= Polyvinylidene fluoride
SEM	= Scanning electron microscopy
SQUID	= Superconducting quantum interference device
TE	= Thermoelectric
TEA	= Tetraethylammonium
TEG	= Thermoelectric generator
TGA	= Thermal gravimetric measurements
THF	= Tetrahydrofuran
TTO	= Tetrathiooxalate
UPS	= Ultraviolet photoelectron spectroscopy
XANES	= X-ray absorption near-edge structure
XPS	= X-ray photoelectron spectroscopy
XRD	= X-ray diffraction

XRF	= X-ray fluorescence analysis
ZT	= Figure of merit
α	= Seebeck coefficient ($\mu V\ K^{-1}$)
σ	= Electrical conductivity ($S\ cm^{-1}$)
κ	= Thermal conductivity ($W\ m^{-1}\ K^{-1}$)

Table of Contents

Introduction

- Thermoelectric principles
- Development of metal-bis(dithiolato) complexes
- Thermoelectric advances based on metal-bis(dithiolato) OMCPs

Our group has been focused on the synthesis of linear organometallic coordination polymers in the past four years and comprehensive characterization of their structures. By changing organic ligands to obtain different OMCP systems with various bridging moieties, we proved that this strategy can be used to tune the thermoelectric properties of OMCPs, including electrical conductivity, Seebeck coefficient and power factor.[1] This PhD thesis describes research into the synthesis, purification and characterization of the corresponding ligand precursors and OMCPs, and the key factors of their thermoelectric behavior.

This first chapter will provide a short introduction to the background of thermoelectric materials, devices and recent advances based on both inorganic and organic thermoelectric materials, which has been previously discussed in details in our published book chapter.[2] Then, a short overview of the development of metal-tetrathiolate (MS_4) complexes and the multiple applications of relevant OMCPs in this system in the literature will be introduced. In the third part, recent research of OMCPs based on MS_4 coordination for thermoelectric candidates will be listed and discussed.

Chapter 1. An introduction to organometallic coordination polymers for thermoelectric application

1.1 Introduction to thermoelectric principles

Annual primary energy consumption has been soaring all over the world in the past

decades and will keep rising to around 7.62×10^{20} J by 2030.[3] The geologic processes however cannot create non-renewable sources, such as oil, natural gas, and coal at a useful rate to meet human's requirement. Concern has quickly grown over the past decades about energy consumption and the associated environmental impact, which calls for technological innovation to seek and use novel, reliable and affordable energy sources to replace the conventional carbon based sources. Viable greener technologies using renewable energy sources, including hydro, solar, wind, biomass, tidal, sea waves and geothermal, are still under development and largely rely on specific geographical settings.

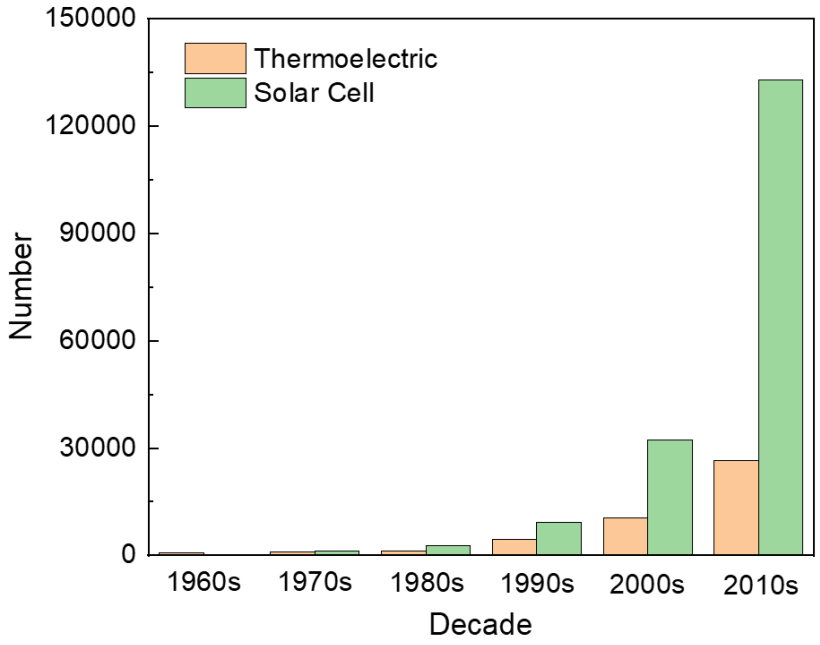

Figure 1. *Publications in the area of thermoelectric and solar-cell technology over the past six decades (to May2020) based on search in Web of Science.*

Harvesting waste energy rather than dissipating it into atmosphere instead is an alternative prospecting way to the quest for rendering fossil fuel combustion obsolete. Among various technologies to capture different types of waste energy, thermoelectric

technology is one of the most promising to transfer waste thermal energy into electrical output, whose energy source is countless, cheap and pollution-free.[3] The number of publications involving *"thermoelectric"* directly reflects the increasing importance of this field, which still needs extensive exploration compared with the very popular solar-cell technology (Figure 1b). This section is to provide a summary on the basic effect and remarkable progress of thermoelectric materials. Firstly, the principles of thermoelectric effect will be introduced. Then, the benchmark thermoelectric materials, both inorganic and organic, reported in recent progress will be present in details.

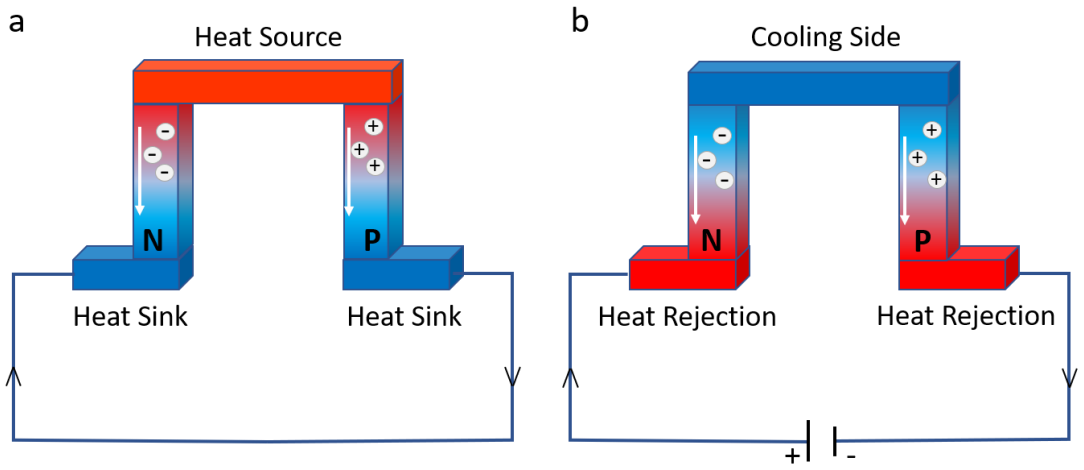

Figure 2. *Illustration of (a) Seebeck effect and (b) Peltier effect.*

Thermoelectric effect is identified as the direct generation of electromotive force when a temperature gradient is applied to p and n-type thermoelectric materials, where the charge carriers (holes or electrons, respectively) diffuse from the hot side to the cold side, and vice versa. This effect consists of three individual effects: the Seebeck effect, Peltier effect and Thomson effect, where the former two are most well-known.

Seebeck effect refers to the direct conversion of temperature difference to

electricity and the electromotive force generated by Seebeck effect, is defined by Equation (1):

$$\alpha = \pm \frac{\Delta V}{\Delta T} \quad (1)$$

where ΔV and ΔT are thermoelectric voltage and temperature difference observed between two terminals, and α is the thermopower or Seebeck coefficient of a material. The absolute thermopower of a material is hardly measurable because the electrodes attached with a voltmeter must be placed onto the material in order to measure the generated voltage, which flows across one leg of the electrodes.[3] Hence, the experimentally measured α is based on the measure of the thermocouple, both the material of interest and the material of electrodes used, which is termed as:

$$\alpha_{AB} = \alpha_B - \alpha_A = \frac{\Delta V_B}{\Delta T} - \frac{\Delta V_A}{\Delta T} \quad (2)$$

Peltier effect is the presence of the reverse process: the cooling or heating effect led by voltage applied across two conductors. When the current *I*, is applied through a junction between conductor A and conductor B, the Peltier heat generated at the junction per unit time, $\dot{Q}$, can be given by:

$$\dot{Q} = I \prod_{AB} = (\prod_A - \prod_B) I \quad (3)$$

where Π_A and Π_B are the Peltier coefficients of material A and B, respectively.

The Thomson effect introduces the Seebeck coefficient's dependence on temperature, regarding the continuous occurrence of Peltier heating or cooling effect when a current flowing through a conductor with a temperature gradient. The heat

production per unit volume can be described as:

$$\dot{Q} = - \beta J \cdot \nabla T \quad (4)$$

where a current density J is applied through, ∇T is temperature difference and β is the Thomson coefficient. Based on these, the Thomson coefficient and Peltier coefficients are related to Seebeck coefficient as follows:

$$\beta = T\frac{d\alpha}{dT} \quad (5)$$

$$\Pi = \alpha T \quad (6)$$

which are known as the first and second Thomson relation, respectively.

The dimensionless figure of merit (ZT) of a thermoelectric material is given by:

$$ZT = \frac{\alpha^2 \sigma T}{\kappa} \quad (7)$$

where α (μV K^{-1}) is the Seebeck coefficient, σ (S cm^{-1}) is the electrical conductivity and κ (W m^{-1} K^{-1}) is the thermal conductivity. Alternatively, for the TE material without available thermal data or organic-polymer based materials with intrinsically low κ, Power factor (PF) is also widely used as the other criterion to evaluate the thermoelectric quality of a material:

$$PF = \alpha^2\sigma \quad (9)$$

However, the output power is not a comprehensive evaluation of a thermoelectric material like ZT, as it disregards the thermal conductivity.

Accordingly, ideal n-type and/or p-type thermoelectric materials should simultaneously possess high α, high σ and low κ for high performance thermoelectric

generators (TEG). Unfortunately, finding such materials that fullfil both requirements is very difficult. The three key factors (α, σ and κ) have complex interconnection and cannot be optimized individually without a counteraction to another parameter in bulky thermoelectric materials (Figure 3).

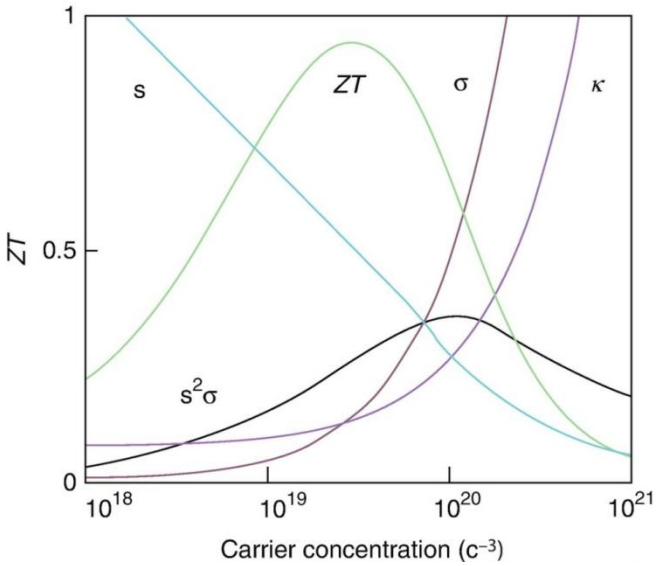

***Figure 3**. Optimizing ZT through carrier concentration tuning, which involves a compromise of κ and s (α) with σ. The thermoelectric between the peak in $\alpha^2\sigma$ and ZT is greater for the newer lower- κ_l shown were modelled from Bi_2Te_3, based on empirical data in report. Reused with permission .[4] Copyright 1969, Springer Nature.*

Electrical conductivity is determined by three factors, carrier charge (e), free carrier concentration (n)and carrier mobility (μ), given by the following formula:

$$\sigma = en\mu \tag{8}$$

Equation (8) can be applied to both n-type and p-type materials, regardless of the type of charge carrier in semiconductors. When the electrons and holes co-exist in a semiconductor, then the electrical conductivity will be the sum of both types conductivity.

Thermal conductivity is composed of the electron thermal conductivity (κ_e) and lattice

thermal conductivity (κ_l), as:

$$\kappa = \kappa_e + \kappa_l \quad (9)$$

Enhancing σ will inevitably lead to the increase of κ_e according to the Wiedemann-Franz law, expressed as:

$$\kappa_e = L\sigma T \quad (10)$$

where L is the Lorentz number. Therefore, the thermal conductivity can be reduced only by reducing the κ_l.[5]

Conventional inorganic TE materials have been established since the middle of 20th century, heavily relying on several toxic elements with quite low abundancy in the earth's crust, including Ge (1.5 ppm), Se (0.05 ppm), Sb (0.2 ppm), Sn (2.3 ppm), Te (0.001 ppm), Pb (14 ppm), Bi (0.0085 ppm), etc.[6] In the following decades, tremendous efforts have been made to optimize the previous systems for high ZT value (~1), as well as developing novel inorganic TE materials by introducing cheap and non-toxic elements (Mg, Cu, Mn, Ag).[7] However, the preparation, element doping and optimization process of most inorganic TE materials involve complex processes, such as ball-milling, high temperature (melting and thermal evaporation) and high pressure techniques (high-pressure synthesis, hot press, spark plasma sintering, extrusion methods).[8]

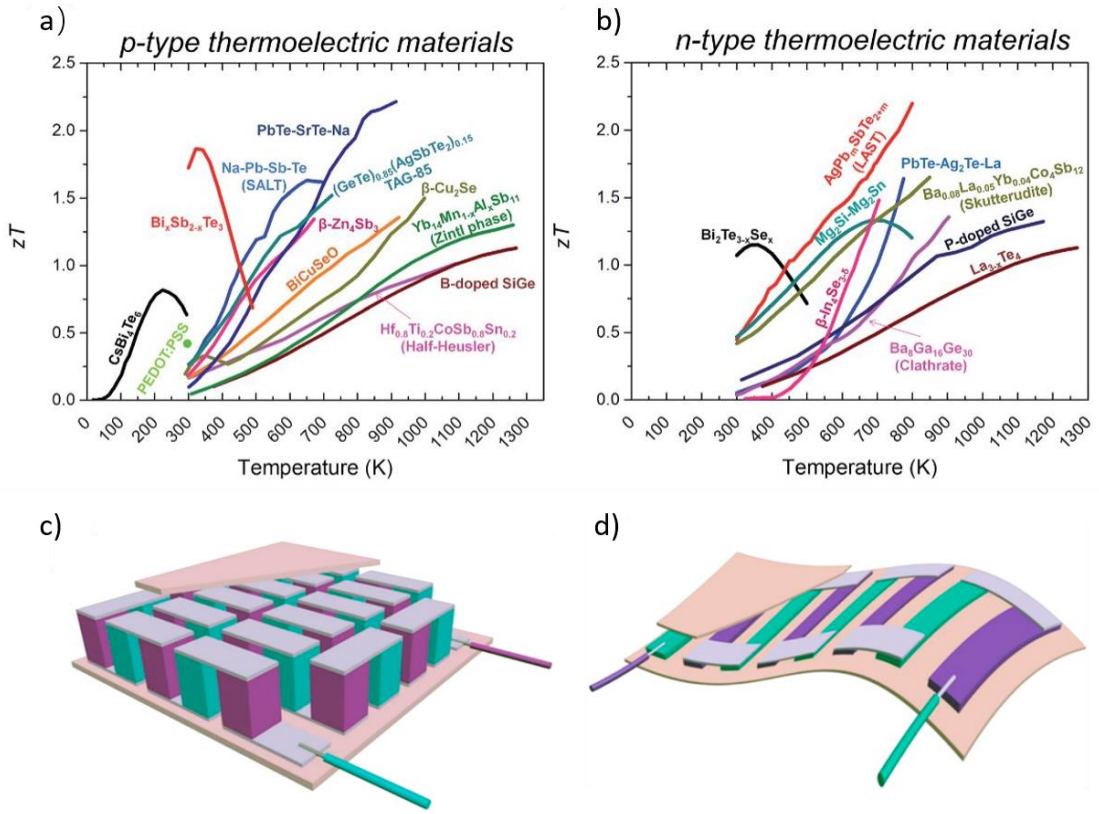

Figure 4. *(a-b) Summary of some of the best ZT for inorganic thermoelectric materials, reproduced with permission from the Royal Society of Chemistry;[9] schematic of (c) traditional TEG and (d) flexible TEG reused with permission.[8]Copyright 2020, Elsevier Ltd.*

Currently, inorganic TE materials are dominating the field, with the commercial supply of inorganic-based TE generators available from companies like II-VI Marlow and Tecteg MFR. Nonetheless, as aforementioned, most of the reported inorganic semiconductors as TE candidates are expensive, rare, heavy, fragile, high-toxic, difficult to process and impractical to harvest low-temperature-range waste heat (Figure 4a and 4b). These inevitable disadvantages together limit their massive production and wide application. To the contrary, organic polymers hold great promise for wearable and stretchable thermoelectric devices to harvest energy from non-planar heat sources (Figure 4d), although their TE performance is currently inferior to that of inorganic TE

materials.

On one hand, the organic thermoelectric (OTE) materials are appealing due to their milder synthesis conditions and simpler procedures. On the other hand, their light-weight, flexibility and solubility makes most of the existing manufacturing routes feasible for device fabrication, both the conventional ways (subtractive or formative manufacturing) and the new-emerging additive manufacturing, such as solution printing, fused deposition, stereolithography apparatus, selective laser melting or sintering, etc.[8]

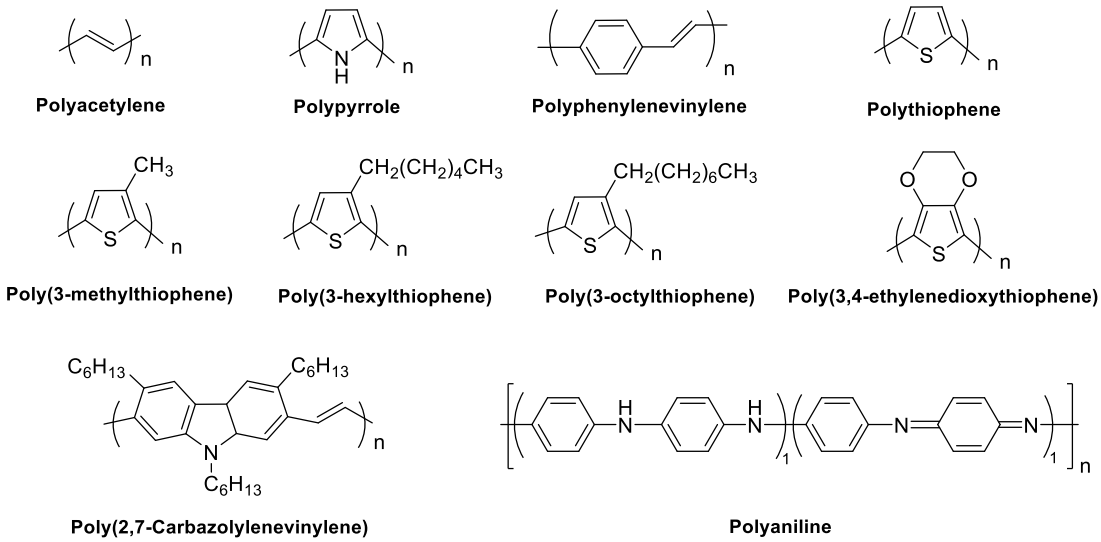

***Figure 5**. Typical conjugated polymers for OTE.*

Conjugated polymers are the organic macromolecules with backbone chains formed by repeating units with alternating single- and double-bonds, giving the overlapping p-orbitals and delocalized π-electrons throughout the backbones. In those polymer semiconductors, charge transport is not via the band transport of highly delocalized charges, but the hopping of polarons or bipolarons between localized

states.[2] Typical organic polymers used as thermoelectric materials are summarized in Figure 5. At present, the most prevalent organic polymers explored for TE materials are polypyrrole (PPy), poly(3,4-ethylenedioxythiophene) (PEDOT), poly(3-hexylthiophene) (P3HT), polyaniline (PANI), polyacetylene, polythiophenes, polyphenylenevinylene, poly(3-methylthiophene), poly(3-octylthiophene) and polyvinylidene fluoride (PVDF). Those intrinsic conductive polymers have dominated the development of TE devices, among which many still cannot achieve desirable ZT values due to their intrinsically low α and σ. There are mainly three strategies to overcome the restrictions of organic TE materials: (i) Tune the thermoelectric properties of conjugated polymers by changing the basic structure of monomer unit; (ii) Introduce chemical or electrochemical doping into the bulk polymer to control the concentration of charge carriers and optimize the ZT of thermoelectric materials. However, the dopants or counterions introduced via doping can cause stacking disorder, reduce the carrier mobility and degrade thermoelectric properties; (iii) Prepare composites via blending with other high-conductive materials such as carbon nanotubes and graphene, or develop hybrid organic-inorganic composites with metal-clusters. While the drawbacks associated with the mixing method cannot be simply downplayed: the conductivity of composites highly relying on processing conditions, the formation of insulating surface layer on the conductor and the depressed mechanical stability with additional loading of conductive materials.

It is notable that more remarkable progresses have been made on p-type TE materials but the development of stable and durable n-type organic polymers is still laggard. Many n-type organic materials can only be stable under inert or vacuum atmosphere because of their low ionization energy and incidental reaction with oxygen and moisture,[10] For example, n-type carbon nanotube (CNT) prepared by chemical reduction transforms into p-type under ambient condition due to oxygen exposure.[11] Hence, finding new n-type organic TE materials is of great importance. Lately, developing hybrid (inorganic-organic) thermoelectric composites has also driven attention as another potential approach to combine the advantages of pure inorganic and organic TE materials by incorporating both together, namely, the inherent low thermal conductivity of the organic and the high Seebeck coefficient and electrical conductivity of the inorganic.[12-15]

Briefly, more effort is required for finding high performance TE materials which can operate at the low/room-temperature-range, for harvesting body heat and household application.

1.2 Development of metal-bis(dithiolato) based complexes and polymers

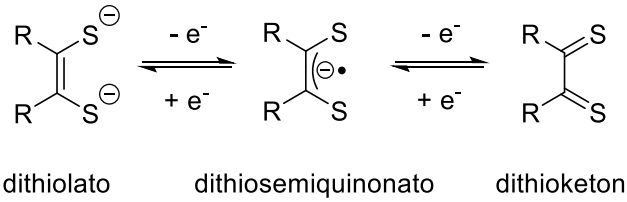

***Figure 6**. Typical redox behaviour of a dithiolato ligand involving three oxidization states.*

Developing OMCPs based on metal-bis(dithiolato) coordination in fact originated from the understanding of well-defined systems of small MS_4 complexes. The MS_4 complex systems has long attracted much interest and growing attention for their good chemical and physical properties, such as electronic conductivity, superconductivity, electro- and/or photo-catalytic hydrogen evolution capability, ferromagnetism, spin frustration, nonlinear optical properties and etc.[16-24] Such multifunction are based on their special electronic structures of coordinated moieties, where the redox activity exists on both center metal and dithiolato ligand and thereby redox reaction can happen through multi-step electron transfer (Figure 6).

Since the early days of development of small molecular metal-bis(dithiolato) complexes, much work has been done to investigate the oxidation states of the ligand and metal ion in specific complexes systems. To understand the electronic structures of small molecular bis(dithiolato)-metal complexes, many state-of-art characterization has been explored together, including single-crystal X-ray diffraction (XRD), X-ray absorption spectroscopy (XAS), resonance Raman spectroscopy, absorption

spectroscopy, electron paramagnetic resonance (EPR) and magnetic circular dichroism (MCD) techniques, and density-functional theory (DFT) and ab initio electronic structure calculations.[25]

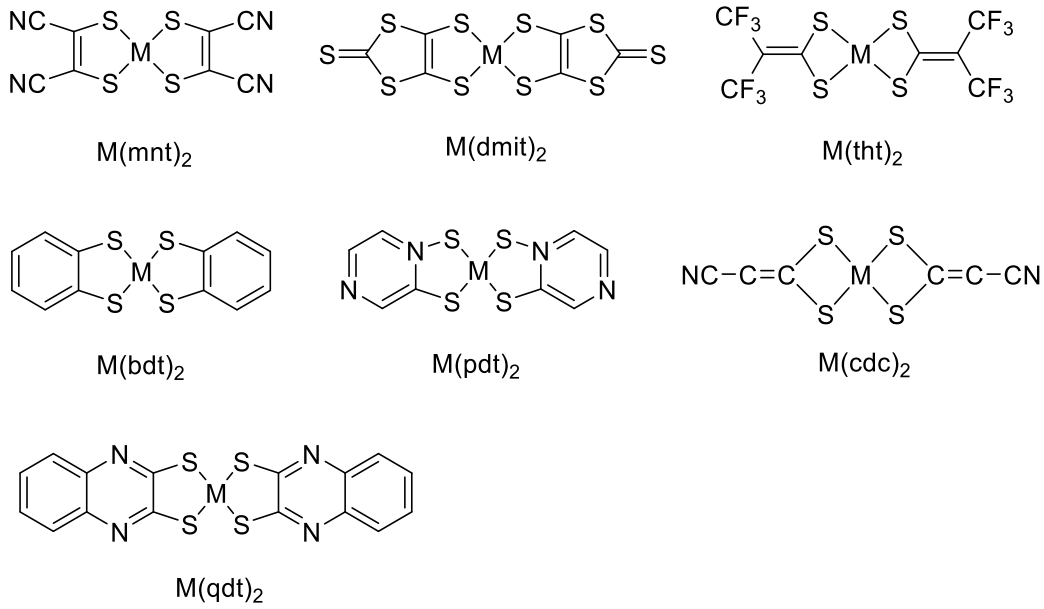

***Figure** 7. Metal bis-dithiolene complexes reported with available data of thermoelectric power. M = metal cation, cdc = cyanodithiocarbimate, dmit = 1,3-dithiole-2-thione-4,5-dithiolato, bdt = benzene-1,2dithiolate, mnt = cis-2,3-dimercapto-2-butenedinitrile, pdt = pyrazine-1,2-dithiolate, qdt = quinoxaline-2,3-dithiolate, THT = [bis(trifluoromethyl)ethylene]dithiolate.*

The thermopower behaviour of metal bis-dithiolene complex systems has also received much attention, corresponding reported structures and properties summarized in Figure 7. For instance, the single crystals of $M(mnt)_2$ (mnt = cis-2,3-dimercapto-2-butenedinitrile) have been studied as a typical family since 1990s for their thermoelectric properties. Almeida et al. synthesized p-type $(Per)_2Cu(mnt)_2$ and $(Per)_2Ni(mnt)_2$ (Per = perylene) with two phases, where the α-phase was metallic and β-phase exhibited semiconducting character.[26] Owing to the close packing and uniform stacking of perylene and $M(mnt)_2$ units, the α-phase single crystals showed better

thermoelectric properties with $\sigma_{RT} \approx 700$ S cm^{-1} and $\alpha_{RT} = 35$ μV K^{-1} along the stacking axis than the β-phase ($\sigma_{RT} \approx 50$ S cm^{-1} and $\alpha_{RT} = 22$ μV K^{-1}). Good thermoelectric properties were also found for $(Per)_2Fe(mnt)_2$ and $(Per)_2Co(mnt)_2$ with $\sigma_{RT} \approx 200$ S cm^{-1} and $\alpha_{RT} = 42$ μV K^{-1}.[27] Analogous conductive compound $PerCo(mnt)_2(CH_2Cl_2)_{0.5}$ showed metal-like thermopower behavior at room temperature ($\sigma_{RT} \approx 60$ S cm^{-1}, $\alpha_{RT} = -8$ μV K^{-1}) and had two metal-insulator transitions at lower temperature range (277 K and 188 K).[28] The high electric conductivity of this complex was attributed to its special structure with dimerized polymeric chains of $Co(mnt)_2$ and uniform molecular stacking (perylene). For the other bis-dithiolene complexes such as $M(dmit)_2$ (dmit = 1,3-dithiole-2-thione-4,5-dithiolato) and $M(dmit)_2$ (qdt = quinoxaline-2,3-dithiolate), the thermoelectric properties are summarized in Table 1.

Table 1 *Thermoelectric properties at room temperature of some metal bis-dithiolene complexes (based on single crystals). DT = dithiophene, bedt = bis(ethylenedithio), Per = perylene, TTDM = thiophenothiodimethylene, TTF = tetrathiafulvalene, TMTSF = tetramethyltetraselenafulvalene,*

Compound	σ (S cm^{-1})	α (μV K^{-1})	PF (μW m^{-1} K^{-2})	Ref
$(Per)_2Ni(mnt)_2$	700	35	85.8	[26]
$(Per)_2Cu(mnt)_2$	700	38	101.1	[26]
$(Per)_2Pd(mnt)_2$	300	32	71.7	[26]
$(Per)_2Pt(mnt)_2$	700	32	71.7	[26]
$(Per)_2Au(mnt)_2$	700	32	71.7	[26]
$PerCo(mnt)_2(CH_2Cl_2)_{0.5}$	60	-8	0.38	[28]

$(Per)_2[Co(mnt)_2]$	200	42	35.3	[27]
$(Per)_2[Fe(mnt)_2]$	200	42	35.3	[27]
$(TTDM\text{-}TTF)_2Au(mnt)_2$	0.15-1	73	0.08 - 0.53	[29]
$(TTF)[Ni(dmit)_2]_2$	300	-31	28.8	[30]
$TTF[Ni(dmit)_2]_2$	-	-46	-	[31]
$(Per)_2Au(cdc)_2$	150	35	18.4	[32]
$(DT\text{-}TTF)[Au(bdt)_2]_3$	3	-60	1.1	[33]
$(DT\text{-}TTF)[Cu(bdt)_2]_3$	0.5	-190	1.8	[33]
$[bedt\text{-}ttf][Cu(qdt)_2]$	1.4×10^{-4}	-662	6.3×10^{-3}	[34]
$[TMTSF][Au(qdt)_2]$	3.3×10^{-4}	-195	1.3×10^{-3}	[34]
$[TMTSF][Cu(qdt)_2]$	2.5×10^{-3}	-460	0.05	[34]
$(TMTSF)_2Ni(THT)_2$	50	1	5×10^{-3}	[35]

In the past decade, despite the promising performances of small molecular complexes, attention has shifted to one-dimensional (1D) and two-dimensional (2D) MS_4 coordination materials formed by extended π-conjugated ligands, with square planar coordination throughout the linear polymer chains or 2D lamellar framework. The good charge delocalization of the OMCP framework is attributed to the planar geometry and the absence of rotational disorder in polymer backbone. Both experimental results and theoretical work show great performance or potential of the electronic properties of those novel topologic materials. Their good electrical

conductivity comes from the through-bond coupling between the metal d-orbitals and ligand p-orbitals, where a good frontier molecular orbital alignment between the MS_4 fragment and the organic π-conjugated spacer is especially crucial to reduce the electron–phonon coupling, facilitate higher mobility and obtain high TE performance.[36]

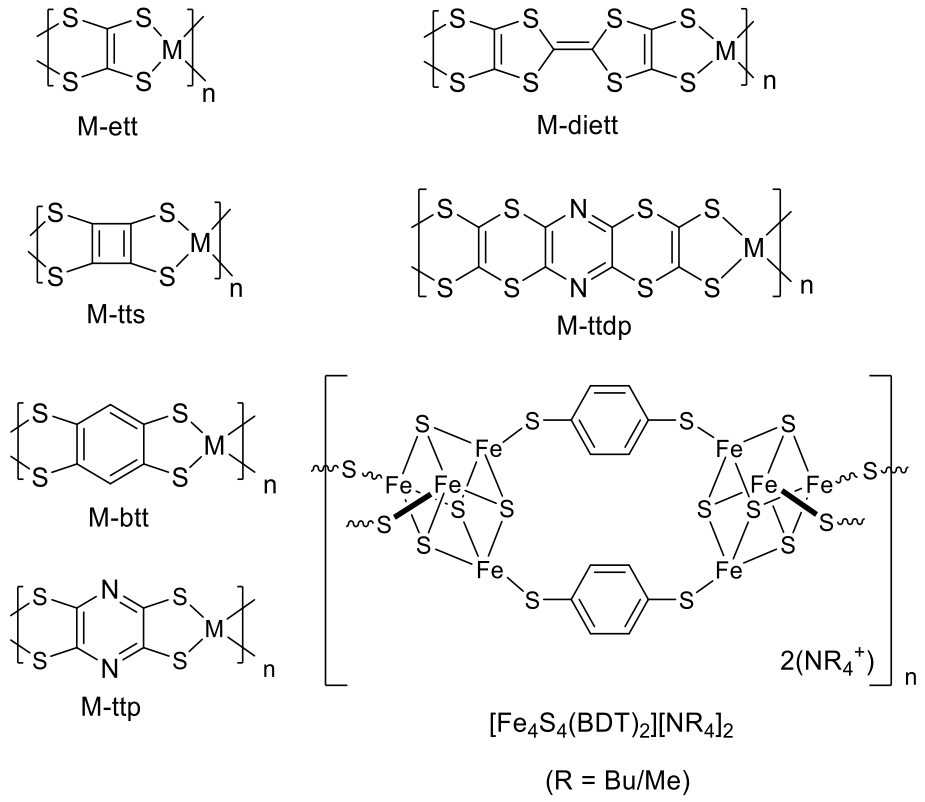

***Figure 8**. 1D OMCPs structures based on M-S coordination have been experimentally synthesized in literatures.*

To date, several 1D OMCPs have been developed or proposed with different tetrathiolate ligands, including 1,2,4,5-benzenetetrathiolate (btt), ethylenetetrathiolate (ett), 2,3,7,8-tetrathiolato-bis[1,4]dithiino-[2,3-*b*:2',3'-*e*]pyrazine) (ttdp), tetrathiafulvalenetetrathiolate (ttftt or diett), 2,

3,5,6-tetrathiolatopyrazine (ttp) and tetrathiosquarate (tts), shown in Figure 8.[37-44]

Most of these conductive 1D polymers were obtained as amorphous powders, while crystalline films have also been achieved by electrochemical growth and interlayer synthesis in the cases of M-ett and M-btt.[44-45] Co-btt deposited on glassy carbon or Si electrodes was reported as very efficient photocathode material for solar-driven hydrogen evolution from water, which achieved photocurrents of 3.8 mA cm^{-2} at 0 V vs RHE under simulated 1 Sun illumination.[46] Beyond the 1D polymers formed by metal ions and organic chelate linkers, novel OMCPs combining inorganic clusters have also been reported recently. For instance, 1D polymers based on organic 1,4-benzenebiligands and redox-active metal sulfide clusters were synthesized, namely $[Fe_4S_4(BDT)_2][NR_4]_2$. These 1-D anionic polymer chains keep the redox-active feature of inorganic (Fe_4S_4) cluster, whose electrical conductivity can be tuned from 10^{-9} to 10^{-5} S cm^{-1} via chemical reduction, in the case R = CH_3.[38] 1D metal-tetrathiolate polymers developed for thermoelectric purpose will be discussed in section 1.3.

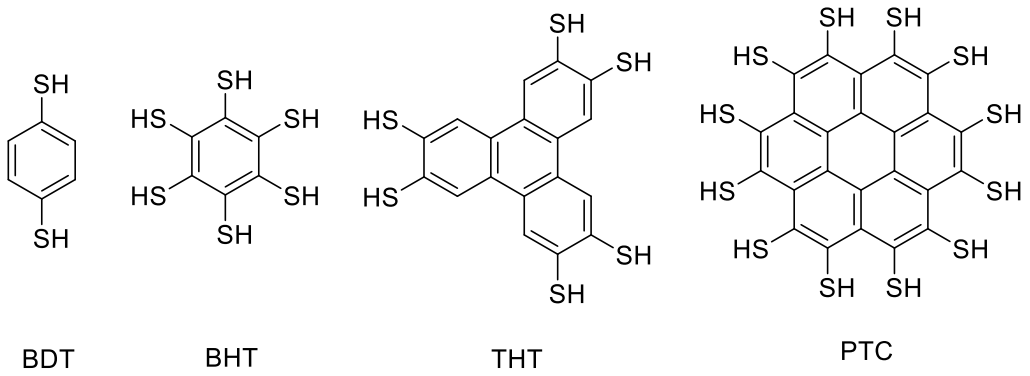

***Figure 9**. Compounds used for building M-S coordination 2D OMCPs in literatures.*

On the other hand, 2D OMCPs have attracted attention due to the coexistence of their good properties, like high conductivity, metallic behavior, electrocatalytic

activeness, self-resemblance, high porosity and surface area. As molecular self-assembly is a feasible method to get high-crystalline and free-standing film of such 2D polymers, several types of metal-bis(dithiolato) OMCPs have been synthesized in the past years (Figure 9).

For example, 2D nanosheets of coordination polymer, Ni-BDT, formed with Ni(II) and 1,4-benzenedithiol (BDT) grown on conductive carbon cloth was reported to exhibit high activity for hydrogen evolution reaction (HER) with an overpotential of 80 mV to reach 10 mA cm^{-2}.[47] The synthetic route of this 2D nanosheets involved two steps: (i) the 2D nanosheets of $Ni(OH)_2$ upon carbon cloth as substrates (cc- $Ni(OH)_2$) were prepared by hydrothermal method, whose thickness was around 20 nm; (ii) then via a subsequent hydrothermal process, the (cc- $Ni(OH)_2$) nanosheets transformed into Ni-bdt, in the presence of 1,4-benzenedithiol (BDT) solution in ethanol.

Another more popular OMCP system is based on the benzenehexathiolate (BHT) coordination frameworks, which has been systematically studied with various metals, including Au, Ag, Cu, Ni, Co.[48-54] Peculiarly, the high electrical conductivity of this OMCP system arouse much research interest, with the highest value of 2500 S cm^{-1}, 250 S cm^{-1} and 160 S cm^{-1} found for Cu-BHT (film), Ag-BHT (film) and Ni-BHT (single crystal), respectively.[55,49, 56] A larger derivative compound 2,3,6,7,10,11-triphenylenehexathiol (THT) was also used to synthesize 2D superconductive frameworks, as well as to form small molecular complexes.[57-59] Analogously, the

extensive π-conjugation system was obtained from 1,2,3,4,5,6,7,8,9,10,11,12-perthiolated coronene (PTC) to produce another 2D OMCP, PTC-Fe, a ferromagnetic material with a high electrical conductivity of ~10 S cm^{-1} at 300 K.[60-61]

Researchers further uncover the mechanism of the intrinsic high conductivity and metallic-like behavior of these 2D OMCPs. In Li et al.'s report, the metallicity of the 2D multilayered nickel bis(dithiolene) sheets mainly comes from the covalent-like interlayer interaction between the $3p_z$ orbitals of S atoms in adjacent layers. According to their first-principles calculations, the monolayer material is semiconducting, while the out-of-plane orbital hybridization in multilayers imparts the material metal-like behavior.[62] Another theoretical work also gives insight to the exceptionally high electron mobility and the low lattice thermal conductivity of monolayered of 2D $(NiC_4S_4)_n$ (namely Ni-BHT) nanosheet, whose calculated ZT and peak PF value at 300 K can get 0.92 and 73 μW m^{-1} K^{-2}. There are two reasons of such high thermoelectric promise are: (i) the high electron mobility was facilitated by the weak electron-acoustic-phonon coupling, with a very small acoustic phonon contribution (~20%) of the total scattering rate, which originates from the mixed bonding–antibonding nature of conduction band; (ii) the framework allows flat phonon dispersion, as well as providing good phonon-phonon scattering channels and crossovers between optical and acoustic phonons, which leads to the reduced thermal transport.[63]

Apart from acting as superconductive materials and electrocatalysts for hydrogen

evolution or oxygen reduction, other applications of these metal-organic frameworks (MOFs) have also gradually been recognized. For example, OLEDs devices using Ni-BHT nanosheets as the hole buffer layer, instead of conventional poly(3,4-ethylenedioxythiophene):poly-styrene sulfonate (PEDOT:PSS) was proved to increase the device lifetime by nearly 2 fold, without depressing efficiency.[64]

1.3 Thermoelectric advances based on metal-bis(dithiolato) OMCPs

In this section, the organometallic coordination polymers that have been experimentally considered as thermoelectric candidates will be discussed, summarizing the synthetic methods, composition, thermoelectric performance, optimization strategies and devices. The design strategies illustrated by relevant theoretical work of thermoelectric OMCPs based on the view of physics will also be included.

OMCPs are a promising class of materials for thermoelectric applications as they have shown promising electrical conductivities and low thermal conductivities. Among different OMCP systems, metal dithiolenes are of great interest due to their easy formation, ambient stability and the various oxidation states involving open-shell molecular orbitals, which are crucial for good conductivity.

Among this branch, the M-ett (metal-ethylenetetrathiolate) system has been studied. The polymer chain in a M-ett complex was believed to carry a two net negative charge per monomer unit, which assists the electron hopping along the chain. In addition to conduction along the polymer backbone, it was assumed the inter-chain stacking would

allow effective adjacent overlays of the orbitals on the sulfur atoms and thus provide a secondary conduction pathway.[65] Since its good thermoelectric properties were reported afresh with a ZT value of 0.2 around 400 K in the year of 2012, extensive efforts have been focus on optimization and processing due to its insoluble nature.[66]

Morphology can greatly influence the transport properties of organometallic semiconductors, with higher electrical conductivity or/and Seebeck coefficient found in crystalline samples than amorphous powder in many other coordination polymers and small metal-organic complex systems.[67-69] This is due to the high structure ordering and thereby improved orbital overlap, as well as the decrease or absence of grains boundaries and cracks in crystalline samples or thin films, reducing the interface scattering toward the carrier transport. Efforts have also been put on controlling the morphology of Ni-ett samples by different techniques. For example, Ni-ett nanoparticles with size distribution in the range of 10-20 nm was synthesized by adding ionic liquid [BMIM][BF_4], [DMIM][BF_4] (BMIM = 1-Butyl-3-methyl imidazolium, DMIM = 1-decyl-3-methyl imidazolium) as stabilizing agent during the polymerization step.[70] In the following reports, Ni-ett films electrochemically deposited on insulating substrates were fabricated, exhibiting decent ZT values up to 0.30 ± 0.03 at room temperature.[45, 71] Remarkably, a device based on poly (Ni-ett) film was fabricated to explore the Peltier effect, achieving a maximum temperature differences of 41 K at the two contacts and a cooling of 0.2 K under heat-insulated condition.[72]

The other widely reported method for processing and optimizing Ni-ett is blending with soluble binder polymers to obtain composite materials for facilitated film fabrication.[73-75] In our collaborative work, Ni-ett was made into composites, whose thermoelectric response was used for multi-sensors application. The composite Lycra®/Na_x(Ni-ett)$_n$ was developed via hot pressing technique with the composites blending Ni-ett with stretchable binder Lycra.[75] The composite with optimised weight ratio of Lycra®: Na_x(Ni-ett)$_n$ (1:1) presented a good strain-at-break more than 200 %, preserving a Seebeck coefficient of -32.3 μV K^{-1} and electrical conductivity of 0.011 S cm^{-1}. Moreover, a wearable device with n-type leg (Lycra®/Na_x(Ni-ett)$_n$) and p-type leg (Lycra®/PEDOT:PSS) was manufactured, which worked as a self-powered sensor to both strain and light irradiation within only 10-20 K temperature gradient.

Except for the M-ett system, the thermoelectric properties of many other metal dithiolenes polymers are either unexploited or only the electrical conductivity or/and Seebeck coefficient at room temperature are available in reports, such as M-ttftt and the 2D frameworks mentioned above.[41] Another example is a family of paramagnetic conductive OMCPs prepared from 1,2,4,5-tetrabenzenethiol and various transition metal ions, with conductivities (at room temperature) in the following sequence Fe^{3+} (0.2 S cm^{-1}) > Ni^{2+} and Co^{2+} (2×10^{-3} S cm^{-1}) > Cu^{2+} (2×10^{-5} S cm^{-1}).[76] While in a later report, the same nickel complex synthesized from 1,2,4,5-tetrabenzenethiol by liquid–liquid interfacial synthesis had a lower conductivity by two orders of magnitudes (10^{-5}

S cm^{-1} at 298 K).[44] The possible reason comes from the different synthetic routes used: in the former case, Ni^{2+} directly coordinated with the ligand intermediate to form polymer Ni-btt in base environment, while the interlayer method is more likely to contain disulfide moieties in the obtained polymer due to the oxidation of thiols.

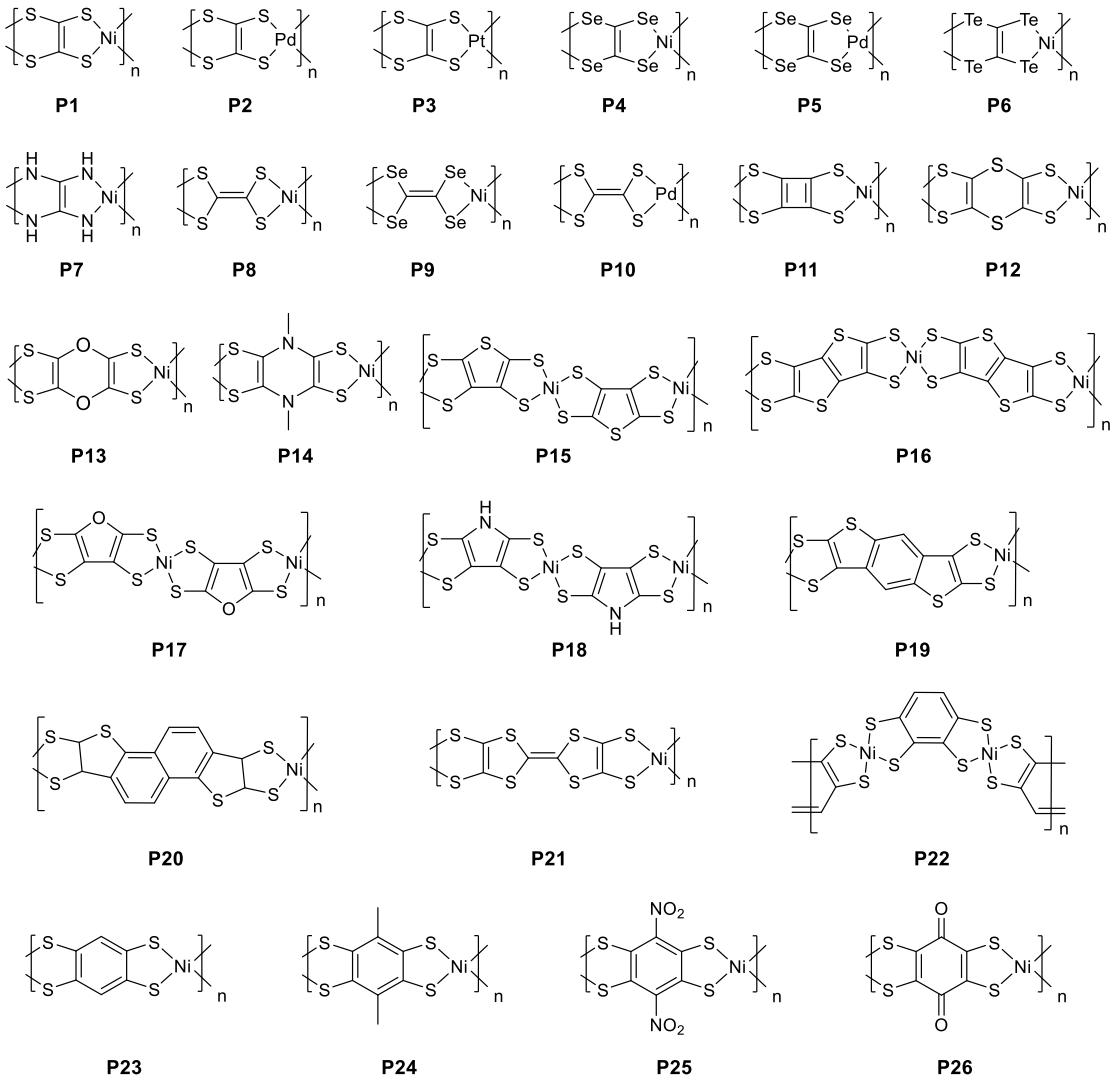

***Figure 10**. 1D square planar OMCPs structures P1-P25 in recent computational work with predicted thermoelectric properties.*[36, 62, 65]

However, many techniques used for characterizing small soluble molecular complexes cannot be directly translated to insoluble OMCP powder, which limits the

thorough understanding of their structural characteristics. For instance, the compositional information of polymer Ni-ett synthesized from one-pot method has long been controversial, which will be thoroughly explained in Chapter 2. Therefore, the number of the linear square planar OMCPs have been synthesized and experimentally characterized is still very limited hitherto.

In the meantime, with rising interest, more theoretical calculation work has been published to evaluate a variety of linear square planar OMCP structures and their thermoelectric potentials (Figure 10). The DFT calculations highlighted the importance of a high degree of π-d conjugation along the polymer backbones of these candidates. The overall contribution to the states near Fermi energy is from the d-orbitals of metal centers (Ni, Cu, Pd, Pt), p orbitals of coordination atoms (S/Se) and sp^2 hybridized carbon linking-bridge.[36, 62]

On the one hand, the theoretical work is very valuable to study the tunability of TE properties by substituting different elements, as it avoids many variables like impurity, oxidization state, structural defects and amorphous morphology, providing insights to the molecular design for good thermoelectric performance. On the other, most DFT work predicts much higher conductivities and Seebeck coefficients for OMCPs, by orders of magnitude, compared to experimentally validated values. This is because realistic OMCPs prepared via different synthetic techniques involve both crystalline domains and amorphous regions, where the former one involves both intrachain (within

a polymer chain) and interchain (between the polymer chains) TE transport.[62] While, the theoretical simulation usually only focusses on a simplified model without sub-chain interaction when exploring their TE properties.

Based on the aforementioned discussion, it is of great research interest to develop new OMCP systems and deepen the understanding of their structures, both by looking for novel thermoelectric candidates and by gathering a fundamental understanding of the underlying physics. In the following chapters, our work on developing different OMCPs by ligand design, structural and thermoelectric characterization will be discussed in detail, as well as the effect of the metal centers on specific OMCP properties.[1]

Chapter 2. Linear organometallic thermoelectric materials with different ligands

In spite of the limited amount of organometallic coordination polymers synthesized to date, recent theoretical works illustrate the potential of many π-conjugated transition OMCPs to be high-performance TE candidates.[36, 62, 65] However, in-depth understanding of the structural and electronic properties of insoluble organo-metallic polymers is still very challenging. Consequently, experimental studies to develop OMCPs with different organic ligands as TE materials are scarce.

This chapter mainly focuses on the synthesis and characterization of three organic ligands and their incorporation into linear OMCPs, **Ni-ett**, **Ni-diett** and **Ni-btt**. The correlation between the ligand/OMCP geometries and thermoelectric properties are discussed based on both experimental and DFT results. Besides, we demonstrate for the first time that the n- or p-type thermoelectric character of the materials can be tuned via exchanging ligand. The study also highlights the importance of proper purification of these insoluble polymers to understand the intrinsic thermoelectric properties from the polymers themselves, excluding any potential effects of contaminants.

Most data and images in this chapter have been published recently, which are reused or reproduced accordingly.

2.1 Design and synthesis of square planar polymer Ni-ett, Ni-diett and Ni-btt

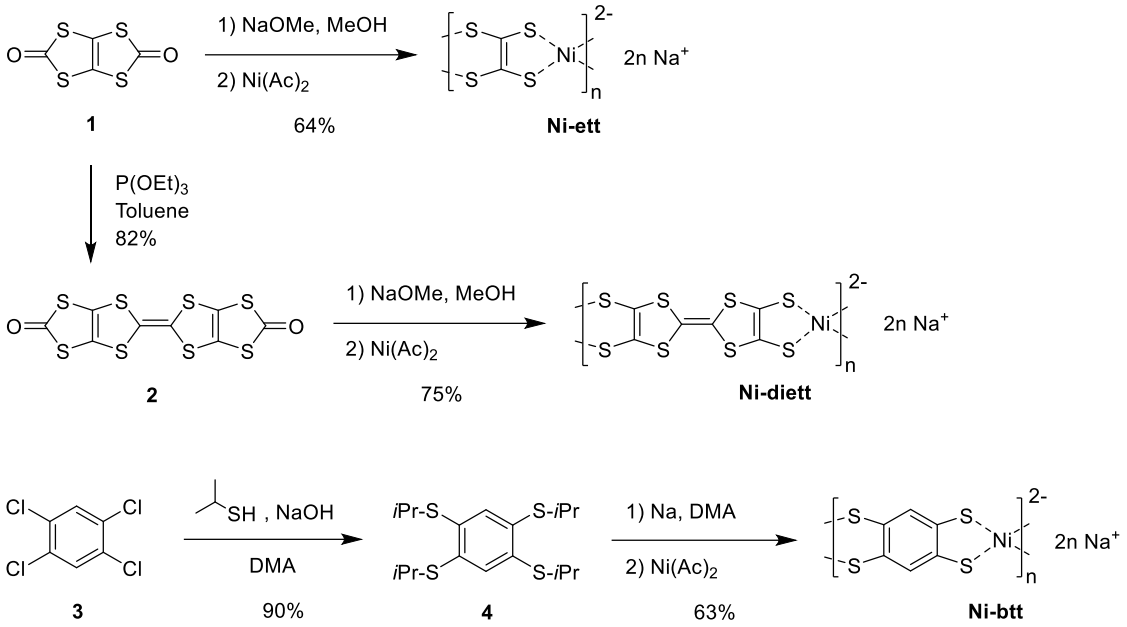

Scheme 1. *Synthetic pathway towards the different OMCPs, Ni-ett, Ni-diett and Ni-btt, and their idealized chemical structures with sodium counter cations. Reused from our recent published article.*[1]

The poly(nickel-ethylenetetrathiolate) (**Ni-ett**) was synthesized from [1,3]dithiolo[4,5-*d*][1,3]dithiole-2,5-dione (**1**) with the reported procedure ,[43] followed by an extra purification step. Then, the dimerization of **1** was carried out in the presence of triethyl phosphite to obtain [2,2'-bi[1,3]dithiolo[4,5-*d*][1,3]dithiolylidene]-5,5'-dione (**2**), which provides a longer ligand and increases the bridging distance between Ni atoms (Scheme 1). The polymerization of **2** to poly(nickel-[2,2'-bi(1,3-dithiolylidene)]-4,4',5,5'-tetrakis(thiolate)) (**Ni-diett**) used the same conditions as that for **Ni-ett**, also via a tetra anion intermediate.[77]

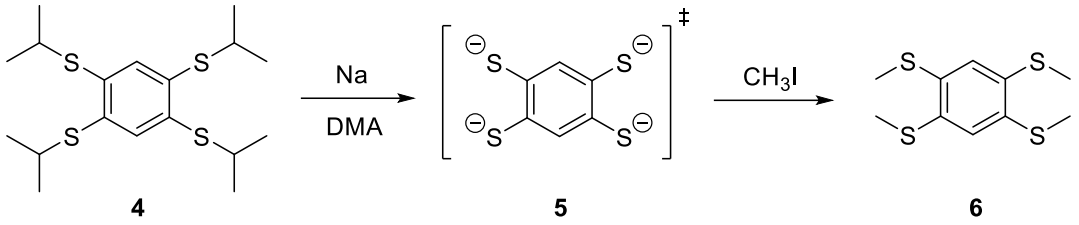

*Scheme 2. Mechanism study of the intermediate **5** confirmed by the formation of compound **6**. Reused from our recent published article.*[1]

Poly(nickel-benzene-1,2,4,5-tetrakis(thiolate) (**Ni-btt**), the third OMCP, consists of the aromatic ligand based on benzene-1,2,4,5-tetrathiol. 1,2,4,5-tetrachlorobenzene (**3**) was firstly reacted with propane-2-thiol via nucleophilic aromatic substitution (S_NAr) to yield 1,2,4,5-tetrakis(isopropylthio)benzene (**4**), which was dealkylated by sodium and coordinated with nickel (II) to form **Ni-btt** via the intermediate 1,2,4,5-benzenetetrathiolate (**5**). To verify the reaction mechanism, quenching reaction (Scheme 2) was carried out with methyl iodide (CH_3I) to produce 1,2,4,5-tetrakis(methylthio)benzene (**6**).

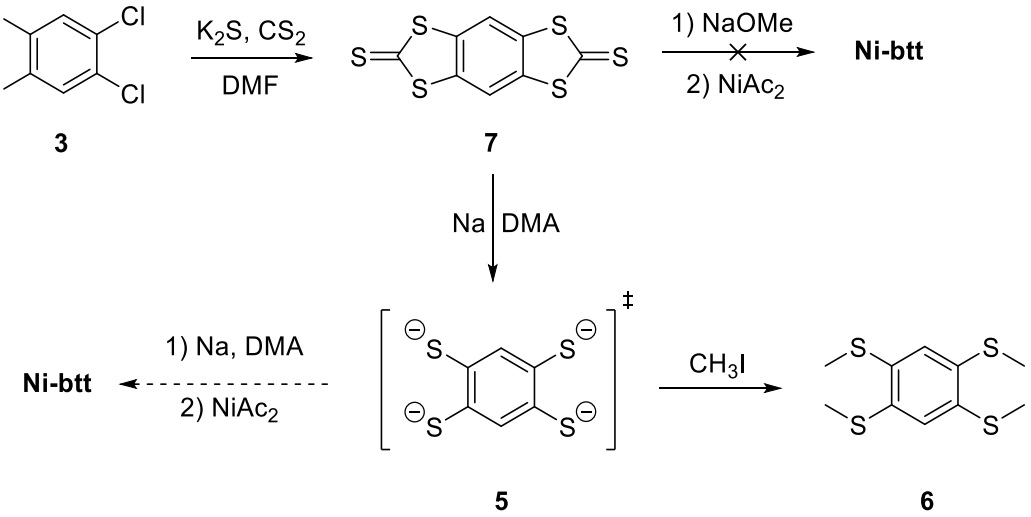

***Scheme 3**. Alternative synthetic route for Ni-btt.*

Alternatively, another route via 1,3,5,7-tetrathia-s-indacene-2,6-dithione (**7**) was

designed for the synthesis of **Ni-btt** (Scheme 3). This new route avoids the massive use of the volatile propane-2-thiol and the precursor **7** for **Ni-btt** is less stinky than **4**. Initial attempt to synthesize the **Ni-btt** from **7** with sodium methoxide in methanol, the same conditions used for **Ni-ett** and **Ni-diett**, cannot work. Even changing methanol with other solvents such as tetrahydrofuran (THF) and N,N-Dimethylformamide (DMF), or increasing reaction temperature from 65 °C to 100 °C. The eventually obtained powder from this route were dim, brown and insulating. This result indicated the sodium methoxide, as the base, is not strong enough as to react with the thionone in compound **7**, like how it reacted with the ketone moieties in compound **1** and **2**. Therefore, the sodium reduction route was applied to confirm that this reaction can form the benzene-1,2,4,5-tetrathiolate intermediate, which can be used to synthesize the polymer **Ni-btt** alternatively. All the synthetic procedures and mechanism study are provided in details in last chapter.

To synthesize all the three OMCPs, nickel chloride was initially used as the starting material due to its lower price, however, nickel acetate tetrahydrate was then used instead for all the chelation reactions due to its better solubility in polar solvents (methanol and water), allowing us to more accurately control the reaction ratio of nickel acetate to organic ligand as 1:1. However, the bulky OMCP materials are very likely to contain low molecular-weight oligomers and ionic impurities due to their insoluble nature as the OMCP chains increase in molecular weight. The OMCPs were therefore purified via Soxhlet extraction in deionized water and methanol (24 hours for each) to

exclude any effect of impurities on TE properties. Here, the efficient purification was proved to be very beneficial to the reproducibility of physical properties and reduce the batch-to-batch variations, a common problem in the synthesis of OMCPs. The effect and necessity of purification will be discussed in details in section 2.2.

2.2 Structural characterization and DFT calculation

2.2.1 Compositional and structural characterization

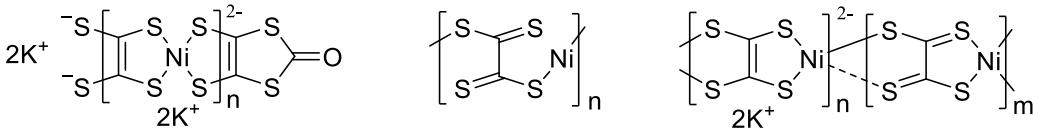

Poly[K_2(Ni-ett)] Poly(Ni-tto) Poly[K_x(Ni-ett)$_n$(Ni-tto)$_m$]

Figure 11. *Proposed structures of Ni polymer synthesized from [1,3]dithiolo[4,5-d][1,3]dithiole-2,5-dione or tetrathiooxalate salts, tetraethylammonium tetrathiooxalate (TEATTO) or sodium tetrathiooxalate (Na_2TTO) in published reports.*[39, 66, 78-79]

The valence states of Ni and the ligands are 2+ and 4-, respectively. Thus each repeat unit of the three polymers should be dianionic to form a negatively charged backbone and therefore requires compensation by two monovalent cations to give an charge-balanced structure $(Ni^{2+}L)_n^{2-} \bullet 2n\ A^+$, where A represents counter cation and L represents organic ligand, respectively. However, in the case of the well-studied Poly[A_x(Ni-ett)], the metal cations A (Li^+, Na^+ or K^+) were always found far below the stoichiometric quantities to balance the charge of the polymer framework as counter cations (Ni/ A ratios in Table **2**). There are three proposed interpretations concerning the polymer structure (Figure 11): (i) one is that the Ni partially acts as counter cations in the polymer, rather than completely being coordinated metal centres based on X-ray

photoelectron spectroscopy (XPS) analysis; (ii) while other researchers put forward a neutral polymer structure, known as Ni-tto;[78] (iii) the third proposed structure involves both ett and tto is present to be $[A_x(Ni\text{-}ett)_n(Ni\text{-}ett)_m]$.[79] Herein, in order to further understand the specific chemical composition of such OMCPs, the effects of extra purification and a series of spectroscopic measurements was performed.

***Table 2**. Summary of previously reported elemental analysis of Poly[A_x(Ni-ett)] and Ni-tto materials, where A represents the alkali counter cation. Reproduced from our recent published article.[1]*

	[K_x(Ni-ett)]				[Li_x(Ni-ett)]	[Na_x(Ni-ett)]			Ni-tto
status	powder	powder	film	powder	powder	powder	powder	powder	powder
S/Ni	3.33	-	3.5	3.51	4.77	3.53-5.93	-	5.19	4.35
Ni/A	3.39	30.21	45.78	17.58	9.02	2.57-95.7	3.61	7.64	9.39
Ref.	79	80	81	82	82	82	80	83	79

** The elemental ratios listed were provided in the cited references or calculated based on the reported data, obtained by inductively coupled plasma optical emission spectrometer (ICP-OES) and CHNS analyser.*

In this work, the three materials, **Ni-ett**, **Ni-diett** and **Ni-btt**, were all further purified by Soxhlet extraction with water and methanol before characterization. As the obtained insoluble OMCPs cannot be fabricated into film, their morphology and composition were directly examined by scanning electron microscopy (SEM) and energy-dispersive X-ray spectroscopy (EDS). SEM images showed the nonuniform size

distribution of pristine OMCP samples, with the big particles >100 μm. To avoid the subsequent roughness and batch-to-batch variations in compressed pellets, each polymer material was therefore mechanically ball-milled (Figure 12) to obtain homogenous OMCP pellets, proved by the smooth-surface images with minor cracks and imperfections (Figure 13-15).

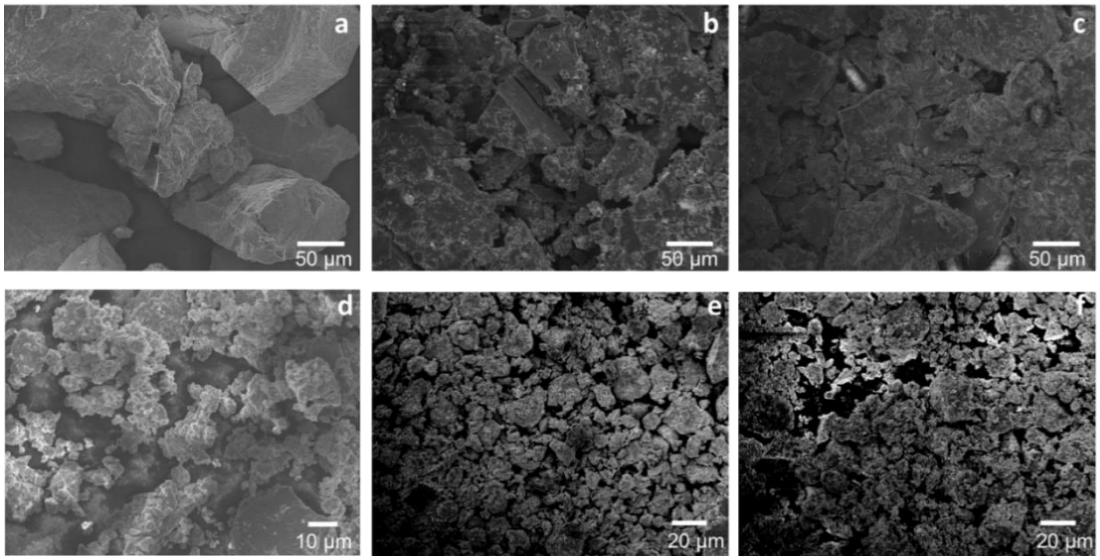

Figure 12. *SEM images of as-prepared (a)**Ni-ett**, (b) **Ni-diett** and (c) **Ni-btt** powder, and after 15-minutes of ball-milling (d) **Ni-ett**, (e) **Ni-diett** and (f) **Ni-btt** powder. Reused from our recent published article.*[1]

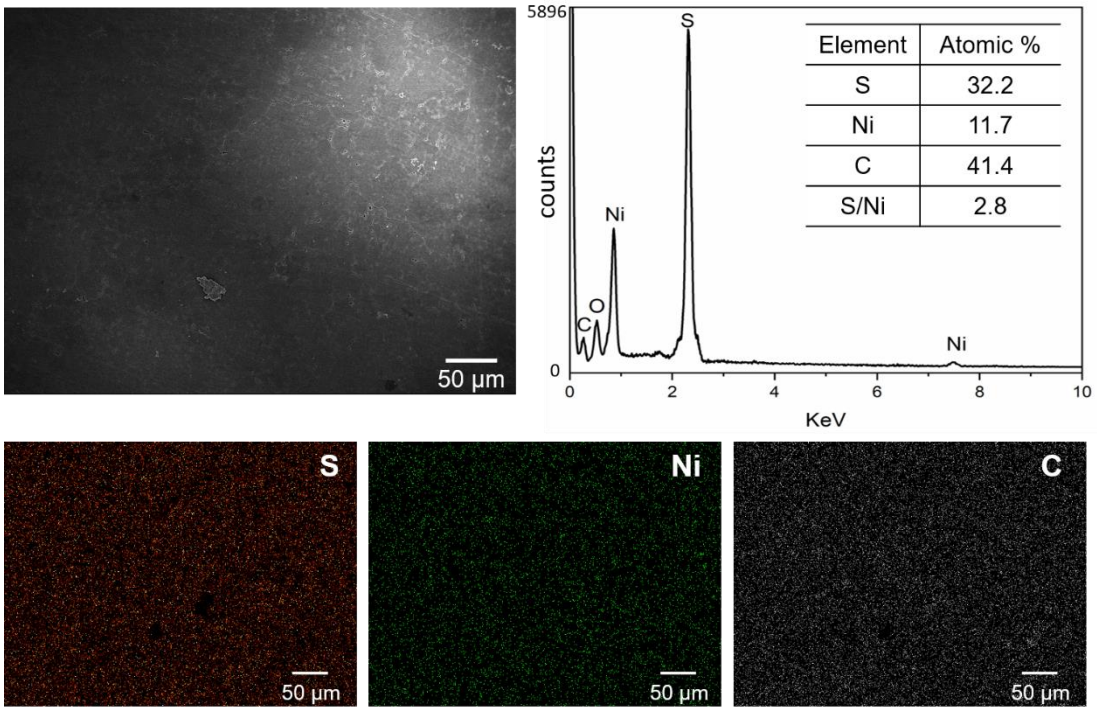

Figure 13. *SEM (top left) and EDS spectrum (top right) of the element distribution in compressed* ***Ni-ett*** *pellets. (Bottom row) Element composition maps in the compressed pellets of sulfur (S), nickel (Ni) and carbon (C). Reused from our recent published article.*[1]

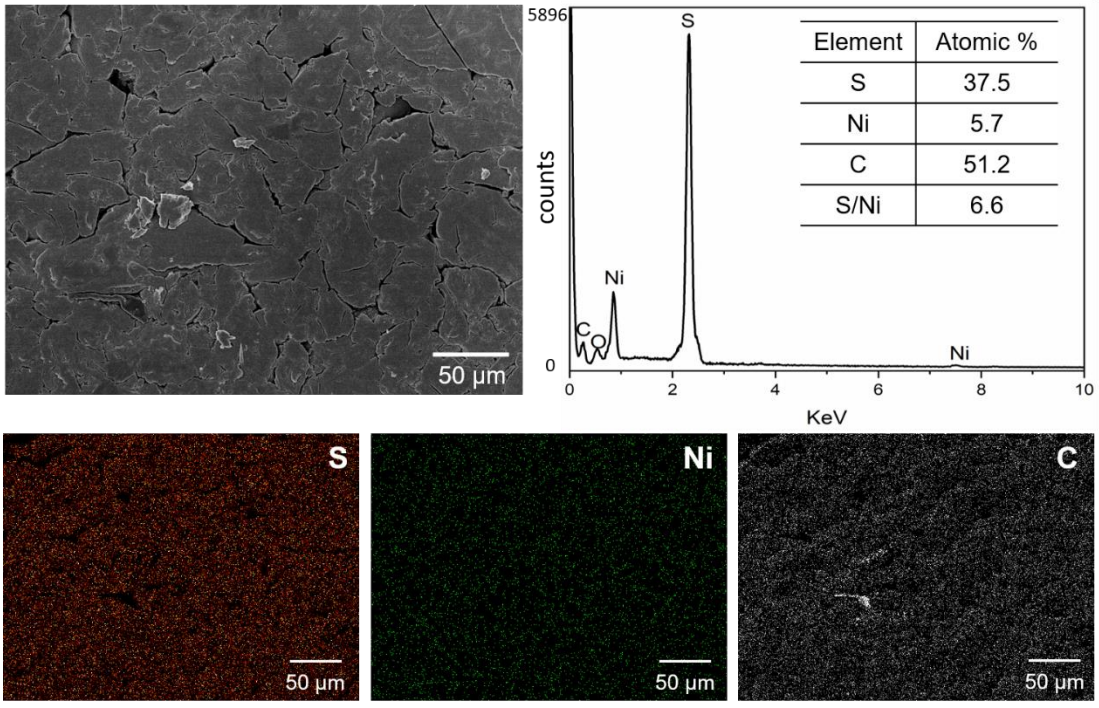

Figure 14. *SEM (top left) and EDS spectrum (top right) of the element distribution in compressed* ***Ni-diett*** *pellets. (Bottom row) Element composition maps in the compressed pellets of sulfur (S), nickel (Ni) and carbon (C) Reused from our recent published article.*[1]

.

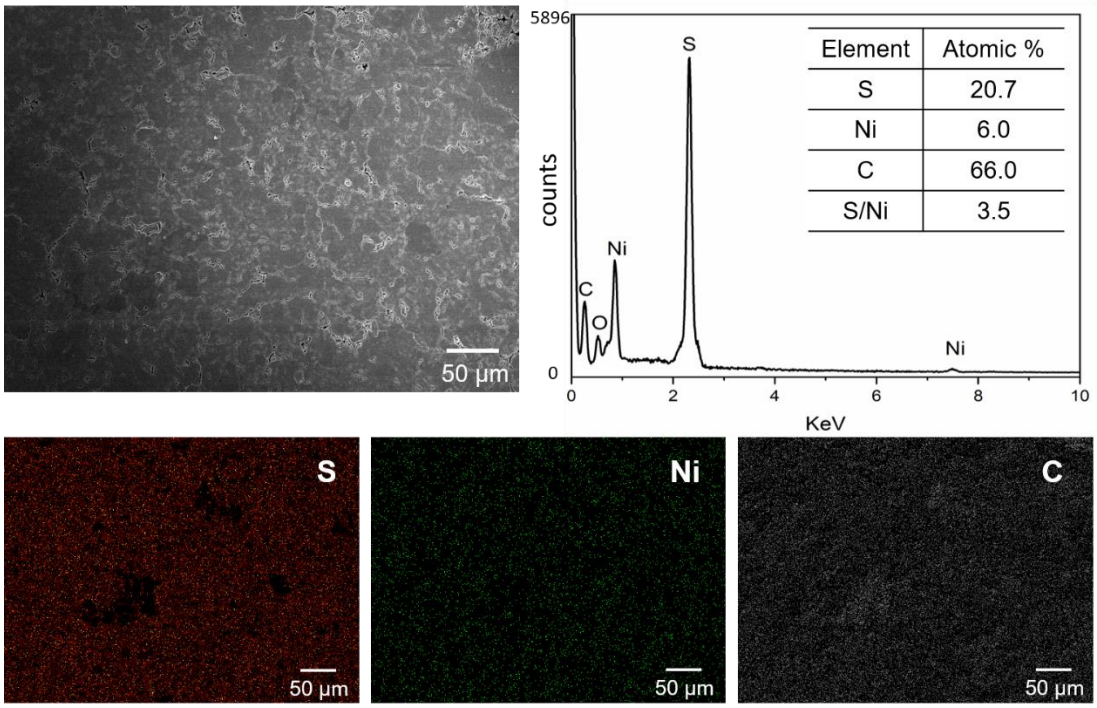

***Figure 15**. SEM (top left) and EDS spectrum (top right) of the element distribution in compressed **Ni-btt** pellets. (Bottom row) Element composition maps in the compressed pellets of sulfur (S), nickel (Ni) and carbon (C). Reused from our recent published article.*[1]

The contents of C, O, S and Ni and their compositional homogeneity in **Ni-ett**, **Ni-diett** and **Ni-btt** pellets was confirmed by EDS mapping (Table 3 and Figure 13 to 15). In terms of the overall observed deviations in the S/Ni ratios, we believe it is due to the structural defects along the polymer backbone rather than excess nickel in the OMCPs, as the later one is very unlikely after the extensive Soxhlet purification was performed. **Ni-diett** and **Ni-btt** have the experimental S/Ni ratios much closer to the corresponding theoretical values. We suggest that their larger tetra-thiolate intermediates stabilize better and facilitate the growth of higher quality polymers possible during the synthesis. However, the stabilization of the much smaller tetra-anion intermediate during the synthesis of **Ni-ett** is more difficult. Accordingly, it may lead to a richer chemistry and formation of defects and isomers during the preparation for **Ni-ett**, resulting in a less

ideal S/Ni ratio.[78-79] Compared with XRF, the EDS is a micro-regional analysis, which may also contribute to the different values of S/Ni ratio.

Table 3. *Elemental atomic percentages of C, S and Ni in compressed pellets obtained by EDS analysis. Reused from our recent published article.*[1]

Sample	C	S	Ni	S/Ni ratio[a]	S/Ni ratio[b]
Ni-ett	41.4	32.2	11.7	2.6	4
Ni-diett	51.2	37.5	5.7	6.6	8
Ni-btt	66.0	20.7	6.0	3.5	4

[a] *experimental and* [b] *theoretical values.*

XPS was employed to investigate the composition of **Ni-ett**, **Ni-diett** and **Ni-btt**. For the as-prepared polymers, XPS data showed the presence of Ni 2p, C 1s, S 2p and Na 1s core levels (Figure 16 to 18).

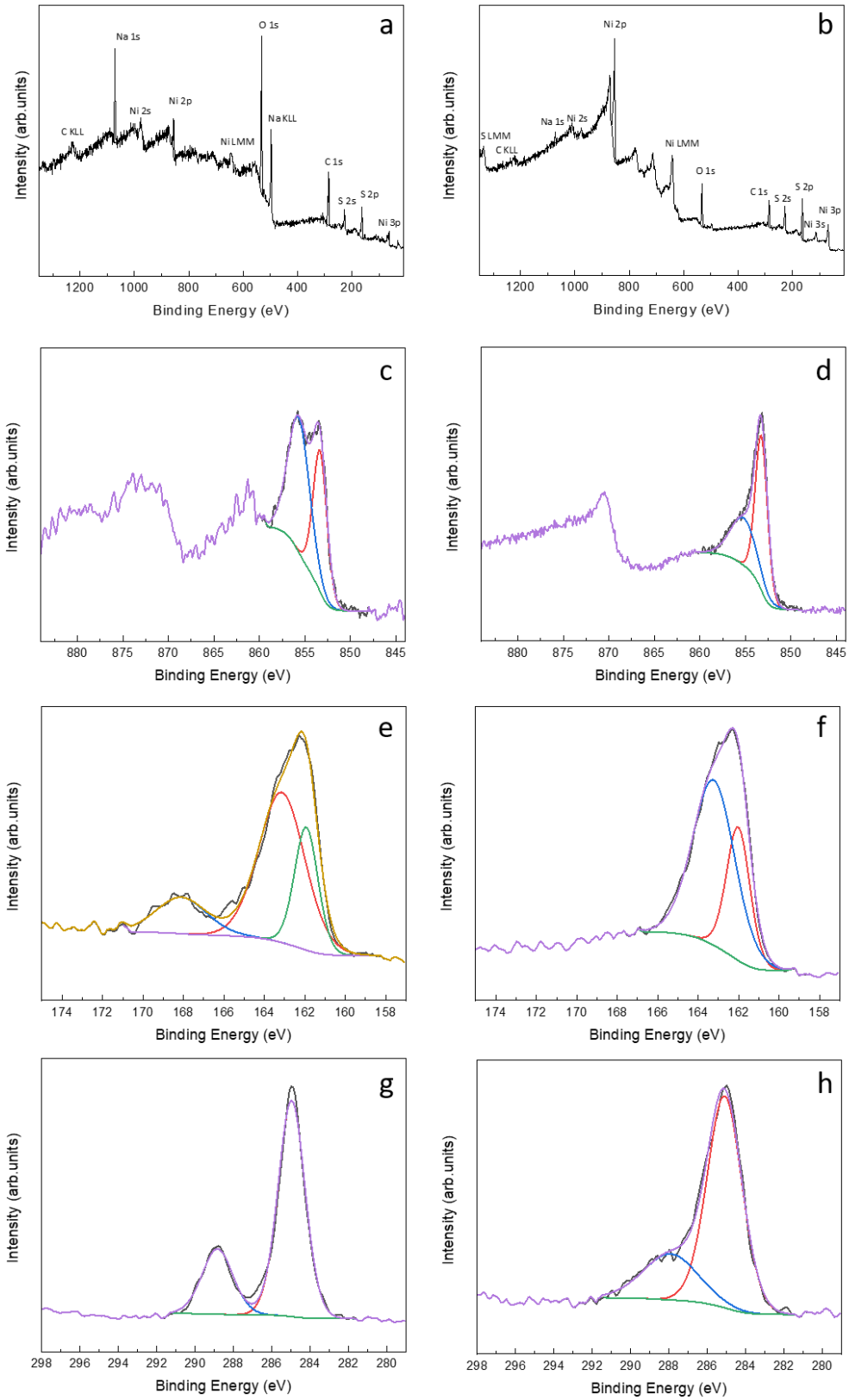

Figure 16. *XPS spectra of* ***Ni-ett****: survey spectra of (a) pristine and (b) purified; Ni 2p core level spectrum of (c) pristine and (d) purified; S 2p core level spectrum of (e) pristine and (f) purified; C 1s core level spectrum of (g) pristine and (h) purified. Reused from our recent published article.*[1]

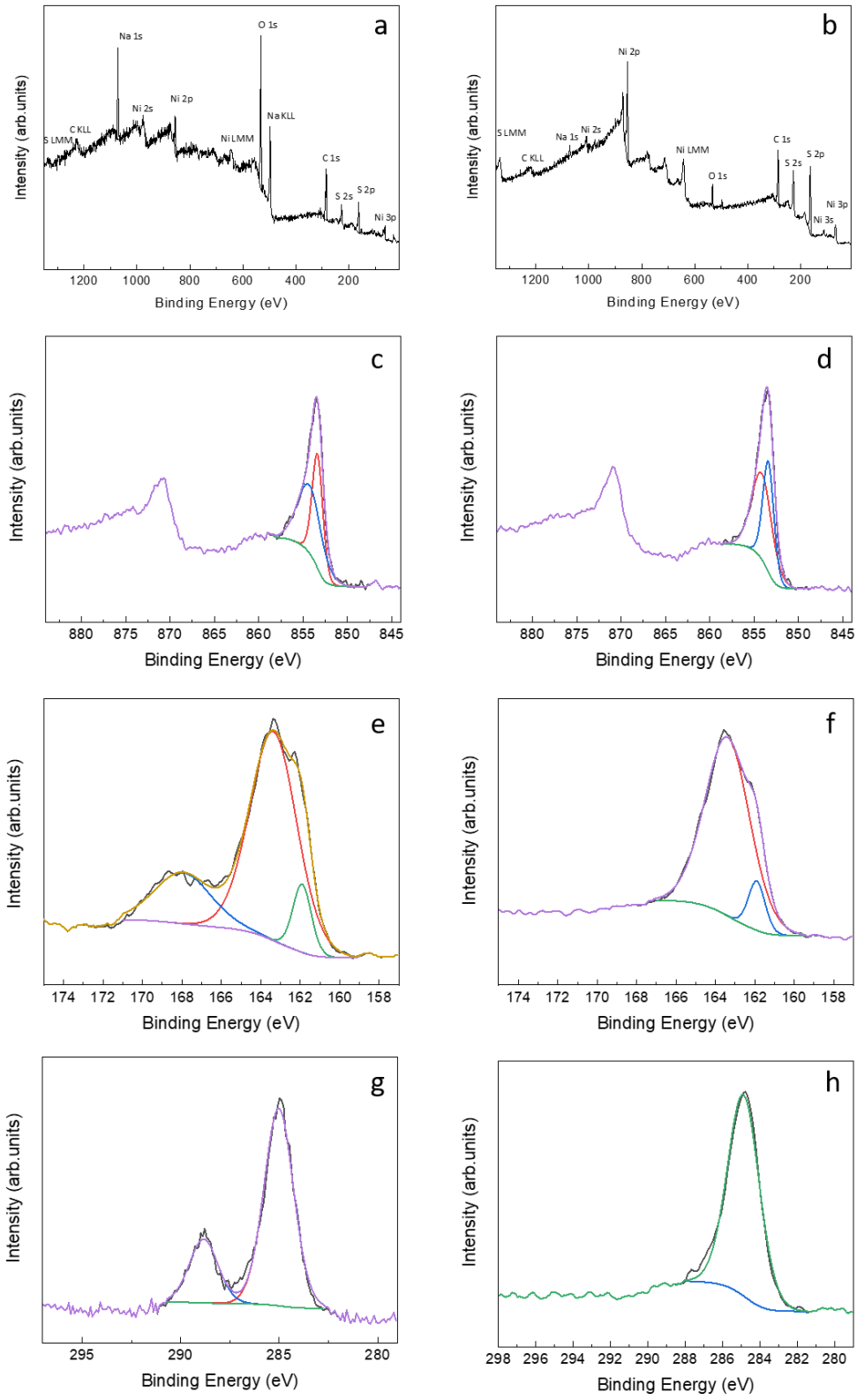

***Figure 17**. XPS spectra of **Ni-diett**: survey spectra of (a) pristine and (b) purified; Ni 2p core level spectrum of (c) pristine and (d) purified; S 2p core level spectrum of (e) pristine and (f) purified; C 1s core level spectrum of (g) pristine and (h) purified. Reused from our recent published article.*[1]

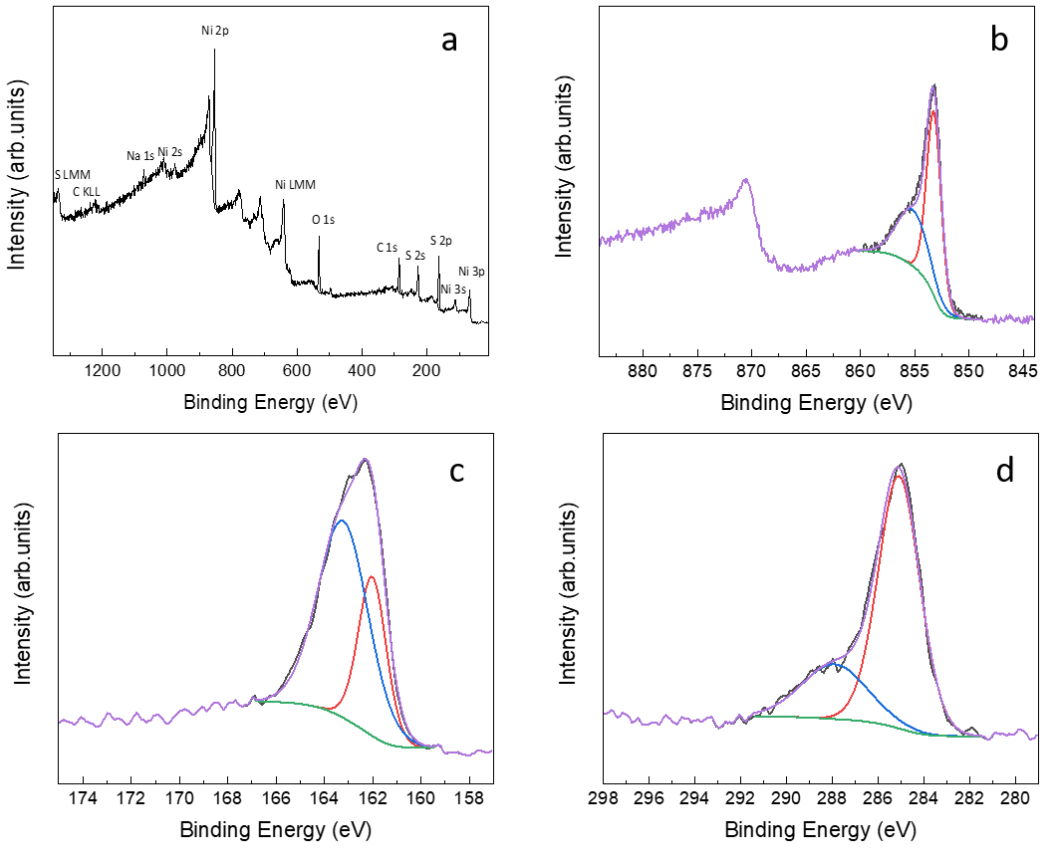

***Figure 18**. (a) XPS energy survey spectra, (b) Ni 2p, (c) S 2p and (d) C 1s core level spectra of purified **Ni-btt**. Reused from our recent published article.[1]*

In earlier studies, the Na 1s signal in the XPS energy survey spectra of **Ni-ett** was assigned to Na^+ as counter ions, coming from the sodium methoxide (NaOMe) used during the reaction.[80, 82] A sharp decrease of the Na 1s peak initially located at 1071 eV was observed in the carefully purified OMCPs via Soxhlet extractions. X-ray fluorescence (XRF) results (Table 4) did not show the presence of Na in purified **Ni-ett**, **Ni-diett** and **Ni-btt**, however alternative XRF analysis with thin beryllium window X-ray tube is suggested here for higher sensitivity for such light element in future work. Meanwhile, the C 1s peak centered around 289 eV, representing the carbonyl functional

groups formed during the synthesis of **Ni-ett** and **Ni-diett**, was not detectable after the OMCPs were purified. These results are consistent with EDS and XRF analysis, together verifying the successful removal of inorganic impurities and confirming the efficacy of Soxhlet extraction to purify the OMCP polymers. Hence, the obtained overall higher quality materials allow us to largely exclude ionic effects on the intrinsic TE properties of the polymers, improving the reproducibility of these OMCPs and reducing the effect of the cation with fluctuating content from batch to batch, like the case of the well-studied Poly[A_x(Ni-ett)] in Table 2.

***Table 4**. XRF of element contents (weight % and atomic %) and corresponding atomic S/Ni ratio of **Ni-ett**, **Ni-diett** and **Ni-btt**. Reused from our recent published article.[1]*

Ni-ett S/Ni = 3.01			**Ni-diett** S/Ni = 7.33			**Ni-btt** S/Ni = 3.31		
Element	**wt%**	**at%**	**Element**	**wt%**	**at%**	**Element**	**wt%**	**at%**
S	**61.6%**	**68.3%**	**S**	**79.1%**	**78.4%**	**S**	**62.5%**	**67.9%**
Ni	**37.5%**	**22.7%**	**Ni**	**19.7%**	**10.7%**	**Ni**	**34.5%**	**20.5%**
Al	0.64%	0.85%	Al	0.70%	0.82%	P	1.01%	1.14%
Si	0.12%	0.15%	P	0.24%	0.24%	Si	0.85%	1.05%
Fe	571.8 ppm	363.7 ppm	Si	0.12%	0.13%	Ca	0.61%	0.53%
Ca	279.6 ppm	247.8 ppm	Fe	778.8 ppm	443.1 ppm	Zn	0.20%	0.11%
Y	200.9 ppm	80.3 ppm	Ca	593.2 ppm	470.3 ppm	Er	0.12%	0.03%
Zn	144.7 ppm	78.6 ppm	Y	107.0 ppm	38.2 ppm	Br	679.4 ppm	296.3 ppm
Zr	53.0 ppm	20.6 ppm	Os	45.6 ppm	7.6 ppm	I	661.9 ppm	181.8 ppm
Re	37.1 ppm	7.1 ppm	Zr	32.0 ppm	11.1 ppm	Fe	351.6 ppm	219.4 ppm
Au	22.1 ppm	4.0 ppm	Au	19.0 ppm	3.1 ppm	Sb	164.0 ppm	46.9 ppm
			Ge	7.8 ppm	3.4 ppm	Sn	138.8 ppm	40.7 ppm
						Te	105.7 ppm	28.9 ppm
						Ti	57.0 ppm	41.5 ppm
						Ba	30.4 ppm	7.7 ppm
						Pb	13.3 ppm	2.2 ppm
						As	11.8 ppm	5.5 ppm
						Sr	6.4 ppm	2.5 ppm
						Se	1.7 ppm	0.75 ppm

In the Ni 2p photoemission spectra of the purified OMCPs, the set of peaks with binding energies of 853 and 873 eV, were assigned to the Ni $2p_{3/2}$ and Ni $2p_{1/2}$, respectively. Here we suggest these peaks majorly origin from the Ni^{2+} species in Ni-S coordination. This result excluded the unlikely contribute from Ni^{4+} species, whose main peak of Ni $2p_{3/2}$ usually emerges at higher binding energy range (> 856 eV).[84-85]

Meanwhile, the super weak signals found by EPR suggested the possible presence of Ni^{3+} impurities, whose peak might originating from polymer ending and be difficult to distinguish from Ni^{2+} species (further discussed below). In case of pristine **Ni-ett**, two distinct Ni $2p_{3/2}$ peaks, derived from XPS fitting at 855.8 eV and 853.4 eV. Earlier reports suggested this is because the co-existence of the center Ni atoms in square planar coordination and the Ni atoms acting as counter cations, in other words, two nickel environments. Other reports attributed a similar Ni $2p_{3/2}$ spectra to a single type of centered Ni atom in a two-dimensional organic framework.[80, 86] However, an evident decrease of the fitted peak at 855.8 eV and a disappearance of satellite peaks at 861 eV were observed in purified **Ni-ett**, in the comparison of the Ni $p_{3/2}$ peaks of as-prepared **Ni-ett**. Without existence of nickel impurities in OMCPs suggested by EDS or XRF measure, here we believe the two Ni $2p_{3/2}$ signals is due to multiplet-splitting rather than different nickel environments. The multiple-splitting is very common phenomenon in inorganic nickel compounds, such as like NiO, $Ni(OH)_2$ and NiS.[87-88] The reason behind is that following the photoelectron emission, the remaining unpaired electron might couple with other unpaired electrons within the atom, which causes different electronic configurations with varying energies and thereby forming asymmetric splitting.

For the as-prepared materials, the S 2p narrow range scans of all the three purified polymers all showed main peaks with binding energies of 161.9 and 163.3 eV, deriving from the complexation between Ni and S units (Figure 16 to 18). Prior to purification,

there was a weak peak at 168.3 eV observed in the S 2p spectra of both **Ni-ett** and **Ni-diett**, which is assigned to sulfate moieties, consistent with reported values.[89]

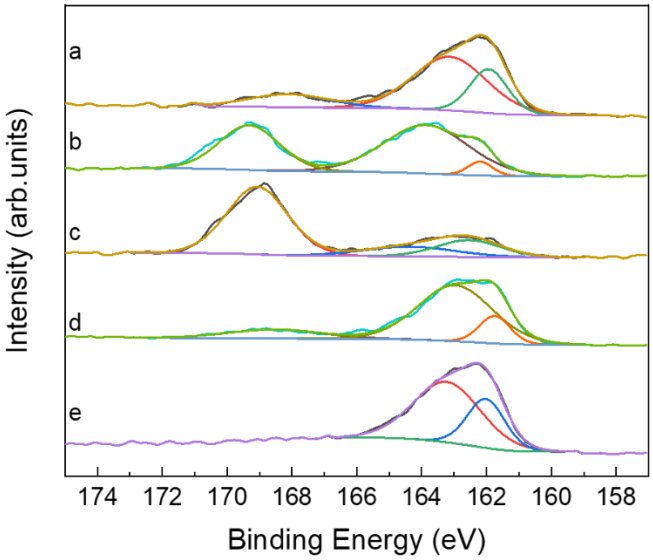

Figure 19. *S 2p core level XPS spectrum of various* ***Ni-ett*** *samples (a) as-prepared and without purification; (b) 12-month-exposure to ambient conditions; (c) 18-month exposure to ambient conditions; (d) purified Ni-ett after 12-month air exposure; (e) as-prepared Ni-ett after purification. Reused from our recent published article.*[1]

Further evidence regarding the partial sulfur oxidation was found in the S 2p XPS spectra of polymer **Ni-ett** samples exposed to air over 12 to 18 months under ambient environment (Figure 19). After 12 months, an intense peak centered around 168.5 eV was observed in the **Ni-ett** sample. The sulfate peak of the sample after 18-month air exposure was more pronounced, even surpassing that of Ni-S. Additionally, the oxidation did not only happen at the OMCP surface, as reflected by the depth profiling (Figure 20), showing the presence of the sulfate peak around 168.5 eV as well.

Notably, these results proved that the purification via Soxhlet extraction can efficiently remove the oxidized impurities, as evidenced by the significant decrease of the signal from sulfate groups in S 2p spectra of **Ni-ett** and **Ni-diett**, for both as-

prepared and oxidized samples (Figure 16, 17 and 19). The soluble oxidized impurities formed over time are assumed to occur with partial depolymerization during the oxidation, as no reductive conditions were involved during the purification. Thus, the Soxhlet extraction was adopted as a general procedure for all the other OMCPs in our work.

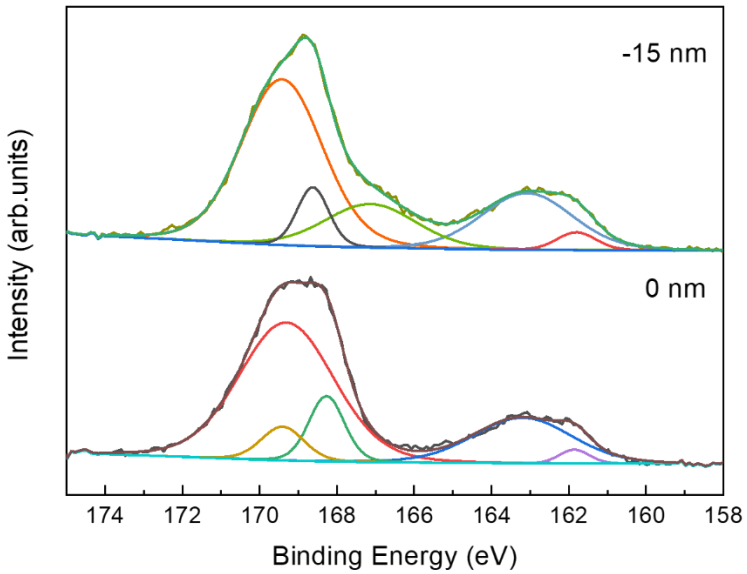

Figure 20. *S 2p core level XPS spectrum of* ***Ni-ett*** *at the surface (a) and 15 nm beneath (b) after 18-month of oxidation. Reused from our recent published article.*[1]

To deepen the understanding of the geometry of the Ni-S complexes in the three OMCPs, nickel k-edge X-ray absorption near-edge structure (XANES) measurements were performed (Figure 21 and Table 5). On one hand, the similar position of the absorption edge in the three samples implies their identical oxidation states for Ni atoms. On the other hand, the obvious differences observed at the top of the edge between 8340 and 8370 eV indicate structural variations in the Ni-S environments.

The magnitude of the first peak in the Fourier transforms represents Ni-S distances,

where the three samples show obvious differences due to the different degree of disorder in the Ni-S environment (Figure 21b). The lowest degree of disorder was observed for **Ni-diett** and the highest for **Ni-ett**. Though the origins of the increased disorder in such insoluble OMCPs cannot be determined, it could be related with the resonance structures: there would be fewer variations in Ni-S bond lengths given the limited resonance structure in **Ni-diett**, compared with the more extensive resonance ones in **Ni-ett** and **Ni-btt** (Scheme 4).

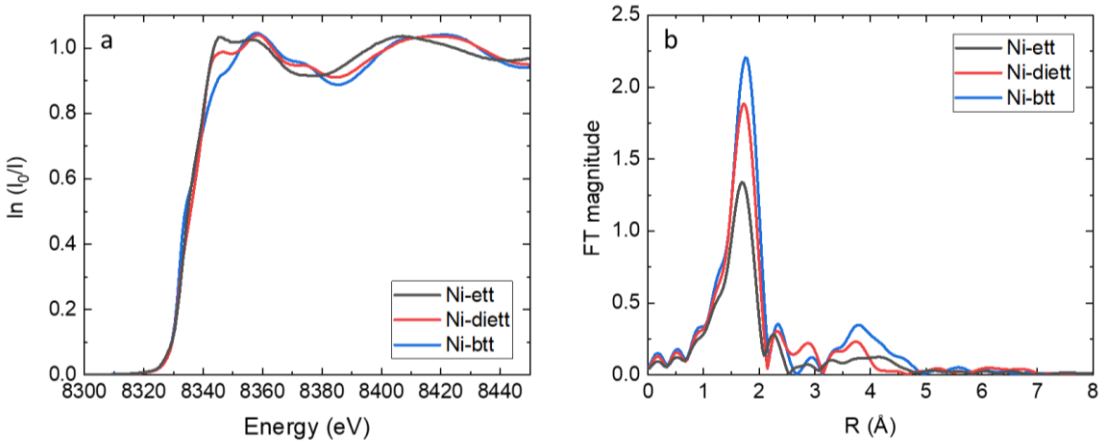

Figure 21. *(a) Ni K-edge XANES spectra of **Ni-ett**, **Ni-diett** and **Ni-btt**; (b) Fourier transform magnitudes of the Ni K-edge EXAFS. Reused from our recent published article.*[1]

Table 5. *Extracted XANES parameters for **Ni-ett**, **Ni-diett** and **Ni-btt**. Data reused from our recent published article.*[1]

Sample	N [a]	σ^2 ($\times10^{-3}$) [b]	*R* (Å)
Ni-ett	3.39	5.7	2.17
Ni-diett	3.91	2.8	2.18
Ni-btt	3.28	2.5	2.16

[a] number of neighbours; [b] mean-squares deviation for a Gaussian distribution of R

As **Ni-ett**, **Ni-diett** and **Ni-btt** all contain thioether bonds and organic ligands with differing electron-donating character, understanding the nature of Ni-S bonding is of great interest for parallel comparison. Hence, a combination of attenuated total reflection Fourier transform infrared (ATR-FTIR) and resonance Raman spectroscopies were explored to characterize the three Ni^{2+}-thiolate coordinated polymers in more details (Figure 23 and 24). The corresponding spectra of small molecular complex as model and compounds (1, 2 and 4) were also recorded (Figure 22 and 25).

There have been few studies involving the spectroscopic details and the correlation to structural characters of analogous MS_4 organometallic polymers. Notably, a series of square planar complexes formed with Ni(II) and methyl or butyl substituted benzene-1,2-dithiolate, namely $(L^{Me})^{2-}$ or $(L^{Bu})^{2-}$ have been thoroughly understood. Especially, the monoanionic structure $[Ni^{II}(L^{alkyl})(L^{alkyl\cdot})]^-$ presents strikingly air-stability other than neutral dianionic $[Ni^{II}(L^{alkyl\cdot})_2]^0$, and both are associated with π-radical-anion character.[90-92] Recent research have also revealed that the C=S· stretching vibration mode, in the range of 1082-1114 cm^{-1} in IR spectra, represents the S,S-coordinated radicals in the coordinated complexes based on 3,5-ditertbutyl-benzene-1,2-dithiolato ligand and divalent metal centers (Ni, Pd, Pt).[93]

Hence, we also synthesized a complex compound based on Ni^{2+} and ligand benzenedithiolato (bdt), $(NBu_4)[Ni(bdt)_2]$, where NBu_4^+ is tetra-n-butylammonium cation. The spectroscopic features of its obtained single crystal were examined as the model for the three OMCPs. The complex $[Ni(bdt)_2]^{\bullet-}$ showed a set of strong spilt peaks

at 1020 and 1048 cm^{-1} in IR spectra (highlighted with red arrows in Figure 22a), in line with the C=S· feature in abovementioned reports. Correspondingly, an evident band at 1098 cm^{-1} present in the Raman spectra of this complexes (Figure 22b).

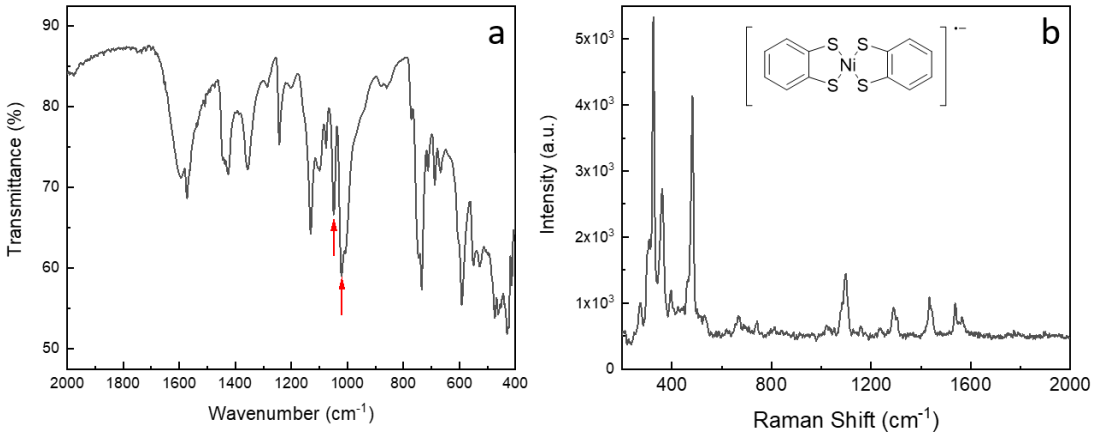

***Figure 22**. (a) FTIR spectra and (b) Resonance Raman spectra of complex model $[Ni(bdt)_2]^{\cdot -}$.*

In this study, **Ni-ett** shows the C=S˙ stretching mode with an obvious peak at 1074 and a weak shoulder peak at 1163 cm^{-1} in IR spectrum. Similarly, the spilt peaks located at 1173-1142 cm^{-1} and a weaker peak at 1038 cm^{-1} were observed in **Ni-diett**. This feature can be easily distinguished from the IR absorption bands of υ(C=S·), previously demonstrated as strong bands (no split peak) at wavenumbers around 1146 cm^{-1} in Ni^{2+} complexes.[94]

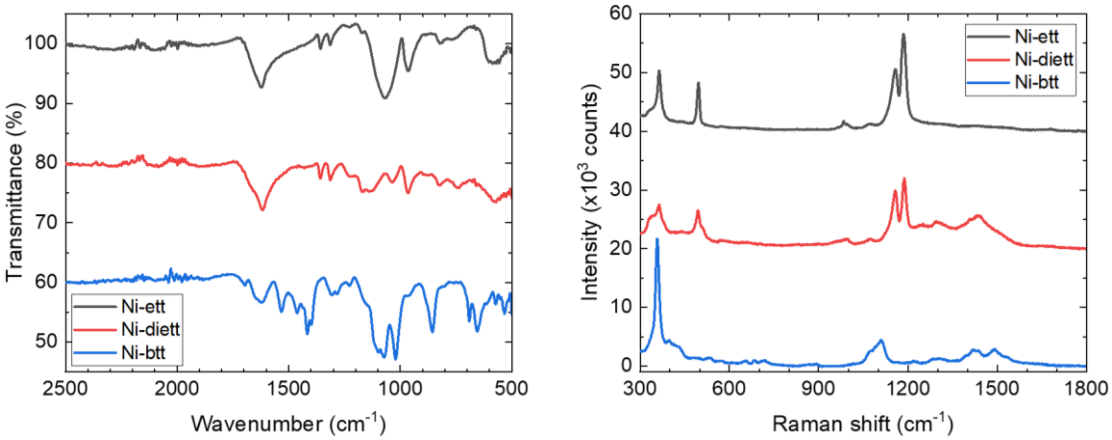

***Figure 23**. (a) FTIR and (b) resonance Raman spectra of the three OMCPs after purification with 785 nm excitation. The spectra have been stacked for clarity. Reused from our recent published article.[1]*

The results from the IR-spectra are further underscored by Raman spectra. Similar split peaks at 1158 and 1186 cm^{-1} were found in Raman spectra of **Ni-ett** and **Ni-diett**, confirming the presence of thiocarbonyl radicals (C=S˙). In addition, both **Ni-ett** and **Ni-diett** possess same peaks at 364 and 496 cm^{-1}, representing the υ(Ni-S) and ring deformation, respectively.[95] The overall very similar Raman spectrum of the two OMCPs can be understood by their intrinsic similarity in terms of the organic ligands or chemical bonds, especially in the lower wavenumbers range (<1200 cm^{-1}). However, **Ni-diett** have several weak and broad peaks at larger wavenumbers (>1200 cm^{-1}), absent in **Ni-ett** spectrum. Equal features were also found in **Ni-btt** with weak peaks at 1297, 1430 and 1491 cm^{-1}, which are assigned to the H-C-C scissor vibration, aromatic semicircular stretching and the ring quadrant stretching mode, respectively. Correspondingly, the peaks observed in complex $[Ni(bdt)_2]^{\bullet-}$ are more clearer at highly close locations at 1290 cm^{-1}, 1433 cm^{-1} and a spilt peak at 1537-1564 cm^{-1}, with its coherent structural similarity to polymer **Ni-btt**. These signals related to benzene ring

were also found in the Raman spectra of compound **4**, as starting material (Figure 25).[96] By the same token, those peaks in **Ni-diett** are assigned to the remaining inner-ring and ring-bridging C=C stretch vibration compared with the spectrum of its starting material (compound **2)**, supported by the presence of sharp peaks at 1474 and 1495 cm^{-1}.

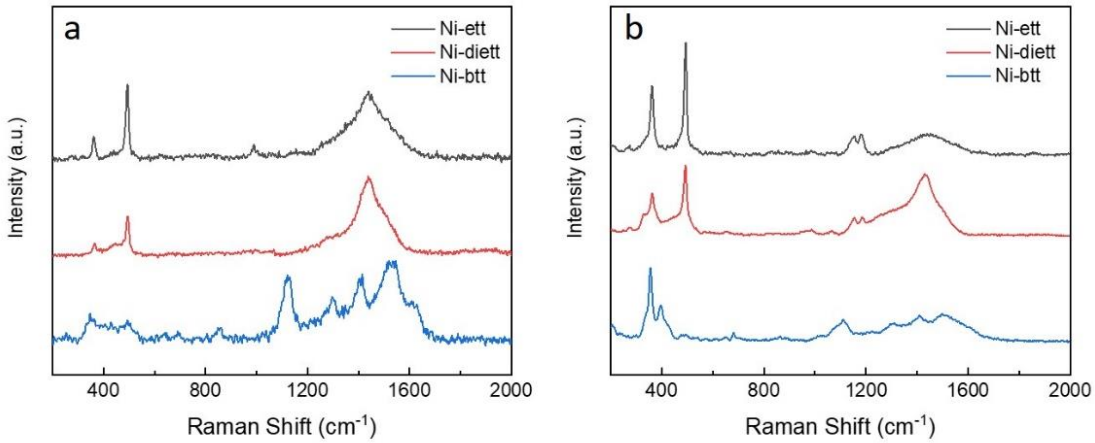

***Figure 24**. Resonance Raman spectra of the three OMCPs after purification with (a)524 nm excitation and (b) 633 nm excitation. The spectra have been stacked for clarity.*

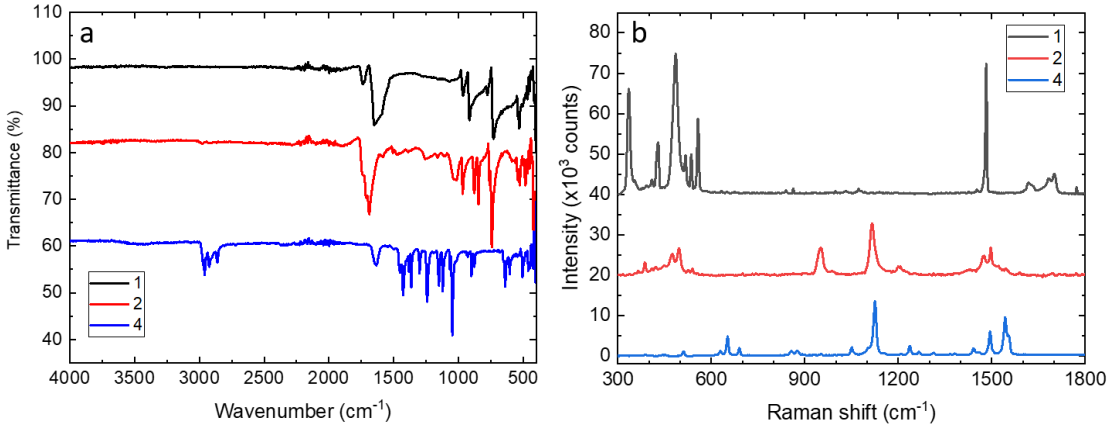

***Figure 25**. (a) FTIR spectra of the organic ligands 1, 2, and 4 before polymerisation; (b) Resonance Raman spectra of compounds 1, 2 and 4 with 785 nm excitation. The spectra have been stacked for clarity. Reused from our recent published article.[1]*

Analogously, the broad peak around at 1100 cm^{-1} found in Raman spectra of **Ni-btt** is assigned to the (Ar)C=S stretching vibration in the ligand. Corresponding signals in the IR spectra of **Ni-btt** are the split peaks at 1110-1073 cm^{-1} and an intense peak at

1019 cm^{-1}, as the υ(C=S˙) feature involving radical anion ligands. Besides, **Ni-btt** has a sharp peak at 357 cm^{-1} associated with the Ni-S stretch vibration.

All the observed spectroscopic features, together with the elemental composition obtained by EDS and XRF, suggest the three OMCPs possess neutral backbones without a significant number of counter cations. With the confirmed presence of thiocarbonyl radicals (C=S˙) by IR and Raman studies, the OMCPs are interpreted as the radical forms in Scheme 4.

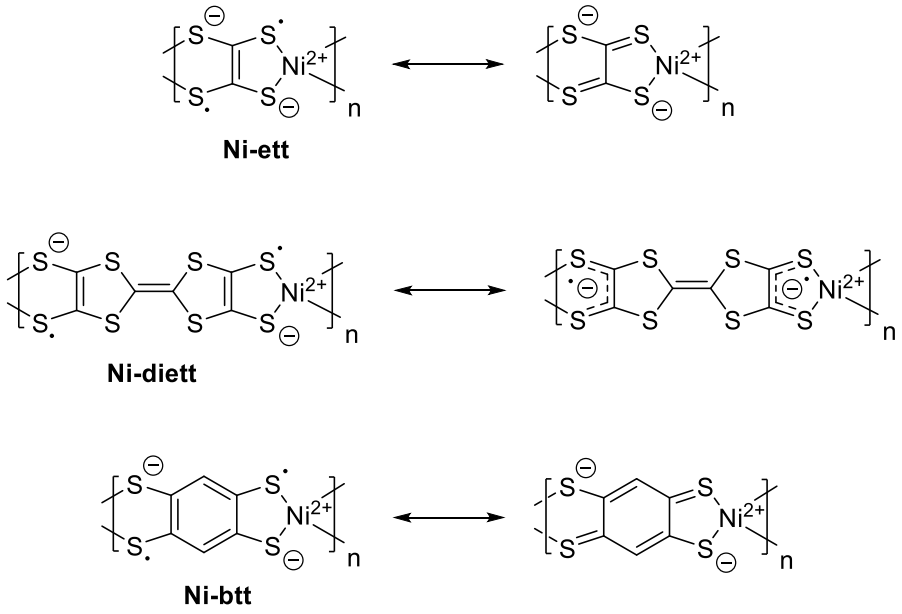

Scheme 4. *Proposed chemical structures of charge neutral OMCPs based on this work. Reused from our recent published article.*[1]

Here, although DFT data of IR or Raman spectrum for the OMCPs is unavailable without having recourse to long and costly computations. Fortunately, using IR and Raman spectroscopy and employing the air-stable radical MS_4 complexes as models allowed us to further understand the radical features of the obtained OMCPs and shine light on the nature of the polymer structures.

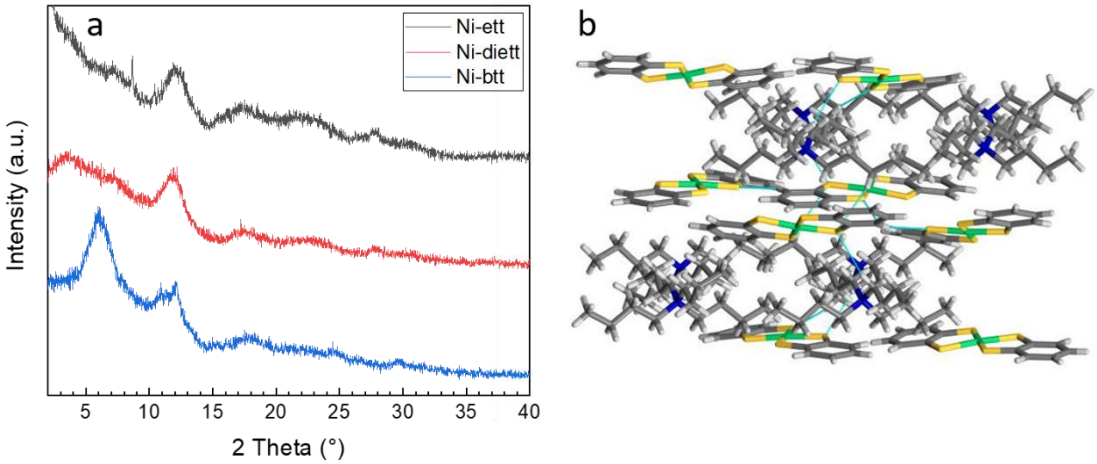

***Figure 26**. (a) Powder X-ray diffraction spectra of the three OMCP materials; (b) single crystal X-ray diffraction of $(NBu_4)[Ni(bdt)_2]$, where element Ni, S, N, C, H were represented by green, yellow, navy, grey and white, respectively. Graph (a) is reused from our recent published article.[1]*

The single crystal X-ray diffraction applied for the small complex model (Figure 26b) revealed its square planar Ni-S coordination, as well as its stoichiometric ratio between the counter cation (NBu_4^+) and Ni-S complex to be 1:1, which confirmed its structure as $(NBu_4)[Ni(bdt)_2]$. The core complex units, $[Ni(bdt)_2]^{\cdot-}$, present a parallel stacking between the layers, where the NBu_4^+ cations intercalate between. The bond distance between Ni-S in $(NBu_4)[Ni(bdt)_2]$ was measure to be 2.15, very close to that of Ni-btt (2.16) measured by XANES (Table 5).

As the film X-ray diffraction or the single crystal X-ray diffraction is impractical to investigate the polymer chain packing for the three OMCP materials due to their insolubility, the powder X-ray diffraction patterns were recorded to investigate the solid-state samples of the OMCP materials, shown in Figure 26a. The lamellar stacking distance d-spacing in both **Ni-ett** and **Ni-diett** was found to be 3.42 Å, according to the equivalent broad peak at 11.9° for both materials. This is not surprising given the structural similarity of both materials. In spite of a weak and spilt peak at 11.9°, a unique

and intense peak at 6.0° was observed in the diffraction pattern of the **Ni-btt** powder, indicating a larger d-spacing of 6.78 Å compared with **Ni-ett** and **Ni-diett**. It can be understood by its bulkier π-conjugated spacer with the six-membered benzene ring (benzene-1,2,4,5-tetrathiolate). Overall, the OMCP materials synthesized here are not entirely amorphous, showing several weak and broad peaks. Meanwhile, the structure of the ligand directly affects the polymer packing, especially reflected on the lamellar stacking distances.

2.2.2 Electronic structure characterization.

Ultraviolet photoelectron spectroscopy (UPS) was performed to obtain the work functions (Φ) and densities of valence electronic states (Figure 27). **Ni-btt** present the lowest Φ value of 4.9 eV, whereas the Φ values for **Ni-ett** (4.7 eV) and **Ni-diett** (4.6 eV) were close due to the high structural similarity between the two OMCPs. In general, disorder induced tails extending towards the Fermi energy (EF) level were observed in all the three OMCPs, rather than sharp edge. In a similar case of PEDOT:PSS, the disorder within the polymer structure was also believed to cause the tail associated with localized filled states.[97]

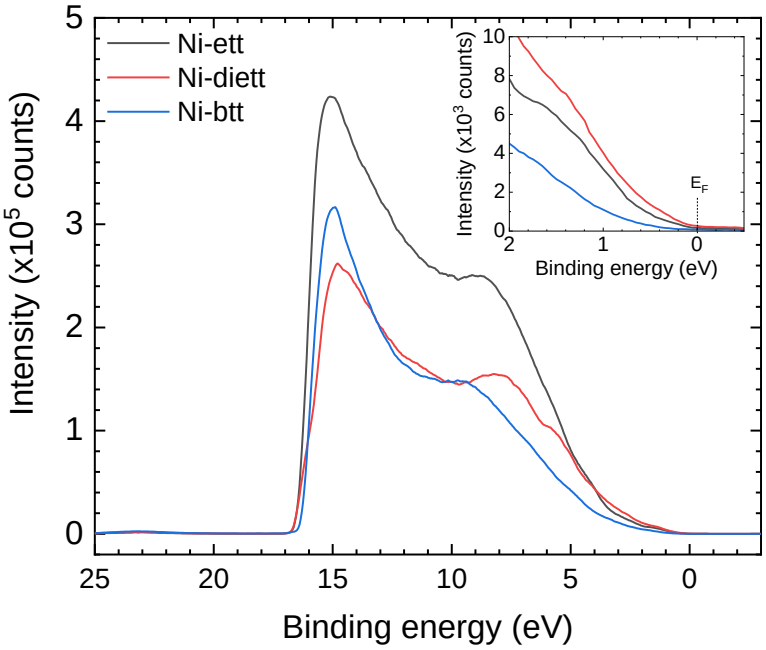

Figure 27*. UPS valence band spectra of the three OMCPs. The enlarged Fermi edge region energy region is shown in the inset. Reused from our recent published article.*[1]

The superconducting quantum interference device (SQUID) was used to measure the temperature dependence of the OMCP's magnetization (*M*), shown in Figure 29. Typical antiferromagnetic behavior was observed for both **Ni-ett** and **Ni-btt**, with small magnetic moments and peaks present around 8 K in the zero-field cooling (ZFC) in the corresponding respective *M-T* curves. However, as no peak was shown in the field cooling (FC) *M-T* curves, it was assumed that the applied magnetic field induced the weak spontaneous magnetization, which was supported by the hysteresis loops in the *M-H* curves at 2 K. Despite the high magnetic fields (up to 50 kOe), the magnetization did not saturate, implying that it is instigated by spin canting in antiferromagnetic states. **Ni-ett** had similarities with **Ni-btt** in terms of *M-T* and *M-H* curves, while the former OMCP has one order of magnitude stronger magnetization. The FC curves of both obey

the Curie-Weiss equation, $\chi_m = C_m/(T - T_c)$, where T_c is the critical temperature and C_m is the Curie constant. In contrast, **Ni-diett** has a much smaller magnetization, whose FC curve follow the simple Curie-Weiss law, $\chi_m = C_m/(T-\theta)$, where θ represents Weiss temperature.

Further, EPR spectra were measured for the three polymers to provide more insight into their electronic structures. Without exception, all the OMCPs showed only weak EPR signals, among which **Ni-ett** was the most different in terms of signal strength and shape (Figure 28). For **Ni-ett**, the very broad signal showing around 100 mT could be associated to a biradical with an integer spin state (S = 1 and g ~ 2), whose zero-field splitting parameter (b_2^0) is comparable to reported values regarding Ni^{2+} cations in inorganic materials (Table 6).[98] The super weak EPR signal of **Ni-diett** and **Ni-btt** cannot be determined yet, here we provide two possible explanations as follows: (i) One possible origin is hypothesized to be the Ni^{3+} impurities with a half-integer spin (S = ½).[99] The XPS results did not specifically reflected the existence of Ni^{3+} within these polymers, as the peak might be mingled with the peak of Ni $2p_{3/2}$ located at ~855 eV from Ni^{2+} species and thereby difficult to distinguish. However, it also does not contradict the possible presence of Ni^{3+} suggested by EPR findings; (ii) The second possibility is relevant to the inevitable defects existing at the chain ends, where the localization of unpaired electrons could occur. Then, the spin concentration of unpaired electrons in these materials was estimated by using the EPR areal integral, where the electron spin was assumed to be S = ½ (Table 6). The three OMCP samples all present

very comparable to highly conducting polyaniline in terms of spin concentrations, around one per hundred repeating units (converted from 10^{20}-10^{22}/mol).[100] Furthermore, the three OMCPs were demonstrated to be mostly EPR silent, with higher magnetic moments per repeating unit according to the SQUID measurements than those converted from EPR signals. Hence, the weak signals shown in EPR spectra are likely generating from chain-tail defects or EPR-active impurities.

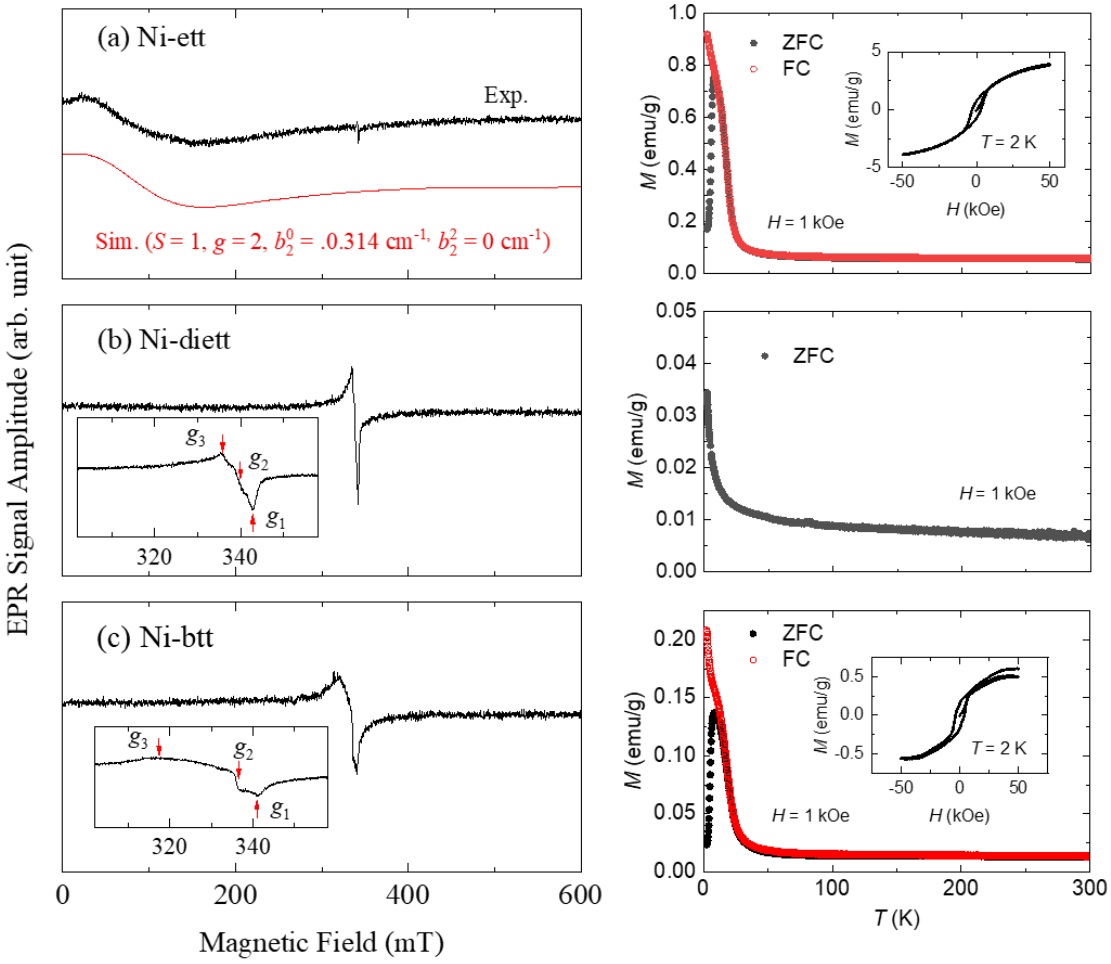

Figure 28. *(a-c) First derivative EPR spectra of* ***Ni-ett***, ***Ni-diett*** *and* ***Ni-btt*** *samples at 77 K and their corresponding SQUID measure (right column) with M-H hysteresis curve at 2 K (inset). The simulated EPR pattern for* ***Ni-ett*** *was processed by EasySpin software. Reused from our recent published article.*[1]

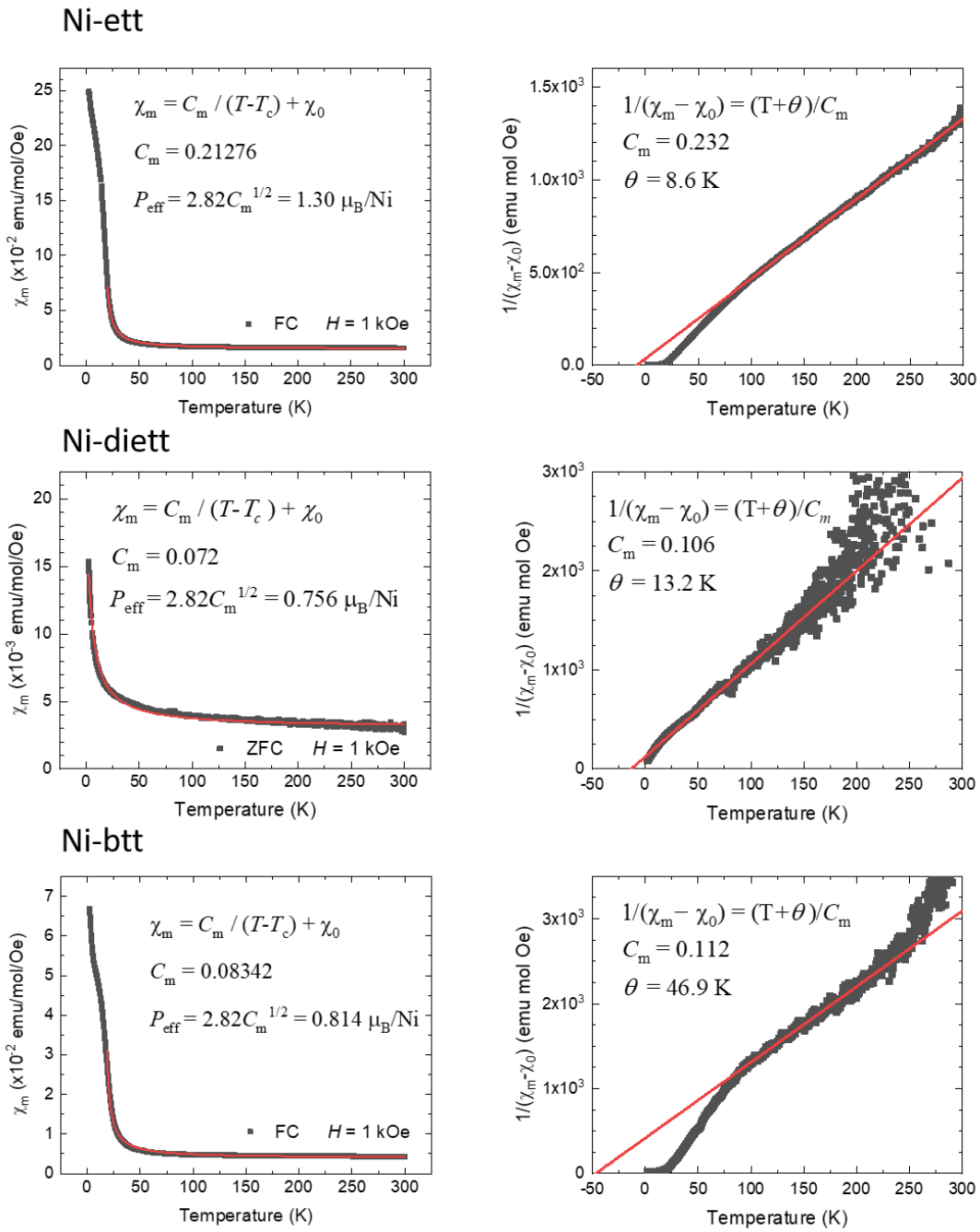

Figure 29. *Temperature dependence of magnetic susceptibility (χ_m) of* ***Ni-ett***, ***Ni-diett*** *and* ***Ni-btt*** *measured by SQUID. Reused from our recent published article.*[1]

Table 6. *Summary of the EPR parameters for* ***Ni-ett***, ***Ni-diett*** *and* ***Ni-btt***. *μ_B is the Bohr magneton. Data Reused from our recent published article.*[1]

Sample	Spin	EPR parameters	Spin concentration (S = ½)	Moment/repeat
Ni-ett	S = 1	g ~ 2, b_2^0 = 0.314 cm^{-1}, b_2^2 = 0 cm^{-1}	4.0 × 10^{22}/mol	0.50 μ_B
Ni-diett	S = 1/2	g_1 = 2.003; g_2 = 2.025; g_3 = 2.047	7.0 × 10^{20}/mol	0.06 μ_B
Ni-btt	S = 1/2	g_1 = 2.015; g_2 = 2.050; g_3 = 2.178	1.3 × 10^{21}/mol	0.09 μ_B

2.2.3 DFT calculation of .Ni-ett, Ni-diett and Ni-btt

To understand the geometric and electronic structures of the three OMCPs, DFT calculations of both the corresponding oligomers consisting of four Ni atoms and five ligands, in the form of either dianion or neutral state ($[Ni_4L_5]^{2-}$ or ($[Ni_4L_5]^0$), and the free ligands were performed. Here, in a typical neutral structure of the oligomer, the terminal S atoms of the capping ligands were replaced with H atoms as proxies, to avoid the possible complex electronic behavior if using sulfonic acids (-SO_3H), sulfates (-SO_4) or disulfides (S-S). For example, the neutral oligomer in the case of ett refers to edt-[Ni_4ett_3]-edt, where edt is 1,2-ethenedithiol.

In terms of ligand diett, its oxidation state was suggested to be a dianion ($diett^{2-}$), existing as an open-shell biradical. In contrast, the other two, ett^{2-} and btt^{2-}, are both predicted to remain closed-shell. As a whole, a symmetric decrease in the bond-length of the terminal C-S bonds occurs simultaneously with the oxidation of each ligand, by 0.1-0.2 Å.

Among the dianionic oligomers, the ground state of the $[Ni_4ett_5]^{2-}$ oligomer is a

closed-shell singlet according to the calculated result. On contrary, the ground states of the dianionic oligomers $[Ni_4diett_5]^{2-}$ and $[Ni_4btt_5]^{2-}$ are both predicted to be open-shell single, but differ in their major distribution of the unpaired spin density, with the former showing on diett ligand and the later present over the four Ni atoms and the four terminal S atoms, respectively. It remains unsolved if the polarized electronic solution of Ni-btt case is an artefact based on the computational model used here or would occur experimentally. Herein, the calculation is mainly to emphasize the unique open-shell singlet state in $[Ni_4diett_5]^{2-}$, unusual with the dianionic $[Ni_4btt_5]^{2-}$ and $[Ni_4ett_5]^{2-}$ oligomers.

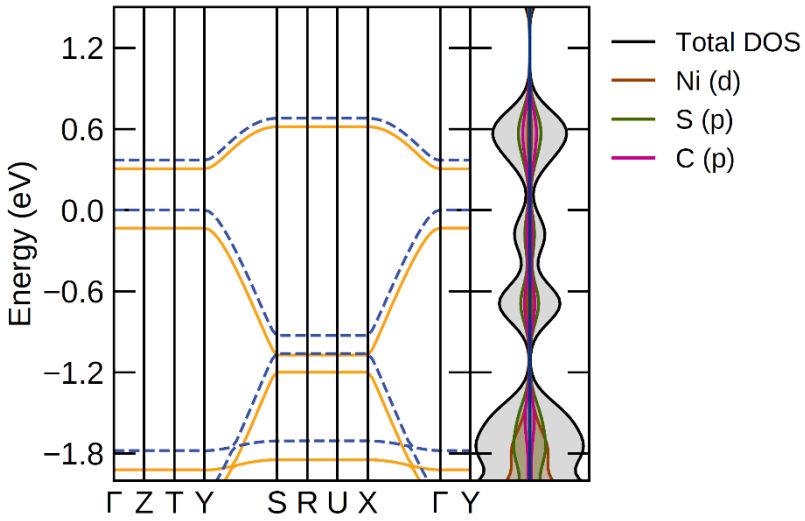

Figure 30. *Electronic band structure and density of states of* ***Ni-diett****, calculated with HSE06, where the dash blue and full orange lines represent the spin up and spin down band respectively. The two have the same occupation but are not quite degenerate, which is a sign of the open shell singlet. This figure is reused from our recent open access article.*[1]

In terms of the neutral oligomers ($[Ni_4L_5]^0$) with hydrogen terminated ligands, all the three ground states are open-shell singlet, with very close energy to the corresponding triplet state. Similar to the dianionic oligomers, the spin is predominantly localized on the ligand moieties. The spin localization occurs either near the end or at

center of the chain in the neutral **Ni-ett** oligomer and **Ni-btt** oligomer, respectively. But for the neutral $[Ni_4diett_5]^0$, the spin is delocalized over the whole chain.

Particularly, the electronic band structure and density of states of **Ni-diett** was further studied by periodic DFT calculations (Figure 30), which is based on a unit cell with vacuum (30 Å per monomer) setting on non-chain directions to avoid interchain interactions. Accordingly, the ground state was predicted to be an open-shell singlet state, with the majority contribution comes from the conjugated S 3p and C 2p states in the ligands, for both valence and conduction bands, giving a narrow band gap (< 0.5 eV). The observation of spin-localization here is consistent with the spin density found on the ligands rather than Ni atoms for both $[Ni_4diett_5]^0$ and $[Ni_4diett_5]^{2-}$ oligomers above, as well as the presence of Ni^{2+} species rather than Ni^{4+}, proved by XPS data and earlier published reports.[93, 101]

2.3 Analysis of the effect of ligands on thermoelectric performance

As all the three OMCPs were obtained as black brittle solids, pellet fabrication and composite film by introducing processable binder polymers are the most viable ways to examine thermoelectric properties. Here we focus on intrinsic TE performance of pressed pellets, excluding the effects of the binder, the composite morphology and processing conditions of the OMCPs. The pellets were then annealed at 150 °C for 5 hours in air to determine the effect of thermal annealing and the simultaneous removal of low boiling point impurities on the thermoelectric performance of the OMCP pellets.

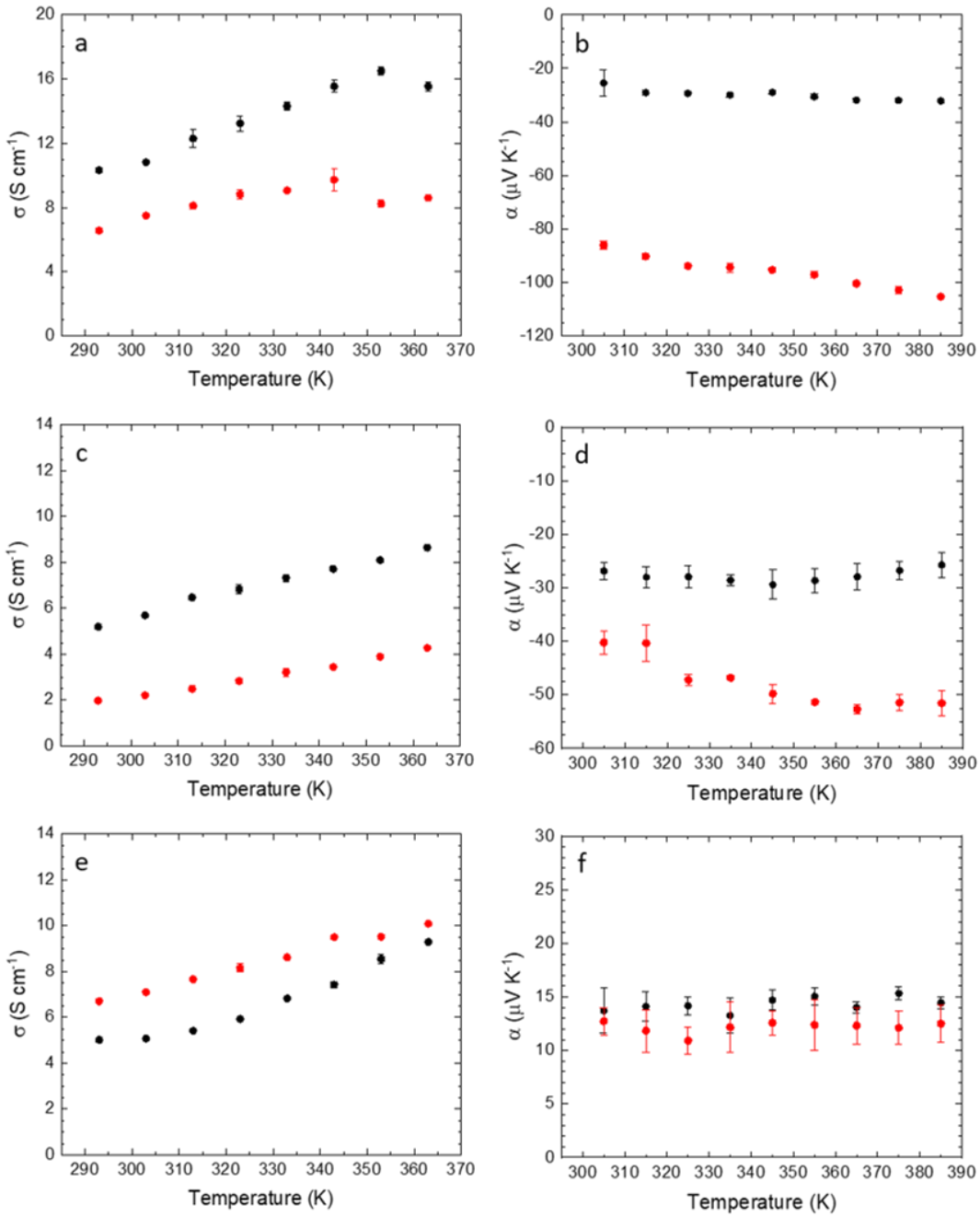

Figure 31. *Electrical conductivities (a, c and e) and Seebeck coefficients (b, d and f) of* ***Ni-ett***, ***Ni-diett*** *and* ***Ni-btt***, *respectively. Data measured from pristine (black) and annealed pellet (red). Reused from our recent published article.*[1]

All the three OMCP structures possess a square planar configuration, where the metal center Ni act as d^8 electron transition metal and coordinate with four ligands according to their dsp^2 hybridization. Without rotary bond in the π conjugated moieties of the ligands, the polymers adopt high rigidity and consistent electron conjugation

alongside the backbones to facilitate charge transport. Here, the three polymers consistently present a positive correlation between temperature and charge transport (Figure 31), which is typical behavior for semiconductors. The highest electrical conductivity was found for **Ni-ett** (~10 S cm^{-1} at room temperature) and lowest for **Ni-diett** (~2 S cm^{-1}), with **Ni-btt** in between (~5 S cm^{-1}).

The thermal annealing showed a minimal effect on the σ values but a very significant impact on the Seebeck coefficients. Most obviously, the Seebeck coefficient of **Ni-ett** was decreased from -26 μV K^{-1} to -86 μV K^{-1} at room temperature by annealing. The Seebeck coefficients decreased from -26 μV K^{-1} to -40 μV K^{-1} at 305 K in the case of **Ni-diett**, while remaining almost unchanged for **Ni-btt**. The reason of this significant improvement in α value requires further investigation and here we provided two possible factors: (i) It is due to the removal of solvent impurities from the OMCP pellet over annealing process, which was witnessed with brownish smoke formed on the beaker used to cover the pellets. This is also in line with the slight weight loss, less than 3% before thermal decomposition temperature recorded by thermal gravimetric measurements (TGA), respectively 250 °C for **Ni-ett** (Figure 32); (ii) The interchain array-arrangement of the polymers may be promoted via the annealing process, resulting in the decrease of the disorder and higher crystallinity in bulk material. The enhancement of thermoelectric properties by annealing was also previously reported on composite films consisting of **Ni-ett** and PVDF, where annealing was believed to allow composite domains to form highly interconnected pathways in bulky material.[73]

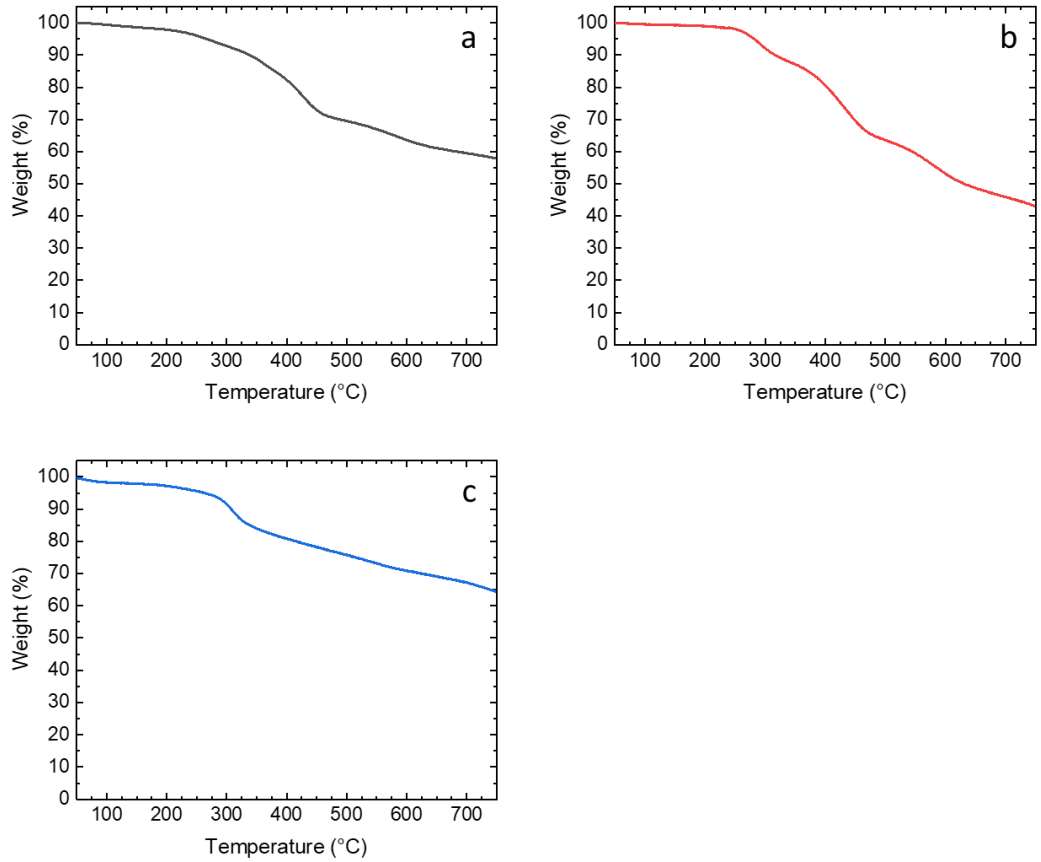

***Figure 32**. TGA analysis of (a) **Ni-ett**, (b) **Ni-diett** and (c) **Ni-btt** recorded in nitrogen. Reused from our recent published article.[1]*

With a positive Seebeck coefficient value around 15 μV K^{-1}, **Ni-btt** strikingly acts as a p-type semiconductor, contrary to the n-type sign of **Ni-ett** and **Ni-diett**. Previously, the n/p type behavior of poly(M-ett) was reported to be switchable by changing the metal centers. Here, we firstly demonstrate that the dominating charge carrier of OMCP can be tuned by changing organic ligands.[80] **Ni-btt** showed very comparative electrical conductivities at 293K, with the value of 5 S cm^{-1} and 7 S cm^{-1} for pristine and annealed pellet, respectively. To note, the value of the **Ni-btt** film prepared from benzene-1,2,4,5-tetrathiol via liquid-liquid interfacial method was previously reported on the order of 10^{-5} S cm^{-1}.[102] This striking improvement is likely due to the different synthetic route

used here, where Ni^{2+} directly coordinated with the ligand intermediate to form polymer **Ni-btt** in strong basic environment, largely avoiding the oxidation of thiols into disulfide within the OMCP backbones.

To check the the durability of **Ni-ett** and **Ni-diett**, the electrical conductivity of the two polymer samples experienced 18-month air exposure were also examined. At room temperature, the oxidized **Ni-ett** and **Ni-diett** showed deteriorating electrical conductivity only on the order of 10^{-3} and 10^{-5} S cm^{-1}, respectively, which can be brought back to the original level of as-prepared samples after purification (Figure 33a and 33c). In line with aforementioned XPS data, these results indicate that the polymer powder was gradually oxidized under air exposure, resulting in the diminished conductivity. This result also suggest it is better to store these polymer samples in the form of pellets rather than powder. To a certain extent, this also explains the mutable electrical conductivity on **Ni-ett** from batch to batch in earlier studies, which might due to not only the assumptive different oxidation extent of polymer backbones but also the variable impurity content.

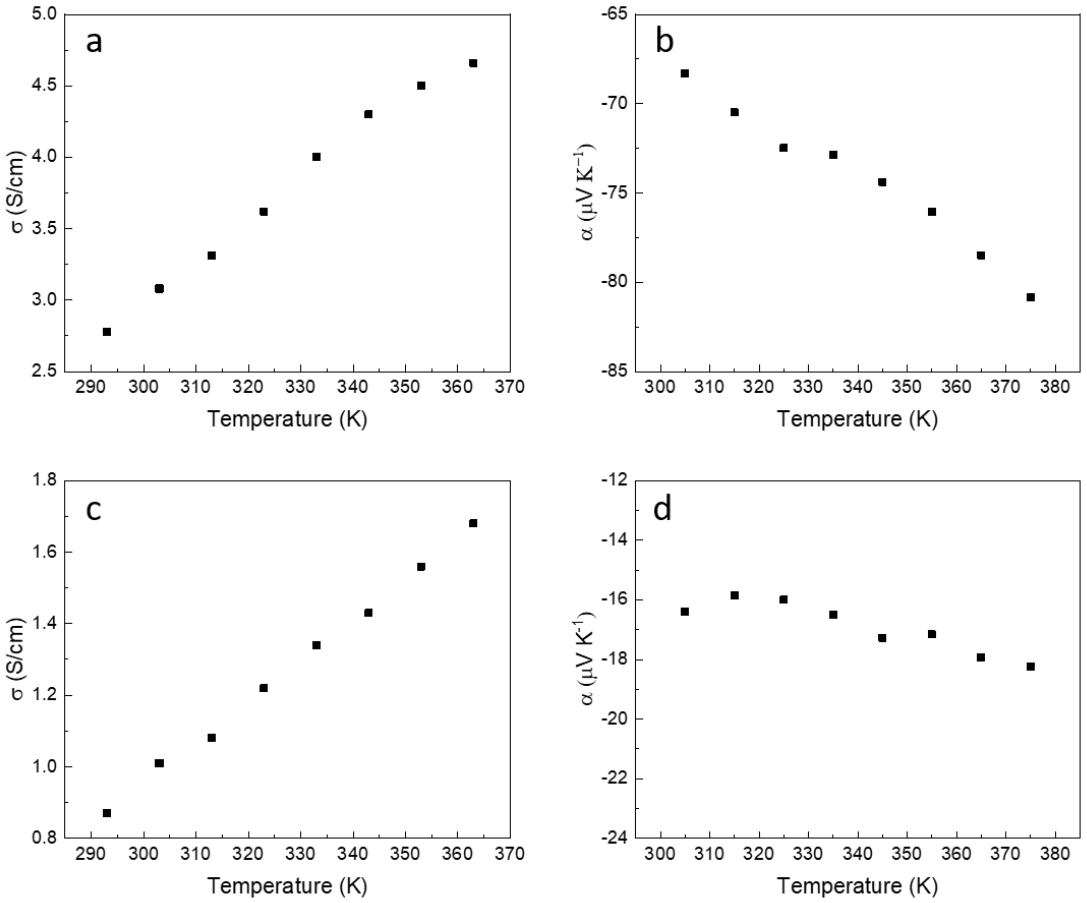

***Figure 33**. Electrical conductivity of purified (a) **Ni-ett** and (c) **Ni-diett** after 18-month air exposure; Seebeck coefficient of purified (b) Ni-ett and (d) Ni-diett after 18-month air exposure.*

The thermal conductivity was measured by Raman thermometry, where a laser was used to heat the OMCP samples and excite the resonant Raman signal simultaneously. Then the temperature the samples required via absorbing the phonon energy was determined by the calibrated shifts of the specific Raman peaks (~360 cm^{-1} and 490 cm^{-1}) induced by illumination.[103-104] A typical example is illustrated in Figure 34 and more experimental details are included in the last chapter regarding *general experimental*. All the pellets of the three OMCPs present low κ values in the sequence of **Ni-btt** (1.2 W m^{-1} K^{-1}) < **Ni-diett** (1.5 W m^{-1} K^{-1}) **<** **Ni-ett** (1.7 W m^{-1} K^{-1}). In the case of **Ni-ett**,

the κ value in previous report was lower than the one present here, which we attribute to alternative measure technique and the extensive purification procedure applied in this work.[80] With certain impurities being efficiently removed from the bulky OMCP solid by the Soxhlet extraction, the reduced defects, including impurity clusters or grain boundaries, led to reduced boundary scattering and therefore a higher but more intrinsic thermal conductivity.

***Table** 7. Summary of the average thermoelectric properties at 305 K of annealed OMCPs. Reused from our recent published article.[1]*

Sample	σ (S cm^{-1})	α (μV K^{-1})	κ (W m^{-1} K^{-1})	PF (μW m^{-1} K^{-2})	ZT
Ni-ett	7.49 ± 0.05	-86.1 ± 1.2	1.7 ± 0.2	5.55 ± 0.19	1×10^{-3}
Ni-diett	5.70 ± 0.05	-40.2 ± 1.6	1.5 ± 0.4	0.94 ± 0.08	2×10^{-4}
Ni-btt	7.11 ± 0.01	12.7 ± 1.2	1.2 ± 0.5	0.12 ± 0.02	3×10^{-5}

Raman imaging of the pellet surface under laser illumination (1 mW) was studied in order to confirm the different κ values of the three OMCPs stem from their different molecular structures, rather than being caused by inhomogeneous factors such as roughness, composition or impurities (Figure 35). Raman spectra further investigated the chemical composition of the materials, given the inhomogeneity reflected by the optical images of pellet surfaces. **Ni-ett** and **Ni-diett** pellets exhibited very uniform chemical compositions, with unchanged peak locations appeared from different domains in their Raman spectra. For example, the surface of **Ni-ett** consist of two

regions, the smoother in red and the rougher in blue (Figure 35), where the only observed difference between the two regions was the peak intensity. Similarly, **Ni-diett** exhibited two domains and present a porous-like morphology. Meanwhile, the **Ni-btt** present to be the most complex sample, with three different domains revealed by the cluster analysis. The green and orange regions were identified as distinct signals, associated with uniform Raman characteristics, and the purple part was identified as noise.

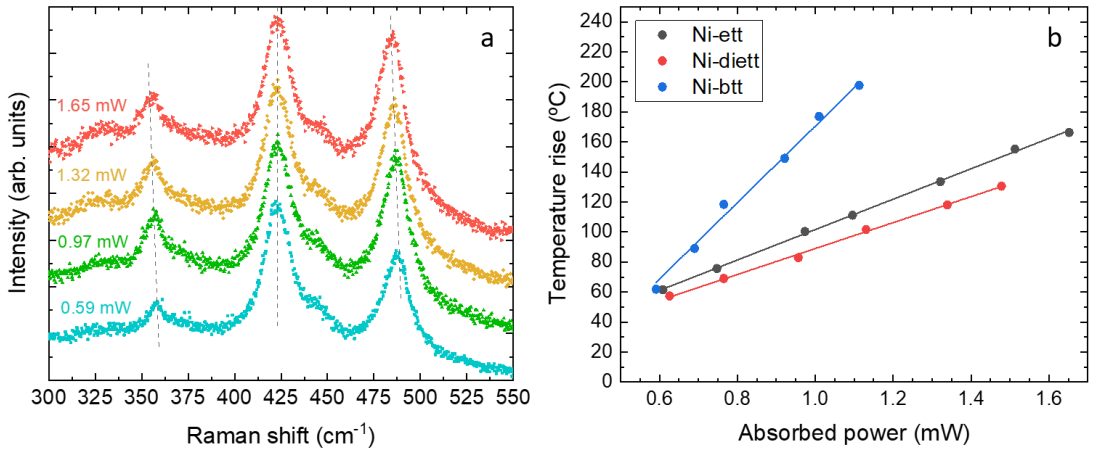

***Figure 34**. (a) The Raman spectrum of **Ni-diett** under different power level of laser illumination, showing the red shift of the peaks around 360 cm^{-1} and 490 cm^{-1} with power increase; (b) Calibrated temperature increase as a function of the absorbed power for the three OMCPs. Reused from our recent published article.*[1]

Due to the different chemical compositions, the three OMCPs slightly differed in their peak position in Raman spectra, resulting in the highest standard deviation of the κ value for **Ni-btt**. To further understand on the surface composition, the Raman spectra of the samples were specifically scanned in the spectral range. As shown in Figure 36, the features in the 300-500 cm^{-1} range originate from the vibration modes regarding the

heavy metal atoms. The very broad signals in the 1200-1600 cm^{-1} range involve the carbon-based bridging ligands, indicating the amorphous state and complex chemical environments of these carbon bonds. In the meantime, the observed changes in the intensity ratio of the inorganic and organic vibrations at different domains in three OMCPs suggest the variable stoichiometry differs from point to point, which can also explain the slight change of the κ value in the various regions of the OMCP samples.

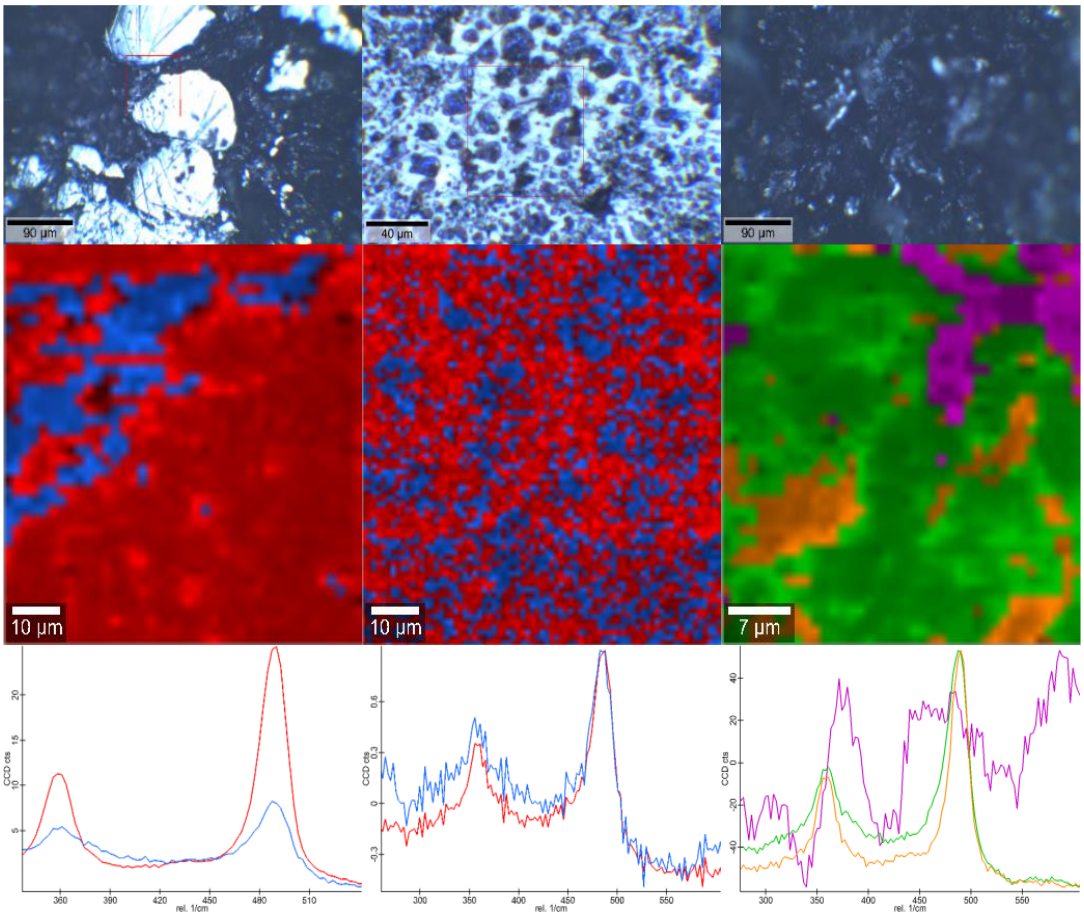

Figure 35. *Optical images (top) of* ***Ni-ett*** *(Left),* ***Ni-diett*** *(Center) and* ***Ni-btt*** *(Right). The red boxes represent the Raman scan area (middle and bottom). The Raman spectra are analysed to show clusters, i.e. similar types of spectra throughout the sample. Reused from our recent published article.*[1]

Thus, in order to further quantify the potential difference of the various regions shown in the optical images, the spectra of the three polymer samples were fitted according to the spectral peak at ~360 cm^{-1} and their histogram of the distribution of

this specific peak position recorded (Figure 37). **Ni-ett** showed the most concentrated distribution in the range 360±5 cm^{-1}, while the distribution of **Ni-ett** and **Ni-btt** was relatively broader with the data deviation around ±25 cm^{-1}, coinciding with the findings in the Raman thermometry experiment above. The careful surface analysis indicates that the most likely cause of the differences in thermal conductivity for these OMCPs is not experimental bias but the different chemical composition.

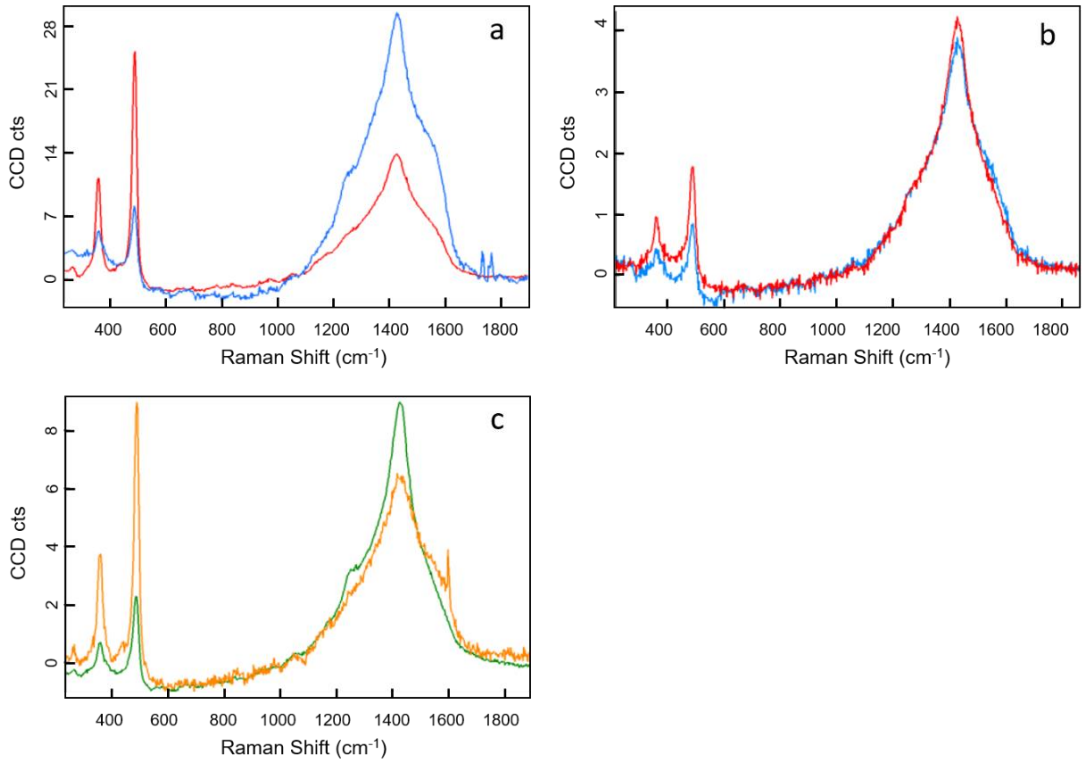

***Figure 36**. Average Raman spectra for the different regions of (a) **Ni-ett**, (b) **Ni-diett** and (c) **Ni-btt**. The colours correspond to those in the images of Figure 36.*

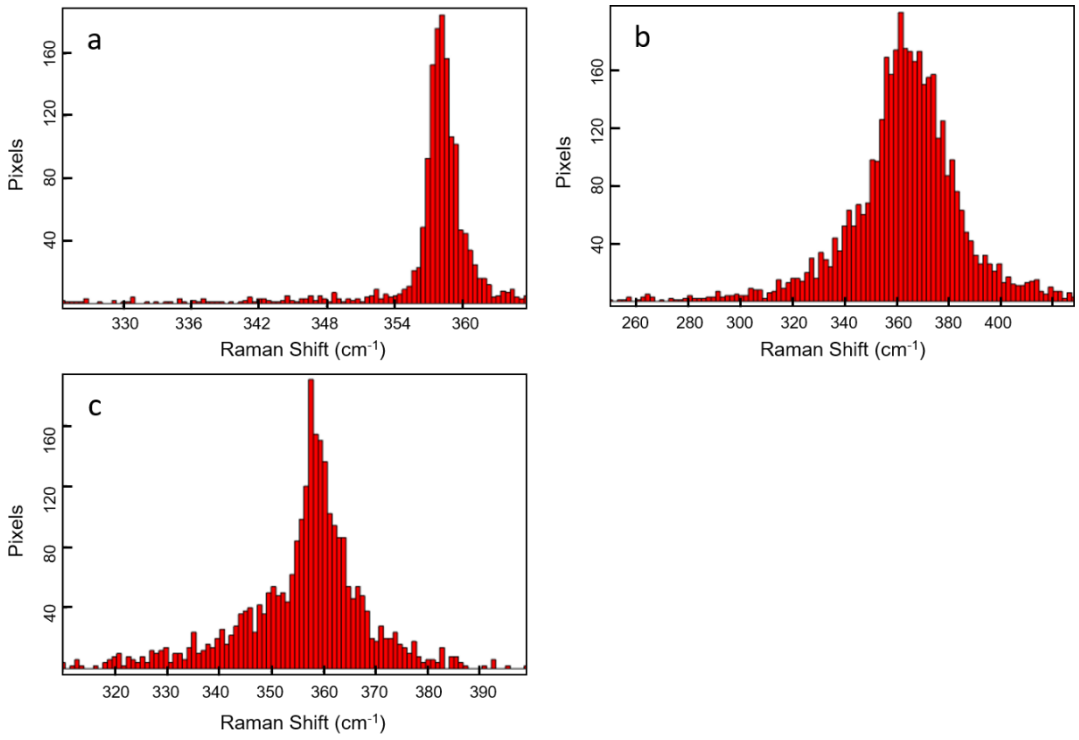

Figure 37*. Histograms of first Raman peak (around 360 cm-1) positions for the (a)* ***Ni-ett****, (b)* ***Ni-diett*** *and (c)* ***Ni-btt*** *sample. Reused from our recent published article.*[1]

In case of **Ni-ett**, our study showed different thermoelectric properties from the reported ones. First reason is the different morphology of **Ni-ett** samples obtained from different synthetic routes. In general, the **Ni-ett** pellet compressed from the powder by one-pot-synthesis showed lower electrical conductivity, compared with the **Ni-ett** film gown by the electrochemical method (~220 S cm^{-1}).[45] With the same molecular composition, the enhanced electrical conductivity of the crystalline film is due to the higher structure order and consequently less interfacial scattering. More importantly, the extra purification we adopted here is of necessity and importance to exclude the potential effect of contaminants, improve the reproducibility of one-pot-synthesis and understand both the intrinsic structure and thermoelectric properties from these

insoluble OMCPs, with the detailed comparison between the polymer samples prior to and after the purification (section 2.2). Herein, the electrical conductivity measurement was performed on the purified OMCPs, which possess neutral charged and radical-involving backbones interpreted based on a series of spectroscopic characterization.

2.4 Chapter conclusions

In summary, a series of linear OMCPs with different ligands, **Ni-ett**, **Ni-diett** and **Ni-btt** have been designed and synthesized to illustrate the link between the thermoelectric properties of materials and the electronic structure and geometry of ligands. The extra sample purification proved to be crucial and allowed the investigation of the accurate molecular structures and the intrinsic properties of these OMCPs. The polymer backbones of three OMCPs are most likely radical in nature, as evidenced by the spectroscopic studies for these polymers and correlated small molecular complex. In addition, combined techniques including DFT calculations, EPR and SQUID pointed out the open-shell character of the **Ni-diett** with the unpaired spin primarily localized on the organic ligand.

The study highlighted changing organic ligands as a successful strategy to tune the thermoelectric properties and opens-up new ligand design strategies for OMCPs for thermoelectric use.

Chapter 3. Effect of isomeric ligand geometry on thermoelectric properties

This chapter will describe the synthesis, structural characterization and thermoelectric properties of two isomeric polymers.

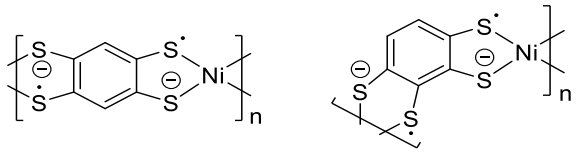

Scheme 5. *Idealized structure of isomeric OMCPs,* ***Ni-btt*** *and* ***Ni-ibtt***.

Specifically, we developed a new OMCP structure based on benzene-1,2,3,4-tetrakis(thiolate) (ibtt), an isomeric ligand of btt. Ligand ibtt shows only a difference in substitution site of S atoms on aromatic ring from the isomer btt. Consequently, it can form into square-planar C_{2v}-symmetric polymer, **Ni-ibtt** (Scheme 5), when coordinated with a central metal. With its curved polymer backbone, **Ni-ibtt** is supposed to possess a larger interchain stacking, reduced crystallinity and ideally higher polymer solubility, allowing us to investigate the effect of molecular geometry on the TE properties of OMCPs by comparing it with linear Ni-btt.

Another isomer of btt, benzene-1,2,3,5-tetrakis(thiolate) candidate has been excluded in this work as it is less likely to polymerize defect-free, leading to more structural complexity and disorder.

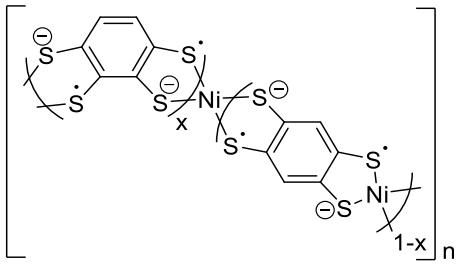

$Ni_1(ibtt)_x(btt)_{1-x}$

Scheme 6. *Idealized structure of dual-ligand OMCPs Poly[* ***Ni(ibtt)$_x$(btt)$_{1-x}$****].*

To further tune the polymer geometry and properties, the two isomeric ligands, btt and ibtt, were copolymerized into **Ni(ibtt)$_x$(btt)$_{1-x}$** (Scheme 6). It was assumed the mix-ligand system would generate more structural complexity, resulting from the difference from btt and ibtt in their coordination capability and topology. The mix-ligand OMCPs was then characterized and compared with the mono-ligand OMCPs, **Ni-ibtt** and **Ni-btt**, to further reflect the correlation between the thermoelectric behaviors and isomeric configuration.

3.1 Synthesis of isomer polymers Ni-ibtt and $Ni(ibtt)_x(btt)_{1-x}$

3.1.1 Synthesis of Ni-ibtt and $Ni(ibtt)_x(btt)_{1-x}$

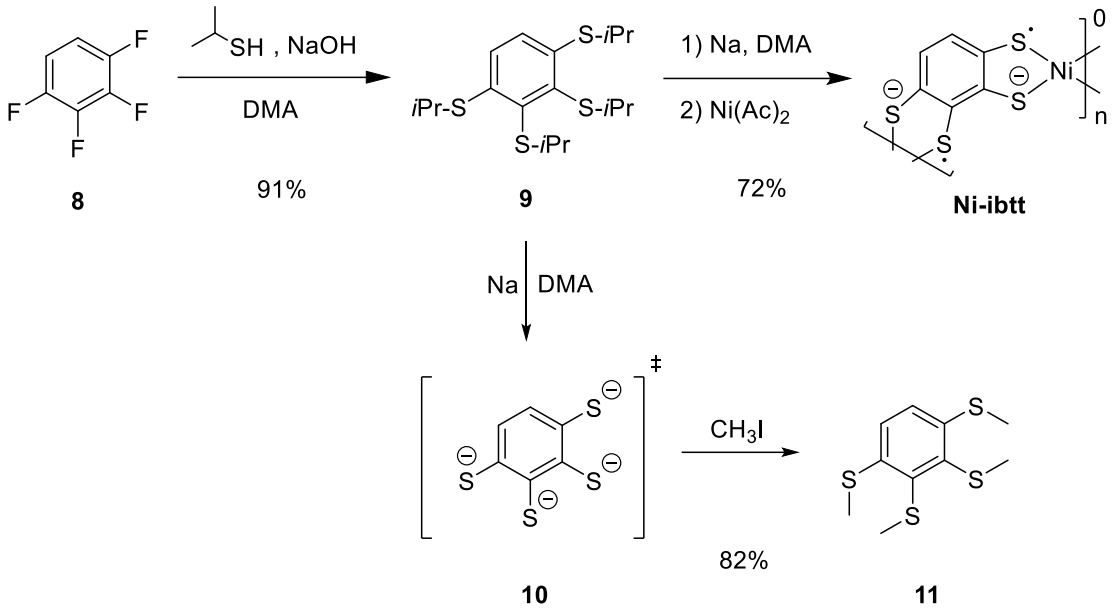

***Scheme** 7. Synthetic pathway towards compound **11** and **Ni-ibtt** in the idealized chemical structure and the mechanism study.*

The aforementioned synthetic route to construct metal-thiolato complex (**Ni-btt**) by sodium reduction of corresponding isopropylthiol precursor (**4**) has been proven to be reliable. An analogous procedure was followed to synthesize the isomer polymer **Ni-ibtt** (Scheme 7). First, 1,2,3,4-Tetrakis(isopropylthio)benzene (**9**) was synthesized from commercially available 1,2,3,4-tetrafluorobenzene (**8**) via the nucleophilic aromatic substitution to replace the fluoro with isopropylthiol group.

Initially, 1,2,3,4-tetrachlorobenzene ($C_6H_2Cl_4$) **12** was used as the starting reagent due to its lower price, instead of **8**. However, $C_6H_2Cl_4$ present lower reactivity with a longer reaction time and the presence of numerous byproducts, most likely partially substituted chlorobenzene isomers (Table 8). This is due to the lower electron density

of chlorine and thereby weaker electronic repulsion, compared with fluorine, which leads to the lower rate for isopropyl substitution. Similarly, previous studies also proved fluoride anions act as the best leaving group in hexahalogenobenzene system for the nucleophilic substitution by sodium alkylthiolate, requiring shorter time and lower temperature to achieve high yield of hexakis(alkylthio)benzene.[51, 105] Hence, **8** was eventually chosen as the starting material for the synthesis of **9**.

Then, **9** was reacted with Na and quenched by CH_3I, yielding 1,2,3,4-tetrakis(methylthio)benzene (**11**). This result confirmed the formation of the intermediate **10**, 1,2,3,4-benzenetetrakis(thiolate) by sodium reduction, which directly formed the black polymer **Ni-ibtt** when Ni(II) salt was used for quenching instead.

Table 8. *Synthesis of 1,2,3,4-Tetrakis(isopropylthio)benzene by Different Starting Materials*

Starting Reagent	Temp (°C)	Time (h)	Number of Byproducts	Yield (%)
$C_6H_2Cl_4$	100	48	2	51
$C_6H_2F_4$	35	20	2	-
$C_6H_2F_4$	80	2	1	-
$C_6H_2F_4$	100	1.5	0	91

Furthermore, to deepen our understanding of the impact of ligand geometry on thermoelectric properties, mixed-ligand or dual-ligand polymers, **Ni(ibtt)$_x$(btt)$_{1-x}$** (Scheme 8), were synthesized using **9** and **4** simultaneously, following the similar procedure of the mono-ligand OMCPs (**Ni-ibtt** and **Ni-btt**).

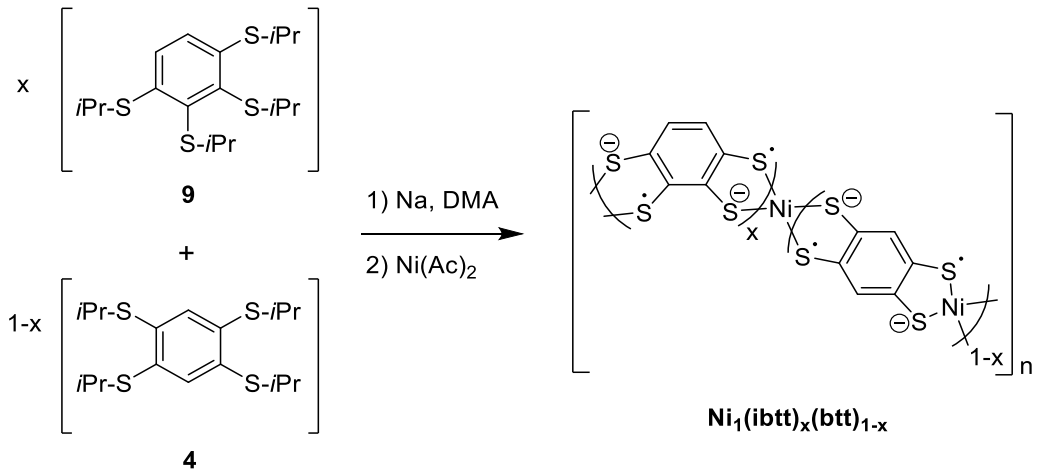

***Scheme 8**. Synthetic pathway towards the Poly[**Ni(ibtt)$_x$(btt)$_{1-x}$**] in ideal conditions.*

3.1.2 Alternative route for Ni-ibtt and derivatives

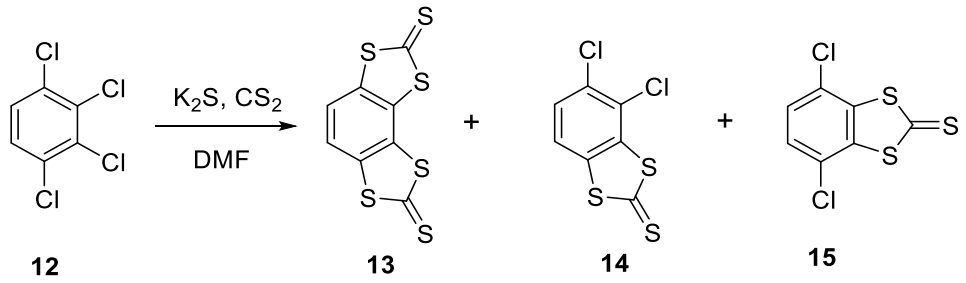

***Scheme 9**. Synthetic routes for compound **13** and corresponding byproducts **14** and **15**.*

As alternative route to obtain Ni-btt from compound **7** (1,3,5,7-tetrathia-s-indacene-2,6-dithione) was proved to be feasible, it was of peculiar interest to examine if an alternative synthetic pathway can be also developed for the synthesis of **Ni-btt**. Thus, 1,2,3,4-tetrachlorobenzene (**12**) was reacted with the same reaction procedure applied to compound **3** to synthesize **7**, aiming to get benzo[1,2-*d*:3,4-*d'*]bis([1,3]dithiole)-2,7-dithione (**13**) via substituting cholorine with carbonotrithioate (Scheme 9). However, compound **13** was obtained as the main product companying with a couple of isomeric byproducts, as shown in Scheme 9, 4,5-dichlorobenzo[*d*][1,3]dithiole-2-thione (**14**) and 4,7-dichlorobenzo[*d*][1,3]dithiole-2-

thione (**15**).[1]

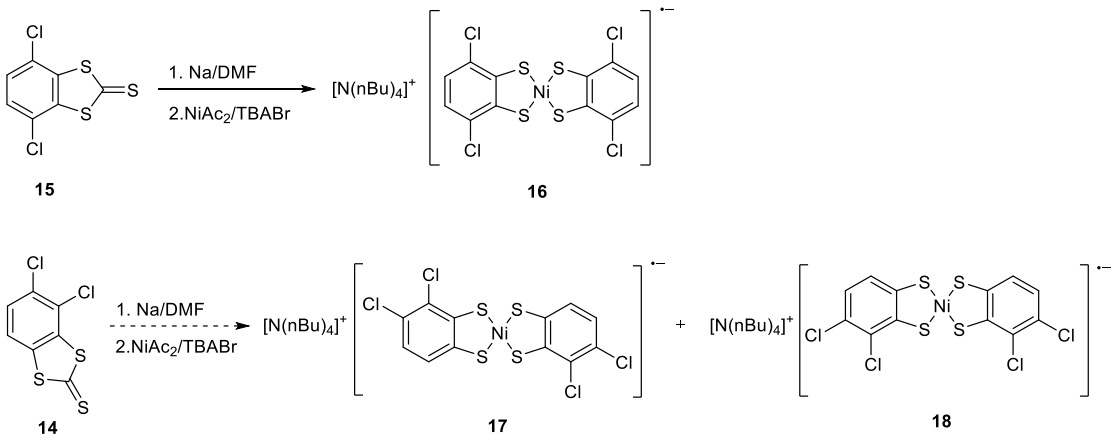

***Scheme 10**. Synthetic routes for small complexes (NBu4)[Ni(dcbdt)2] (**16**) and (NBu4)[Ni(dcbdt')2] (**17** or/and **18**).*

In earlier reports, both analogous smaller complexes systems and derivatives OMCPs based on the coordination of benzenethiolate and transition metals were found to be highly catalytic-active for hydrogen evolution from water.[46, 54] Hence, compound **14** and **15** were used to develop small Ni-based complex for application interest (Scheme 10). The compound **16**, (NBu4)[Ni(dcbdt)2] were obtained and characterized, where dcbdt represents 3,6-dichlorobenzene-1,2-bis(thiolate). Meanwhile, the analogous isomeric complex were prepared from compound **14**, which is supposed to be (NBu4)[Ni(dcbdt')2], where dcbdt' represents 3,4-dichlorobenzene-1,2-bis(thiolate). Further investigation is ongoing to confirm its configuration as cis- and/or trans-

[1] The feasibility of using compound **13** for synthesis of Ni-btt requires further experiment (delayed due to Covid-19).

(structure **17** and/or **18**). All the synthetic procedures in details are provided in last chapter.

3.2 Structural characterization and DFT calculation of Ni-btt and Ni-ibtt

To investigate the composition and structure of the mono and mix ligand polymers synthesized from the two isomeric ligands, **Ni-ibtt**, **Ni-btt** and **Ni(ibtt)$_x$(btt)$_{1-x}$**, XPS, FTIR, Raman and UV-vis spectroscopy were employed, as well as DFT calculations. The results reflect both their configurational similarities upon the participation of thiolate groups into the coordination with nickel, and the inherent difference in their linear and/or twisting polymer chains due to isomerism.

XPS was used to investigate the chemical composition of polymer **Ni-ibtt** and **Ni(ibtt)$_{0.5}$(btt)$_{0.5}$** (Figure 38 and 39). Based on the earlier detailed study of Soxhlet purification and XPS depth profiling (chapter 2), herein all the XPS were performed with purified as-prepared sample without surface oxidation, to reveal the accurate compositional information. The survey spectra of **Ni-ibtt** proves the presence of the element Ni, S and C in this OMCP. The couple of peaks at 853 and 873 eV in the Ni 2p photoemission spectrum of **Ni-ibtt** are assigned to the Ni 2p$_{3/2}$ and Ni 2p$_{1/2}$, respectively, which proves the presence of a sole type of Ni(II) species as the central metal. Similar to the isomer polymer **Ni-btt**, the S 2p XPS narrow range scan with fitting shows peaks with binding energies of 161.8 and 163 eV for **Ni-ibtt**, which originate from Ni-thiolate

complexation. The XPS energy survey spectrum shows no signal involving Na, the Na 1s XPS narrow range was checked (Figure 39e) to reconfirm the absence of Na element and exclude its possible role as counterion. The elementary composition of **Ni-ibtt** by XPS is in accordance with the radical-involving **Ni-btt** (discussed in Chapter 2). Likewise, XPS data confirmed the presence of Ni, S and C elements, showing no presence of sodium in the dual-ligand polymer **Ni(ibtt)$_{0.5}$(btt)$_{0.5}$**. However, Ca element was also found by XPS analysis (Figure 39) in polymer **Ni(ibtt)$_{0.5}$(btt)$_{0.5}$**, whose origin was unclear as the synthesis procedure involved no Ca-containing chemical and needs further investigation, as no matching was found to be related to Ca salts based on the powder XRD data below (Figure 45).

XRF characterization (Table 9) consistently confirmed the absence of Na in **Ni-ibtt**, pointing to the neutral radical-involving backbone of this OMCPs, likewise abovementioned MS_4 based OMCPs and $M(NH)_4$ based OMCPs in reports.[106-107] Identical to **Ni-btt**, the theoretical value of the S/Ni ratio of both **Ni-ibtt** and **Ni(ibtt)$_{0.5}$(btt)$_{0.5}$** is 4, to which the experimental values by XRF were both reasonably close (3.15 and 3.61, respectively).

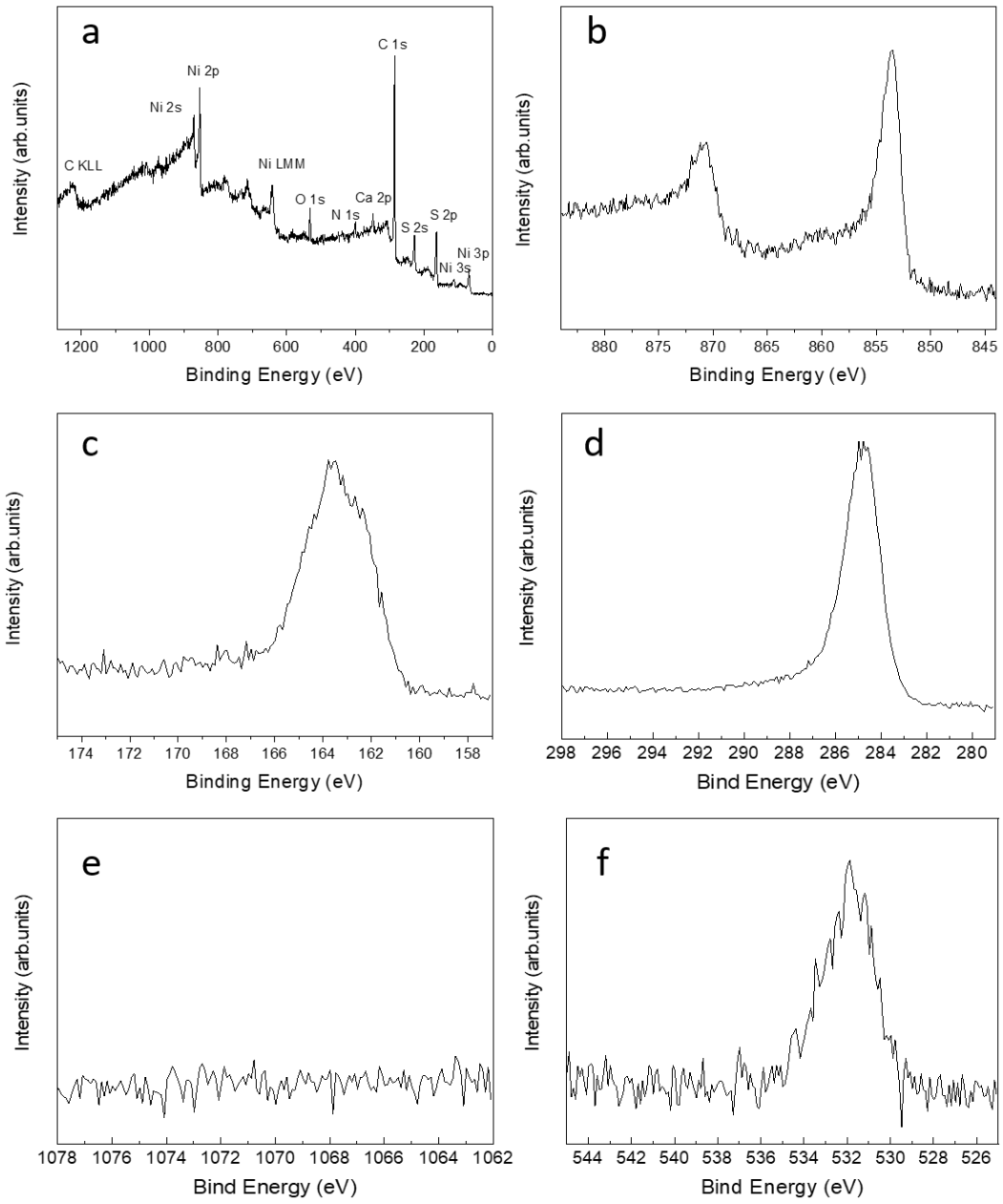

Figure 38. *XPS spectrum of obtained* ***Ni-ibtt****: (a) XPS energy survey spectra; (b-f) Ni 2p, S 2p, C 1s, Na 1s and O 1s core level XPS spectrum.*

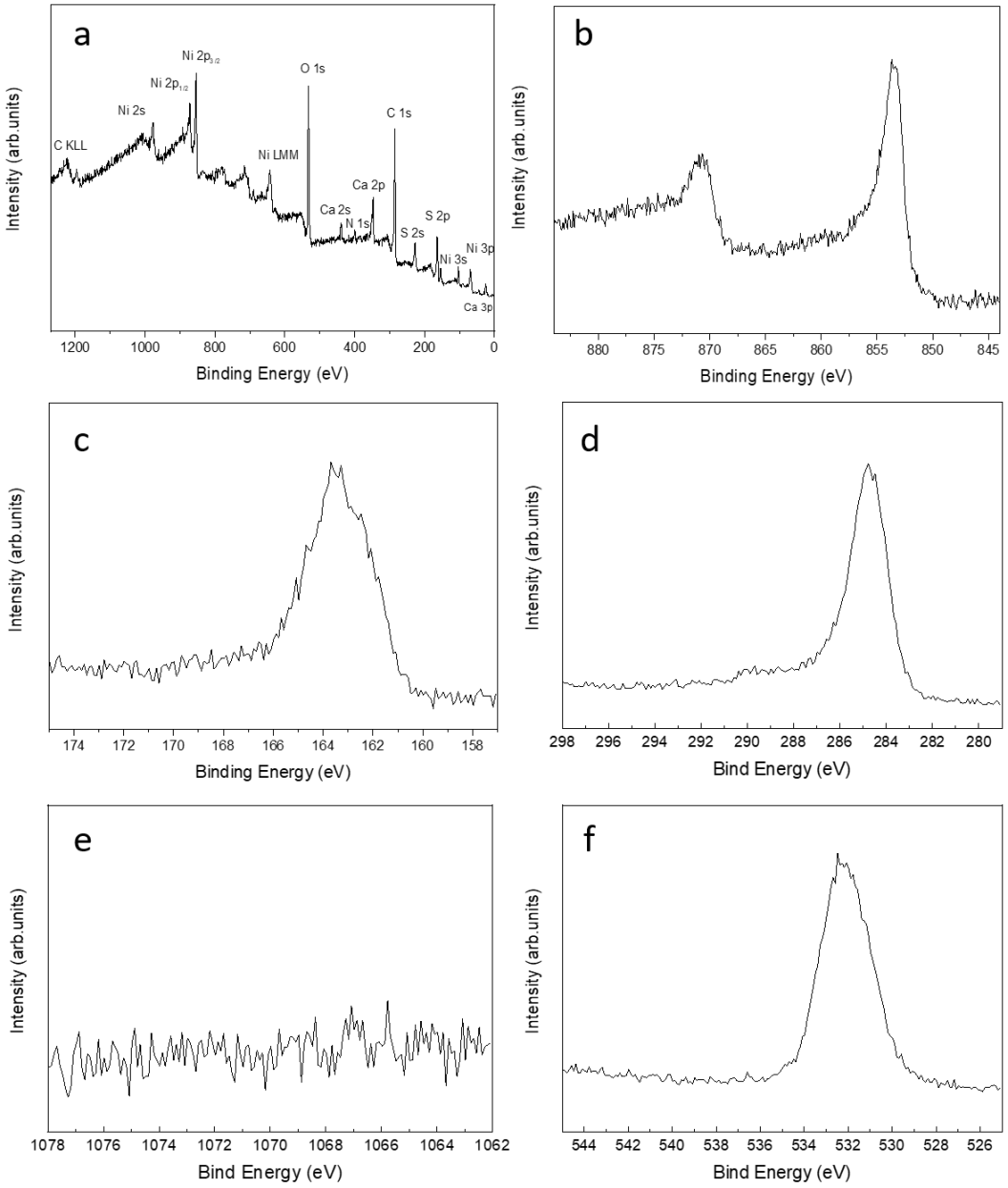

***Figure 39**. XPS spectrum of **Ni(ibtt)$_{0.5}$(btt)$_{0.5}$**: (a) XPS energy survey spectra; (b-f) Ni 2p, S 2p, C 1s, Na 1s and O 1s core level XPS spectrum.*

***Table 9**. XRF of atomic S/Ni ratio based on the observed element contents (weight % and atomic %) of **Ni(ibtt)$_{0.5}$(btt)$_{0.5}$**, **Ni-ibtt** and **Ni-btt**.*

$Ni_1(ibtt)_{0.5}(btt)_{0.5}$			**Ni-ibtt**			**Ni-btt**		
S/Ni = 3.61			S/Ni = 3.15			S/Ni = 3.3.1		
Element	wt%	at%	Element	wt%	at%	Element	wt%	at%
S	**63.497 %**	**77.54%**	**S**	**59.92 %**	**74.80%**	**S**	**62.473 %**	**74.3%**
Ni	**32.167 %**	**21.46%**	**Ni**	**34.800 %**	**23.70%**	**Ni**	**34.511 %**	**22.4%**
Mg	0.469 %	0.76%	Si	894.0 ppm	0.13%	Si	0.85 %	1.15 %
Si	686.3 ppm	0.01%	Cl	1.133 %	1.27%	P	1.01 %	1.24 %
Ca	3.549 %	3.5 %	Ca	2.99 %	2.98%	Ca	0.607 %	0.58 %
Ti	25.2 ppm	20.6 ppm	Ti	182.5 ppm	153 ppm	Ti	57 ppm	45.4 ppm
Fe	255.8 ppm	179.4 ppm	Fe	391 ppm	280 ppm	Fe	351.6 ppm	240 ppm
Zn	0.178 %	0.11%	Zn	237.3 ppm	145 ppm	Zn	0.201 %	0.12 %
As	7.2 ppm	376.3 ppm	As	8 ppm	4.27 ppm	As	11.8 ppm	6 ppm
Se	3.2 ppm	1.6 ppm	Se	2.7 ppm	1.4 ppm	Se	1.7 ppm	0.8 ppm
Br	57.8 ppm	28.3 ppm	Br	65.9 ppm	33 ppm	Br	679.4 ppm	324 ppm
Sr	113.3 ppm	50.6 ppm	Sr	98.9 ppm	45.2 ppm	Sr	6.4 ppm	2.8 ppm
Zr	19.3 ppm	8.3 ppm	Zr	14.9 ppm	6.5 ppm	Sn	138.8 ppm	44.6 ppm
Sn	104.3 ppm	34.4 ppm	Sn	162.2 ppm	54.7 ppm	Sb	164 ppm	51.4 ppm
Sb	35.7 ppm	11.5 ppm	Sb	65.7 ppm	21.6 ppm	Te	105.7 ppm	31.6 ppm
Te	94.4 ppm	29 ppm	Te	140.8 ppm	44.2 ppm	I	661.9 ppm	199 ppm
Pb	16.5 ppm	3.1 ppm	I	132.5 ppm	41.8 ppm	Ba	30.4 ppm	8.5 ppm
			Re	0.5 ppm	0.1 ppm	Er	0.123 %	274 ppm
			Pb	9.4 ppm	1.8 ppm	Pb	13.3 ppm	2.5 ppm

ATR-FTIR and resonance Raman spectroscopies (Figure 40 to 42) were employed to validate the change between starting material and obtained polymer. Moreover, the spectrographic characterization can also elucidate the difference from the structural isomerism between both the two formed isomeric OMCPs (**Ni-ibtt** and **Ni-btt**) and their isomeric starting materials.

In the IR spectrum, compound **9** shows a peak at 808 cm^{-1}, representing the characteristic vibration of adjacent Ar-H in 1,2,3,4 -tetra substituted benzene systems.[108] Like compound **4** and **9** have unifying strong peaks in the region around

3000 cm^{-1}, which are assigned to the stretching mode of $-CH_3$ and $-CH(Me)_2$. Those intense peaks completely disappeared in the OMCPs they formed, following the removal of the isopropyl groups. For polymer **Ni-ibtt**, C=S˙ stretching vibration modes at 1133 cm^{-1} and 1071-1012 cm^{-1} (split peak) are observed in the FTIR spectrum. The bands at 1398, 1444, 1495 and 1596 cm^{-1} are related to the aromatic semicircular stretching and the ring quadrant stretching (Figure 40a), which are correspondingly observed in the spectra of compound **9** (Figure 40b). The remaining Ar-H vibration of **Ni-ibtt** showed a weak peak at 870 cm^{-1}, while that of **Ni-btt** is relatively stronger at 857 cm^{-1}.

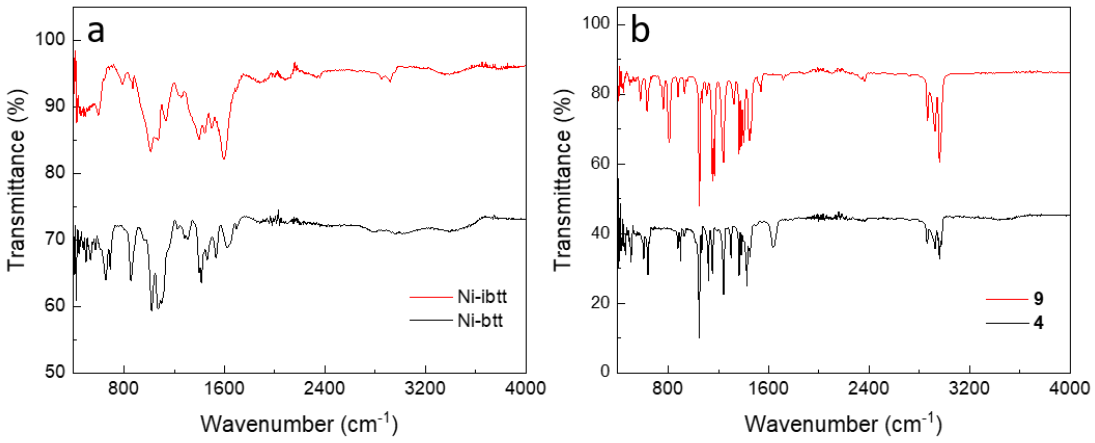

***Figure 40**. FTIR spectra of (a) **Ni-ibtt** and **Ni-btt**; (b) precursors compound **9** and **4**. The spectra have been stacked for clarity.*

In terms of Raman spectra, starting material compound **4** and **9** (Figure 41) have high similarities of the signals from the benzene ring, S-Ar and $S-CH(CH_3)_2$. Meanwhile, they differ in the bands of aromatic protons (Ar-H), where the two adjacent C-H wag peaks of compound **9** show up at 810 and 875 cm^{-1} and the lone C-H wag signal of compound **4** present at 857 and 875 cm^{-1}. As aromatic protons are unaffected

by the polymerization, their vibrational Raman bands were expected to remain unchanged in the obtained OMCPs. However, unlike the corresponding starting materials, the features of Ar-H were no longer visible in the Raman spectra of the obtained OMCPs.

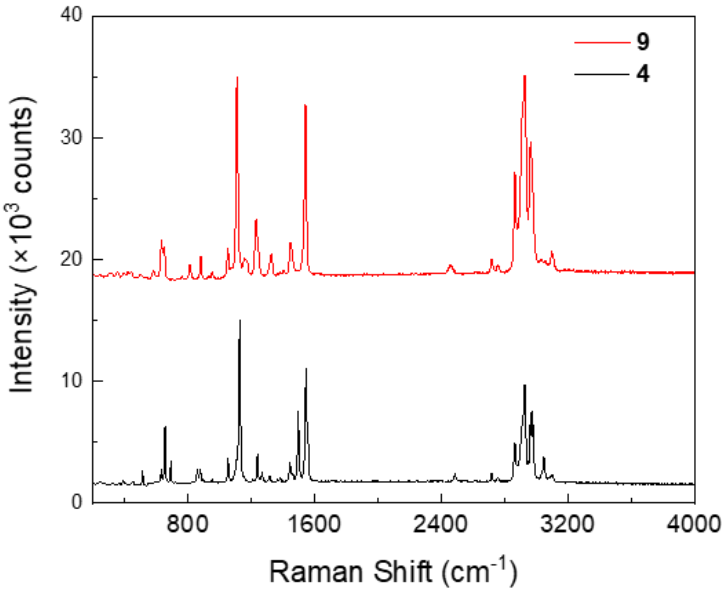

***Figure 41**. Resonance Raman spectra by 728 nm excitation of precursors compound **9** and compound **4**. The spectra have been stacked for clarity.*

Unsurprisingly, the Raman spectra of **Ni-ibtt** and **Ni (ibtt)$_{0.5}$(btt)$_{0.5}$** are similar due to the similarity of ligands ibtt and btt and the unifying chelate bonds in polymer backbones they formed. The characteristic band at 357.5 cm^{-1} in both **Ni-ibtt** and **Ni(ibtt)$_{0.5}$(btt)$_{0.5}$** is assigned to Ni-S vibration (Figure 42a), in accordance with **Ni-btt**. Noticeably, there is a positive correlation between the btt content in polymer and the intensity of υ(Ni-S) peak. **Ni-ibtt** displays lower peak integration of υ(Ni-S) against the aromatic peaks, compared with that of **Ni-btt**. This is because the four adjacent C-S

bonds cause electric charge deviation from the benzene ring center and lead to higher dipole moment μ (μ = q ×d, q is charge; d is distance) in ligand ibtt, compared with that of btt. Raman vibrations from higher polar moieties are usually weaker. Here, the external electric field cannot induce a change in the dipole moment of Ni-S in Ni-ibtt as significant as that in **Ni-btt**. In the same way, **Ni(ibtt)$_{0.5}$(btt)$_{0.5}$** also shows a more intense υ(Ni-S) than neat **Ni-ibtt**.

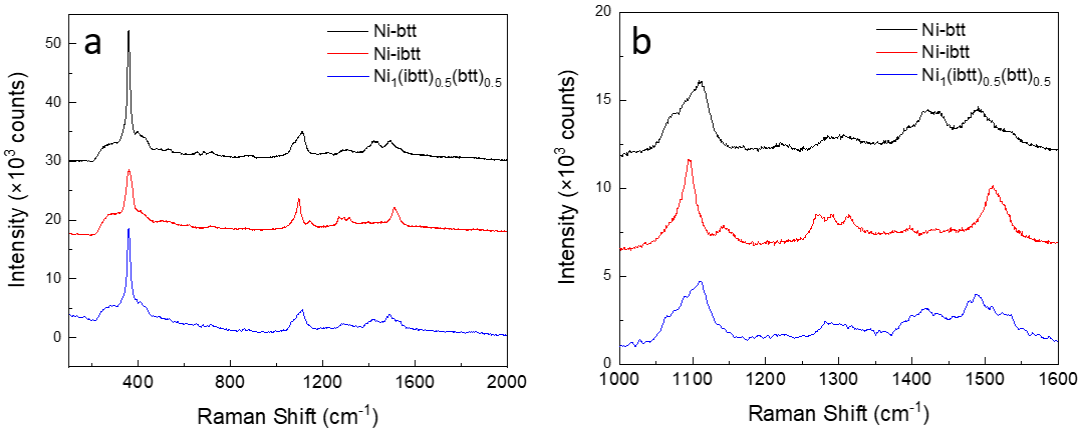

***Figure 42**. (a) Resonance Raman spectra by 728 nm excitation of **Ni-btt**, **Ni-ibtt** and **Ni(ibtt)$_{0.5}$(btt)$_{0.5}$**; (b) the enlarger range between 1000-1600 cm^{-1} of image a. The spectra have been stacked for clarity.*

Meanwhile, **Ni(ibtt)$_{0.5}$(btt)$_{0.5}$**, synthesized with the mixed isomer ligands, reflect the features from both **Ni-ibtt** and **Ni-btt** in Raman spectra (Figure 42). Overall, it presents a more similar pattern with **Ni-btt** rather than **Ni-ibtt**: 1) The υ(C=S˙) stretching vibration in **Ni-ibtt** is located at 1095 cm^{-1} as a sharp signal, companying with a weak one at 1141 cm^{-1}. With a slight bathochromic shift, the analogous signal in **Ni(ibtt)$_{0.5}$(btt)$_{0.5}$** appears at 1100 cm^{-1}, which is identical with that in **Ni-btt** in terms of both the broader shape and peak location. 2) **Ni-ibtt** has a single peak at 1313 cm^{-1} and a set of split peaks at 1271 and 1291 cm^{-1}, while **Ni(ibtt)$_{0.5}$(btt)$_{0.5}$** shows only a

ambiguous hump like **Ni-btt** in the same range. The possible reason why **Ni(ibtt)$_{0.5}$(btt)$_{0.5}$** share a lot common with **Ni-btt** in the Raman spectra is: the interval of ligand btt disturb the continuous organized twisting mode (in neat **Ni-ibtt**), to further prolong and thereby obscured the feature from ibtt fractions in the mixing ligand polymer.

Unlike the insoluble linear **Ni-btt, Ni-ibtt** can be partially dissolved, which might originate from its compositional complexity, namely linkage (cis-trans) isomerism. Though the ring-like *cis* **Ni-ibtt** might not be entropically favored by looking at the structure, the observed partial solubility of bulky **Ni-ibtt** material suggested the assuming existence of *cis* **Ni-ibtt** in the actual polymer system. To test the possibility of the co-existing waving and ring-like *cis* **Ni-ibtt**, UV-vis spectroscopy and DFT calculation were investigated to deepen the understanding of this OMCP.

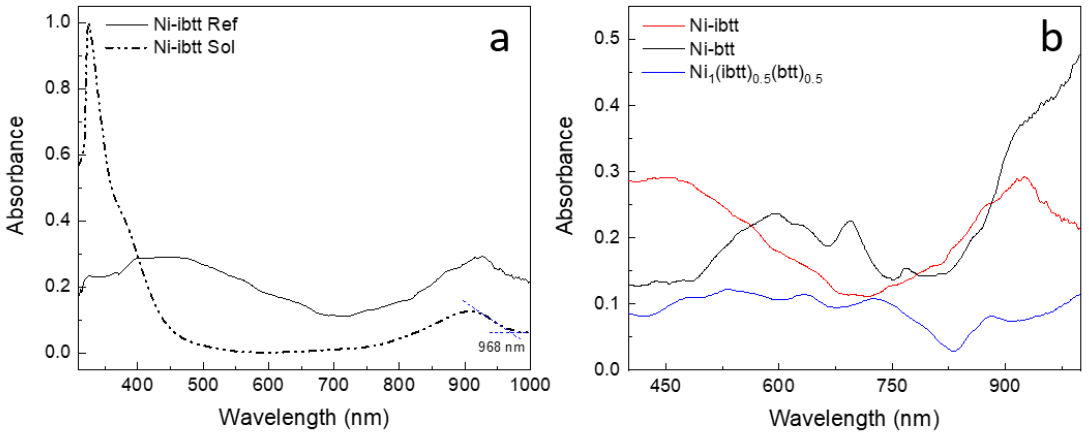

***Figure 43**. (a) UV-vis spectrum of **Ni-ibtt** solution in acetone (dash line) and UV-vis Diffuse Reflectance Spectroscopy (solid line); (b) UV-vis Diffuse Reflectance Spectroscopy of **Ni-ibtt**, **Ni(ibtt)$_{0.5}$(btt)$_{0.5}$** and **Ni-btt**.*

The soluble **Ni-ibtt** in acetone showed an apparent absorption peak centering at

900 nm in its UV–vis absorption spectra, representing the ligand-ligand charge transfer (LLCT) in Figure 43a. LLCT peaks in the range 800-1100 nm region have been previously reported for several redox-active nickel-bis(chelate) complexes as soluble small molecules, with S, O or NH as coordination donors.[21] The hypothesized origin of this observed peak here relates to the cyclic (*cis*) **Ni-ibtt** due to its nature as a smaller complex system. However, such redox-active complex feature were not observed for the other two samples, **Ni-btt** and **Ni(ibtt)$_{0.5}$(btt)$_{0.5}$**, in this spectrum, whose corresponding bands should extend into the near-IR region. For proper comparison, further UV-vis-NIR measurements need to be performed to confirm the band edge.

Accordingly, the bandgap of **Ni-ibtt** calculated based on the peak located at 968 nm is 1.28 eV. This experimental result is fairly close to that of DFT calculation at the B3LYP/6-31 g(d) level of theory, where the bandgap value of *trans* and *cis* **Ni-ibtt** (Figure 44 and Table 10) based on six-unit-oligomer is found to be 1.40 eV and 1.36 eV, respectively. As only **Ni-ibtt** was slightly soluble to provide UV-vis absorption spectra, UV-vis Diffuse Reflectance Spectroscopy of **Ni-ibtt**, **Ni-btt** and **Ni(ibtt)$_{0.5}$(btt)$_{0.5}$** were also examined, to compare their bandgaps. Figure 43b shows the absorption peak of and **Ni-ibtt** around 920 nm, which is consistent with that in Figure 43a.

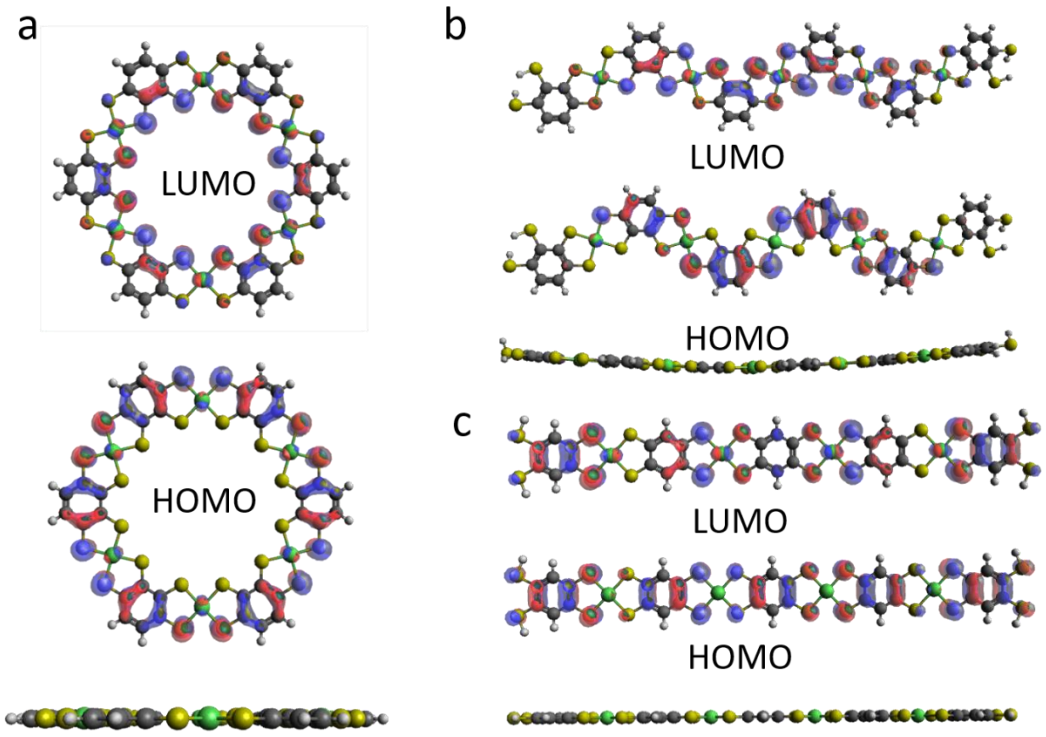

Figure 44. *The iso-surfaces of the highest occupied orbitals (HOMOs) and lowest unoccupied orbitals (LUMOs)calculated at the B3LYP-6-31 g(d) level of (a) cis* ***Ni-ibtt*** *based on six-unit oligomeric ring; (b) trans* ***Ni-ibtt*** *based on six-unit oligomeric chains;(c)* ***Ni-btt*** *based on five-unit oligomeric chains.*

To understand the difference in the frontier molecular orbital wave function distributions of the isomer polymers, DFT calculations were explored. In the linear polymer **Ni-btt** (Figure 44c), the HOMO wave function is delocalized over the whole chain, while the HOMOs are localized in both *cis* and *trans* **Ni-ibtt**, excluding most of the sulfur atoms. In the case of cyclic Ni-ibtt (Figure 44a), the HOMOs exclude all the S atoms in the inner ring on each ibtt (1,2,3,4-benzenetetrathiolate) ligand, consistent with the observation on the waving **Ni-ibtt** (Figure 44b). Among the three calculated structures, *trans* **Ni-ibtt** is not entirely planar as shown by the side view below, which might lead to wider π-π stacking distances in the solid state.

***Table 10**. Bond distances, HOMO, LUMO and bandgaps data from DFT calculation of trans/cis **Ni-ibtt** and **Ni-btt** based on six and five repeating-unit oligomers, respectively.*

Ni-ibtt

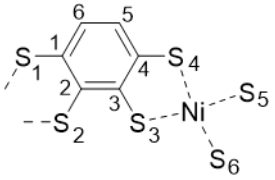

Ni-btt

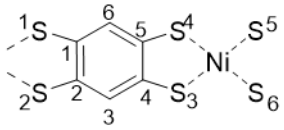

Bond distance (Å)	**trans Ni-ibtt**	**cis Ni-ibtt**	Bond distance (Å)	**Ni-btt**
C1-C2	1.418	1.393	C1-C2	1.391
C2-C3	1.433	1.412	C2-C3	1.399
C3-C4	1.418	1.394	C3-C4	1.399
C4-C5	1.426	1.398	C4-C5	1.391
C5-C6	1.369	1.395	C5-C6	1.399
C6-C1	1.426	1.398	C6-C1	1.399
C1-S1	1.722	1.724	C1-S1	1.766
C2-S2	1.726	1.724	C2-S2	1.766
C3-S3	1.726	1.724	C3-S3	1.766
C4-S4	1.722	1.724	C4-S4	1.766
Ni-S3	2.150	2.210	Ni-S3	2.210
Ni-S4	2.149	2.184	Ni-S4	2.210
Ni-S5	2.150	2.204	Ni-S5	2.210
Ni-S6	2.149	2.188	Ni-S6	2.210
LUMO	-4.660 eV	-4.650 eV	LUMO	-5.273 eV
HOMO	-6.064 eV	-6.007 eV	HOMO	-5.938 eV
Bandgap	1.404 eV	1.357 eV	Bandgap	0.665 eV

The theoretical HOMO level of *cis* **Ni-ibtt**, *trans* **Ni-ibtt** and **Ni-btt** present not a huge difference (-6.01, -6.06 and -5.94 eV), **Ni-btt** has a significantly lower LUMO at -5.27 eV and thereby the narrowest bandgap (0.67 eV) among the three. Meanwhile, the comparison of the atomic distances (Table 10) revealed that **Ni-ibtt** possesses more polarization and less homogenous electron distribution than **Ni-btt**. **Ni-btt** and *trans* **Ni-ibtt** showed very uniform length of Ni-S bonds (with deviation less than 0.001 Å),

while the maximum different of Ni-S length in and *cis* **Ni-ibtt** is 0.026. The aromatic C-C bonds in **Ni-btt** also show more homogenized distance with a maximum difference at 0.008 Å, while the values of *cis*- and *trans*-**Ni-ibtt** are 0.019 and 0.064 Å, respectively (Table 10).

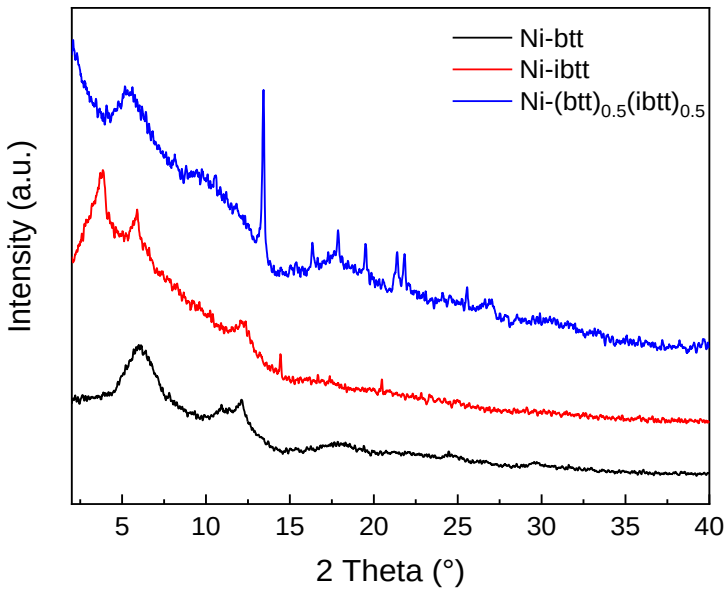

Figure 45. *Powder X-ray diffraction spectra of the three OMCPs.*

To compare the crystallinity of these OMCPs based on isomeric ligands, powder XRD spectra were recorded. Despite the two broad peaks (5.9° and 12.1°) at similar positions with those of the linear **Ni-btt**, **Ni-ibtt** showed another peak at 3.8°, indicating its wider d-spacing (10.7 Å) due to its waving backbone (Figure 45). The peaks observed at 14.4° and 20.5° were very weak in Ni-ibtt, whereas **Ni(ibtt)$_{0.5}$(btt)$_{0.5}$** showed more features in this region, with the presence of a sharp peak at 13.4° and several weak but apparent peaks at 16.3°, 17.8°, 19.5°, 21.4° and 21.8°. Isomeric polymer with intrachain dipole moment has been reported to possess better

crystallinity.[109] Here, the polarization exists in the angular-shape chains of both **Ni-ibtt** and **$Ni_1(ibtt)_{0.5}(btt)_{0.5}$**, while no permanent dipole moment occurs in the linear-shape backbone of **Ni-btt**. Though a significant higher crystalline degree of the dual-ligand polymer than that of the two mono-ligand polymers is less likely, the polymer obtained here, **$Ni_1(ibtt)_{0.5}(btt)_{0.5}$**, is possibly to possess a richer environment and complicated compositions. It might contain both the desired alternating/dual-ligand polymer and mono-ligand polymer (Ni-btt or/and Ni-ibtt) as impurity, though the ratio of ibtt and btt used for the synthesis was 1:1. Further evaluation of the difference of coordination capability between the two ligands and systematic optimization of reaction conditions, including temperature, solvents, reaction time and the ligand ratio, are required for preparing the pure crystalline dual-ligand polymer. On the other hand, both XRF (Table 9) and XPS (Figure 39) analysis showed the presence of Ca element in polymer **$Ni(ibtt)_{0.5}(btt)_{0.5}$**, whose origin was unclear as the synthesis procedure involved no Ca-containing chemical. This needs further investigation upon the possible existence of any Ca-based inorganic impurity and consequent effect on XRD data.

Compared with **Ni-btt**, **Ni-ibtt** was less thermal stable and started to degrade gradually from around 150 ℃ shown in the TGA analysis (Figure 46). Meanwhile, the degrading of **Ni-ibtt** was much slower as no sharp weight loss present around 300 ℃, like the one shown in **Ni-btt**.

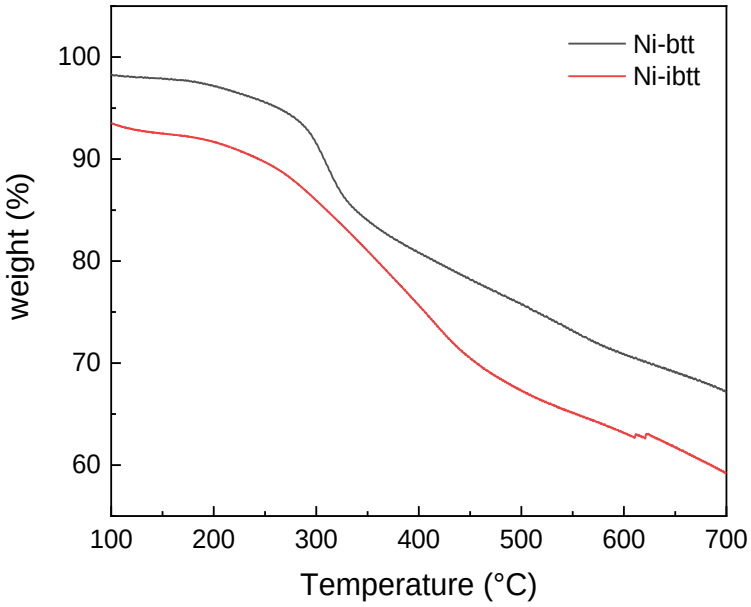

***Figure 46**. TGA spectra of **Ni-ibtt** recorded in nitrogen.*

3.3 Discussion of thermoelectric properties of isomeric polymers

Both polymers **Ni-ibtt** and **Ni-btt** are based on chelation between Ni^{2+} and a tetrathiolate ligand. The difference in their thermoelectric performance can be only addressed to the critical change in the coordination mode caused by the tetrathiolate-linker.

3.3.1 Thermoelectrical behavior of Ni-ibtt

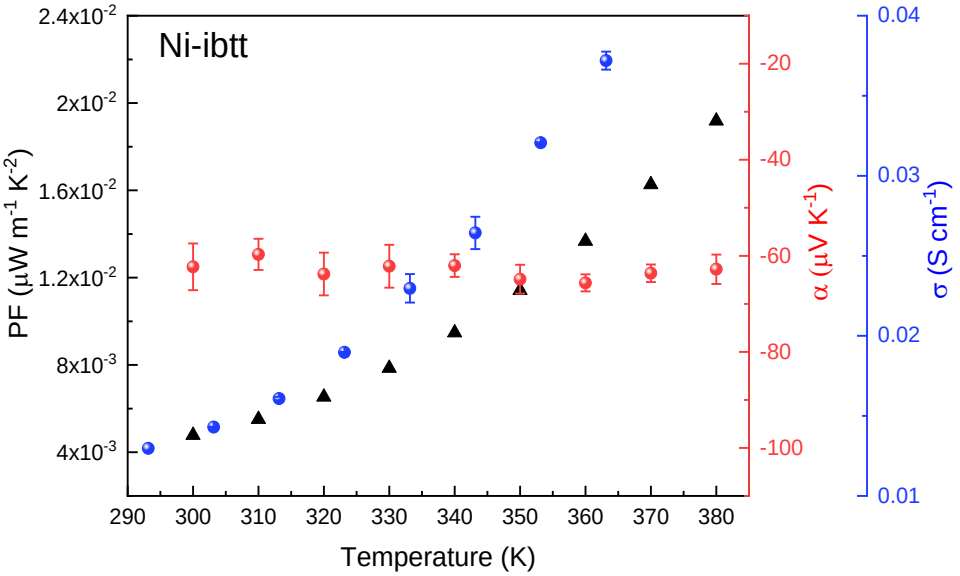

***Figure 47**. Electrical conductivities (blue), Seebeck coefficients (green) and power factors of **Ni-ibtt**.*

The electric conductivity of **Ni-ibtt** pellet increased from 0.014 S cm^{-1} to 0.037 S cm^{-1} between 303 and 363 K (Figure 47). This conductivity value is two orders of magnitude lower than that of the linear isomer **Ni-btt** (Table 11). Generally, the electrical conductivity of a coordination polymer depends on the polymer length, extent of conjugation, structural disorder or number of electron donor sites (coordinated sulfur in this work) of the linker for particular nodes.[110] As here we cannot evaluate the first factor due to the insolubility of those OMCPs, the below discussion will just focus on the following two aspects.

***Table 11**. Summary of the average thermoelectric properties at 305 K of **Ni-ibtt** and **Ni-btt**.*

Sample	σ (S cm^{-1})	α (μV K^{-1})	PF (μW m^{-1} K^{-2})
Ni-ibtt	1.33×10^{-2}	-62.0	5.11×10^{-3}

Ni-btt	7.11	+12.7	0.12

Firstly, the DFT calculation revealed the conjugation extent of both *cis* and *trans*-**Ni-ibtt** configuration, explaining its lower σ compared with **Ni-btt**: (i) In each repeating unit, the LUMO of the *cis* configuration shows an electron delocalization mainly concentrating on the inner ring (four S atoms and four C atoms connected with them) but the other two C atoms on the fringe hardly get involved; in the HOMO of *cis*-**Ni-ibtt** (Figure 44a), sulfur atoms were all cut out. Similarly, the LUMO of *trans* **Ni-ibtt** (Figure 44b), reveals only its center-most part involving the delocalization, excluding the marginal aromatic carbon atoms. (ii) The *trans* **Ni-ibtt** (zig-zag) display a bending polymer chain from side view, which might widen the stacking between polymer interchain and reduce the π-orbital overlapping, while the *cis* **Ni-ibtt** and **Ni-btt** backbones are fairly planar. Despite the more extended intrachain π-d conjugation of **Ni-btt**, its linear and planar backbone also promotes interchain π-stacking and therefore enhance polymer chain aggregation and dense packing, which is beneficial to charge carrier transport and explain the higher conductivity of **Ni-btt** compared to its isomeric counterpart.[111]

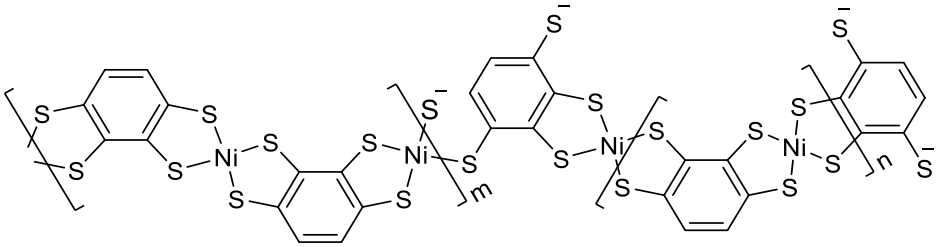

Scheme 11. *Potential* ***Ni-ibtt*** *structure defects.*

Despite the DFT description focusing on ideal intrachain structures in the gas phase, **Ni-ibtt** may have more defects and fewer donor sites (coordinated sulfur) in its natural structure. In the ideal hypothesis, four S atoms in each ligand all coordinate with a center metal and certain uncoordinated defects exist at the two ends of each polymer chain. Under this circumstance, the defect only comes from the un-coordinated S or Ni on two ends of the straight chains in **Ni-btt**, while **Ni-ibtt** chains are more complex. Ideally, the two couples of S atoms in ibtt ligands (S_1-S_2 and S_3-S_4) chelate with two Ni atoms on both sides of the axis and extend conjugation in trans or cis way. However, we cannot exclude the possibility that a portion of ibtt ligands may participate into the coordination with the central two sulfur atoms (S_2-S_3). This will cause polymer coordination being terminated or the formation of unfavorable complex with the remaining S_1 and/or S_4 (Scheme 11). Consequently, the lower conductivity of **Ni-ibtt** can be explained in two ways: (i) the free S atoms will act as potential charge trapping sites rather than donor sites or be oxidized into sulfate, which inevitably reduces the number of free charges in either way; (ii) bulky **Ni-ibtt** has shorter conjugation lengths along the chain and more interchain structural disorder. Similar finding has also been reported in another isomeric OMCPs based on copper-dicarboxylate coordination, where the structure with higher-coordination degree has lower transfer resistance and higher electrical conductivity.[110]

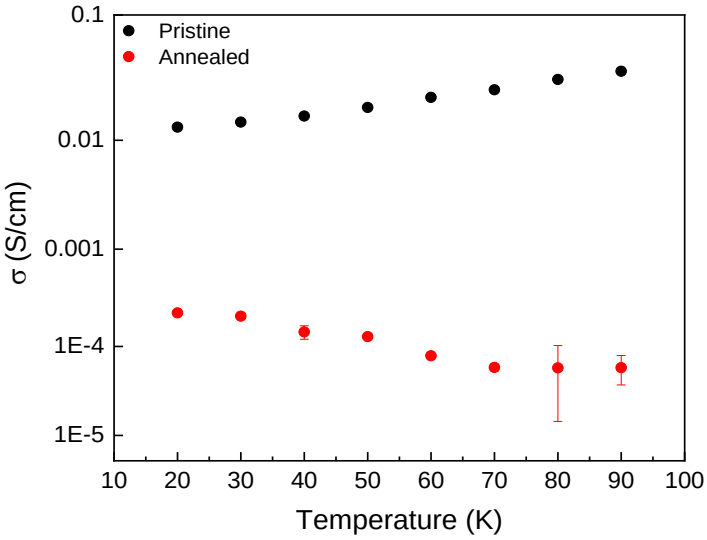

Figure 48. *Electrical conductivities of pristine (black) and annealed (red)* ***Ni-ibtt*** *pellet.*

In order to examine the annealing effect on the thermoelectric performance, the **Ni-ibtt** pellet was heated to 150 ℃ for 5 hours in ambient lab conditions. It showed a significant decreased conductivity by two orders of magnitude (Figure 48). XPS spectrum reveals that the loss of conductivity is most likely due to the oxidization according to the new emerging signature of the S 2p peak at 168 eV, representing the formation of sulfate during the heating process in air (Figure 49). Meanwhile, this oxidization occurred only on the surface of the pellet: Firstly, the bulk material 15 nm beneath showed no obvious composition change on XPS spectrum, compared with that of pristine. Second, when the pellet surface was slightly physically polished, it showed the electrical conductivity just same as that of pristine, without increase or decrease. Another reason may attribute to the loss of electrical conductivity is thermal decomposition, which starts from around 150 ℃ according to the TGA analysis above (Figure 46).

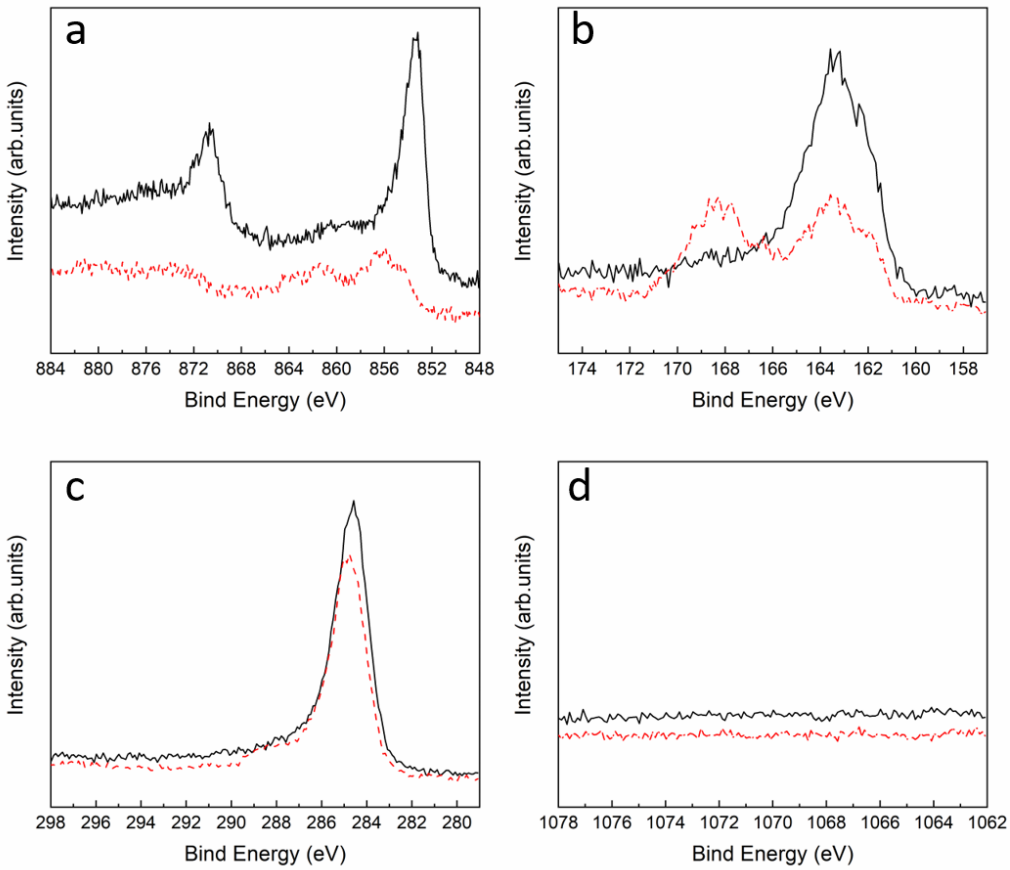

Figure 49. *XPS spectra of the annealed pellet of* ***Ni-ibtt*** *on the surface (red dash) and 15 nm beneath (black solid): (a-d) Ni 2p, S 2p, C 1s and Na 1s core level XPS spectrum.*

Existing air-stable n-type organic TE materials are quite scarce, among which most are composites or doped materials. The available neat n-type polymers are even rare and need further development. Of particular interest, **Ni-ibtt** is another air-stable n-type OMCP with a negative sign of Seebeck since the widely reported poly(**Ni-ett**). Neat **Ni-ibtt** showed a fairly stable Seebeck value as -60 μV K^{-1} between RT to 373 K (Figure 47). Reversely, the isomeric polymer of **Ni-ibtt**, **Ni-btt**, present to be p-type in our previous work. This means the two OMCPs have opposite predominant charge carriers due to ligand isomerism.

In the only report regarding *trans* **Ni-ibtt**, DFT stimulation was used to evaluated its TE potential together with several other OMCPs as p-type candidates, including **Ni-btt**.[36] The *trans* **Ni-ibtt** was predicted to be detrimental for hole transport, with only the orbital conjugation between its para-S atoms and bounded C–C bonds acting as the hole-conducting channel. This result is in agreement with our experimental measure that **Ni-ibtt** shows a negative sign of Seebeck coefficient as a n-type material.

3.3.2 Thermoelectrical behavior of $Ni(ibtt)_x(btt)_{1-x}$

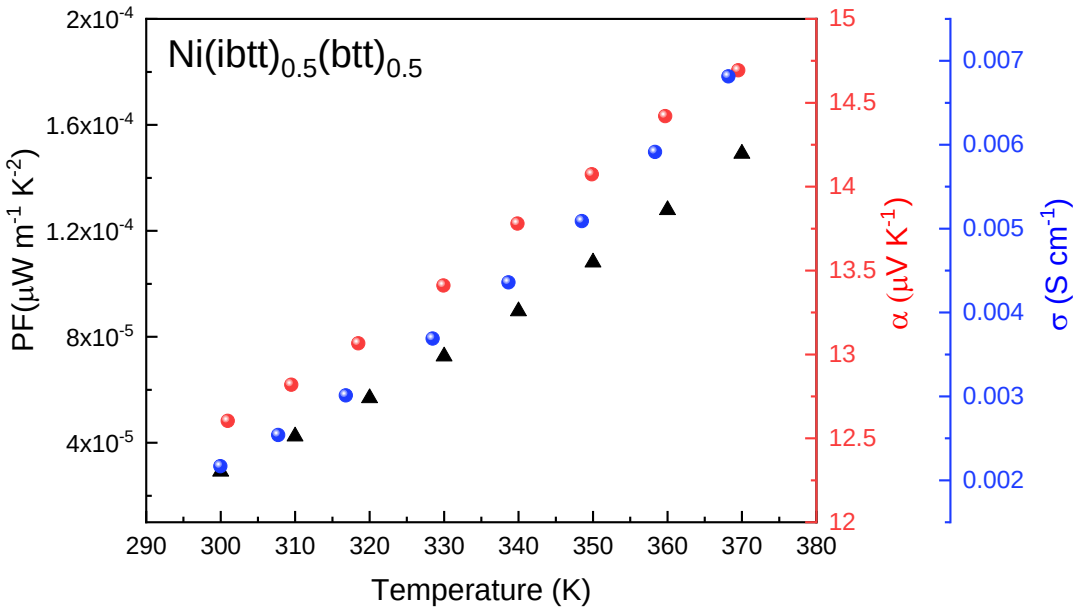

***Figure 50**. Electrical conductivities, Seebeck coefficients and power factors of **Ni(ibtt)$_{0.5}$(btt)$_{0.5}$**.*

Initially, for the attempt to investigate how the geometric change affects the thermoelectric properties by combining the pair of isomeric ligands, 1:1 was used as the ratio of ibtt : btt for the mixing-ligand polymer. Unsurprisingly, the obtained **Ni(ibtt)$_{0.5}$(btt)$_{0.5}$** showed a suppressed electrical conductivity at the order of 10^{-3} S cm^{-1} at room temperature (Figure 50), in comparison with mono-ligand OMCPs, either **Ni-**

ibtt or **Ni-btt** (Table 12). Consequently, the PF value of **Ni(ibtt)$_{0.5}$(btt)$_{0.5}$** (3.65×10^{-5} at 305 K) was also much lower than the waving **Ni-ibtt** (5.11×10^{-3} at 305 K). This can be explained by the more intrachain structural defects and polymer interchain disorder, caused by the mixing ligands.

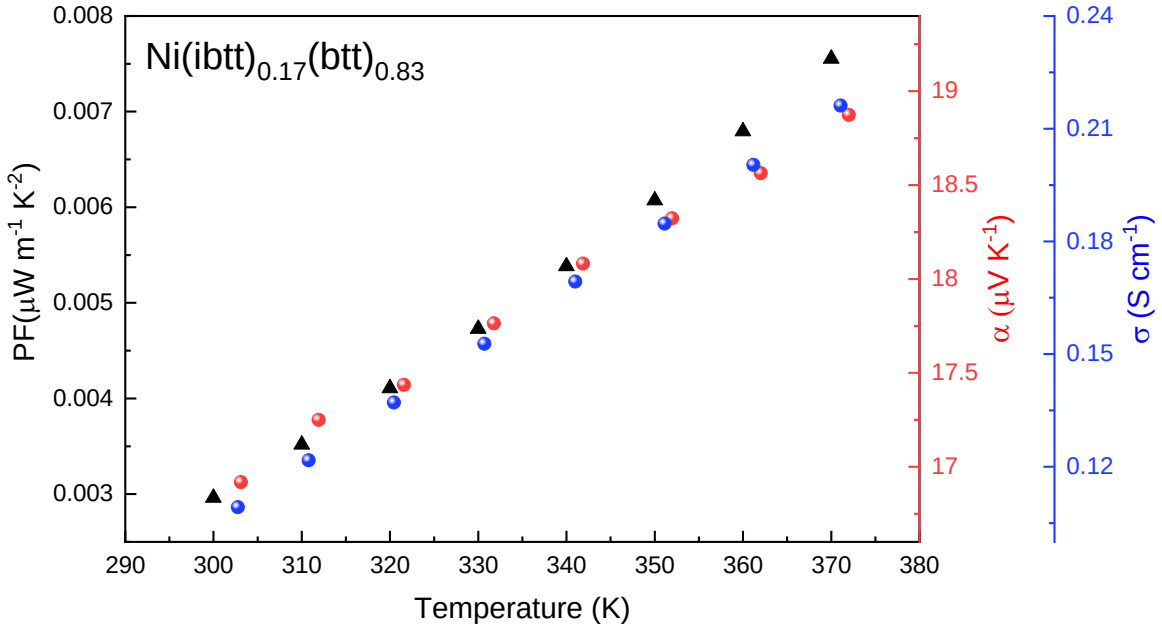

Figure 51**. Electrical conductivities, Seebeck coefficients and power factors of **Ni(ibtt)$_{0.17}$(btt)$_{0.83}$

The depressed thermoelectric performance of **Ni(ibtt)$_{0.5}$(btt)$_{0.5}$** makes it less likely to be used for thermoelectric purpose. Thus, the ibtt content was reduced to let the btt ligand be more dominant, attempting to optimize the properties and pursue a higher electrical conductivity. The polymer **Ni(ibtt)$_x$(btt)$_{1-x}$** were prepared with 5:1 as the ratio of btt/ibtt. As expected, the electrical conductivity of obtained **Ni(ibtt)$_{0.17}$(btt)$_{0.83}$** increased by nearly 8 times compared to neat **Ni-ibtt**, up to 0.11 S cm^{-1} at 303 K (Figure 51 and Table 12). This lower ligand ratio of btt/ibtt used for synthesis is beneficial to the electrical conductivity. The reason is the higher conjugation degree with the addition

of btt ligand, in line with the discussion above upon the higher intrinsic conductivity of **Ni-btt** than that of **Ni-ibtt**.

Table 12. *Summary of thermoelectric properties at 305 K of* ***Ni-ibtt***, ***Ni-btt***, ***Ni(ibtt)$_{0.17}$(btt)$_{0.83}$*** *and* ***Ni(ibtt)$_{0.5}$(btt)$_{0.5}$***.

Sample	σ (S cm^{-1})	α (μV K^{-1})	PF (μW m^{-1} K^{-2})
Ni-ibtt	1.33×10^{-2}	-62.0	5.11×10^{-3}
Ni-btt	7.11	12.7	0.12
Ni(btt)$_{0.83}$(ibtt)$_{0.17}$	1.12×10^{-2}	17.0	3.24×10^{-3}
Ni(btt)$_{0.5}$(ibtt)$_{0.5}$	2.28×10^{-3}	12.7	3.68×10^{-5}

In brief, the ratio of the isomeric ligands is the key factor to tune the electrical conductivity of the dual-ligand system. To note, the σ value of dual-ligand OMCPs is not proportional to the ligand ratio. A dual-ligand OMCP formed by 2,3,6,7,10,11-hexahydrotriphenylene (HHTP) and tetrahydroxy1,4-quinone (THQ), Cu_3(HHTP)(THQ) was found more conductive than the mono-ligand OMCPs, Cu-HHTP and Cu-THQ, rather than in between.[112] Optimization can only be achieved by examining the impact of the stoichiometry in such dual-ligand OMCP systems.

In terms of Seebeck coefficient of the dual-ligand OMCPs, introducing 1/6 ibtt in the whole ligands leads to no significant change in the Seebeck coefficient, compared with the one formed with neat btt. **Ni$_1$(ibtt)$_{0.17}$(btt)$_{0.83}$** shows the same positive Seebeck (p-type) as **Ni-btt** (13 μV K^{-1}) with a slightly higher value (17 μV K^{-1}) at room temperature.

3.4 Sidechain effect on the thermoelectric properties of benzenetetrathiolate (btt) based polymers

Introducing sidechains is a commonly used route for promoting solubility of semiconducting polymers. Meanwhile, the sidechain addition can greatly impact the electronic properties of semiconducting polymers, by tuning intra- and inter-molecular ordering and the complicated interrelationship between ordering of sidechains and conjugated backbones.[113]

The application of the reported OMCPs in the thermoelectric field is still limited due to the insolubility and the consequent difficulty to process. Hence, we also attempt to explore the possibility to increase the solubility by introducing different sidechains to the bridging ligand, as well as investigating the effect of the introduced sidechains, their donating or withdrawing character, on the thermoelectric performance of the corresponding OMCPs.

Specifically, we tried to introduce nitro (-NO_2) and methyl (-CH_3) sidechains onto the core structure of **Ni-btt** and obtained another two π-d conjugated polymers based on Ni-S coordination. Though, the resulting materials showed poorer thermoelectric performance based on initial measurement, further synthesis and characterization is ongoing, aiming to establish the correlation between the length and inductive effect of introduced sidechains, with the configuration and geometry of the obtained OMCPs.

3.4.1 Design and synthesis of btt-based coordination polymers with different sidechains

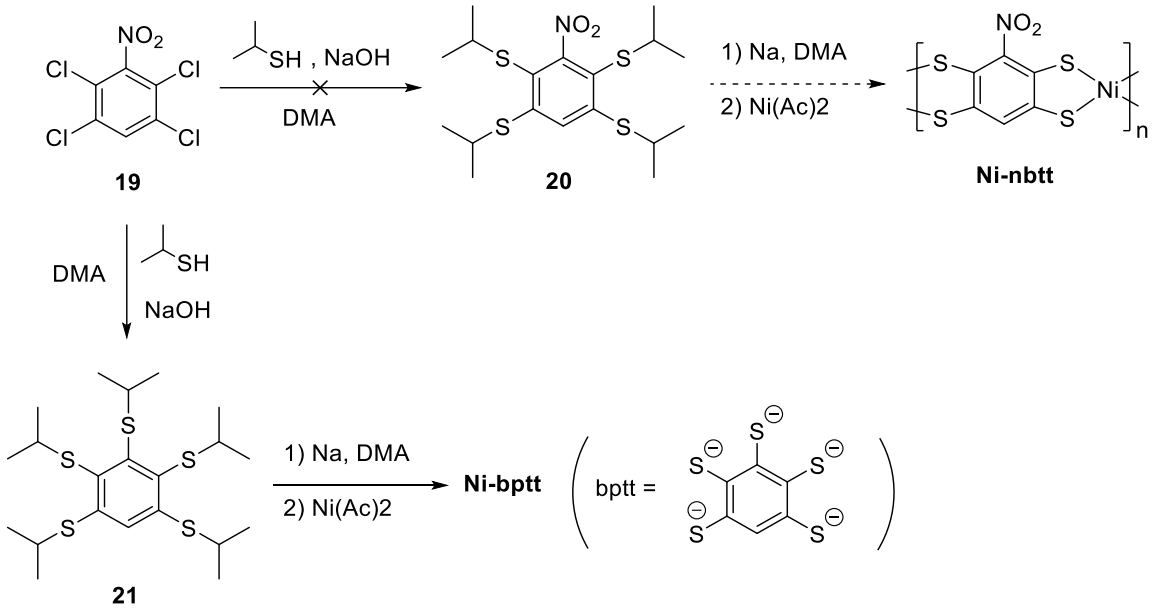

Scheme 12**. Synthetic pathway towards compound **21** and **Ni-bptt** in practical case, instead of the proposed **Ni-nbtt

Initially, the reaction in Scheme 12 was designed to synthesize (3-nitrobenzene-1,2,4,5-tetrayl)tetrakis(isopropylsulfane) **20**, with which we attempted to form the 3-nitrobenzene-1,2,4,5-tetrakis(thiolate) ligand, to obtain the proposed OMCP structure **Ni-nbtt**. The aim was to introduce electron withdrawing group (-NO_2) and investigate its effect on thermoelectric performance, in comparison with **Ni-btt**. However, this synthetic route generated the compound **21**, benzene-1,2,3,4,5-pentaylpentakis(isopropylsulfane), via the nucleophilic aromatic substitution (S_NAr) reaction of nitroarene. This kind of S_NAr reactions are commonly known, especially for the structures with strong electron-withdrawing groups at the ortho or para positions of -NO_2 group.[114] Based on this, we obtained the ligand benzene-1,2,3,4,5-

pentakis(thiolate) (bptt) by sodium reduction and formed the polymer Ni-bptt in the following steps.

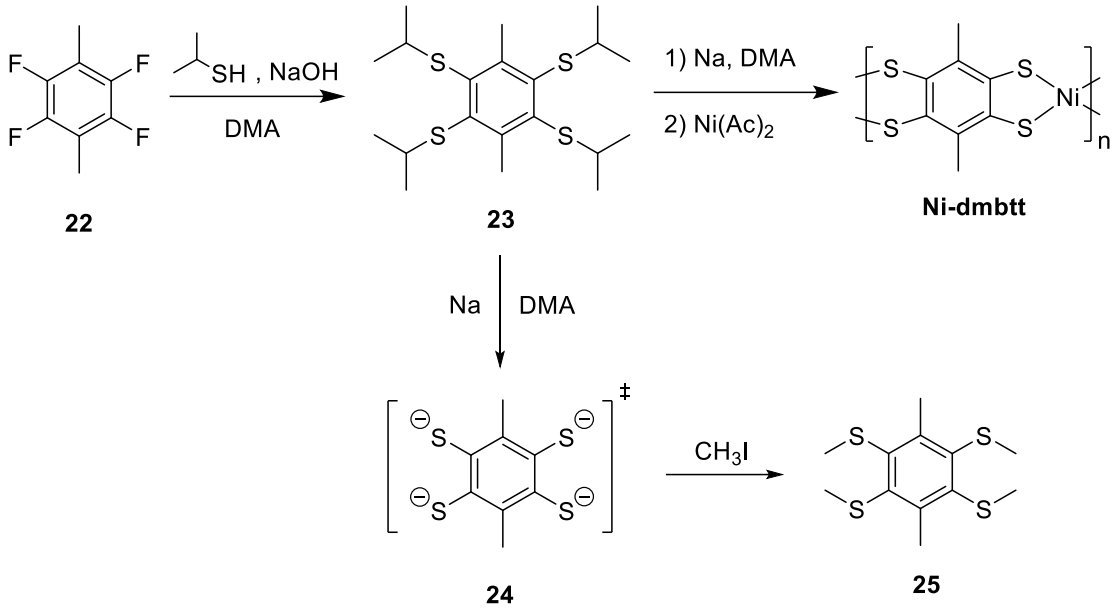

***Scheme 13**. Synthetic pathway towards compound **25** and **Ni-dmbtt**.*

Then, the **23** was synthesized and polymerized into the OMCP structure **Ni-dmbtt**, allowing the introduction of two methyl groups onto the aromatic ring (Scheme 13). The reaction mechanism for the formation of **Ni-dmbtt** proceeded via a 3,6-dimethylbenzene-1,2,4,5-tetrathiolate intermediate, was confirmed by the formation of 1,2,4,5-tetrakis(methylthio)benzene (**25**) after quenching with methyl iodide instead of nickel salt.

3.4.2 Initial characterization of Ni-bptt and Ni-dmbtt

The electrical conductivity of **Ni-dmbtt** at room temperature was initially determined to be on the order of 10^{-3} -10^{-4} S cm^{-1}. Thermoelectric measurement of **Ni-bptt** (Figure 52) shows its moderate conductivity but a highest Seebeck coefficient (150

$\mu V\ K^{-1}$ at room temperature) among all the OMCPs presented in this work.

FTIR and Raman spectra (Figure 53 and 54) of **Ni-dmbtt** and corresponding starting material, compound **12**, were recorded to provide spectroscopic features. For instance, the remaining but depressed bands at 2956, 2920 and 2860 cm^{-1} in the FTIR of polymer **Ni-dmbtt** originate from two remaining -CH_3 groups from starting material, compound **12**. The presence of peaks involving thiocarbonyl radicals (C=S) are also observed in the FTIR and Raman spectra of **Ni-dmbtt**.

Most characterization of these OMCPs are still under investigation (delayed by covid-19 situation) for further systematic discussion.

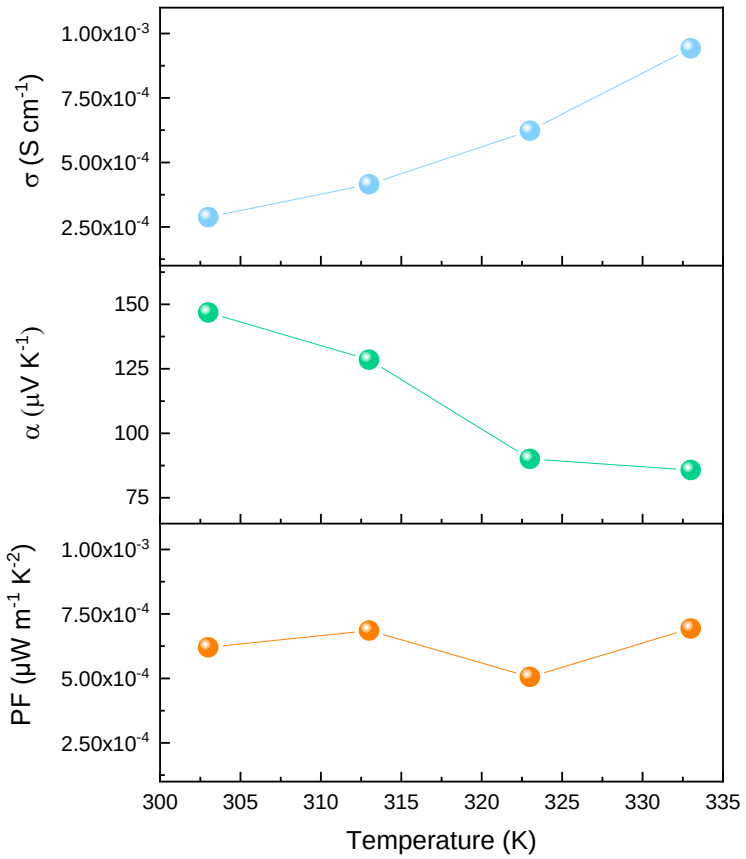

***Figure 52**. Electrical conductivities, Seebeck coefficients and Power Factor of **Ni-bptt** as a function of temperature.*

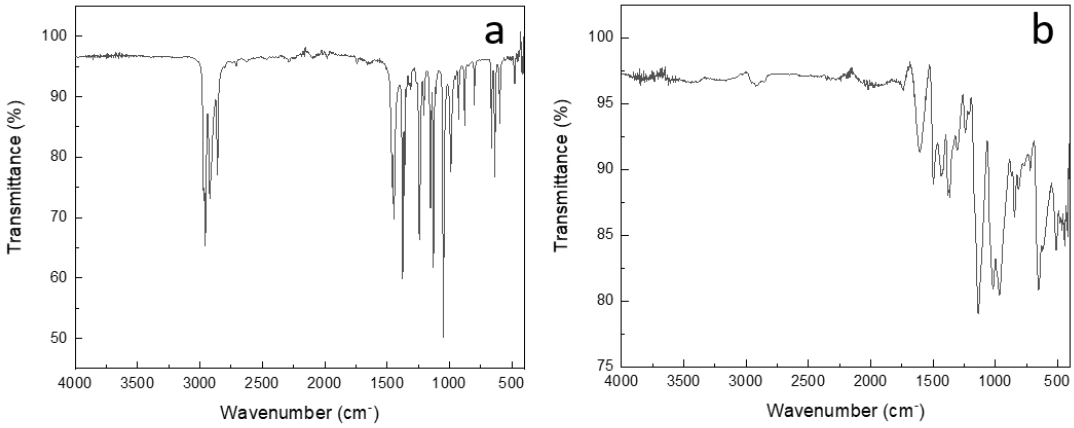

***Figure 53**. FTIR spectra of (a) compound **12** and (b) **Ni-dmbtt**.*

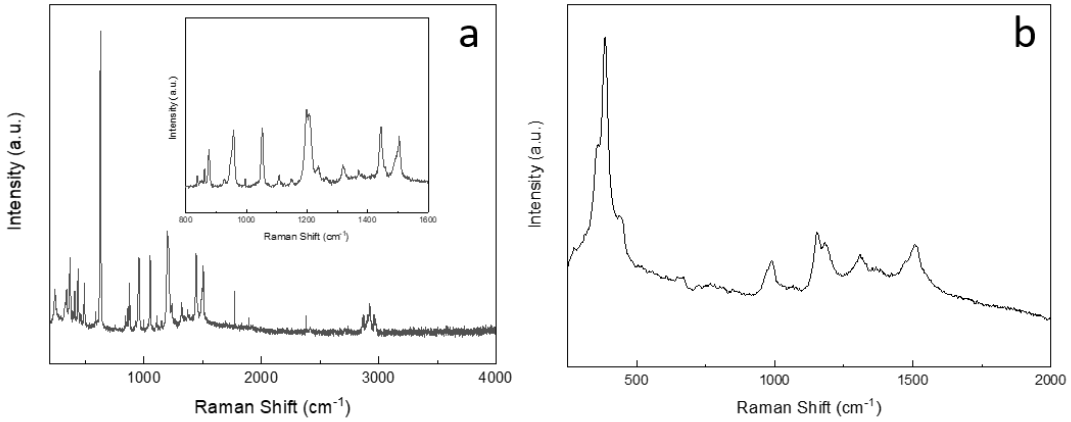

***Figure 54**. Raman spectra of (a) compound **12** and (b) **Ni-dmbtt**.*

3.5 Chapter conclusions

In this work, two geometrical isomeric bridging ligands, ibtt and btt, were used to form mono- or dual-ligand OMCPs with Ni(II). The structural characterization and thermoelectric behaviors of obtained OMCPs were studied.

Ni-ibtt was found to be a new n-type TE with good air-stability, showing very different thermoelectric properties from its isomer, which proves the impact of the structural isomerism on polymer behavior. Further DFT calculation is being

investigated to study the possible helix structure of *cis* **Ni-ibtt**.

The dual-ligand system synthesized with a large portion of btt (5/6) shows an enhanced σ value, while that of less btt (1/2) decreased. This seemingly controversial effect of introducing ligand btt on the σ value implies that both the intrachain conjugation extent and interchain packing/disorder are vital to such TE OMCPs. Meanwhile, both dual-ligand OMPCs present here are p-type like **Ni-btt**, which is worthy further investigation. The complexity of various structural factors has to be valued when designing and optimizing new thermoelectric OMCPs. As present in this chapter, thermoelectric properties can be tuned not only by using different isomer ligands but also by controlling the ligand composition.

Additionally, the obtained small complexes in this chapter will be examined as electrocatalysts or photocatalysts for hydrogen production from water, as nickel bis(chelate) complexes have been previously reported as good candidates for the application.[21]

Chapter 4. Impact of metal centers on thermoelectric properties of organometallic coordination polymers

The metal centers play a key role in determining the thermoelectric properties of OMCPs and can be explored to tune the thermoelectric performance of OMCP materials. Due to different effective nuclear charge and relativistic potential, transition metals differ in d-orbital energy levels, leading to their different electronic structures around the frontier orbitals and specific electronic properties of the complexes, when the ligand π-orbitals are fixed. For example, in the case of $[M(bdt)_2]^{n-}$ system (Figure 55), redox processes are metal oriented for the metals lighter than cobalt, while ligand oriented for the heavier ones.

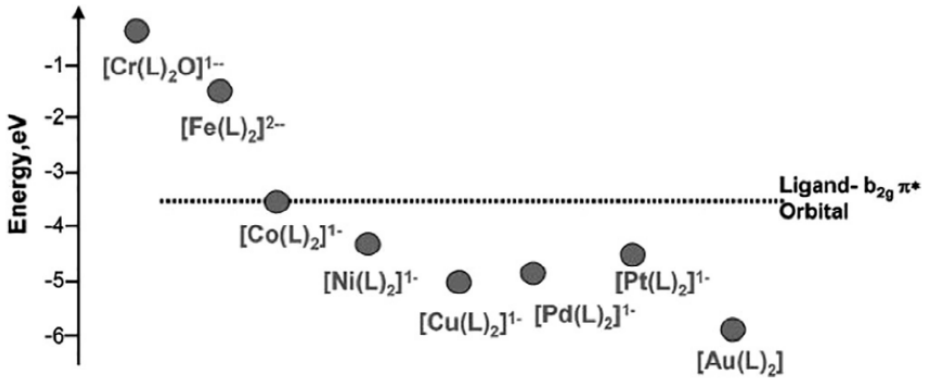

Figure 55. *Energy of d_{xz} orbital of metals in $[M(bdt)_2]^{n-}$ in published report. The energies are shown relative to that of ligand π* orbital with b_{2g} symmetry. Reused with permission [25] Copyright 2019, Elsevier.*

On the other hand, the size of metal centers, together with the coordination atoms, decides the coordination bond lengths of OMCPs. For instance, Yang's calculation work reported that the coordination bond lengths of Pd-based OMCPs are longer than that of

Ni-based OMCPs, as the van der Waals radius of Ni(II) and Pd(II) are 0.83 and 1.00 Å, respectively.[62] Moreover, poly(Pd-ett) also present longer interchain distances as well as parallel-chain distances due to its wider backbone (interchain b-axis) when intermolecular interactions (interchain and parallel-chain) were considered.[65] However, despite the theoretical work, systematic comparison among different metals for certain OMCP systems are still limited by a lack of experimental data to validate the theoretical findings. Especially, chemical composition and properties for a certain OMCP formula usually (like **Ni-ett**) differ from report to report and involve multiple factors, such as various reaction conditions, product morphology and measurement technique. These all disable the parallel comparison among OMCPs with different metal centers across reports.

Hence, this chapter focuses on OMCPs formed by ligand ett or btt with various metal centers, including Fe(II), Co(II), Ni(II), Cu(II), Pd(II) and Pt(II), to investigate the effect of transition metals on the thermoelectric behavior of these two OMCP systems. All the OMCPs were synthesized via one-pot method with unifying reaction conditions, including temperature, time, concentration and purifying process. Based the primary characterization and compared with the known data, how the metal centers influence the TE performance of M-ett and M-btt systems will be discussed.

4.1 Polymers M-ett with various center metals

Instead of Ni(II), Co(II), Cu(II) and Pd(II) were employed to synthesize the class

of ett-based OMCPs to study the effect of metal centres on the thermoelectric performance in this system. Among these OMCPs, only **Cu-ett** has been reported as a p-type candidate with systematic evaluation of the thermoelectric properties, while the analogous OMCPs, **Pd-ett** and **Co-ett**, have not drawn much attention.

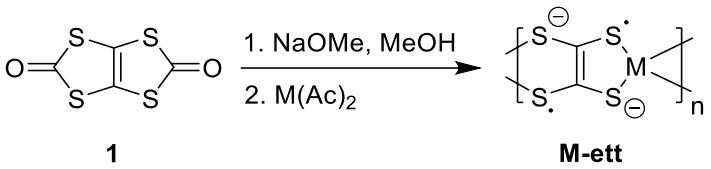

1 **M-ett**

Scheme 14*. Synthetic pathway towards* ***M-ett****.*

Here, via the same procedure used for preparing **Ni-ett** in Chapter 2**,** copper(II) acetate hydrate, palladium(II) acetate and cobalt(II) acetate tetrahydrate were used as the metal source to synthesize **Cu-ett**, **Pd-ett** and **Co-ett**, respectively (Scheme 14).

4.1.1 Poly(copper-ethylenetetrathiolate) (Cu-ett)

In the M-ett system, switching n/p type can be easily achieved by changing metal centers from nickel to copper. The underlying mechanism causing the Seebeck sign to change in OMCPs is still unknown, making the study of **Cu-ett** crucial to gather deeper insight into these materials. Here, we synthesized and purified **Cu-ett** and characterized its composition and thermoelectric performance.

To investigate the composition of **Cu-ett**, XPS and XRF were explored. XPS energy survey scans on the purified polymer showed the presence of Cu 2p, C 1s, S 2p core levels (Figure 56). Similar to the previously mentioned OMCPs, neither do XPS energy survey spectra, nor the Na 1s core level spectrum show any signal assigned to

Na^+ counter ions, which should locate at a binding energy of 1071 eV. XRF results (Figure 57) also showed no presence of Na in **Cu-ett**. The S 2p narrow range scans of **Cu-ett** present two main peaks with binding energies of 162.0 and 163.0 eV, stemming from the complexation between Cu and S atoms. This set of peaks is slightly shifted towards lower binding energy, compared with that of **Ni-ett**, **Ni-diett** and **Ni-btt** at 161.9 eV and 163.3 eV.

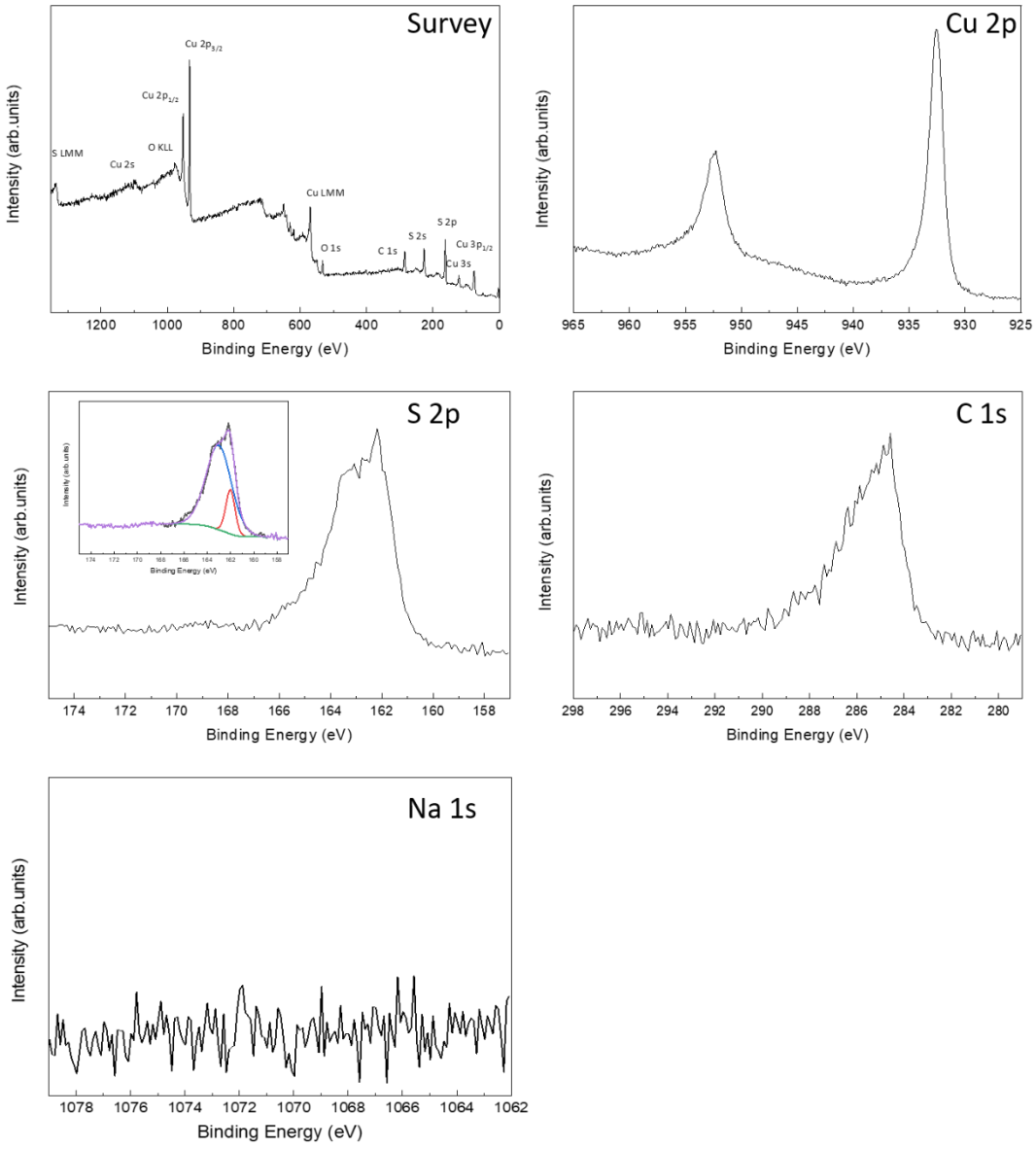

***Figure 56**. XPS energy survey spectra of purified **Cu-ett** and corresponding Cu 2p, S 2p, C 1s, Na 1s core level XPS spectra.*

In the Cu 2p photoemission spectra of this OMCP, the set of peaks with binding energies of 932.6 eV and 952.4 eV were assigned to the Cu $2p_{3/2}$ and Cu $2p_{1/2}$, respectively. The couple of sharp peaks confirm the presence of Cu^{+} species as the single type of centered Cu atom in this OMCP. Cu^{2+} would be expected to have very strong satellite features with binding energy around 943 eV.[115] Here Cu L3VV Auger line is suggested to be further examined to exclude the existence of Cu^{0}, whose XPS peaks are difficult to be differentiated from those of Cu^{+}.

Given the Cu atoms exist in the +1 valence state based on the XPS result, each ett ligand should coordinate with two Cu^{+} for the neutral charge backbone and thereby the theoretical ratio of S and Cu elements in this **Cu-ett** should be 2. This is in agreement with the XRF data of **Cu-ett**, where the atomic ratio of S and Cu is found to be 1.9.

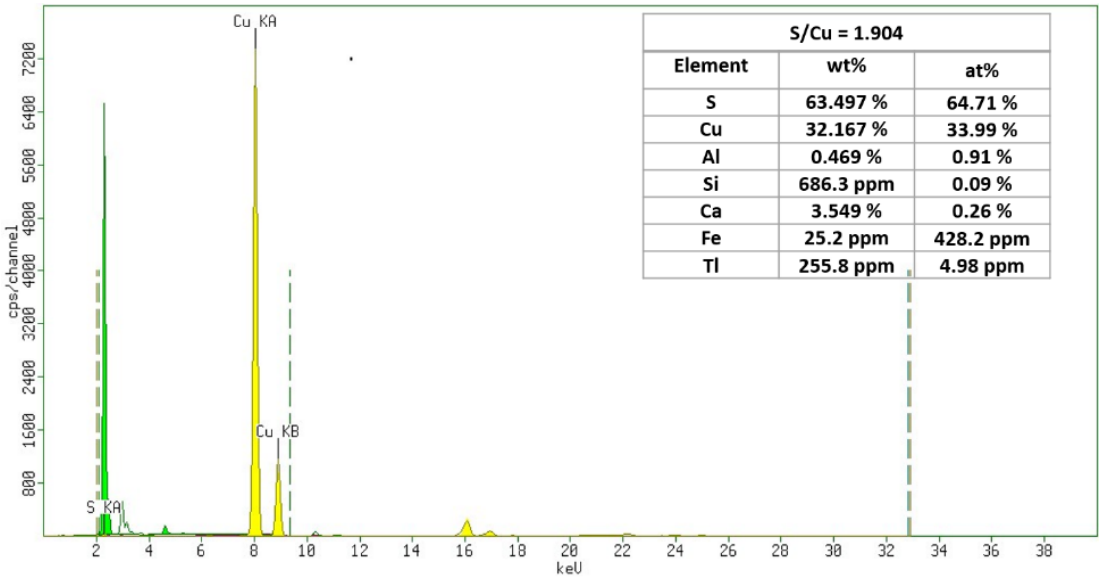

***Figure 57**. XRF of element contents (weight % and atomic %) and corresponding atomic S/Cu ratio of Cu-ett.*

It is notable that the reagent used for the synthesis of **Cu-ett** was a Cu(II)- salt ($CuAc_2 \cdot x\ H_2O$) while the copper in the formed polymer seemed to have been reduced to +1 during either the synthesis or the purification. Similarly, no typical Cu(II) configuration satellite peak was observed in the XPS Cu 2p spectrum of both poly[Na_x(Cu-ett)] and poly[Cu_x(Cu-ett)] synthesized from copper chloride ($CuCl_2$).[66, 116] In the late 1980s, the structure of poly[Cu_x(Cu-ett)] was assumed to be the rigid chains linked by the sub-coordination between S atoms and the Cu atoms off the chains (shown in Figure 58c).[37, 117] A recent study revealed the XANES spectra of poly[Cu_x(Cu-ett)] has similar features with the MS_4 model complexes with reduced Cu $4p_z$ character and enhanced in-plane p_z-π bonding of ligands, which was recognized as suggestive evidence of the extended π overlapping of the former proposed structure.[116] However, with the presence of two kinds of Cu atoms, this proposal cannot explain the equality of all Cu atoms or single Cu chemical environment in the polymer found by XPS.

Inspiringly, the XPS characterization of a two-dimensional π–d conjugated copper coordination polymer based on benzenehexathiol (BHT) also witnessed the oxidation state change of Cu atoms from +2 in the starting reagent, $Cu(NO_3)_2$, to +1 in the formed $[Cu_3C_6S_6]_n$ complex (shown in Figure 58a).[67] This 2D framework Cu-BHT showed a very close atomic S/Ni ratio (1.824 ~ 1.857) to that of the **Cu-ett** (1.902) we synthesized and analyzed here. However, the specific pathway for the unexpected change in copper oxidation state from Cu(II) to Cu(I) in poly(**Cu-ett**) and Cu-BHT is to date unanswered.

The similar formation of Cu(I) species from Cu(II) sources has also been observed in many other experiments for fabricating nanostructures based on copper (I/II) oxides, in the absence of reducing agent or even exposed under oxidizing conditions.[118-120]

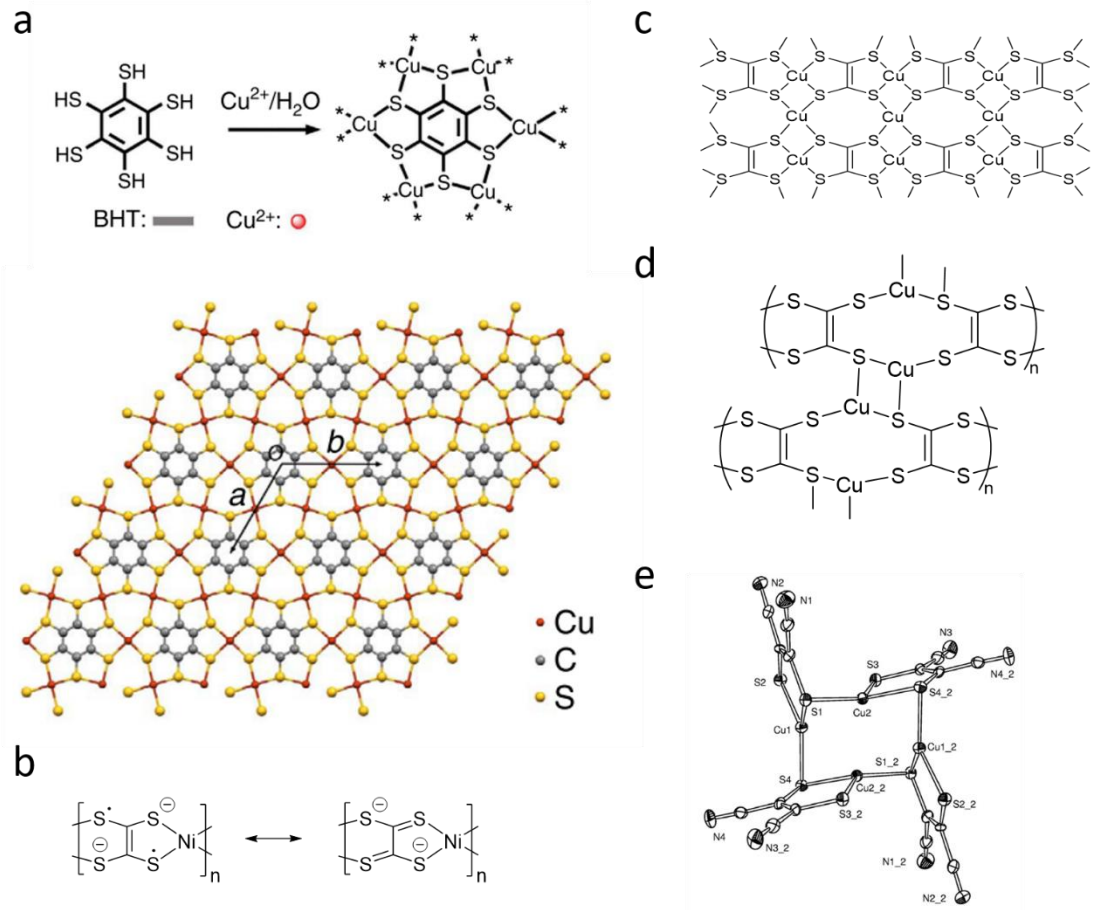

***Figure 58**. (a) Reported 2D lattice of [Cu3(C6S6)]n derived from the in-plane GIXRD pattern (a= b= 8.76 Å); [67] (b) Proposed structure of poly(Ni-ett); (c) Proposed structure of poly(Cu-ett) in literatures;[37, 117] (d) Proposed structure of poly(Cu-ett) in this work; (e) Structure of [Cu4(mnt)4]4- reused with permission.[121]Copyright 2011, Elsevier B.V.*

Later, cuprous salt was also used to synthesize the cuprous ethylenetetrathiolate (Cu(I)-ett), whose thermoelectric properties was also optimized via $LiBHEt_3$ reduction.[122] Based on the similar features observed in the comparison of Cu K-edge absorption spectra of Cu(I)-ett and a trigonal Cu-S coordination reference complex ($(Me_4N)_4Cu_4(mnt)_4$) (anionic unit shown in Figure 58e), the previous report suggested

tetragonally and trigonally coordinated Cu atoms co-existed in Cu(I)-ett. Together with those abovementioned findings, the experimental results here suggest a complex cross-linking structure in **Cu-ett** with numerous interchain interactions or in other words a trigonal Cu-S coordination (Figure 58d), instead of the previously hypothesized square-planar coordination form (Figure 58c) or the type of **Ni-ett** (Figure 58b). The similar interaction has also reported for complex $[Cu(dcbdt)_2]_2$ (dcbdt = dicyanobenzodithiolate) in its pseudo-dimer geometry.[123] This is irrelevant with the oxidation state of copper salt used for the synthesis of this OMCP. Only Cu(I) species can stabilize in the **Cu-ett** system, no matter Cu(II) or Cu(I) was used for synthesis. Analogous XPS scans were also performed at 15 nm beneath the surface of **Cu-ett** by surface etching (Figure 59). With no significant change found compared with the XPS spectrum of the surface, this data confirmed the homogenous chemical composition and elemental oxidation states in **Cu-ett**.

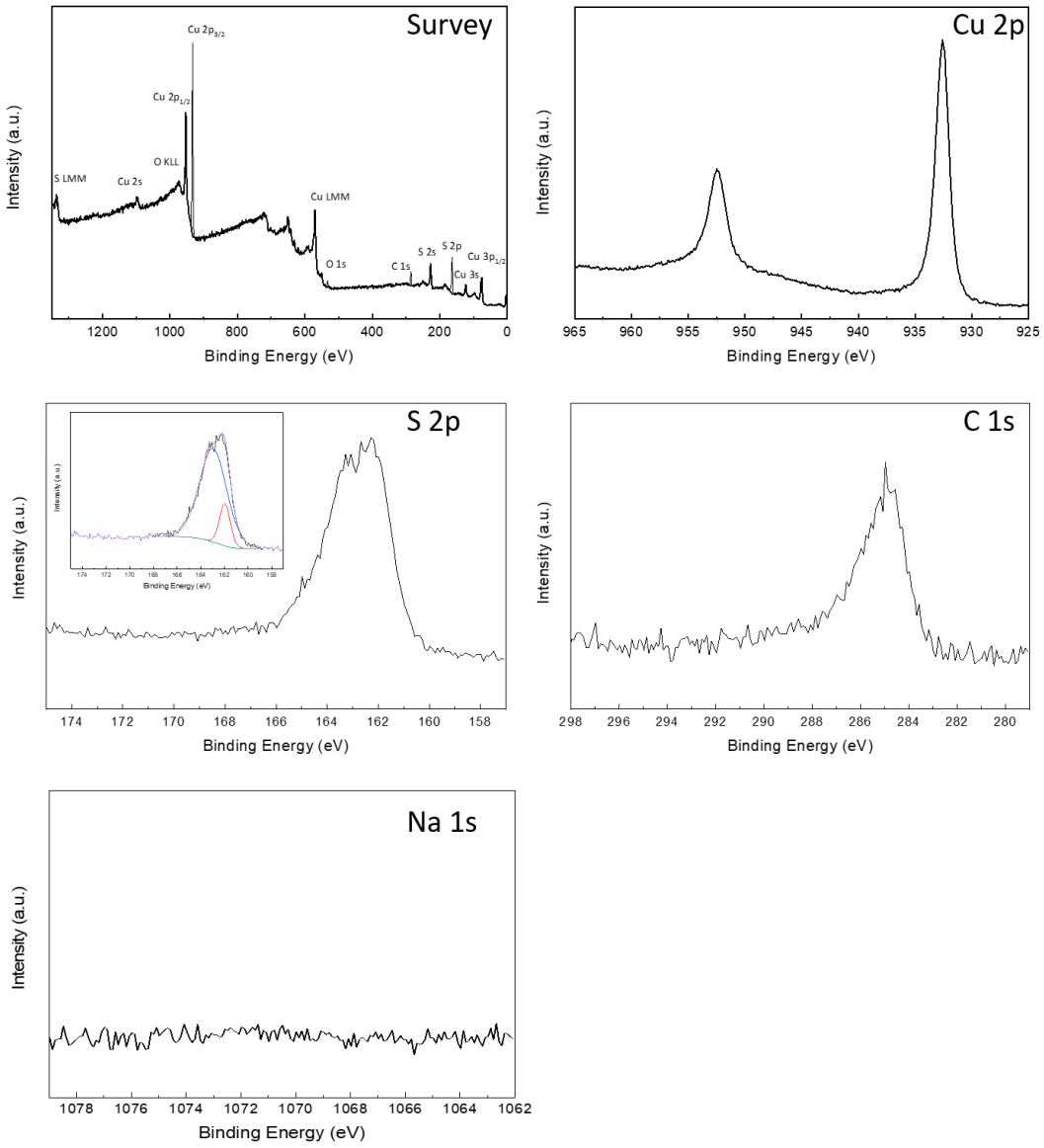

Figure 59. *XPS energy survey spectra of purified* ***Cu-ett*** *at 15nm beneath and corresponding Cu 2p, S 2p, C 1s, Na 1s core level XPS spectra. The inset figure in the S 2p spectra is corresponding XPS peak fitting.*

Among all the reported analogues **Cu-ett** or **Cu-TTO** materials summarized in Table 13, the **Cu-ett** in present work showed the highest electrical conductivity (93.9 S cm^{-1}). Here, there is a quite apparent trend that the better electrical conductive Cu-based OMCPs showed lower Seebeck coefficient. Among all the reports regarding Cu-ett, the Cu(I)-ett synthesized with cuprous starting reagent showed the highest PF value of 26.6 μW m^{-1} K^{-2}, but its ZT value (0.015) was marginally lower than the previously

reported Poly[Cu_x(Cu-ett)] (0.018).[66, 116] Undoubtedly, those experimental data reveal the difficulty to optimize the thermoelectric properties of this neat OMCP system. In earlier works (Scheme 15), the analogous class of Poly(Cu^y-TTO) where y = I or II, were prepared from tetraethylammonium tetrathiooxalate (TEATTO) or sodium tetrathiooxalate (Na_2TTO), and various Cu(II) salts, including $CuCl_2$, CuCl, $Cu(SAL)_2$ (SAL = salicylaldehyde), $Cu(OAc)_2$• H_2O and $Cu(NO_3)_2$ • H_2O.[39, 124] These reported CuTTO showed moderate thermoelectric performances but a uniform reverse sign of thermopower (n-type), compared with all the other p-type **Cu-ett** reported in the recent decade. The unknown reason of this n/p type switching needs further systematic investigation, including different copper sources, ligand designs, reaction temperatures and solvents, etc.

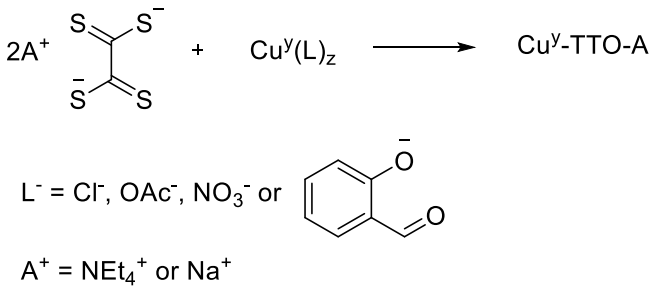

Scheme 15. *Synthetic pathway of Cu^y-TTO-A in literature, where z = 1 or 2 and y = I or II.*

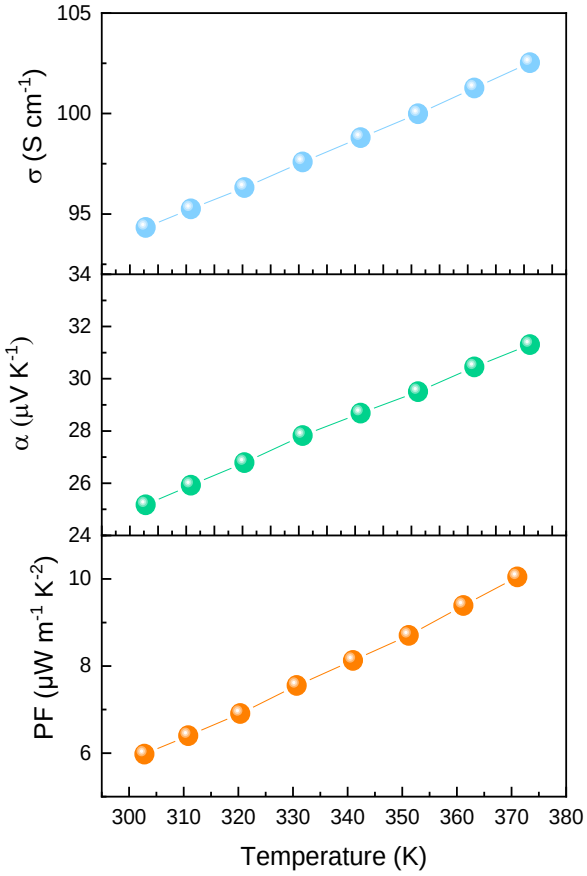

***Figure 60**. Electrical conductivities, Seebeck coefficients and Power Factors of **Cu-ett** as a function of temperature. Data points obtained from pellet annealed at 100 °C for 24 hours in glovebox.*

In conclusion, a new proposal for the structure of **Cu-ett** is provided here, to match well with its stoichiometric composition based on elemental analysis. Also, **Cu-ett** present herein showed a very good conductivity and moderate Seebeck value as a p-type material (Figure 60), to achieve a comparable PF value (5.82 μW m^{-1} K^{-2}) to that of the **Ni-ett** (5.55 μW m^{-1} K^{-2}) previously prepared.

***Table 13**. Summary of the thermoelectric properties at 300 K of **Cu-ett** related OMCPs. Ref 114 involves four different reaction conditions to polymerize poly(CuTTO) from TEATTO with: (a) $Cu(OAc)_2 \cdot H_2O$ at 45 °C; (b-d) $Cu(SAL)_2$ (SAL = salicylaldehyde), $Cu(OAc)_2 \cdot H_2O$, and $Cu(NO_3)_2 \cdot H_2O$ at 80 °C, respectively.*

Sample	σ_{300K} (S cm^{-1})	α_{300K} (μV K^{-1})	PF (μW m^{-1} K^{-2})	ZT_{300K}	Ref

Poly[Na_x(Cu-ett)]	0.2	79	1.2×10^{-1}	-	[66]
Poly[Cu_x(Cu-ett)]	9.5	83	6.5	1.8×10^{-2}	[66]
Cu(I)-ett	88.6	54.8	26.6	1.5×10^{-2}	[122]
Cu-ett	93.9	24.9	5.82	-	this work
Poly(CuTTO-a)	0.4	-	-	-	[124]
Poly(CuTTO-b)	0.06	-130	1.0×10^{-1}	-	[124]
Poly(CuTTO-c)	0.6	-10	6×10^{-3}	-	[124]
Poly(CuTTO-d)	3	-12	4.32×10^{-3}	-	[124]
Cu^{I}-TTO-TEA	0.1-1.2	-	-	-	[39]
Cu^{I}-TTO-Na	45-77	-8.3	$3.1 - 5.3 \times 10^{-1}$	-	[39]
Cu^{II}-TTO-TEA	0.5-17	-16.5	$14 \times 10^{-2} – 4.6 \times 10^{-1}$	-	[39]
Cu^{II}-TTO-Na	3.3	-20.5	1.39×10^{-1}	-	[39]
$Cu^{I}Cu^{II}$-TTO-Na	0.6	-15	1.35×10^{-2}	-	[39]

4.1.2 Pd-ett and Co-ett

Following the same synthesis and purification procedure used for **Ni-ett** and **Cu-ett**, the pellets of **Pd-ett** and **Co-ett** were fabricated. Initial measurement of electrical conductivity for **Pd-ett** and **Co-ett** pellets showed σ_{RT} values on the order of 10^{-4} S cm^{-1} and 10^{-7}-10^{-8} S cm^{-1}, respectively. Though the DFT prediction (Table 14) suggested **Pd-ett** having comparative or even better thermoelectric properties than **Ni-ett**, on the contrary to our experimental results. The possible reasons could be: (i) the OMCPs obtained in reality contain both crystalline domains and amorphous regions, where the later factor is usually waived for simplified calculation.[62] (ii) The uncertain existence of diverse interchain interactions, like the formation of dimer or stacks between metal-metal or metal-sulfur found in small complexes is sometimes out of the scope.

***Table 14**. Calculated N_{opt} (optimal electron density), μ (Intrinsic mobility) and the related TE Properties, including α , σ and PF at 298 K in publications.*

Sample	N_{opt} (10^{20} cm^{-3})	σ (S cm^{-1})	α (μV K^{-1})	PF (μW m^{-1} K^{-2})	μ (cm^2 V^{-1} s^{-1})	ref
poly(Ni-C_2S_4)	8.88	1.17 ×10^5	214	~10^5	840	36
poly(Ni-C_2S_4)	9.896	5.524 ×10^5	-210.5	1.516 ×10^6	2537.5	62
poly(Pd-C_2S_4)	13.24	1.993 ×10^7	-156.3	4.87×10^8	63804	62
poly(Ni-C_2S_4)	30.1	3.22 ×10^4	20	1240	66.65	65
poly(Pd-C_2S_4)	7.34	915.6	−106	1034	7.764	65
poly(Pt-C_2S_4)	11.6	1.4 × 10^3	4	2.308	7.367	65

Initial XPS investigation of **Pd-ett** (Figure 63) showed a single type of Pd species as metal centers. While in the case of **Co-ett**, the chemical environment of Co atoms is more complex. The Co 2p core level spectrum of **Co-ett** (Figure 61b) present three peaks in Co $2p_{3/2}$ region, derived from XPS fitting at 786.3 eV, 781.3 eV and 779.2 eV, which are very likely from a mixed oxidation state of Co(II) and Co(III), as well as satellite features of both states. Regardless of the peak at 284.8 eV, the C 1s core level spectrum (Figure 61d) of **Co-ett** showed another peak at 288.7 eV, indicating the presence of C=O moieties. Meanwhile, sulfate peak was also observed in S 2p core level spectrum the sample. As the accurate purification being confirmed by Na 1s core level spectrum, we suggest both the sulfate peak and C=O peak originate from the structural complexity or oxidized backbone of **Co-ett** rather than inorganic impurity.

The depth-profile XPS spectrum of this sample uniformly present the same characters (Figure 62). Besides, obvious shifts were observed in the etched sample due to the reduction of cobalt during sputtering, with the set of three fitted Co 2p3/2 peaks shifted from 786.6, 781.6 and 779.2 eV to 785.4, 780.9 and 778.7 eV. These results will be further discussed in Section 4.2 concerning poly(M-btt) with various metal centers.

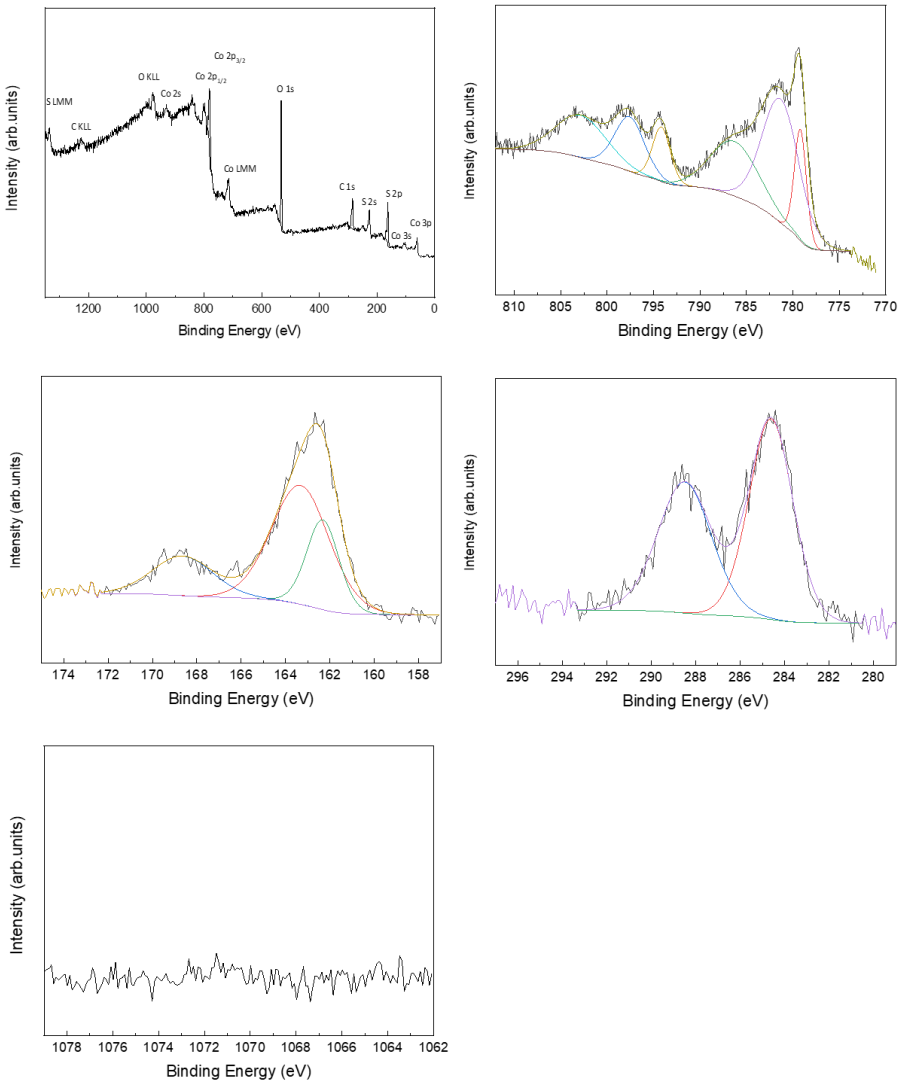

***Figure 61**. XPS energy survey spectra of purified **Co-ett** at surface and corresponding Co 2p, S 2p, C 1s, Na 1s core level XPS spectra.*

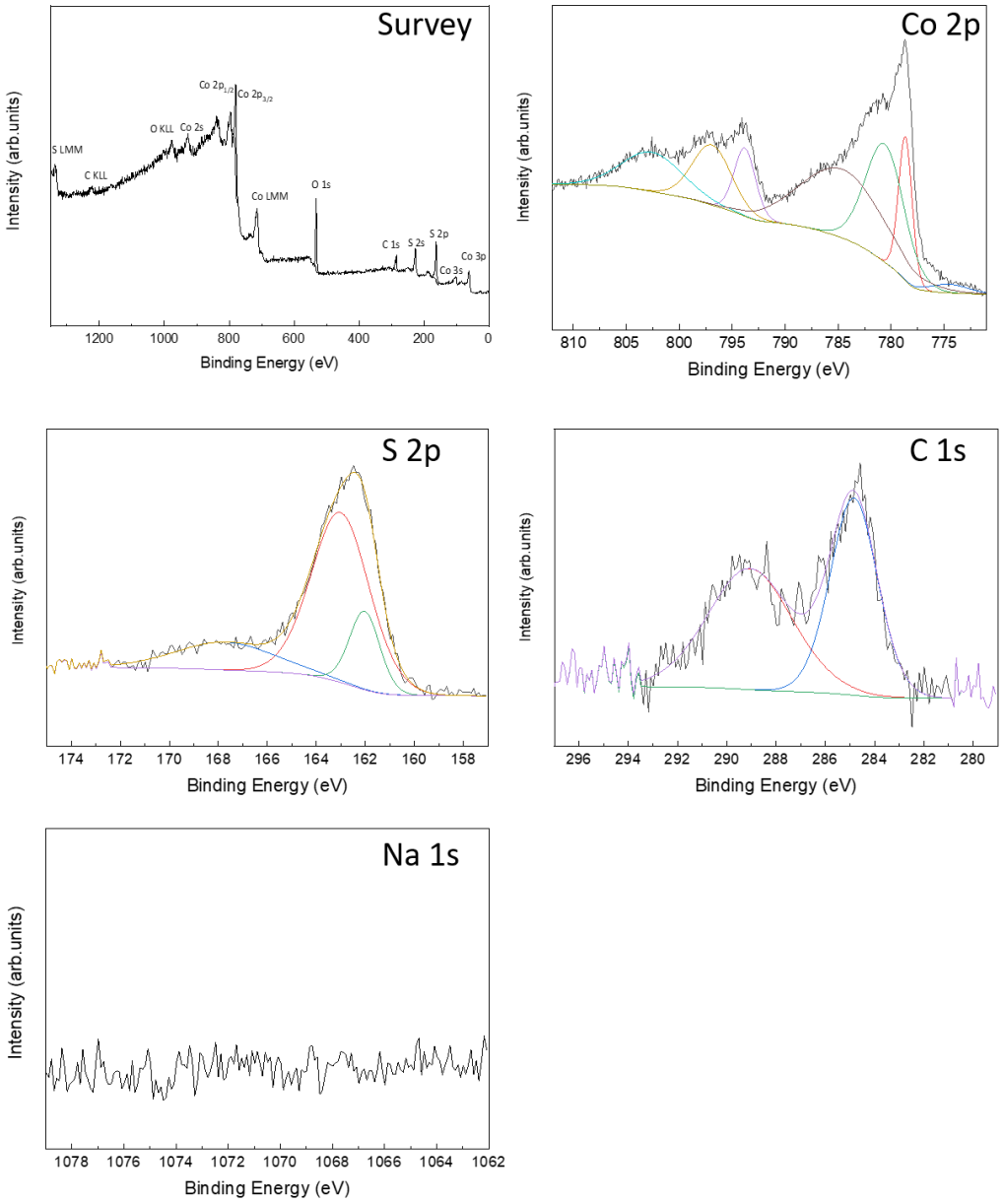

***Figure 62**. XPS energy survey spectra of purified **Co-ett** at 15nm beneath and corresponding Co 2p, S 2p, C 1s, Na 1s core level XPS spectra.*

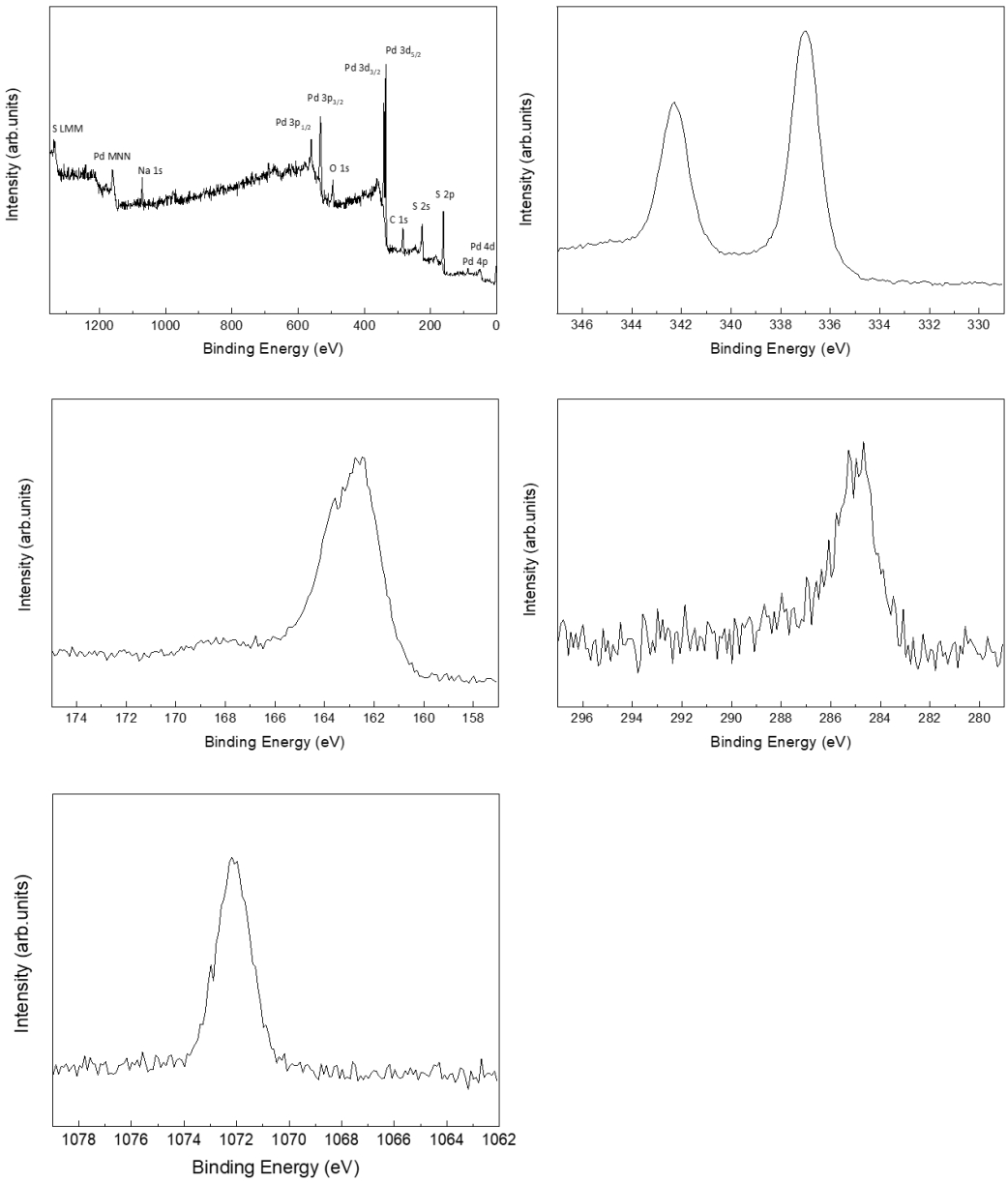

***Figure 63**. XPS energy survey spectra of purified **Pd-ett** at surface and corresponding Pd 3d, S 2p, C 1s, Na 1s core level XPS spectra.*

4.2 Poly(M-btt) with various metal centers

More metal cations, including Fe(II), Co(II), Cu(II), Pd(II) and Zn(II), were employed to synthesize the btt-based OMCP materials and study the effect of metal centres on the thermoelectric performance in this system**. Fe-btt**, **Cu-btt**, **Pd-btt** and

Co-btt were prepared via the same procedure (Scheme 16) used for preparing **Ni-btt** from nickel(II) acetate tetrahydrate, using iron(II) acetylacetonate, copper(II) acetate hydrate, palladium(II) acetate and cobalt(II) acetate tetrahydrate as the metal source respectively.

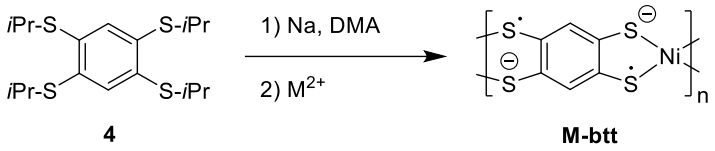

4 **M-btt**

Scheme 16*. Synthetic pathway towards M-btt.*

Zn^{2+} was initially used to synthesize the hypothesized **Zn-btt** structure, with interest to investigate the effect of its closed electron shell on the structure and properties of the resulting polymer, which was assumed to base on tetrahedral coordination. However the intermediate (btt) solution did not formed any precipitate along with Zn^{2+} addition and the color of the reaction mixture remained unchanged. In a typical complexation reaction for analogous OMCPs in this work, the reaction mixture changed color immediately into dark along with several drops of metal cation solution added (*e.g.* Ni^{2+}, Fe^{2+}, Co^{2+}, Cu^{2+}, Pd^{2+}), due to the formation of metal-sulfur coordination and the involving charge transfer, followed by the emergence of blackish particles in minutes to hours and the transformation from solution or slurry to sol-gel status overnight. The exceptional case of Zn^{2+} here could be relevant with its dsp2 hybridization and thereby the tetrahedral chelate configuration, which has been found in many other ZnS_4 complexes,[123, 125] but this distorted complexation probably is unfavorable to polymerize with btt ligand.[126]

***Table 15**. Summary of the electrical conductivity level by hall-effect measure system and available Seebeck data of **M-btt** materials at room temperature.*

M-btt	Fe	Co	Ni	Cu	Pd	Zn
σ_{RT} (S cm^{-1})	10^{-1}	10^{-5}-10^{-6}	10^{0}	10^{-8}-10^{-10}	10^{-4}	-
α_{RT} (μV K^{-1})	-33.8	-	13.7	-	-	-

Hence, electrical conductivity was investigated only for the other five obtained OMCPs, discussed below. First, Hall effect measurements were performed to evaluate the electrical conductivity. Except **Ni-btt**, **Fe-btt** was observed to be the most conductive material among all the other btt-based OMCPs, with the σ_{RT} value on the order of 10^{-1} S cm^{-1}, while the other three OMCP samples (**Co-btt**, **Cu-btt** and **Pd-btt**) showed lower conductivity with the the σ_{RT} value on the order of 10^{-5} to 10^{-8} S cm^{-1} (Table 15). The main reason for the low conductance for the three OMCPs cannot be elucidated yet. One possibility is that the larger metal centers may reduce π-d orbital overlapping and hence the charge transport in polymer skeleton. Another more likely reason involves the interchain interaction. This hypothesis is based on the earlier findings on small molecular MS_4 systems, where the metal centers dominated the specific structural properties of the complexes, including the formation of metal-metal (M-M) dimer, metal-sulfur (M-S) dimer, M-M slipped stacking, M-M irregular stacking, M-M stacking, quasi M-M dimer and M-S dimer.[117]

It is noteworthy that the results in **M-btt** system are consistent with those in **M-ett**

system, where the much poorer electrical conductivity were also found or Co and Pd based OMCPs. Due to the detection limit of the equipment we used, the reliable thermoelectric measure at different temperature, as performed for **Ni-btt**, are not available for **Co-btt**, **Cu-btt** and **Pd-btt**. Therefore, the decent thermoelectric measure was only performed for **Fe-btt**, showing its promising conductivity of 0.26 S cm^{-1} at room temperature and increased to 0.74 S cm^{-1} at 370 K. It is noteworthy that **Fe-btt** was found to be another n-type OMCP with the Seebeck coefficient of -33.8 μV K^{-1} at room temperature, shown in Figure 64.

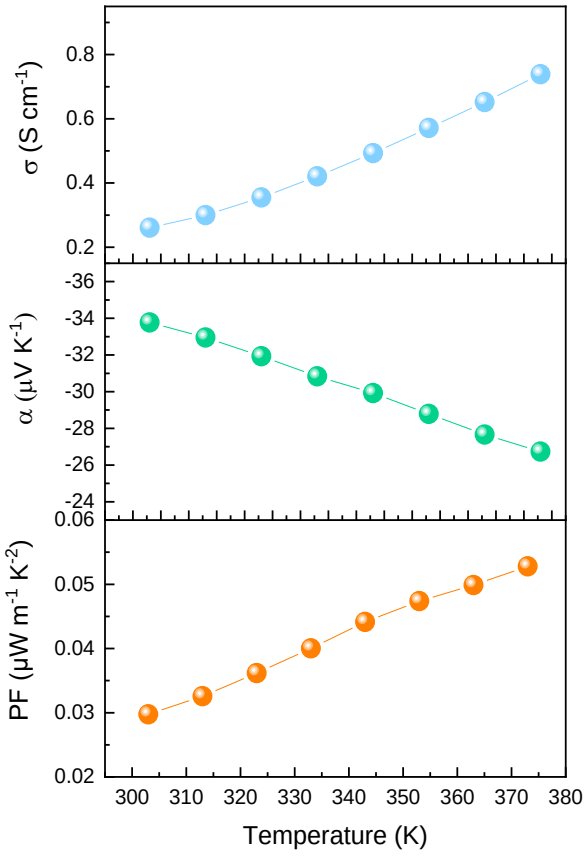

Figure 64. *Electrical conductivities, Seebeck coefficients and Power Factor of* ***Fe-btt*** *as a function of temperature.*

To extend the investigation of the impact from metal cations and seek the potential

to optimize the thermoelectric properties, we synthesized a bi-metallic OMCP with $Fe^{2+}$and Ni^{2+} cations, given that the **Ni-btt** and **Fe-btt** showed the best thermoelectric properties among the btt-based OMCPs. The ratio of Fe^{2+}, Ni^{2+} and btt ligand used in synthesis was 0.5:0.5:1 to obtain the **$Fe_{0.5}Ni_{0.5}$-btt**. As shown in Figure 65, the mixed-metal OMCP exhibited an increased conductivity on the order of 10^{-2} S cm^{-1} from room temperature to 373K, lower than the corresponding mono-metal polymers, both **Ni-btt** and **Fe-btt**. This inhibited conductivity may be due to the structural disorder and the presence of more oligomeric impurities impeding molecular packing and charge transport. In last chapter, the similar phenomenon was observed where the dual-ligand OMCPs, **Ni-ibtt$_{0.5}$btt$_{0.5}$**, showed the lowest conductivity in comparison with mono-ligand polymers (**Ni-ibtt** and **Ni-btt**).

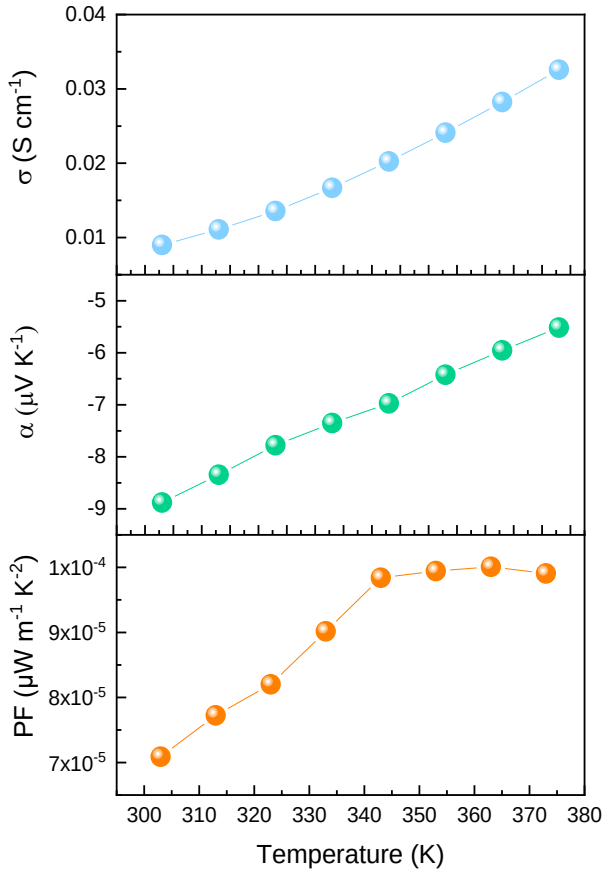

***Figure 65**. Electrical conductivities, Seebeck coefficients and Power Factor of **$Fe_{0.5}Ni_{0.5}$-btt** as a function of temperature.*

On the other hand, the absolute value of the Seebeck coefficient of **$Fe_{0.5}Ni_{0.5}$-btt** is fairly low in magnitude (Figure 65), following the sequence of **$Fe_{0.5}Ni_{0.5}$-btt** < **Ni-btt** < **Fe-btt**. Despite the modest electrical conductivity, such a low Seebeck coefficient is usually typical for metallic-behavior materials, which makes it less favorable as a thermoelectric candidate, as the PF value of **$Fe_{0.5}Ni_{0.5}$-btt** is 10^2-10^3 times lower than the two mono-metal OMCPs.

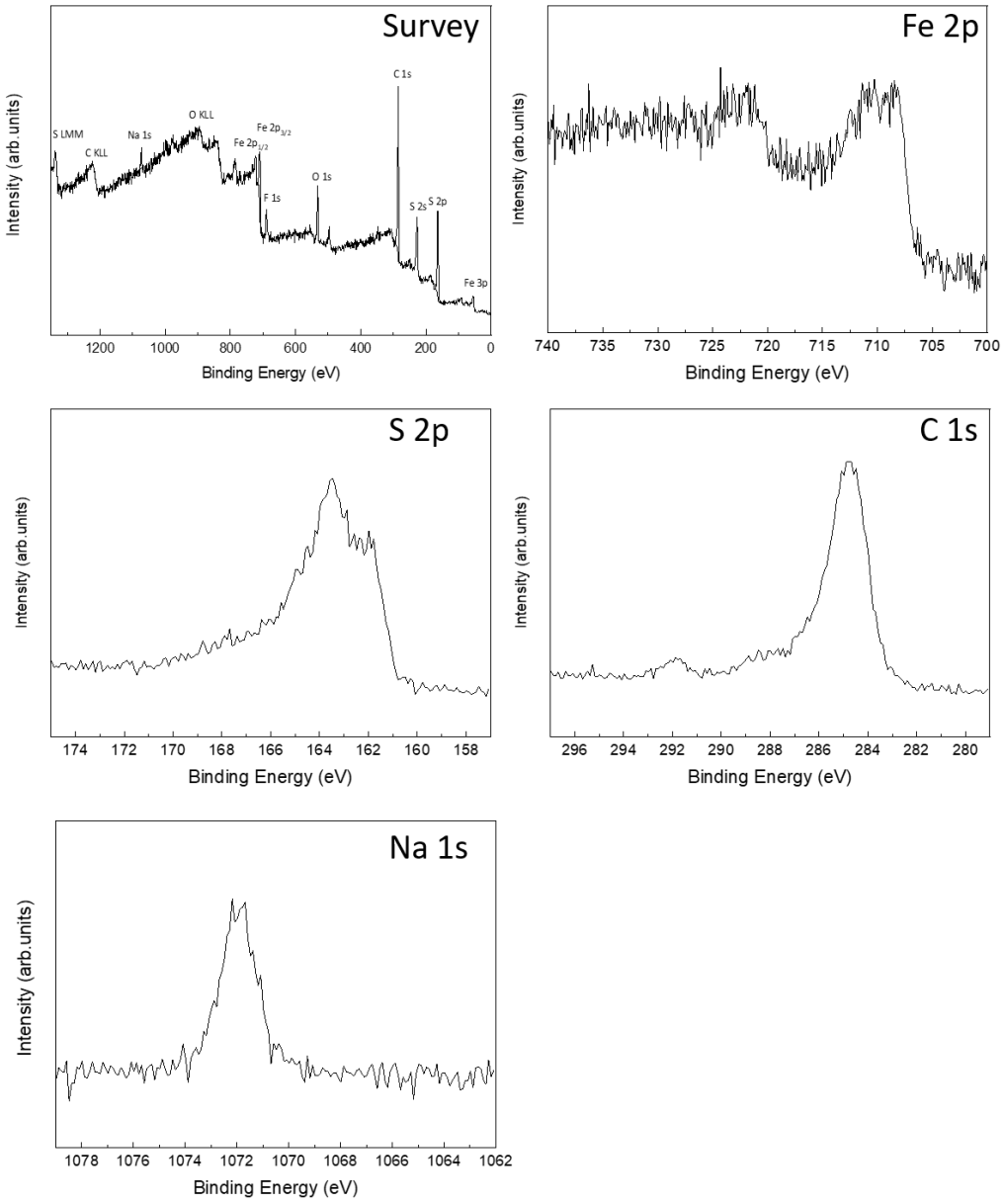

***Figure 66**. XPS energy survey spectra of purified **Fe-btt** at surface and corresponding Fe 2p, S 2p, C 1s, Na 1s core level XPS spectra.*

Initial XPS characterization (Figure 66) confirmed the presence of Fe, S and C but cannot be used for qualitative analysis of the Fe species in these OMCP s, as the Fe 2p core level spectrum was not high-resolution enough. The presence of F also requires further examination as no fluorine-containing reagent was used for the synthesis of Fe-btt.

4.3 Discussion on the effect of metal centers on thermoelectric performance

In both M-ett and M-btt system, changing metal centers was proved to cause obvious difference in the thermoelectric properties of the formed OMCPs. One possible reason could be the impact of specific metals on the interchain packing of OMCPs.

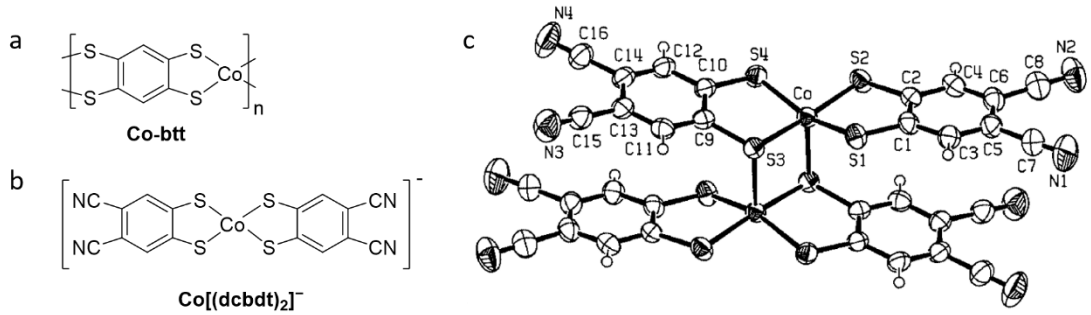

Figure 67*. Formula of (a) idealized polymer* ***Co-btt*** *and (b) $[Co(dcbdt)_2]^-$;(c) the square-pyramidal geometry of the actual dimerized $[Co(dcbdt)_2]_2^{2-}$ reused with permission.* [123] *Copyright 2004, WILEY - VCH Verlag GmbH & Co. KGaA, Weinheim.*

Indeed, even in small molecular complex system, the packing and stacking arrangement heavily depends on metal centers. For instance, Almeida reported the $M[(dcbdt)_2]^{-z}$ complexes with various transition metals, to find much difference in their coordination geometries. In terms of Co-based complex, dianionic $Co[(dcbdt)_2]^{2-}$ has a square planar coordination but monoanionic $Co[(dcbdt)_2]^-$ possess a strong dimerization via a side-by-side interaction between the two cobalt atoms in each unit (Figure 67).[123] The similar intrachain interaction may also exist in **Co-btt** along with mix-valency cobalt (Co^{2+} and Co^{3+}), which might produce more complex environment and structural disorder along the a-axis or cause twist the backbone.

Meanwhile, the mix-valence phenomenon commonly exists in Co-S_4 complexes. For example, in the $M(bdt)_2$ system (bdt = benzenedithiolato) mentioned above, the energy of Co 3d-orbital is comparable to that of ligand-centered orbitals. Hence, the electronic hybridization occurs between bdt and Co to give a complex resonant structures: $[Co^{III}(L^{2-})(L^{2-})]\leftrightarrow[Co^{II}(L^{-\bullet})(L^{2-})]\leftrightarrow [Co^{II}(L^{2-})(L^{-\bullet})]$.[127-128] To note, the co-existence of Co^{2+} and Co^{3+} oxidization states can be directly related to the possible co-existence of square planar and non-planar coordination modes. This can cause more disorder and less conjugation in polymer backbones, which therefore reduce the conductivity.

4.4 Chapter Conclusions

In conclusion, two OMCP systems, M-ett and M-btt, were studied with different metal substitutes. The initial experimental results showed the great influence of metal centers on the electronic properties of the OMCPs, which may involve different interchain (pseudo) dimerizations and stackings. More comprehensive investigation, like the XANES and systematic computational study are required for deeper understanding.

Among all the M-ett OMCPs, p-type poly(**Cu-ett**) shows peculiarly good thermoelectric properties, where we proposed a new cross-linking structure for poly(**Cu-ett**) with trigonal Cu-S coordination.

In M-btt system, **Fe-btt** was proved to be another promising n-type OMCP. Its

analogous OMCP with mixed-metal-cations, **$Ni_{0.5}Fe_{0.5}$-btt** were synthesized and further characterization is ongoing to examine our hypothesis upon the depressed electrical conductivity caused by the structural disorder and complex chemical environment in this dual-metal OMCP. For these Fe-containing OMCPs present here, high-resolution XPS, magnetic susceptibility and Mössbauer Spectroscopy are under investigation to identify the specific oxidation state and electronic structure of the Fe atoms, as pure Fe^{II}, pure Fe^{III} or mix-valence (Fe^{II} and Fe^{III}), to further understand the chemical composition and electron transport behaviors, as well as get insight to their thermoelectric properties.[129]

Conclusions and future work

This research chose the tetrathiolate ligands as synthetic targets to investigate the thermoelectric performance of corresponding coordinated polymers, as well as looking into the key factors of thermoelectric properties on OMCP design.

In the initial investigation towards the linear metal-bis(dithiolato) OMCPs, the air-stable radial feature and neutral backbones of **Ni-ett**, **Ni-diett** and **Ni-btt** were revealed by compositional and spectroscopic study. Our research pointed out the previously neglected importance of the simple purification for insoluble OMCPs, providing better understanding on their intrinsic structure and different views on their formation mechanism. The measurement of these OMCPs proved that changing organic ligands is a facile strategy to tune the thermoelectric properties of OMCPs.

Then, structural isomeric OMCPs were synthesized to achieve another air-stable n-type material (**Ni-ibtt**), allowing an interesting study about the effect of isomerism on thermoelectric behavior by comparing with **Ni-btt**. In addition, dual-ligand OMCPs synthesized with the isomeric bridging ligands, btt and ibtt, to further provide insight into the structural effect on thermoelectric performance. Meanwhile, alternative pathways were developed for the synthesis of **Ni-btt** and **Ni-ibtt**, accompanying with several small MS_4 complexes produced.

Subsequent manipulations on the metal center exchange in M-ett and M-btt systems led to a decent p- type candidate **Cu-ett**, where we proposed a new structure,

as well as another n-type OMCP, **Fe-btt**. Our attempts to broaden the understanding about how the metal centers influence the thermoelectric properties has not been completed, as characterization has not been approached yet. The studies on the effect of sidechain or functional groups were also discontinued due to the lab lockdown during covid-19 period.

Future work would focus on the characterization of obtained small complexes and OMCPs, as well as exploring the other potential applications of the obtained framework, such as hydrogen evolution. Other modifications would also be investigated to propose more efficient synthesis route to scale-up, increase the processibility of these OMCPs and fabricate thermoelectric devices via 3D printing.

Experimental details

General experimental

All reagents and solvents used in this study were purchased from commercial suppliers and used without purification. All reactions were performed under nitrogen atmosphere with standard Schlenk line and the product yields refer to purified compounds, unless otherwise stated. Thin layer chromatography (TLC) and column chromatography were performed with TLC aluminium plates and silica gel (40–63 μm), respectively. Nuclear magnetic resonance (NMR) spectra were performed byBruker NMR spectrometers *Avance III 400* and *Avance Neo 700* at 298 K. Chemical shifts (δ) are reported in parts per million (ppm), using the residual solvent peaks as calibration standard. For ^{1}H-NMR (δ): $CDCl_3$ 7.26. For ^{13}C-NMR (δ): $CDCl_3$ 77.16. Mass spectrometry data was performed with *Thermo Accela LC/LTQ* (EI), *Waters LCT Premier QTOF* (ESI) and *Thermo Scientific TRACE 1310 GC* (EI/CI) mass spectrometers (ESI).

The typical purification of OMCPs via Soxhlet extraction was carried out under nitrogen atmosphere with deionized water and methanol, 24 hours for each (Figure 68).

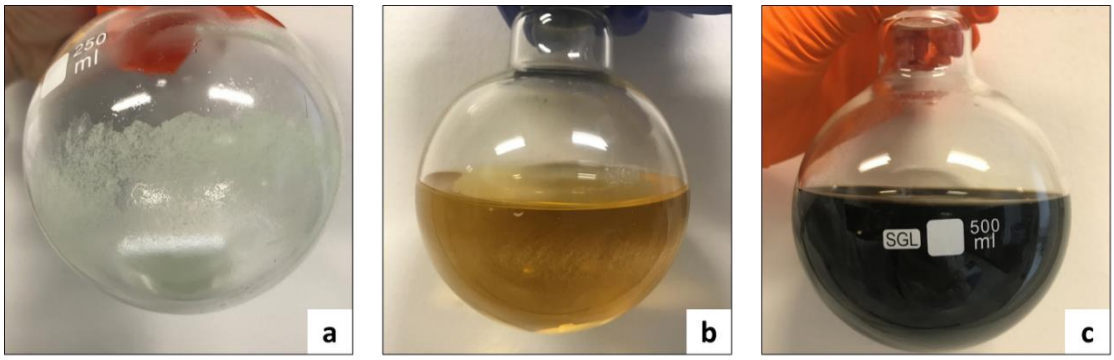

***Figure 68**. Photographs of typical impurities extracted during the Soxhlet purification of the OMCP materials.*

Pellet Preparation

The samples were fabricated into pellet for thermoelectric measurement in following procedure: Firstly, a Retsch MM200 mixer mill was used to ball-mill each sample at 1800 Hz for 15 minutes, as extending the ball-milling time to 30 minutes did not show significant change of the distribution of particle size. Typically, 200 mg of sample and two stainless steel milling balls (diameter = 7 mm) were placed together into a 15 mL stainless steel grinding jar. Then, the obtained powder was pressed (around 2.6 GPa) using a KBr pellet dies into circular pellets (15 mm diameter) with an approximate thickness of 0.6 – 0.8 mm, measured with a digital caliper (0.01 mm resolution).

Characterizations

Fourier-transform infrared spectra (FTIR) were performed by *Bruker Platinum ATR*. Raman spectra was recorded by a *Renishaw inVia* Raman spectrometer coupled to a microscope (Leica DM LM) under ambient conditions. Thermal gravimetric analysis were recorded by *Q500* TGA under nitrogen atmosphere. X-ray fluorescence

(ED-XRF) analysis was conducted with with a *Malvern Panalytical Epsilon 4* spectrometer equipped with a silver anode X-ray tube under inert Helium atmosphere. X-ray diffraction (XRD) was measured by *STOE SEIFERT* diffractometer with Mo Kα (0.7093 Å) radiation with a detected angular range of $2° < 2\theta < 40°$ and a step size of 0.05° at 1 s per step. The obtained XRD data was processed by the MDI Jada 6 software. Field emission scanning electron microscopy (FE-SEM) was conducted by a Hitachi S-4800 with an accelerating voltage of 8.0 kV. The energy dispersive X-ray spectroscope (EDS) fitted to the SEM was used for the elemental mapping analysis.

XPS was performed with *Thermo Scientific K-Alpha* spectrometer equipped with monochromated Aluminium (Al) Kα X-ray source. Etching for depth profiling was by in situ sputtering using a beam of 3keV Ar^+ ions and depth was internal calibrated. All XPS data was analyzed with the CasaXPS processing software and the calibration of binding energy was against the C 1s peak to 284.6 eV. Ultraviolet photoelectron spectroscopy (UPS) were performed by *Thermo Scientific Theta-Probe* spectrometer with a helium discharge lamp emitting in ultraviolet range (He I = 21.22 eV). The Ni K-edge XANES were measured at the XAFCA beam line at the Singapore Synchrotron Light Source (SSLS), Singapore, operating at 0.7 GeV. The data were collected in transmission mode and processed with ATHENA and ARTEMIS software. EPR spectra were recorded by an EMX X-band spectrometer (Bruker, ~10 GHz) at 77 K with a cylindrical microwave resonator and a liquid nitrogen Dewar. The concentration of unpaired electron was estimated by comparing the area of observed absorption peak

with that of $CuSO_4 \times 5\ H_2O$ standard sample (Cu^{2+}, d9, S = 1/2). DC magnetization were measured with a MPMS3 magnetometer (Quantum Design) for the magnetic field of 0 - 7 T.

For the thermoelectric properties based on the OMCP pellets, the electrical conductivity was measured by a 4-point probe equipped with a Keithley 2636B source-meter under ambient condition. The Seebeck coefficients were measured by a *MMR Technologies Inc. SB100 System* under vacuum (1×10^{-5} mbar), where silver paste was used to ensure good contact.

Prior to the measure of thermal conductivity, each sample was polished using grained sand paper to get smoother surface for better quasi-specular reflection. Raman imaging of the sample surface was examined with a Witec alpha300RA piece of equipment. Then, the measure was conducted by single-laser Raman thermometry using a Jobin-Yvon LabRam HR800 grating spectrometer combined with a confocal microscope. The focused laser beam worked as the heat source and the temperature-dependent Raman spectra worked as the "Raman thermometer". The shift of specific Raman peaks (~ 360 cm^{-1} and 490 cm^{-1}) in the laser spot region were recorded as a function of the absorbed laser power (λ = 633 nm). Then, the peak shift was recorded according to the change of temperature, controlled externally by a Linkam cryostat in vacuum conditions, which allows the calibration of the "thermometer" as the peak shift can be related to the temperature rise. The temperature increase for the case of a semi-infinite medium is determined by the laser power absorbed by the sample (P_{abs}),

Gaussian spot radius (R) and thermal conductivity (k), which is given by:

$$\Delta T = \frac{P_{abs}}{\pi R \kappa}$$

DFT Methods

The geometries of the free ligands and oligomers were optimised for different spin/charge states using the B3LYP density functional[130-133] combined with Grimme's D3 dispersion correction[134-135] or the ωB97XD functional and either the def2-SVP or def2-TZVP basis-set.[136-137] For selected systems we tested the effect of ignoring the fact that in experiment the oligomers are part of an amorphous solid by comparing the predictions for molecules in the gas-phase and in the presence of a dielectric screening model (COSMO, ε_r 10).[138] The stability of all closed-shell states with respect to going from a restricted to an un-restricted (open-shell) solution was assessed by means of stability analysis. For selected (ground) states of the different oligomers the optical gap was also predicted using TD-DFT. These latter calculations use the Tamm-Dancoff approximation to avoid stability issues.[139] All (TD-)DFT calculations on free ligands and oligomer models were performed using Turbomole 7.4.[140]

Periodic density functional theory (DFT) calculations were performed on Cs_2ZrCl_6 within the Vienna Ab Initio Simulation Package (VASP),[141-144] using the projector augmented wave (PAW) method to describe the interaction between valence and core electrons;[145] all PAW pseudopotentials used are scalar-relativistic, and 3*p* electrons included as valence for Ni. The hybrid functionals HSE06 and PBE0,[146-147] which incorporate 25% Hartree-Fock exchange in addition to 75% exchange and full

correlation from the PBE functional,[148] were both used to calculate the system, as they counteract the self-interaction and band-gap underestimation inherent in standard DFT. HSE06 differs from PBE0 by only including the Hartree-Fock exchange at short range, determined by the parameter of 0.11 $bohr^{-1}$,[149] and has been used previously to calculate similar conjugated polymers.[36] A plane wave cut-off energy of 600 eV and k-point mesh of 1 x 3 x 1 were sufficient to converge the total energy to within 1 meV per atom. Relaxation of the structure was performed until the forces were below 0.01 eV per Å on each atom, and the total energy was converged to within 10^{-5} eV for all calculations. The sumo package was used for plotting the electronic density of states and band structure,[150] and uses the notation for high-symmetry points in the Brillouin Zone from Bradley and Cracknell.[151]

Synthesis details

Synthesis in Chapter 2

Methyl 2,2-bis((isopropoxycarbonothioyl)thio)acetate (**27)**

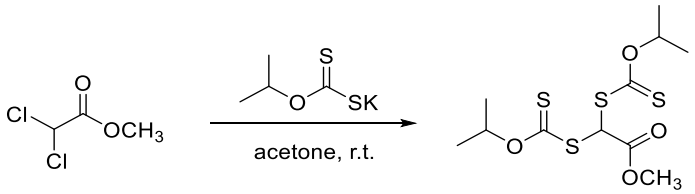

26 **27**

Compound **1** was prepared by adapting a previously published procedure.[152] First, methyl 2,2-bis((isopropoxycarbonothioyl)thio)acetate (**27**) was prepared by addition of

methyl dichloroacetate **26** (1.30 mL, 12.7 mmol) to a suspension of potassium isopropylxanthate (25.6 mmol, 4.45 g) in acetone (25 mL) at room temperature. The mixture was stirred for 5h to form an oily slurry. The crude mixture was diluted by addition of hexane (50 mL) to precipitate any salts. The salts were filtered off and washed with cold acetone. The solvent was removed under reduced pressure and the methyl 2,2-bis((isopropoxycarbonothioyl)thio)acetate (**27**) recovered as a light yellow oil (3.36 g, 9.81 mmol), which was used in the next step without further purification.

[1,3]dithiolo[4,5-*d*][1,3]dithiole-2,5-dione (1)

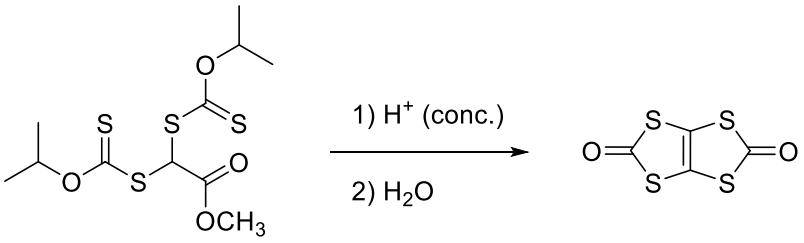

27 **1**

50 mL of concentrated sulfuric acid (98%) were added to a 500 mL conical flask equipped with a large stirrer bar and cooled to 0 °C in an ice-bath. Diethyl ether (4 mL) were cautiously added to the well stirred acid, before the dropwise addition of **27**. After complete addition, the cooling bath was removed, and the reaction mixture warmed to room temperature. The acidic reaction mixture was poured onto crushed ice (300 mL) to precipitate the crude **1**. The solid was filtered off and washed extensively with water and ice-cold diethyl ether (2 × 20 mL). The crude product was recrystallized from chloroform to yield the pure title compound **1** as off-white crystalline needles (1.70 g,

8.16 mmol, 63 %). ^{13}C NMR (700 Hz, $CDCl_3$, δ): 188.0, 111.8. GC-MS (EI, m/z) calcd. for $C_4O_2S_4$ $[M]^+$ 207.88, 209.87, 208.88; obs. 207.16, 208.15, 208.97. FTIR (neat, cm^{-1}): 1738 (w), 1650 (s), 966 (m), 964 (m), 915 (m), 728 (s). Raman (neat, cm^{-1}): 1700 (w), 1682 (w), 1617 (w), 1482 (s), 557 (m), 536 (w), 517 (w), 485 (s), 429 (w), 335 (s), 496 (m), 476 (m).

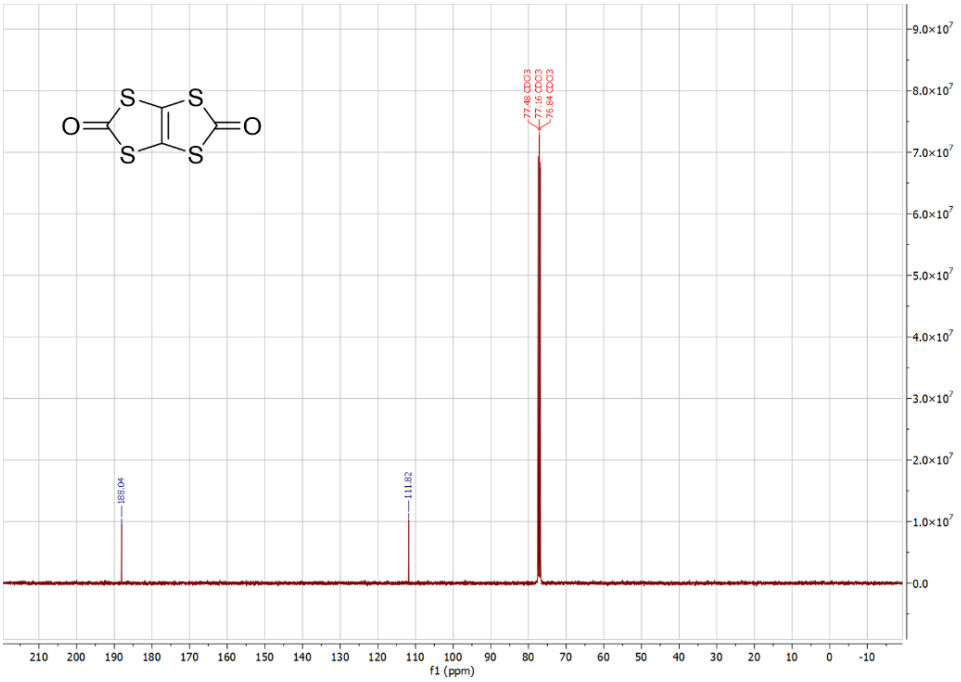

Figure 69. *^{13}C NMR of [1,3]dithiolo[4,5-d][1,3]dithiole-2,5-dione (**1**).*

[2,2'-bi[1,3]dithiolo[4,5-*d*][1,3]dithiolylidene]-5,5'-dione (2)

Compound **2** was prepared by adapting a previously published procedure.[40] [1,3]dithiolo[4,5-*d*][1,3]dithiole-2,5-dione (1.00 g, 4.80 mmol) and triethylphosphite (4.00 g, 24.0 mmol) were dissolved in 100 mL of anhydrous toluene and heated to reflux for 15 hours. After cooling down, the formed precipitate was filtered off, washed with diethyl ether to yield compound **2** as a brown shiny solid (0.75 g, 1.95 mmol, 81%). HRMS (NH_3 CI, m/z) calcd. for $C_8HO_2S_8$ $[M+H]^+$ 384.7737; obs. 384.7736. Anal.

calcd for $C_8O_2S_8$: C 24.99, S 66.69; found: C 26.27, S 61.18. FTIR (neat, cm^{-1}): 1689 (s), 1016 (m), 966 (m), 878 (m), 845 (m), 741 (s). Raman (neat, cm^{-1}): 1497 (m), 1476 (m), 1116 (s), 951 (m), 496 (m), 476 (m). ^{13}C NMR of compound **2** could not be obtained due to its poor solubility.

1,2,4,5-tetrakis(isopropylthio)benzene (4)

Sodium hydroxide (1.24 g, 31.0 mmol) and 1,2,4,5-tetrachlorobenzene **3** (0.88 g, 4.11 mmol) were dissolved in 15 mL of anhydrous *N*,*N*-dimethylacetamide (DMA). Then, 2-propanethiol (2.90 mL, 31.3 mmol) was added dropwise to the solution at room temperature. After complete addition, the reaction was heated at 80 ºC overnight. After the brown solution cooled down, water was slowly added under stirring until a white solid precipitated. The solid was collected by vacuum filtration and re-dissolved in diethyl ether (20 mL). The organic phase was washed twice with water (2 × 20 mL) and brine (20 mL). The organic solution was dried with magnesium sulfate ($MgSO_4$), filtered and evaporated under reduced pressure. The brown oil recovered was precipitated into methanol (10 mL) to yield the title compound **4** as a white crystalline solid (1.37 g, 3.66 mmol, 90%). ^1H NMR (400 Hz, $CDCl_3$, δ): 7.28 (s, 2H), 3.43 (h, J = 6.7 Hz, 4H), 1.31 (d, J = 6.7 Hz, 24H). ^{13}C NMR (400 Hz, $CDCl_3$, δ): 136.0, 132.9, 37.5, 23.0. MS (ESI): calcd. for $C_{18}H_{30}S_4$ $[M]^+$ 375.13, 376.13, 377.13; obs. 375.13, 376.13, 377.13. FTIR (neat, cm^{-1}): 2959 (w), 2947 (w), 2860 (w), 1634 (w), 1427 (m), 1364 (m), 1242 (m), 1180 (m), 1121 (m), 1047 (s), 641 (m). Raman (neat, cm^{-1}): 2974 (m), 2963 (m), 2925 (m), 1543 (s), 1495 (m), 1125 (s), 653 (m).

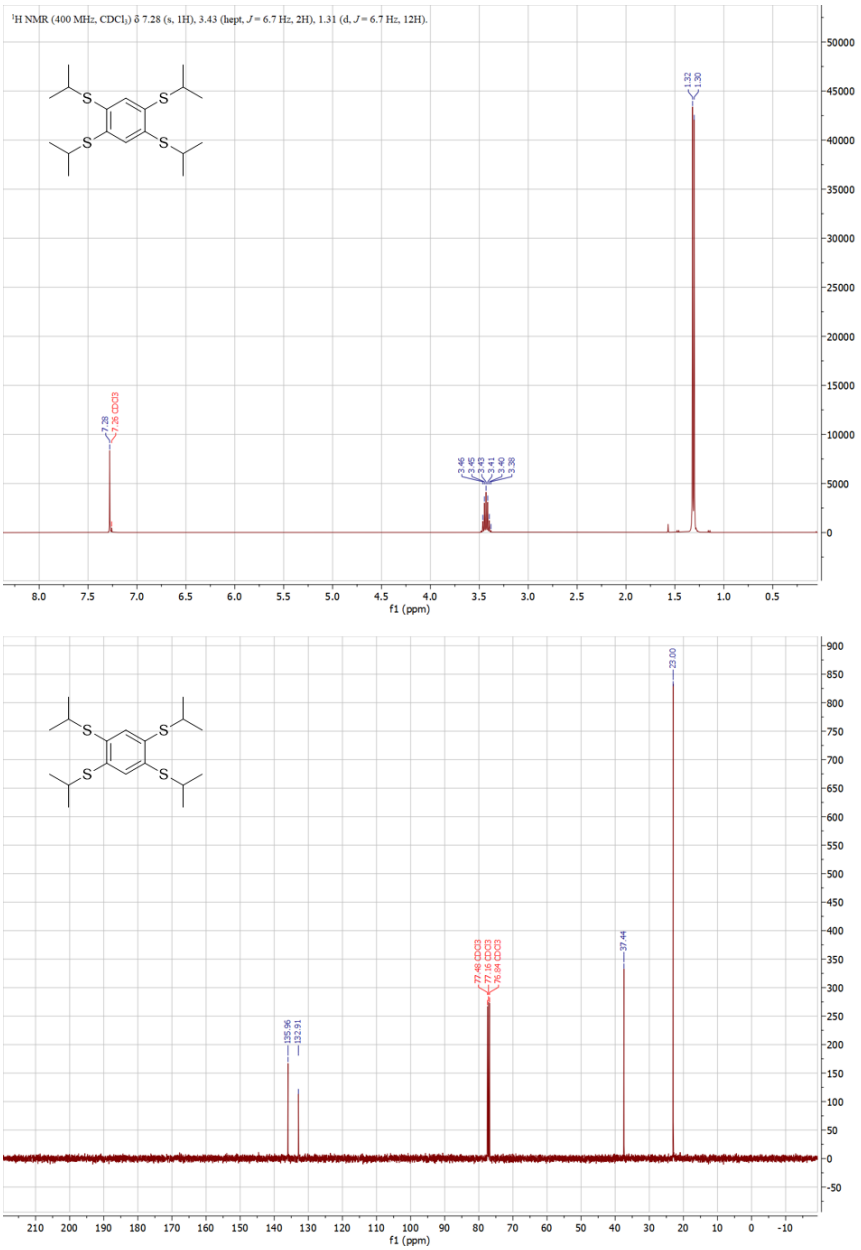

Figure 70. *^{1}H NMR and ^{13}C NMR of 1,2,4,5-tetrakis(isopropylthio)benzene (**4**)*

Poly(nickel-ethylenetetrathiolate) (Ni-ett)

Ni-ett was prepared by adapting a previously published procedure.[124] 1,3,4,6-tetrathiapentalene **1** (1.00 g, 4.81 mmol) and an excess of sodium methoxide (1.20 g, 22.2 mmol) was added into anhydrous methanol (50 mL) and refluxed for 24 hours. Nickel acetate solution was prepared by dissolving nickel acetate tetrahydrate ($NiAc_2$ ·

4 H_2O; 1.20 g, 4.82 mmol) in anhydrous methanol (30 mL). This nickel acetate solution was then added dropwise to the refluxing solution and refluxed for another 24 hours. After cooling to room temperature, the reaction mixture was filtered to get the crude polymer **Ni-ett**. The crude was purified by Soxhlet extraction with deionized water for 24 h and then by methanol for another 24 hours. The purified **Ni-ett** was dried in vacuum at 100 °C for 24 hours to give a black powder (0.65 g, 3.08 mmol, 64%). FTIR (neat, cm^{-1}): 1622 (m), 1067 (m), 964 (w). Raman (neat, cm^{-1}): 1185 (s), 1157 (s), 496 (m), 363 (m).

Poly(nickel-[2,2'-bi(1,3-dithiolylidene)]-4,4',5,5'-tetrakis(thiolate)) (Ni-diett)

Sodium methoxide (0.65 g, 120 mmol) was added to a solution of compound **2** (1.00 g, 2.60 mmol) in anhydrous methanol and refluxed for 24 hours. Nickel acetate tetrahydrate ($NiAc_2 \cdot 4\ H_2O$; 0.65 g, 2.61 mmol) dissolved in 20 mL of anhydrous methanol was added dropwise over 30 minutes to the refluxing solution and further heated for another 24 hours. The mixture was cooled to room temperature and the formed black precipitate was filtered off. The collected crude was further purified by Soxhlet extraction with deionized water and then with methanol (24 hours for each). The purified **Ni-diett** was placed in vacuum at 100 °C for 24 hours and recovered as a dry black powder (0.75 g, 1.94 mmol, 75%). FTIR (neat, cm^{-1}): 1616 (m), 1167 (m), 1134 (m), 1036 (w), 965 (m). Raman (neat, cm^{-1}):1437 (m, broad), 1294 (w), 1250 (w), 1187 (s), 1157 (s), 495 (m), 363 (m).

Poly(nickel-benzene-1,2,4,5-tetrakis(thiolate)) (Ni-btt)

1,2,4,5-tetrakis(isopropylthio)benzene (**4**) (1.76 g, 4.70 mmol) was first dissolved in anhydrous *N*,*N*-dimethylacetamide (75 mL), following with the addition of sodium (5.40 g, 235 mmol). The mixture was heated to 100 °C for 24 hours to form a milky orange slurry. 15 mL of thoroughly degassed water were added dropwise to obtain clear orange-brown solution. Nickel acetate tetrahydrate ($NiAc_2 \cdot 4\ H_2O$; 1.17 g, 4.70 mmol) was dissolved in 20 mL of degassed water and added dropwise to the reaction mixture over 15 minutes. The colour of the reaction mixture quickly deepened to black with the Ni addition. After complete addition, the mixture was heated to 100 °C for 24 hours. After cooling to room temperature, the black solid collected by centrifugation. The crude **Ni-btt** was purified by Soxhlet extraction with deionized water for 24 h, followed by methanol for 24 hours. The purified polymer was dried for 24 hours in vacuum at 100 °C and recovered as a black powder (0.60 g, 2.30 mmol, 49%). FTIR (neat, cm^{-1}): 1614 (w), 1533 (w), 1463 (w), 1417 (w), 1110 (m), 1073 (m), 1019(m), 858 (m), 690 (w), 655 (w). Raman (neat, cm^{-1}):1490 (m), 1422 (m), 1300 (w), 1219 (w), 1110 (m), 1075 (w), 357 (vs).

1,2,4,5-tetrakis(methylthio)benzene (6)

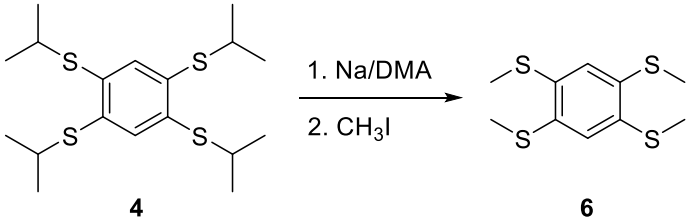

4 **6**

Compound **4** (115 mg, 0.31 mmol) was dissolved in 8 mL of DMA and then sodium

(350 mg, 15.2 mmol) was then added. The solution quickly turned yellow and the reaction was refluxed at 100 °C for 20h. The orange solution was then cooled down to room temperature and quenched by adding an excess of methyl iodide (0.20 mL, 3.21 mmol). After heating at 50 °C overnight, the reaction was cooled to room temperature and diluted with 10 mL of diethyl ether. The organic phase was washed with water (2 × 10 mL) and brine (10 mL). The organic phase was dried with magnesium sulfate ($MgSO_4$), filtered and evaporated under reduced pressure to give crude oil. Then 5 mL of cold methanol was added to the oil to precipitate 1,2,4,5-tetrakis(methylthio)benzene (**6**) as a slight yellow solid (60.0 mg, 0.228 mmol, 74%).^{1}H NMR (400 Hz, $CDCl_3$, δ): 7.10 (s, 2H), 2.47 (s, 12H). ^{13}C NMR (400 Hz, $CDCl_3$, δ) 135.8, 126.6, 16.9. HRMS (ESI) calcd. for $C_{10}H_{15}S_4$ $[M+H]^+$ 263.0057; obs. 263.0062.

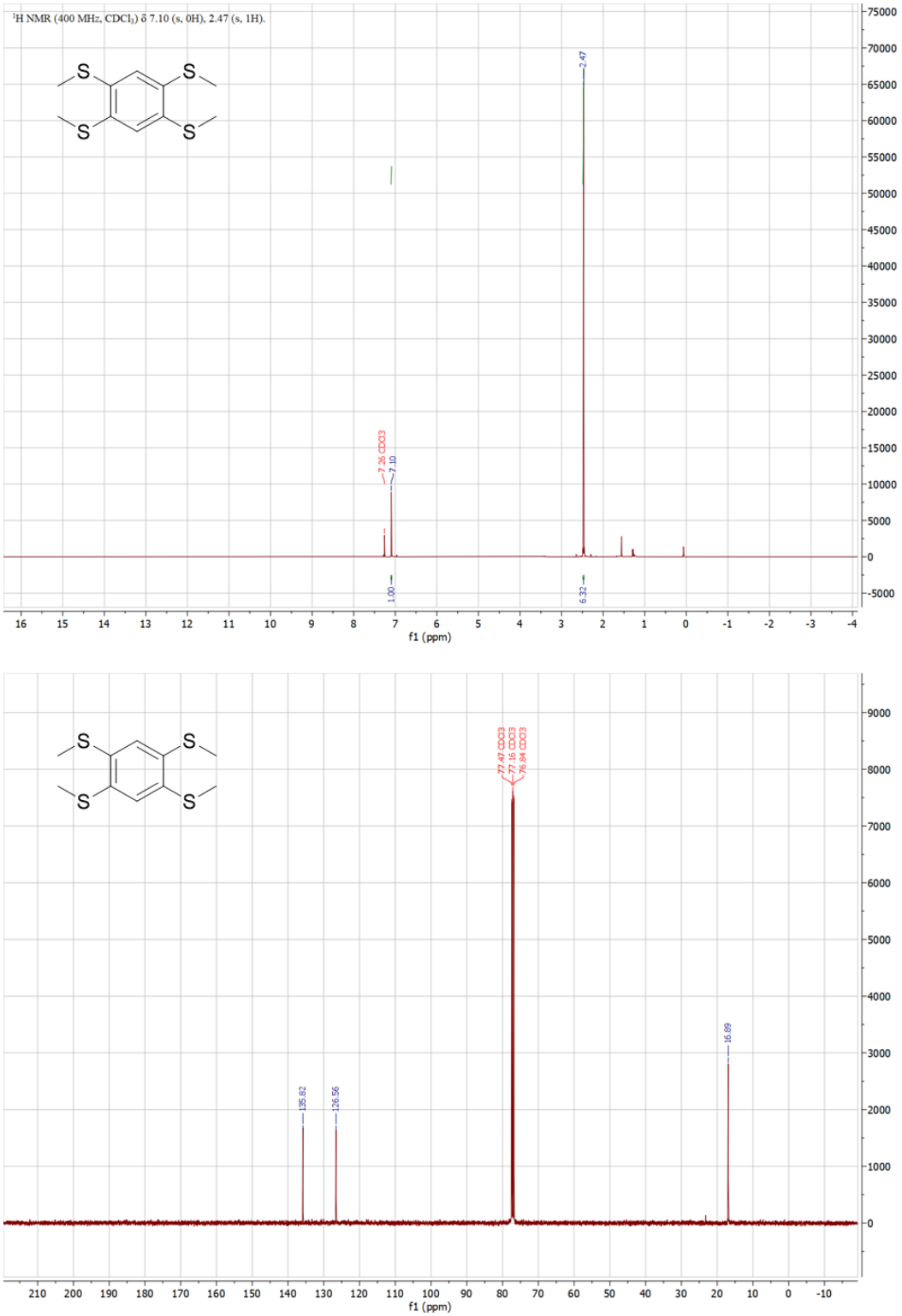

***Figure 71**. 1H NMR and 13C NMR of 1,2,4,5-tetrakis(methylthio)benzene (**6**).*

1,3,5,7-tetrathia-s-indacene-2,6-dithione (7)

3 **7**

Compound **7** was prepared by adapting a previously reported procedure.[153] A mixture of potassium sulphide (43%, 15 g, 58.5 mmol), carbon disulphide (10 mL, 165 mmol) and dimethyl formamide (40 mL) was stirred at 50 °C for 3 h. To the resulting red suspension of potassium trithiocarbonate, 1,2,4,5-tetrachlorobenzene (5.4 g, 25 mmol) was then added, and the mixture was further stirred for 24 h at 100 °C. The mixture was then poured into water (300 mL), filtered and dried in vacuum. The crude solid was then recrystallized with dimethyl sulfoxide (DMSO) to obtain yellow powder (5.88 g, 20.2 mmol, 80.3%). Solid state ^{13}C NMR (δ): 212.2, 143.5, 139.7, 116.4. HRMS (ESI) calcd. for $C_8H_2S_6$ $[M+H]^+$ 290.8553; obs. 290.8553. FTIR (neat, cm^{-1}): 1418 (w), 1335 (w), 1276 (w), 1032 (s), 1010 (s), 876 (m), 857 (m), 641 (w). Raman (neat, cm^{-1}): 1515 (m), 1176 (w), 1141 (s), 1167(w), 1148(w), 696(w), 509 (w), 452 (w), 344 (w), 337 (w), 243 (w).

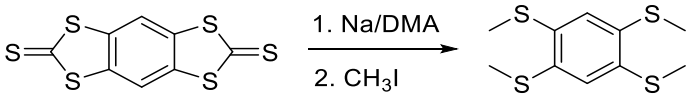

7 **6**

To verify **7** to be another candidate to synthesize **Ni-btt**, the reaction for the formation of benzene-1,2,4,5-tetrathiolate intermediate were out carried out. Compound **7** (55 mg, 0.19 mmol) was dissolved in 10 mL of methonal and then sodium (60 mg, 2.6 mmol) was then added. The solution quickly turned yellow and the reaction was refluxed for 1h. The orange solution was then cooled down to room temperature and quenched by

adding an excess of methyl iodide (0.5 mL, 8 mmol), companying with a sudden color change to light yellow and white solid precipitated. After refluxing overnight, the reaction was cooled to room temperature and concentrated. The obtained crude was dissolved in 10 mL of diethyl ether, which was washed with water (2 × 10 mL) and brine (10 mL). The organic phase was passed through a tiny silica column and evaporated under reduced pressure to obtain 1,2,4,5-tetrakis(methylthio)benzene (**6**) as a slight yellow solid (28 mg, 0.56 mmol, 56 %). NMR and MS results were same as above.

1,3-benzodithiole-2-thione (29)

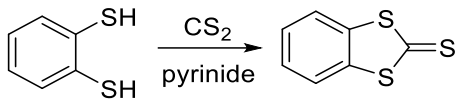

28 **29**

1,2-Benzenedithiol (**28**, 1 g, 7.03 mmol) was dissolved in dry pyridine (27 mL) to give a yellow solution and then carbon disulfide (5.4 mL, 92.4 mmol) was added dropwise over a period of 5 minutes. The reaction was stirred under ambient atmosphere for 4 hours at room temperature and then nitrogen was quickly purged through the solution for 1 hour to elucidate CS_2. The solid was collected by filtering the bulk solution, washed with methanol and dried under vacuum overnight to give yellow powder (1.02 g, 5.53 mmol, 79 %). ^{1}H NMR (400 Hz, $CDCl_3$, δ): 7.43 (m, 2H), 7.49 (m, 2H). ^{13}C NMR (400 Hz, $CDCl_3$, δ): 212.0, 141.1, 127.4, 121.7. FTIR (neat, cm^{-1}): 1432 (m),1292 (w), 1264 (w), 1136 (w), 1119(w), 1053 (m), 890 (m),735 (s), 677 (w). Raman (neat, cm^{-1}): 1572 (w), 1588 (w), 1444 (w), 1168 (w), 1140 (w), 1119 (s), 1051

(w), 1041 (w), 1028 (w), 894 (w), 682 (w), 678 (w), 522 (m), 477 (m), 356 (s).

Complex $(NBu_4)[Ni(bdt)_2]$ (30)

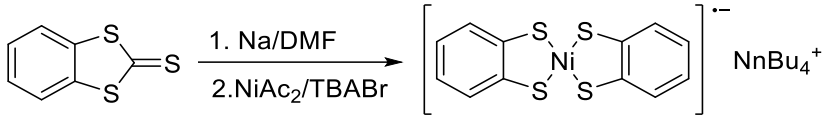

29 **30**

To the solution of 1,3-benzodithiole-2-thione (**29**, 102 mg, 0.55 mmol) dissolved in dimethylformamide (5 mL), Na (110 mg, 4.8 mmol) was added under stirring. The mixture was then heated to 80°C and reacted for 1h. Then, a methanol solution (5 mL) of $NiAc_2 \cdot 4H_2O$ (76 mg, 0.27 mmol) and tetra-*n*-butylammonium bromide (87 mg, 0.27 mmol) was slowly added into the reaction for 1 hour. After cooling to room temperature, the mixture was further stirred under ambient condition for 0.5 hour, following by the removal of methanol *in vacuo*. The obtained crude was then dissolved in H_2O (20 mL) extracted with dichloromethane (DCM, 3 × 10 mL). The organic phase was dried with $MgSO_4$, filtered and evaporated to give crude dark powder, which was recrystallized with DCM and hexane to give darkish-green crystal in needle-shape (127 mg, mmol, 62 %). FTIR (neat, cm^{-1}): 1594 (m), 1572 (m), 1425 (m), 1356 (m), 1243 (w), 1130 (m), 1099 (s), 735 (s), 592 (m). Raman (neat, cm^{-1}): 1537 (w), 1433 (w), 1290 (w), 1098 (w), 482 (s), 360 (m), 326 (s). MS (ESI) calcd. for $C_{12}S_4H_8Ni^-$ 337.89, obs. 337.88; calcd. for $C_{16}H_{36}N^+$ 242.28, obs. 242.28.

*Table 16.Crystallographic parameters of **30**.*

Empirical formula	$C_{28}H_{44}NNiS_4$
Formula weight	581.59
Temperature/K	100(2)

Crystal system	orthorhombic
Space group	$Pna2_1$
a/Å	16.4021(4)
b/Å	19.6402(5)
c/Å	18.5719(5)
α/°	90
β/°	90
γ/°	90
Volume/$Å^3$	5982.8(3)
Z	8
$\rho_{calc}g/cm^3$	1.291
μ/mm^{-1}	0.945
F(000)	2488.0
Crystal size/mm^3	0.566 × 0.318 × 0.154
Radiation	MoKα (λ = 0.71073)
2Θ range for data collection/°	3.018 to 55.964
Index ranges	$-19 \leq h \leq 21$ $-25 \leq k \leq 25$ $-23 \leq l \leq 24$
Reflections collected	53383
Independent reflections	12935 [R_{int} = 0.0989, R_{sigma} = 0.0955]
Data/restraints/parameters	12935/1/621
Goodness-of-fit on F^2	0.990
Final R indexes [I>=2σ (I)]	R_1 = 0.0533, wR_2 = 0.0899
Final R indexes [all data]	R_1 = 0.0995, wR_2 = 0.1057
Largest diff. peak/hole / e $Å^{-3}$	0.54/-0.41
Flack parameter	-0.016(12)

Synthesis in Chapter 3

1,2,3,4-Tetrakis(isopropylthio)benzene (9)

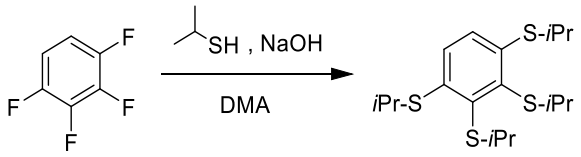

8 **9**

1,2,3,4-tetrafluorobenzene (compound 9; 0.9 g, 6 mmol) and sodium hydroxide (1.83 g, 45.7 mmol) were first dissolved in 20 mL of anhydrous DMA under nitrogen, following by the dropwise addition of 2-propanethiol (2.90 mL, 31.3 mmol) at room temperature. The solution was then refluxed at 100 °C for 2 h. After the solution cooled down to room temperature, 30 mL brine was slowly added under stirring and then ethyl acetate (4 × 25 mL) was used for extraction. The combined organic layer was then filtered through silica plug to remove any remaining DMA and evaporated to give light yellow oily product **6** (2.04 g, 91%). ^{1}H NMR (400 Hz, CDCl3, δ): 7.14 (s, 2H), 3.58 (hept, *J* = 6.8 Hz, 2H), 3.41 (p , *J* = 6.8 Hz, 2H), 1.36 (d, *J* = 6.8 Hz, 12H), 1.22 (d, *J* = 6.8 Hz, 12H). ^{13}C NMR (400 Hz, CDCl3, δ): 141.70 (s), 140.47 (s), 127.23 (s), 41.05 (s), 36.61 (s), 127.23 (s), 23.16 (s), 22.85 (s). MS (ESI): calcd. for $C_{18}H_{30}S_4$ $[M]^+$ 375.13, 376.13,377.13; obs. 375.13, 376.13, 377.13.

Poly[nickel-benzene-1,2,3,4-tetrakis(thiolate)] (Ni-ibtt)

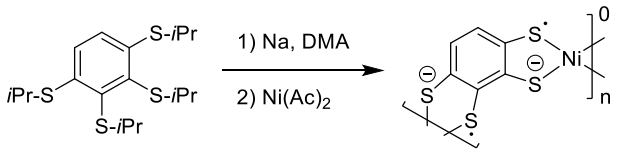

9 **Ni-ibtt**

Compound **9** (1.51 g, 4 mmol, 1 eq.) was added into anhydrous *N*, *N*-dimethylacetamide (75 mL) in an inert atmosphere (N_2). Sodium particles (5.2 g, 226 mmol) was then added in to the solution and heated to 100 °C for 24 h. Then 15 mL degassed water was added dropwise into the muddy mixture to give a orange-brown clear solution. Nickel acetate tetrahydrate ($NiAc_2 \cdot 4\ H_2O$, 1.02 g, 4 mmol) in 20 mL

degassed water was then added dropwise within 15 min, during which the solution gradually turned black. The mixture was further heated at 100°C for another 24 h. Black solid was collected by centrifugation after the reaction cooling down to room temperature and then dried at 100 °C under vacuum overnight to give black **Ni-ibtt** powder (0.75 g, 72 %).

1,2,3,4-tetrakis(methylthio)benzene (8)

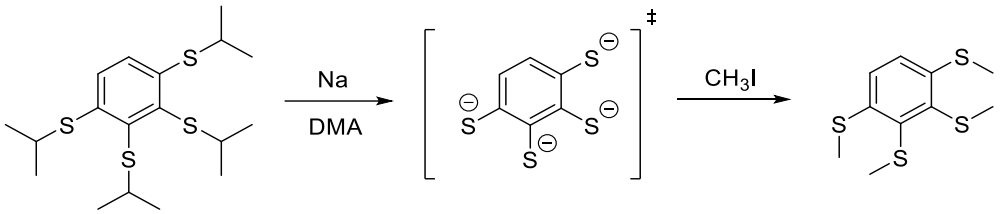

9 **10** **11**

1,2,3,4-benzenetetrakis(thiolate) **10**, $C_6H_2S_4^{-4}$, was proved to be the intermediate formed from compound **9** (110 mg, 0.294 mmol) after sodium reduction, which formed 1,2,3,4-tetrakis(methyl)benzene **11** (63 mg, 0.24 mmol, 82%) by quenching with iodomethane. ^{1}HNMR (400 Hz, $CDCl_3$), δ (ppm): 7.06 (s, 2H), 2.42 (d, J = 7.0 Hz, 12 H); ^{13}CNMR($CDCl_3$), δ (ppm) :142.3, 139.3, 124.7, 20.0, 16.3. HRMS (ESI): calcd. for $C_{10}H_{14}S_4$ $[M]^+$ 263.0057, 265.0020, 264.0082; obs. 263.0058, 265.0048, 264.0079.

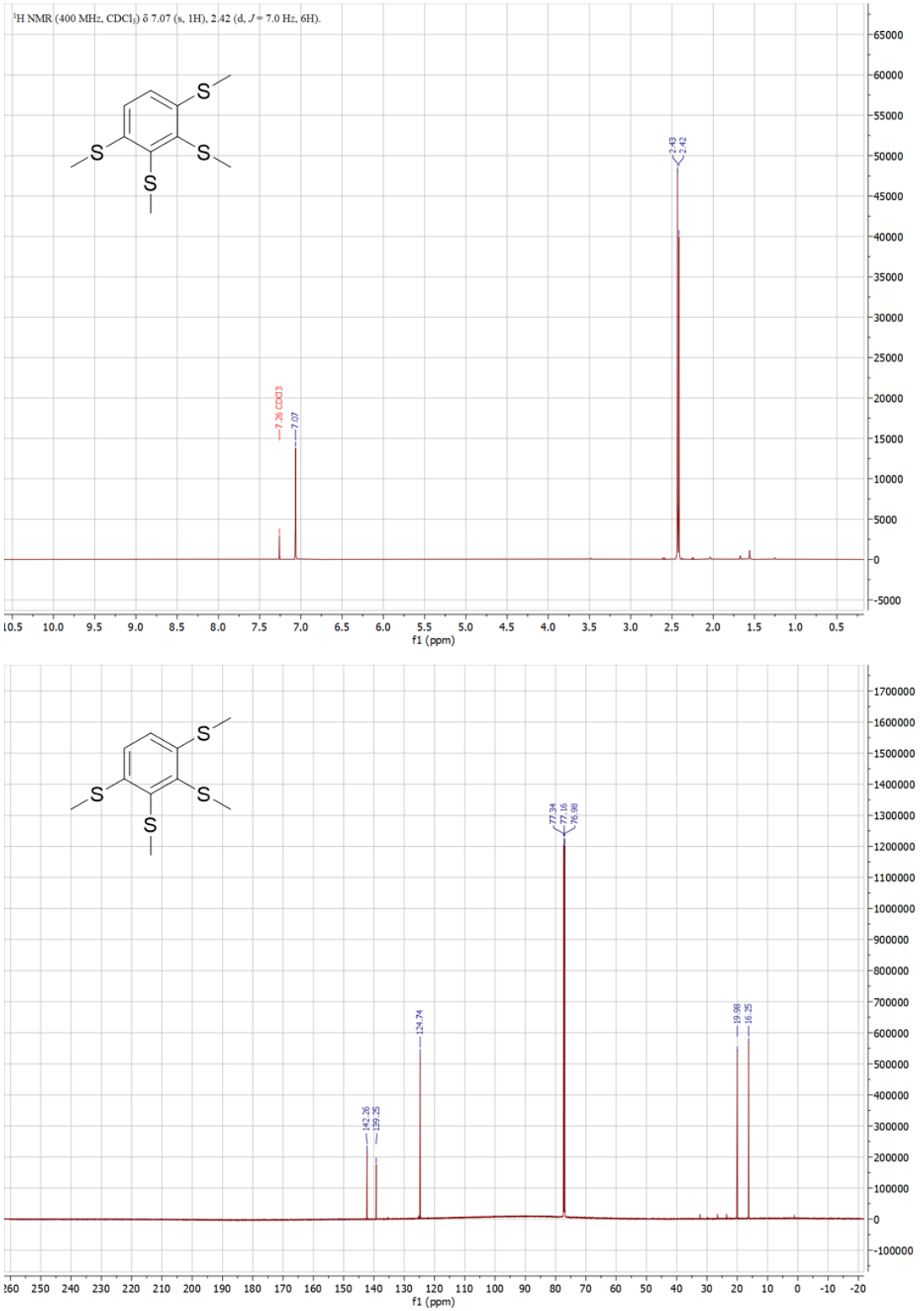

***Figure 72**. 1H NMR and 13C NMR of 1,2,3,4-Tetrakis(methylthio)benzene (**11**).*

Poly[Ni(ibtt)$_x$(btt)$_{1-x}$]

Poly[**Ni(ibtt)$_x$(btt)$_{1-x}$**] was prepared following the similar procedure of Ni-ibtt but with the mixing isomeric ligands, ibtt and btt, where the former one represents benzene-1,2,3,4-tetrakis(thiolate) (**7**). Here, the molar ratio of $NiAc_2 \cdot 4\ H_2O$ and the mixed organic precursors used in each batch was kept as 1:1. Meanwhile, the molar ratio of isomer ligands (ibtt : btt) was ideally assumed to be 1:5 or 1:1, same with the ratio of precursors (compound **4** and **6**) used to obtain polymer **Ni(ibtt)$_{0.17}$(btt)$_{0.83}$** and **Ni(ibtt)$_{0.5}$(btt)$_{0.5}$**, respectively.

Benzo[1,2-d:3,4-d']bis([1,3]dithiole)-2,7-dithione (13), 4,5-dichlorobenzo[d][1,3]dithiole-2-thione (**14**) and **4,7-dichlorobenzo[d][1,3]dithiole-2-thione (15)**

Potassium sulphide powder (43%, 15 g, 58.5 mmol) and carbon disulphide (10 mL, 825 mmol) were added into 40 mL of DMF and stirred at 50 C for 3 h (Scheme 9). Then 1,2,3,4-tetrachlorobenzene **12** (5.4 g, 25 mmol) was then added to the red suspension of potassium trithiocarbonate, and the mixture was heated to 100 °C and reacted overnight. After cooling down to room temperature, the mixture was then poured into water (100 mL) to precipitate solid, which was filtered and dried overnight in vacuum to give crude solid in orange color (7.46 g). Then crude solid was refluxed in mixed solvent (50 mL ethyl acetate and 50 mL chloroform), following by hot filtering to separate an orange solid (4.52 g), confirmed to be compound **13**. The obtained filtrate was evaporated under reduced pressure to give another solid, from which compound **14** (pale yellow solid, 0.65 g) and **15** (bright yellow needle-shape crystal, 1.43 g) were

obtained after column. **Benzo[1,2-d:3,4-d']bis([1,3]dithiole)-2,7-dithione (13)**: Solid state ^{13}C NMR (δ): 208.8, 140.1, 129.4, 122.3. MS (ESI): calcd. for $C_8H_2S_6$ $[M]^+$ 290.9, 292.9, 291.9; obs. 290.9, 289.9, 292.9, 291.9. FTIR (neat, cm^{-1}): 3030 (w), 3011 (w), 2940 (broad), 1739 (m), 1668(w), 1402 (w), 1346 (w), 1267 (w), 1229 (w), 1217 (w), 1205 (w), 1059 (s), 890 (w), 805 (m), 767 (w), 503 (m), 449 (w). **4,5-Dichlorobenzo[d][1,3]dithiole-2-thione** (**14**): MS (ESI): calcd. for $C_7H_2Cl_2S_3$ $[M]^+$ 252.88, 253.88; obs. 252.88, 253.89. FTIR (neat, cm^{-1}): 2958 (w), 2925 (w), 2855 (w), 1426 (w), 1361 (w), 1178 (w), 1077 (w), 834 (w), 808 (w), 775 (w), 465 (w). **4,7-Dichlorobenzo[d][1,3]dithiole-2-thione (15)**: ^{1}HNMR (700 Hz, $CDCl_3$), δ (ppm): 7.31 (s, 2H); ^{13}CNMR(700 Hz, $CDCl_3$), δ (ppm) : 209.1 (s), 140.83 (s), 40.96 (s), 128.31 (s), 124.72 (s); MS (ESI): calcd. for $C_7H_2Cl_2S_3$ $[M]^+$ 252.88, 254.87, 256.87; obs. 252.88, 254.88, 256.89. FTIR (neat, cm^{-1}): 3100 (w), 3061 (w), 1874 (w), 1620 (w), 1426 (w), 1342 (w), 1281 (w), 1180 (m), 1162 (w), 1074 (s), 889 (m), 807 (m), 608 (w), 544 (w), 526 (w), 501 (w), 474 (w), 445 (w).

Complex $(NBu_4)[Ni(dcbdt)_2]$ (16)

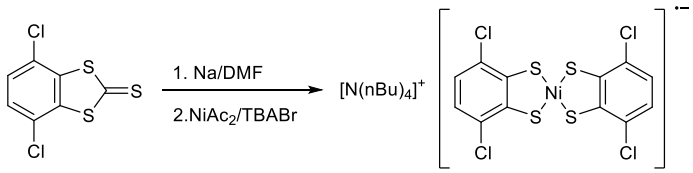

15 **16**

To the solution of 4,7-Dichlorobenzo[*d*][1,3]dithiole-2-thione (101 mg, 0.4 mmol) dissolved in 5 mL of DMF, Na (40 mg, 1.74 mmol) was added under nitrogen atmosphere. The mixture was then heated to 80 °C and reacted for 1h. Then a solution

of $NiAc_2 \cdot 4H_2O$ (56 mg, 0.2 mmol) and tetra-*n*-butylammonium bromide (64 mg, 0.2 mmol) in 5 mL DMF was dropwise added into the reaction for 1 hour. After cooling to room temperature, the mixture was further stirred under ambient condition for 0.5 hour, following by evaporating the methanol *in vacuo*. The obtained crude was then dissolved in H_2O (15 mL) extracted with DCM (3 × 10 mL). The combined organic phase was dried with $MgSO_4$, filtered and evaporated to give dark powder, which was recrystallized with DCM and hexane to give dark green crystal in flake-shape (102 mg, 0.14 mmol, 71 %). MS (ESI) calcd. for $C_{12}H_4Cl_4NiS_4^-$ 475.71, obs. 475.73; calcd. for $C_{16}H_{36}N^+$ 242.28, obs. 242.28.

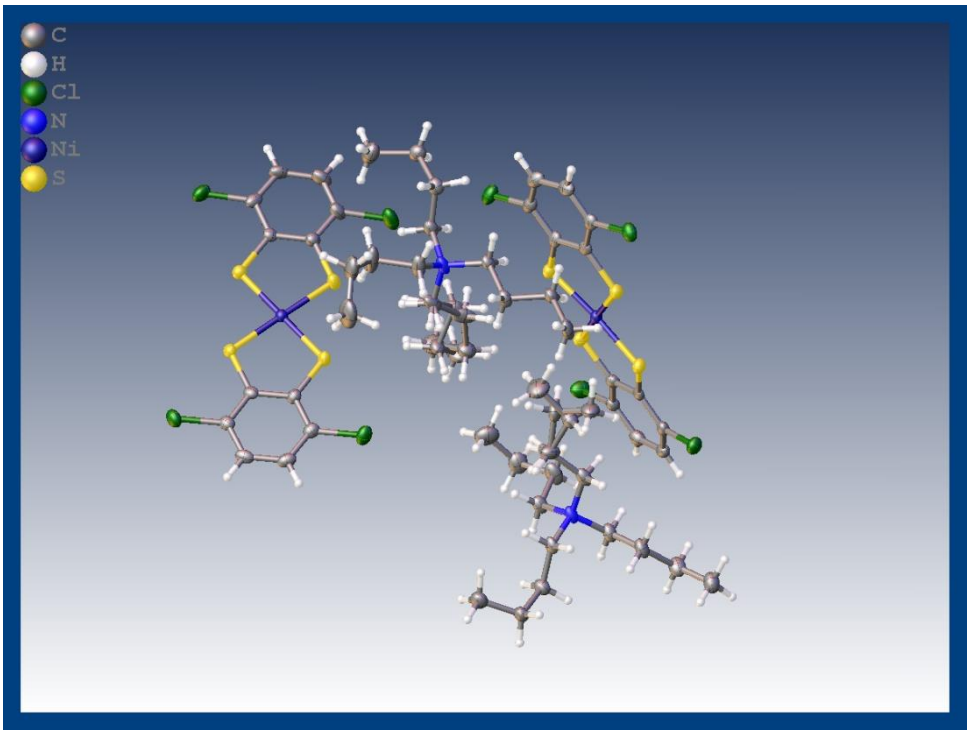

***Figure 73**. Single crystal X-ray diffraction of complex $(NBu_4)[Ni(dcbdt)_2]$ (compound **16**).*

*Table 17. Crystallographic parameters of **16**.*

Empirical formula	$C_{28}H_{40}Cl_4NNiS_4$
Formula weight	719.36
Temperature/K	99.99
Crystal system	orthorhombic
Space group	$P2_12_12_1$
a/Å	15.4897(7)
b/Å	15.6497(7)
c/Å	27.1153(14)
α/°	90
β/°	90
γ/°	90
Volume/Å^3	6573.0(5)
Z	8
ρ_{calc}g/cm^3	1.454
μ/mm^{-1}	1.190
F(000)	3000.0
Radiation	MoKα (λ = 0.71073)
2Θ range for data collection/°	3.004 to 55.992
Index ranges	$-20 \leq h \leq 20$, $-20 \leq k \leq 20$, $-24 \leq l \leq 35$
Reflections collected	60053
Independent reflections	15786 [R_{int} = 0.0623, R_{sigma} = 0.0590]
Data/restraints/parameters	15786/123/742
Goodness-of-fit on F^2	1.016
Final R indexes [I>=2σ (I)]	R_1 = 0.0415, wR_2 = 0.0848
Final R indexes [all data]	R_1 = 0.0592, wR_2 = 0.0914
Largest diff. peak/hole / e Å^{-3}	0.59/-0.39
Flack parameter	0.013(8)

Benzene-1,2,3,4,5-pentaylpentakis(isopropylsulfane) (21)

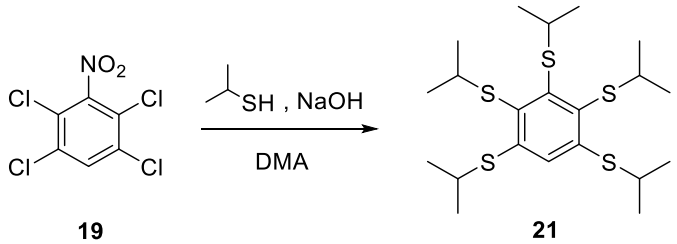

19 **21**

Sodium hydroxide (6 g, 0.15 mol) and 1,2,4,5-tetrachloro-3-nitrobenzene (**19**, 5.22 g, 20 mmol) were dissolved in 40 mL of anhydrous DMA. Then, 2-propanethiol (15 mL, 0.15 mol) was added dropwise to the solution at room temperature. After complete addition, the reaction was heated at 100 ºC for 20 h. After the solution cooled down, water was slowly added under stirring until a solid precipitated. The solid was collected by vacuum filtration and re-dissolved in diethyl ether (40 mL), which was washed twice with water (2 × 40 mL) and brine (40 mL). The organic solution was dried with magnesium sulfate ($MgSO_4$), filtered and evaporated under reduced pressure to yield the title compound **21** as a pale yellow crystalline solid (7.4 g, 16.5 mmol, 82 %). 1H NMR (400 MHz, CDCl3) δ 6.97 (s, 1H), 3.66 (p, *J* = 6.7 Hz, 1H), 3.53 (p, *J* = 6.7 Hz, 2H), 3.39 (p, *J* = 6.7 Hz, 2H), 1.39 (d, *J* = 6.7 Hz, 12H), 1.20 (d, *J* = 6.7 Hz, 12H), 1.17 (d, *J* = 6.7 Hz, 6H). MS (ESI): 449.19.

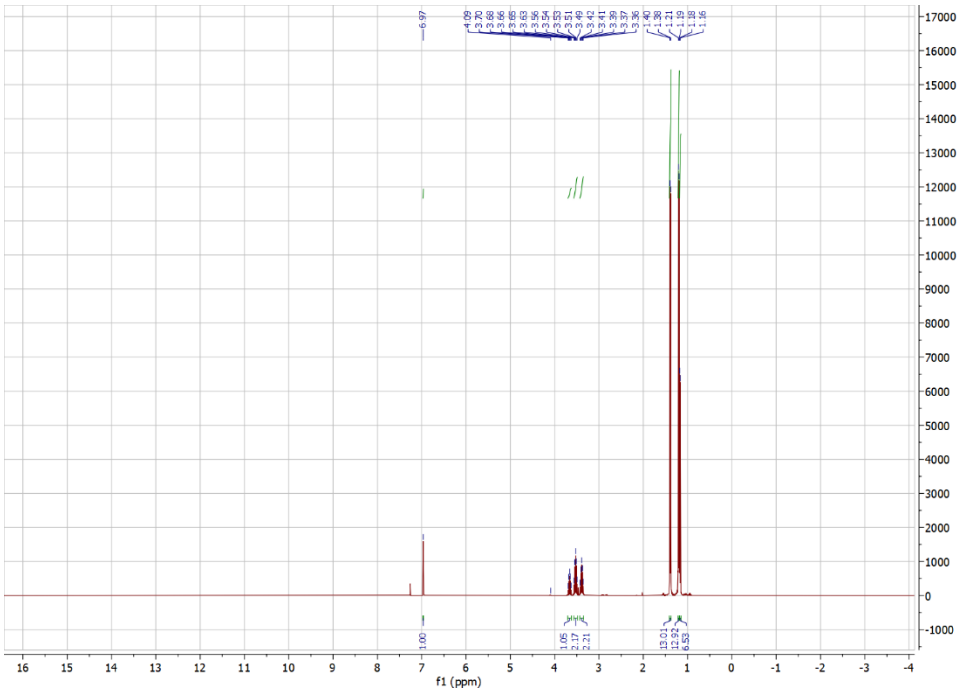

***Figure 74**. HNMR of Benzene-1,2,3,4,5-pentaylpentakis(isopropylsulfane) (**21**).*

Poly[Nickel-benzene-1,2,3,4,5-pentakis(thiolate)] (Ni-bptt)

Compound **21** (1.34 g, 2.98 mmol, 1 eq.) was added into anhydrous *N*, *N*-dimethylacetamide (60 mL) in an inert atmosphere (N_2). Sodium pieces (4.3 g, 107.5 mmol) were then added in to the solution and heated to 100 °C for 24 h. Then 15 mL degassed water was added dropwise into the suspension to give an orange-brown clear solution. Nickel acetate tetrahydrate ($NiAc_2 \cdot 4\ H_2O$, 0.812 g, 2.8 mmol) in 15 mL degassed water was then dropwise added within 15 min, during which the solution gradually turned black. The mixture was further heated at 100°C for another 24 h. Black **Ni-bptt** powder (0.57 g, 62 %) was collected by centrifugation after the reaction cooling down to room temperature and being dried at 100 °C under vacuum overnight.

(3,6-dimethylbenzene-1,2,4,5-tetrayl)tetrakis(isopropylsulfane) (23)

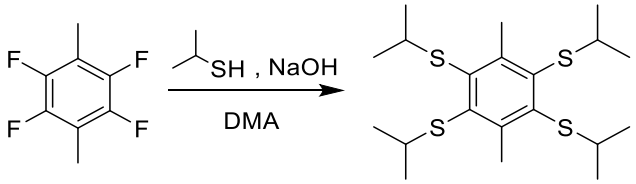

22 **23**

Sodium hydroxide (7 g, 175 mmol) and 1,2,4,5-tetrafluoro-3,6-dimethylbenzene **21** (0.88 g, 4.11 mmol) were dissolved in 60 mL of anhydrous *N*,*N*-dimethylacetamide (DMA). Then, 2-propanethiol (17 mL, 0.18 mol) was added dropwise to the solution at room temperature. After complete addition, the reaction was heated at 100 ºC for 3 days. After the brown solution cooled down, water was slowly added under stirring until a white solid precipitated. The solid was collected by vacuum filtration and re-

dissolved in ethyl acetate (40 mL). The organic phase was washed twice with water (2 × 40 mL) and brine (40 mL). The organic solution was dried with magnesium sulfate (MgSO4), filtered and evaporated under reduced pressure. The brown oil recovered was precipitated into methanol (10 mL) to yield the title compound **23** as white crystalline (4.32 g, 10.73 mmol, 62%). ^{1}H NMR (700 MHz, $CDCl_3$) δ 3.43 (p, J = 6.7 Hz, 4H), 2.86 (s, 6H), 1.17 (d, J = 6.7 Hz, 24H). FTIR (neat, cm^{-1}): 2958 (s), 2920 (m), 2806 (m), 1460 (m), 1375 (s), 1359 (m), 1242 (s), 1152 (m), 1129 (m), 1049 (s), 990 (m), 926 (w), 878 (w), 800 (w), 664 (m), 636 (w), 596 (w). Raman (neat, cm^{-1}): 2948 (w), 2961 (w), 2924 (w), ,2872 (w), 2862 (w), 1504(w), 1444(w), 1319(w), 1207(w), 1198(s), 1052(w), 957 (w), 877 (w), 627 (s), 490 (w), 408 (w), 368 (w), 340 (w), 325 (w), 241 (w).

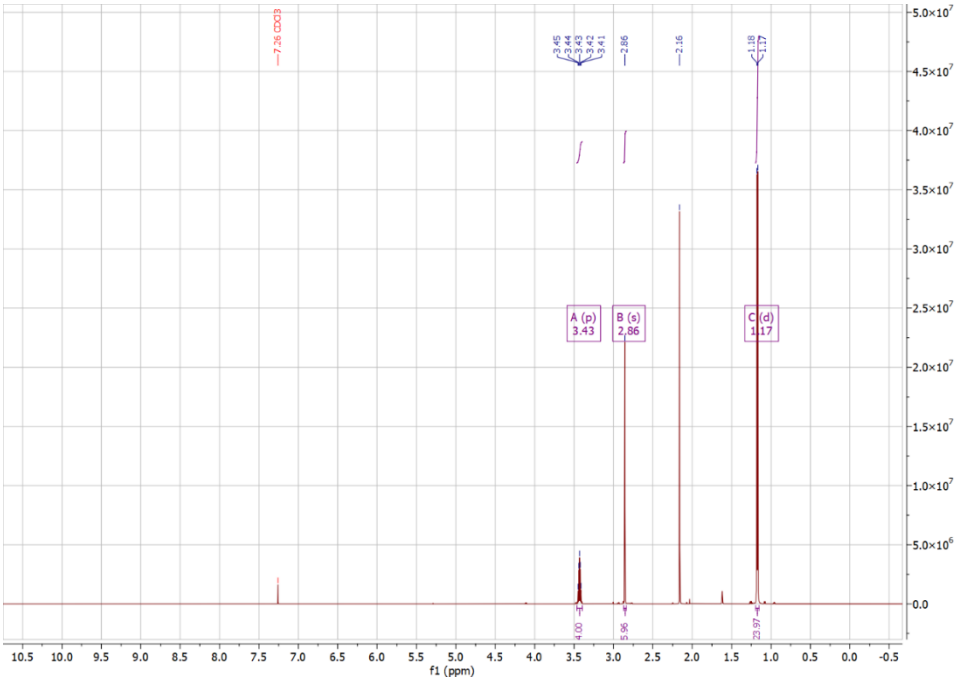

***Figure 75**. HNMR of (3,6-dimethylbenzene-1,2,4,5-tetrayl)tetrakis(isopropthylsulfane) (**23**). The impurity peak is from solvent acetone.*

(3,6-dimethylbenzene-1,2,4,5-tetrayl)tetrakis(methylsulfane) (25)

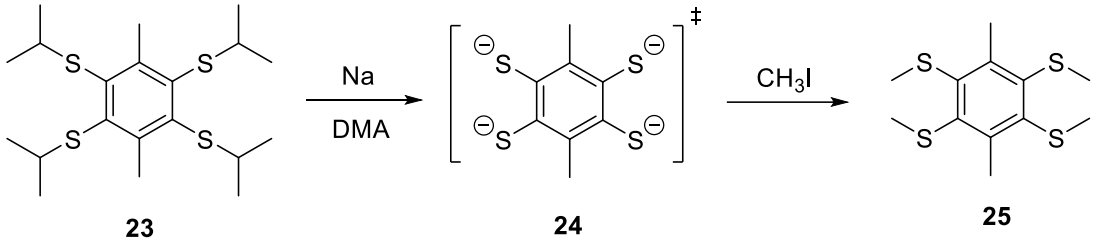

23 **24** **25**

Compound **23** (117 mg, 0.29 mmol) was dissolved in 15 mL of *N*,*N*-dimethylacetamide (DMA) and then sodium (830 mg, 20.75 mmol) was then added. The solution quickly turned yellow and the reaction was refluxed at 100 °C for 20h. The orange solution was then cooled down to room temperature and quenched by adding an excess of methyl iodide (0.40 mL, 3.21 mmol). After heating at 50 °C overnight, the reaction was cooled to room temperature and diluted with 10 mL of diethyl ether. The organic phase was washed with water (2 × 10 mL) and brine (10 mL). The organic phase was dried with magnesium sulfate ($MgSO_4$), filtered and evaporated under reduced pressure to give crude oil. Then 5 mL of cold methanol was added to the oil to precipitate 1,2,4,5-tetrakis(methylthio)benzene (**25**) as a pale yellow solid (60.0 mg, 0.228 mmol, 74%).^{1}H NMR (700 MHz, CDCl3) δ 2.92 (s, 6H), 2.39 (s, *J* = 5.7 Hz, 12H).

Poly[Nickel-3,6-dimethylbenzene-1,2,4,5-tetrakis(thiolate)] (Ni-dmbtt)

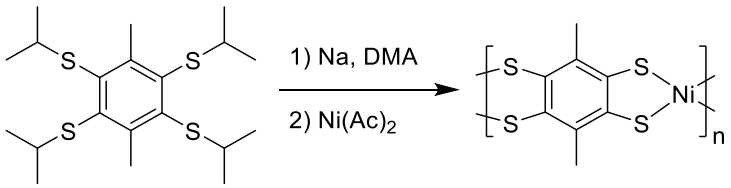

23 **Ni-dmbtt**

Compound **23** (1.206 g, 3 mmol, 1 eq.) was added into anhydrous *N*, *N*-

dimethylacetamide (60 mL) in an inert atmosphere (N_2). Sodium (3.5 g, 87.5 mmol) was then added in to the solution and heated to 100 °C for 24 h. Then 15 mL degassed water was added dropwise into the muddy mixture to give an orange-brown clear solution. Nickel acetate tetrahydrate ($NiAc_2$ 4 H_2O, 0.762 g, 3 mmol) in 15 mL degassed water was then dropwise added within 15 min, during which the solution gradually deepened to black color. The mixture was further heated at 100 °C for another 24 h. Black solid was collected by centrifugation after the reaction cooling down to room temperature and then dried at 100 °C under vacuum overnight to give black **Ni-dmbtt** powder (0.49 g, 68 %). FTIR (neat, cm^{-1}): 2956 (w), 2920 (w), 2860 (w), 1606 (w), 1496 (m), 1429 (m), 1380 (w), 1366 (w), 1304 (w), 1136 (m), 1017 (m), 967 (m), 651 (m), 511 (w). Raman (neat, cm^{-1}): 1057 (w), 1309 (w), 1181 (w), 1153 (w), 989 (w), 444 (w), 385 (s), 357 (w).

References

1. Liu, Z.; Liu, T.; Savory, C. N.; Jurado, J. P.; Reparaz, J. S.; Li, J.; Pan, L.; Faul, C. F. J.; Parkin, I. P.; Sankar, G.; Matsuishi, S.; Campoy‐Quiles, M.; Scanlon, D. O.; Zwijnenburg, M. A.; Fenwick, O.; Schroeder, B. C., Controlling the Thermoelectric Properties of Organometallic Coordination Polymers via Ligand Design. *Advanced Functional Materials* **2020,** *30* (32), 2003106.

2. Bilotti, E.; Fenwick, O.; Schroeder, B. C.; Baxendale, M.; Taroni-Junior, P.; Degousée, T.; Liu, Z., 6.14 Organic Thermoelectric Composites Materials. In *Comprehensive Composite Materials II*, 2018; pp 408-430.

3. Kong, L. B.; Li, T.; Hng, H. H.; Boey, F.; Zhang, T. S.; Li, S., *Waste Energy Harvesting*. Springer 2014; Vol. 24.

4. Snyder, G. J.; Toberer, E. S., Complex thermoelectric materials. *Nature Materials* **2008,** *7* (2), 105-114.

5. Liu, T.; Zhao, X.; Li, J.; Liu, Z.; Liscio, F.; Milita, S.; Schroeder, B. C.; Fenwick, O., Enhanced control of self-doping in halide perovskites for improved thermoelectric performance. *Nat Commun* **2019,** *10* (1), 5750.

6. Haynes, W. M., Abundance of elements in the earth's crust and in the sea, CRC Handbook of Chemistry and Physics. **97th edition (2016–2017)**, 14-17.

7. Soleimani, Z.; Zoras, S.; Ceranic, B.; Shahzad, S.; Cui, Y., A review on recent developments of thermoelectric materials for room-temperature applications. *Sustainable Energy Technologies and Assessments* **2020,** *37*, 100604.

8. Du, Y.; Chen, J.; Meng, Q.; Dou, Y.; Xu, J.; Shen, S. Z., Thermoelectric materials and devices fabricated by additive manufacturing. *Vacuum* **2020,** *178*, 109384.

9. Rull-Bravo, M.; Moure, A.; Fernández, J. F.; Martín-González, M., Skutterudites as thermoelectric materials: revisited. *RSC Advances* **2015,** *5* (52), 41653-41667.

10. Sun, Y.; Di, C. A.; Xu, W.; Zhu, D., Advances in n‐Type Organic Thermoelectric

Materials and Devices. *Advanced Electronic Materials* **2019,** *5* (11).

11. Zhang, Y.; Heo, Y. J.; Park, M.; Park, S. J., Recent Advances in Organic Thermoelectric Materials: Principle Mechanisms and Emerging Carbon-Based Green Energy Materials. *Polymers (Basel)* **2019,** *11* (1), 167.

12. Chen, G.; Xu, W.; Zhu, D., Recent advances in organic polymer thermoelectric composites. *Journal of Materials Chemistry C* **2017,** *5* (18), 4350-4360.

13. Wang, H.; Chu, W.; Chen, G., A Brief Review on Measuring Methods of Thermal Conductivity of Organic and Hybrid Thermoelectric Materials. *Advanced Electronic Materials* **2019,** *5* (11), 1900167.

14. Chen, Y.; He, M.; Liu, B.; Bazan, G. C.; Zhou, J.; Liang, Z., Bendable n-Type Metallic Nanocomposites with Large Thermoelectric Power Factor. *Advanced Materials* **2017,** *29* (4) , 1604752.

15. Jin, H.; Li, J.; Iocozzia, J.; Zeng, X.; Wei, P. C.; Yang, C.; Li, N.; Liu, Z.; He, J. H.; Zhu, T.; Wang, J.; Lin, Z.; Wang, S., Hybrid Organic-Inorganic Thermoelectric Materials and Devices. *Angew Chem International Edition in English* **2019,** *58* (43), 15206-15226.

16. Coomber, A. T.; Beljonne, D.; Friend, R. H.; Bredas, J. L.; Charlton, A.; Robertson, N.; Underhill, A. E.; Kurmoo, M.; Day, P., Intermolecular interactions in the molecular ferromagnetic $NH_4Ni(mnt)_2 \cdot H_2O$. *Nature* **1996,** *380* (6570), 144-146.

17. Harrison, D. J.; Nguyen, N.; Lough, A. J.; Fekl, U., New insight into reactions of $Ni(S_2C_2(CF_3)_2)_2$ with simple alkenes: Alkene adduct versus dihydrodithiin product selectivity is controlled by $[(S_2C_2(CF_3)_2)_2]^-$ anion. *Journal of the American Chemical Society* **2006,** *128* (34), 11026-11027.

18. Valade, L.; de Caro, D.; Faulmann, C.; Jacob, K., $TTF[Ni(dmit)_2]_2$: From single-crystals to thin layers, nanowires, and nanoparticles. *Coordination Chemistry Reviews* **2016,** *308*, 433-444.

19. Kato, R., Conducting metal dithiolene complexes: structural and electronic properties. *Chemical Reviews* **2004,** *104* (11), 5319-46.

20. Kobayashi, A.; Fujiwara, E.; Kobayashi, H., Single-component molecular metals with

extended-TTF dithiolate ligands. *Chemical Reviews* **2004,** *104* (11), 5243-64.

21. Das, A.; Han, Z.; Brennessel, W. W.; Holland, P. L.; Eisenberg, R., Nickel Complexes for Robust Light-Driven and Electrocatalytic Hydrogen Production from Water. *ACS Catalysis* **2015,** *5* (3), 1397-1406.

22. Robertson, N.; Cronin, L., Metal bis-1,2-dithiolene complexes in conducting or magnetic crystalline assemblies. *Coordination Chemistry Reviews* **2002,** *227* (1), 93-127.

23. Serrano-Andres, L.; Avramopoulos, A.; J. Li, P. L.; D. Begue, V. K.; Papadopoulos, M. G., Linear and nonlinear optical properties of a series of Nidithiolene derivatives. *The Journal of Chemical Physics* **2009,** (131), 134312.

24. Zarkadoulas, A.; Koutsouri, E.; Mitsopoulou, C. A., A perspective on solar energy conversion and water photosplitting by dithiolene complexes. *Coordination Chemistry Reviews* **2012,** *256* (21-22), 2424-2434.

25. Kusamoto, T.; Nishihara, H., Zero-, one- and two-dimensional bis(dithiolato)metal complexes with unique physical and chemical properties. *Coordination Chemistry Reviews* **2019,** *380*, 419-439.

26. Gama, V.; Almeida, M.; Henriques, R. T.; Santos, I. C.; Domingos, A., Low-Dimensional Molecular Conductors $(Per)_2M(mnt)_2$: M = High-Conductivity Phases Cu and Ni: Low and High Conductivity Phases. *The Journal of Chemical Physics* **1991,** (95), 4263-4267.

27. Gama, V.; Henriques, R. T.; Bonfait, G.; Pereira, L. C.; Waerenborgh, J. C.; Santos, I. C.; Duarte, M. T.; Cabral, J. M. P.; Almeida, M., Low-Dimensional Molecular-Metals $(Per)_2M(mnt)_2$ (M = Fe and Co). *Inorganic Chemistry* **1992,** *31* (12), 2598-2604.

28. Gama, V.; Henriques, R. T.; Bonfait, G.; Almeida, M.; Meetsma, A.; Vansmaalen, S.; Deboer, J. L., (Perylene)$Co(mnt)_2(CH_2Cl_2)_{0.5}$: a Mixed Molecular and Polymeric Conductor. *Journal of the American Chemical Society* **1992,** *114* (6), 1986-1989.

29. Lopes, E. B.; Alves, H.; Ribera, E.; Mas-Torrent, M.; Auban-Senzier, P.; Canadell, E.; Henriques, R. T.; Almeida, M.; Molins, E.; Veciana, J.; Rovira, C.; Jerome, D., Electronic localization in an extreme 1-D conductor: the organic salt $(TTDM\text{-}TTF)_2[Au(mnt)_2]$. *European Physical Journal B* **2002,** *29* (1), 27-33.

30. Sato, R.; Kiyota, Y.; Kadoya, T.; Kawamoto, T.; Mori, T., Thermoelectric power of oriented thin-film organic conductors. *RSC Advances* **2016,** *6* (47), 41040-41044.

31. Kang, W.; Jerome, D.; Valade, L.; Cassoux, P., Thermopower Measurement of the Organic Conductor TTF[Ni(dmit)$_2$]$_2$ at Ambient Pressure. *Synthetic Metals* **1991,** *42* (3), 2343-2345.

32. Dias, C. B.; Santos, I. C.; Gama, V.; Henriques, R. T.; Almeida, M.; Pouget, J. P., A Perylene Conductor with a Gold Cyanodithiocarbimate Counterion - (Perylene)$_2$Au(cdc)$_2$. *Synthetic Metals* **1993,** *56* (1), 1688-1693.

33. Dias, J. C.; Ribas, X.; Morgado, J.; Seiça, J.; Lopes, E. B.; Santos, I. C.; Henriques, R. T.; Almeida, M.; Wurst, K.; Foury-Leylekian, P.; Canadell, E.; Vidal-Gancedo, J.; Veciana, J.; Rovira, C., Multistability in a family of DT–TTF organic radical based compounds (DT–TTF)$_4$[M(L)$_2$]$_3$ (M = Au, Cu; L = pds, pdt, bdt). *Journal of Materials Chemistry* **2005,** *15* (31).

34. Simao, D.; Lopes, E. B.; Santos, I. C.; Gama, V.; Henriques, R. T.; Almeida, M., Charge transfer salts based on Cu(qdt)$_2$, Ni(qdt)$_2$ and Au(qdt)$_2$ anions. *Synthetic Metals* **1999,** *102* (1-3), 1613-1614.

35. Morgado, J.; Alcker, Z. L.; Henriques, R. T.; Almeida, M., Properties of the organic conductor (TMTSF)$_2$Ni(tht)$_2$. *Synthetic Metals* **1995,** (71), 1943-1944.

36. Yong, X.; Shi, W.; Wu, G.; Goh, S. S.; Bai, S.; Xu, J.-W.; Wang, J.-S.; Yang, S.-W., Tuning the thermoelectric performance of π–d conjugated nickel coordination polymers through metal–ligand frontier molecular orbital alignment. *Journal of Materials Chemistry A* **2018,** *6* (40), 19757-19766.

37. Clark, R. A.; Varma, K. S.; Underhill, A. E.; Becher, J.; Toftlund, H., Preparation and Properties of a Series of Conducting Metal-Complexes Based on 2,3-Dithiolatoquinoxaline, 2,3,5,6-Tetrathiolatopyrazine and 2,3,7,8-Tetrathiolato-Bis[1,4]Dithiino-[2,3-B-2',3'-e]Pyrazine. *Synthetic Metals* **1988,** *25* (3), 227-234.

38. Horwitz, N. E.; Xie, J.; Filatov, A. S.; Papoular, R. J.; Shepard, W. E.; Zee, D. Z.; Grahn, M. P.; Gilder, C.; Anderson, J. S., Redox-Active 1D Coordination Polymers of Iron-Sulfur Clusters. *Journal of the American Chemical Society* **2019,** *141* (9), 3940-3951.

39. JOHN R. REYNOLDS, C. A. J. a. S. K., Poly(metaltetrathiooxalates) - a structural and

chareg-transprt study. *Synthetic Metals* **1989,** *31*, 109-126.

40. Poleschner, H.; John, W.; Hoppe, F.; Fanghanel, E.; Roth, S., Tetrathiafulvalenes .19. Synthesis and Properties of Electron Conducting Poly-Dithiolene Complexes with Ethylene Tetrathiolat and Tetrathiafulvalene Tetrathiolat as Bridge Ligands. *Journal fur Praktische Chemie* **1983,** *325* (6), 957-975.

41. Vogt, T.; Faulmann, C.; Soules, R.; Lecante, P.; Mosset, A.; Castan, P.; Cassoux, P.; Galy, J., A Laxs (Large-Angle X-Ray-Scattering) and Exafs (Extended X-Ray Absorption Fine-Structure) Investigation of Conductive Amorphous Nickel Tetrathiolato Polymers. *Journal of the American Chemical Society* **1988,** *110* (6), 1833-1840.

42. Gotzfried, F.; Beck, W.; Lerf, A.; Sebald, A., Transition-Metal Complexes with the Tetrathiosquarate Dianion as Bridging Bischelate Ligand. *Angew Chem Internatioanl Edition* **1979,** *18* (6), 463-464.

43. Rivera, N. M.; Engler, E. M.; Schumaker, R. R., Synthesis and properties of tetrathiafulvalene–metal bisdithiolene macromolecules. *Journal of the American Chemical Society, Chemical Communications* **1979,** (4), 184-185.

44. Matsuoka, R.; Sakamoto, R.; Kambe, T.; Takada, K.; Kusamoto, T.; Nishihara, H., Ordered alignment of a one-dimensional pi-conjugated nickel bis(dithiolene) complex polymer produced via interfacial reactions. *Chemical communications* **2014,** *50* (60), 8137-9.

45. Sun, Y.; Qiu, L.; Tang, L.; Geng, H.; Wang, H.; Zhang, F.; Huang, D.; Xu, W.; Yue, P.; Guan, Y. S.; Jiao, F.; Sun, Y.; Tang, D.; Di, C. A.; Yi, Y.; Zhu, D., Flexible n-Type High-Performance Thermoelectric Thin Films of Poly(nickel-ethylenetetrathiolate) Prepared by an Electrochemical Method. *Advanced materials* **2016,** *28* (17), 3351-8.

46. Downes, C. A.; Marinescu, S. C., Efficient Electrochemical and Photoelectrochemical H2 Production from Water by a Cobalt Dithiolene One-Dimensional Metal-Organic Surface. *Journal of the American Chemical Society* **2015,** *137* (43), 13740-3.

47. Hu, C.; Ma, Q.; Hung, S.-F.; Chen, Z.-N.; Ou, D.; Ren, B.; Chen, H. M.; Fu, G.; Zheng, N., In Situ Electrochemical Production of Ultrathin Nickel Nanosheets for Hydrogen Evolution Electrocatalysis. *Chem* **2017,** *3* (1), 122-133.

48. Pal, T.; Kambe, T.; Kusamoto, T.; Foo, M. L.; Matsuoka, R.; Sakamoto, R.; Nishihara, H., Interfacial Synthesis of Electrically Conducting Palladium Bis(dithiolene) Complex Nanosheet. *Chempluschem* **2015,** *80* (8), 1255-1258.

49. Huang, X.; Zhang, S.; Liu, L.; Yu, L.; Chen, G.; Xu, W.; Zhu, D., Superconductivity in a Copper(II)-Based Coordination Polymer with Perfect Kagome Structure. *Angew Chem International Edition in English* **2018,** *57* (1), 146-150.

50. Huang, X.; Li, H.; Tu, Z.; Liu, L.; Wu, X.; Chen, J.; Liang, Y.; Zou, Y.; Yi, Y.; Sun, J.; Xu, W.; Zhu, D., Highly Conducting Neutral Coordination Polymer with Infinite Two-Dimensional Silver-Sulfur Networks. *Journal of the American Chemical Society* **2018,** *140* (45), 15153-15156.

51. Chen, I. F.; Lu, C. F.; Su, W. F., Highly Conductive 2D Metal-Organic Framework Thin Film Fabricated by Liquid-Liquid Interfacial Reaction Using One-Pot-Synthesized Benzenehexathiol. *Langmuir* **2018,** *34* (51), 15754-15762.

52. Clough, A. J.; Yoo, J. W.; Mecklenburg, M. H.; Marinescu, S. C., Two-dimensional metal-organic surfaces for efficient hydrogen evolution from water. *J Am Chem Soc* **2015,** *137* (1), 118-21.

53. Downes, C. A.; Clough, A. J.; Chen, K.; Yoo, J. W.; Marinescu, S. C., Evaluation of the H2 Evolving Activity of Benzenehexathiolate Coordination Frameworks and the Effect of Film Thickness on H_2 Production. *ACS Applied Material & Interfaces* **2018,** *10* (2), 1719-1727.

54. Downes, C. A.; Marinescu, S. C., One dimensional metal dithiolene (M = Ni, Fe, Zn) coordination polymers for the hydrogen evolution reaction. *Dalton transactions* **2016,** *45* (48), 19311-19321.

55. Huang, X.; Sheng, P.; Tu, Z.; Zhang, F.; Wang, J.; Geng, H.; Zou, Y.; Di, C. A.; Yi, Y.; Sun, Y.; Xu, W.; Zhu, D., A two-dimensional pi-d conjugated coordination polymer with extremely high electrical conductivity and ambipolar transport behaviour. *Nature communications* **2015,** *6*, 7408.

56. Kambe, T.; Sakamoto, R.; Hoshiko, K.; Takada, K.; Miyachi, M.; Ryu, J. H.; Sasaki, S.; Kim, J.; Nakazato, K.; Takata, M.; Nishihara, H., pi-Conjugated nickel bis(dithiolene) complex

nanosheet. *Journal of the American Chemical Society* **2013,** *135* (7), 2462-5.

57. Dong, R.; Han, P.; Arora, H.; Ballabio, M.; Karakus, M.; Zhang, Z.; Shekhar, C.; Adler, P.; Petkov, P. S.; Erbe, A.; Mannsfeld, S. C. B.; Felser, C.; Heine, T.; Bonn, M.; Feng, X.; Canovas, E., High-mobility band-like charge transport in a semiconducting two-dimensional metal-organic framework. *Nature Materials* **2018,** *17* (11), 1027-1032.

58. Sakamoto, R.; Kambe, T.; Tsukada, S.; Takada, K.; Hoshiko, K.; Kitagawa, Y.; Okumura, M.; Nishihara, H., pi-Conjugated trinuclear group-9 metalladithiolenes with a triphenylene backbone. *Inorganic chemistry* **2013,** *52* (13), 7411-6.

59. Dong, R.; Pfeffermann, M.; Liang, H.; Zheng, Z.; Zhu, X.; Zhang, J.; Feng, X., Large-area, free-standing, two-dimensional supramolecular polymer single-layer sheets for highly efficient electrocatalytic hydrogen evolution. *Angewandte Chemie* **2015,** *54* (41), 12058-63.

60. Dong, R.; Zhang, Z.; Tranca, D. C.; Zhou, S.; Wang, M.; Adler, P.; Liao, Z.; Liu, F.; Sun, Y.; Shi, W.; Zhang, Z.; Zschech, E.; Mannsfeld, S. C. B.; Felser, C.; Feng, X., A coronene-based semiconducting two-dimensional metal-organic framework with ferromagnetic behavior. *Nature Communications* **2018,** *9* (1), 2637.

61. Dong, R.; Pfeffermann, M.; Skidin, D.; Wang, F.; Fu, Y.; Narita, A.; Tommasini, M.; Moresco, F.; Cuniberti, G.; Berger, R.; Mullen, K.; Feng, X., Persulfurated Coronene: A New Generation of "Sulflower". *Journal of the American Chemical Society* **2017,** *139* (6), 2168-2171.

62. Shi, W.; Wu, G.; Yong, X.; Deng, T.; Wang, J. S.; Zheng, J. C.; Xu, J.; Sullivan, M. B.; Yang, S. W., Orbital-Engineering-Based Screening of π-Conjugated d(8) Transition-Metal Coordination Polymers for High-Performance n-Type Thermoelectric Applications. *ACS Applied Material & Interfaces* **2018,** *10* (41), 35306-35315.

63. Deng, T.; Yong, X.; Shi, W.; Gan, C. K.; Li, W.; Hippalgaonkar, K.; Zheng, J. C.; Wang, X.; Yang, S. W.; Wang, J. S.; Wu, G., 2D Single-Layer π-Conjugated Nickel Bis(dithiolene) Complex: A Good-Electron-Poor-Phonon Thermoelectric Material. *Advanced Electronic Materials* **2019,** *5* (4), 1800892.

64. Liu, S.; Wang, Y. C.; Chang, C. M.; Yasuda, T.; Fukui, N.; Maeda, H.; Long, P.; Nakazato,

K.; Jian, W. B.; Xie, W.; Tsukagoshi, K.; Nishihara, H., Solution-processed organometallic quasi-two-dimensional nanosheets as a hole buffer layer for organic light-emitting devices. *Nanoscale* **2020,** *12* (13), 6983-6990.

65. Shi, W.; Wu, G.; Hippalgaonkar, K.; Wang, J. S.; Xu, J.; Yang, S. W., Poly(nickel-ethylenetetrathiolate) and Its Analogs: Theoretical Prediction of High-Performance Doping-Free Thermoelectric Polymers. *Journal of the American Chemical Society* **2018,** *140* (41), 13200-13204.

66. Sun, Y.; Sheng, P.; Di, C.; Jiao, F.; Xu, W.; Qiu, D.; Zhu, D., Organic thermoelectric materials and devices based on p- and n-type poly(metal 1,1,2,2-ethenetetrathiolate)s. *Advanced materials* **2012,** *24* (7), 932-7.

67. Huang, X.; Sheng, P.; Tu, Z.; Zhang, F.; Wang, J.; Geng, H.; Zou, Y.; Di, C. A.; Yi, Y.; Sun, Y.; Xu, W.; Zhu, D., A two-dimensional π-d conjugated coordination polymer with extremely high electrical conductivity and ambipolar transport behaviour. *Nature Communications* **2015,** *6*, 7408.

68. Schlettwein, D.; Wohrle, D.; Karmann, E.; Melville, U., Conduction type of substituted tetraazaporphyrins and perylene tetracarboxylic acid diimides as detected by thermoelectric-power measurements. *Chemistry of Materials* **1994,** *6*, 3-6.

69. Hamann, C., Measurements of Thermoelectric Power of Copper Phthalocyanine Single-Crystals. *Physica Status Solidi A* **1972,** *10* (2), 509-&.

70. Faulmann, C.; Chahine, J.; Jacob, K.; Coppel, Y.; Valade, L.; de Caro, D., Nickel ethylene tetrathiolate polymers as nanoparticles: a new synthesis for future applications? *Journal of Nanoparticle Research* **2013,** *15* (4), 1586.

71. Liu, L.; Sun, Y.; Li, W.; Zhang, J.; Huang, X.; Chen, Z.; Sun, Y.; Di, C.; Xu, W.; Zhu, D., Flexible unipolar thermoelectric devices based on patterned poly[Kx(Ni-ethylenetetrathiolate)] thin films. *Materials Chemistry Frontiers* **2017,** *1* (10), 2111-2116.

72. Jin, W.; Liu, L.; Yang, T.; Shen, H.; Zhu, J.; Xu, W.; Li, S.; Li, Q.; Chi, L.; Di, C. A.; Zhu, D., Exploring Peltier effect in organic thermoelectric films. *Nature Communications* **2018,** *9* (1), 3586.

73. Wolfe, R. M. W.; Menon, A. K.; Fletcher, T. R.; Marder, S. R.; Reynolds, J. R.; Yee, S. K., Simultaneous Enhancement in Electrical Conductivity and Thermopower of n-Type NiETT/PVDF Composite Films by Annealing. *Advanced Functional Materials* **2018,** *28* (37), 1803275.

74. Menon, A. K.; Wolfe, R. M. W.; Marder, S. R.; Reynolds, J. R.; Yee, S. K., Systematic Power Factor Enhancement in n-Type NiETT/PVDF Composite Films. *Advanced Functional Materials* **2018,** *28* (29), 1801620.

75. Wan, K.; Taroni, P. J.; Liu, Z.; Liu, Y.; Tu, Y.; Santagiuliana, G.; Hsia, I. C.; Zhang, H.; Fenwick, O.; Krause, S.; Baxendale, M.; Schroeder, B. C.; Bilotti, E., Flexible and Stretchable Self-Powered Multi-Sensors Based on the N-Type Thermoelectric Response of Polyurethane/Na_x(Ni-ett)$_n$ Composites. *Advanced Electronic Materials* **2019,** *5* (12), 1900582.

76. Dirk, C. W.; Bousseau, M.; Barrett, P. H.; Moraes, F.; Wudl, F.; Heeger, A. J., Metal Poly(Benzodithiolenes). *Macromolecules* **1986,** *19* (2), 266-269.

77. Poleschner, H.; John, W.; Hoppe, F.; Fanghänel, E.; Roth, S., Tetrathiafulvalene. XIX. Synthese und Eigenschaften elektronenleitender Poly-Dithiolenkomplexe mit Ethylentetrathiolat und Tetrathiafulvalentetrathiolat als Brückenliganden. *Journal für Praktische Chemie* **1983,** *325* (6), 957-975.

78. Tkachov, R.; Stepien, L.; Roch, A.; Komber, H.; Hennersdorf, F.; Weigand, J. J.; Bauer, I.; Kiriy, A.; Leyens, C., Facile synthesis of potassium tetrathiooxalate – The “true” monomer for the preparation of electron-conductive poly(nickel-ethylenetetrathiolate). *Tetrahedron* **2017,** *73* (16), 2250-2254.

79. Tkachov, R.; Stepien, L.; Grafe, R.; Guskova, O.; Kiriy, A.; Simon, F.; Reith, H.; Nielsch, K.; Schierning, G.; Kasinathan, D.; Leyens, C., Polyethenetetrathiolate or polytetrathiooxalate? Improved synthesis, a comparative analysis of a prominent thermoelectric polymer and implications to the charge transport mechanism. *Polymer Chemistry* **2018,** *9* (36), 4543-4555.

80. Sun, Y.; Sheng, P.; Di, C.; Jiao, F.; Xu, W.; Qiu, D.; Zhu, D., Organic Thermoelectric Materials and Devices Based on p- and n-Type Poly(metal 1,1,2,2-ethenetetrathiolate)s. *Advanced Materials* **2012,** *24* (7), 932-937.

81. Sun, Y.; Qiu, L.; Tang, L.; Geng, H.; Wang, H.; Zhang, F.; Huang, D.; Xu, W.; Yue, P.; Guan, Y.-s.; Jiao, F.; Sun, Y.; Tang, D.; Di, C.-a.; Yi, Y.; Zhu, D., Flexible n-Type High-Performance Thermoelectric Thin Films of Poly(nickel-ethylenetetrathiolate) Prepared by an Electrochemical Method. *Advanced Materials* **2016,** *28* (17), 3351-3358.

82. Menon, A. K.; Wolfe, R. M. W.; Marder, S. R.; Reynolds, J. R.; Yee, S. K., Systematic Power Factor Enhancement in n-Type NiETT/PVDF Composite Films. *Advanced Functional Materials* **2018,** *28* (29), 1801620.

83. Wolfe, R. M. W.; Menon, A. K.; Fletcher, T. R.; Marder, S. R.; Reynolds, J. R.; Yee, S. K., Simultaneous Enhancement in Electrical Conductivity and Thermopower of n-Type NiETT/PVDF Composite Films by Annealing. *Advanced Functional Materials* **2018,** *28* (37), 1803275.

84. Li, J.; Zhang, Z.; Guo, X.; Yang, Y., The studies on structural and thermal properties of delithiated $Li_xNi_{1/3}Co_{1/3}Mn_{1/3}O_2$ ($0<x\leqslant 1$) as a cathode material in lithium ion batteries. *Solid State Ionics* **2006,** *177* (17-18), 1509-1516.

85. Cheng, X.; Wei, H.; Hao, W.; Li, H.; Si, H.; An, S.; Zhu, W.; Jia, G.; Qiu, X., A Cobalt-Free $Li(Li_{0.16}Ni_{0.19}Fe_{0.18}Mn_{0.46})O_2$ Cathode for Lithium-Ion Batteries with Anionic Redox Reactions. *ChemSusChem* **2019,** *12* (6), 1162-1168.

86. Dong, R.; Pfeffermann, M.; Liang, H.; Zheng, Z.; Zhu, X.; Zhang, J.; Feng, X., Large-Area, Free-Standing, Two-Dimensional Supramolecular Polymer Single-Layer Sheets for Highly Efficient Electrocatalytic Hydrogen Evolution. *Angewandte Chemie International Edition* **2015,** *54* (41), 12058-12063.

87. Grosvenor, A. P.; Biesinger, M. C.; Smart, R. S. C.; McIntyre, N. S., New interpretations of XPS spectra of nickel metal and oxides. *Surface Science* **2006,** *600* (9), 1771-1779.

88. Karthikeyan, R.; Thangaraju, D.; Prakash, N.; Hayakawa, Y., Single-step synthesis and catalytic activity of structure-controlled nickel sulfide nanoparticles. *CrystEngComm* **2015,** *17* (29), 5431-5439.

89. Fantauzzi, M.; Elsener, B.; Atzei, D.; Rigoldi, A.; Rossi, A., Exploiting XPS for the identification of sulfides and polysulfides. *RSC Advances* **2015,** *5* (93), 75953-75963.

90. Gray, H. B.; Billig, E., The Electronic Structures of Square-Planar Metal Complexes. III. High-Spin Planar Cobalt(I) and Iron(I). *Journal of the American Chemical Society* **1963,** *85* (13), 2019-2020.

91. Shupack, S. I.; Billig, E.; Clark, R. J. H.; Williams, R.; Gray, H. B., The Electronic Structures of Square-Planar Metal Complexes. V. Spectral Properties of the Maleonitriledithiolate Complexes of Nickel, Palladium, and Platinum. *Journal of the American Chemical Society* **1964,** *86* (21), 4594-4602.

92. Baker-Hawkes, M. J.; Billig, E.; Gray, H. B., Characterization and Electronic Structures of Metal Complexes Containing Benzene-1,2-dithiolate and Related Ligands. *Journal of the American Chemical Society* **1966,** *88* (21), 4870-4875.

93. Ray, K.; Weyhermüller, T.; Neese, F.; Wieghardt, K., Electronic Structure of Square Planar Bis(benzene-1,2-dithiolato)metal Complexes $[M(L)_2]^z$ (z = 2−, 1−, 0; M = Ni, Pd, Pt, Cu, Au): An Experimental, Density Functional, and Correlated ab Initio Study. *Inorganic Chemistry* **2005,** *44* (15), 5345-5360.

94. Xiong, R.-G.; Song, B.-L.; You, X.-Z.; Mak, T. C. W.; Zhou, Z.-Y., Syntheses and properties of some transition metal complexes with methyl substituted 1-hydroxy-2(1H)-pyridinethione and crystal structure of bis(1-hydroxy)-4-methyl-2-(1H)-pyridinethionato-O,S′)zinc(II). *Polyhedron* **1996,** *15* (5), 991-996.

95. De Mello, M. T. S.; Ribeiro, M. C. C.; Santos, P. S., Resonance Raman spectroscopy of bis(isomaleonitriledithiolato)nickelate(II) as a probe to the chromophore extension. *Journal of Raman Spectroscopy* **1995,** *26* (2), 173-178.

96. Larkin, P. J., *Infrared and Raman Spectroscopy: Principles and Spectral Interpretation*. 2nd Edition ed.; Elsevier: 2017.

97. Bubnova, O.; Khan, Z. U.; Wang, H.; Braun, S.; Evans, D. R.; Fabretto, M.; Hojati-Talemi, P.; Dagnelund, D.; Arlin, J.-B.; Geerts, Y. H.; Desbief, S.; Breiby, D. W.; Andreasen, J. W.; Lazzaroni, R.; Chen, W. M.; Zozoulenko, I.; Fahlman, M.; Murphy, P. J.; Berggren, M.; Crispin, X., Semi-metallic polymers. *Nature Materials* **2014,** *13* (2), 190-194.

98. Remme, S.; Lehmann, G.; Recker, K.; Wallrafen, F., Electron Paramagnetic Resonance of

Ni^{2+} in $BaZnF_4$ Single Crystals. In *Zeitschrift für Naturforschung A*, 1986; Vol. 41, p 619.

99. Stoyanova, R.; Zhecheva, E.; Alcántara, R.; Tirado, J. L., Local Coordination of Low-Spin Ni^{3+} Probes in Trigonal LiAlyCo1-yO2 Monitored by HF-EPR. *The Journal of Physical Chemistry B* **2004,** *108* (13), 4053-4057.

100. Sariciftci, N. S.; Heeger, A. J.; Cao, Y., Paramagnetic susceptibility of highly conducting polyaniline: Disordered metal with weak electron-electron interactions (Fermi glass). *Physical Review B* **1994,** *49* (9), 5988-5992.

101. Sproules, S.; Wieghardt, K., Dithiolene radicals: Sulfur K-edge X-ray absorption spectroscopy and Harry's intuition. *Coordination Chemistry Reviews* **2011,** *255* (7), 837-860.

102. Matsuoka, R.; Sakamoto, R.; Kambe, T.; Takada, K.; Kusamoto, T.; Nishihara, H., Ordered alignment of a one-dimensional π-conjugated nickel bis(dithiolene) complex polymer produced via interfacial reactions. *Chemical Communications* **2014,** *50* (60), 8137-8139.

103. Tsu, R.; Hernandez, J. G., Temperature dependence of silicon Raman lines. *Applied Physics Letters* **1982,** *41* (11), 1016-1018.

104. Abol-Fotouh, D.; Dörling, B.; Zapata-Arteaga, O.; Rodríguez-Martínez, X.; Gómez, A.; Reparaz, J. S.; Laromaine, A.; Roig, A.; Campoy-Quiles, M., Farming thermoelectric paper. *Energy & Environmental Science* **2019,** *12* (2), 716-726.

105. Testaferri, L.; Tingoli, M.; Tiecco, M., Reactions of Polychlorobenzenes with Alkanethiol Anions in Hmpa - a Simple, High-Yield Synthesis of Poly(Alkylthio)Benzenes. *Journal of Organic Chemistry* **1980,** *45* (22), 4376-4380.

106. Chen, Y.; Tang, M.; Wu, Y.; Su, X.; Li, X.; Xu, S.; Zhuo, S.; Ma, J.; Yuan, D.; Wang, C.; Hu, W., A One-Dimensional π-d Conjugated Coordination Polymer for Sodium Storage with Catalytic Activity in Negishi Coupling. *Angew Chem International Edition in English* **2019,** *58* (41), 14731-14739.

107. Dou, J. H.; Sun, L.; Ge, Y.; Li, W.; Hendon, C. H.; Li, J.; Gul, S.; Yano, J.; Stach, E. A.; Dinca, M., Signature of Metallic Behavior in the Metal-Organic Frameworks M3(hexaiminobenzene)$_2$ (M = Ni, Cu). *Journal of the American Chemical Society* **2017,** *139* (39), 13608-13611.

108. Larkin, P., Infrared and Raman Spectroscopy: Principles and Spectral Interpretation. **2011**.

109. Chakraborty, C.; Pandey, R. K.; Rana, U.; Kanao, M.; Moriyama, S.; Higuchi, M., Geometrically isomeric Pt(II)/Fe(II)-based heterometallo-supramolecular polymers with organometallic ligands for electrochromism and the electrochemical switching of Raman scattering. *Journal of Materials Chemistry C* **2016,** *4* (40), 9428-9437.

110. Dutta, S.; Chakraborty, S.; Drew, M. G. B.; Frontera, A.; Ghosh, A., Two Geometrical Isomers of a 1D Coordination Polymer: Rationalization by Theoretical Calculations and Variation of Electrical Properties with the Change in Binding Mode of Dicarboxylate Linker. *Crystal Growth & Design* **2019,** *19* (10), 5819-5828.

111. Guo, X.; Baumgarten, M.; Müllen, K., Designing π-conjugated polymers for organic electronics. *Progress in Polymer Science* **2013,** *38* (12), 1832-1908.

112. Yao, M. S.; Zheng, J. J.; Wu, A. Q.; Xu, G.; Nagarkar, S. S.; Zhang, G.; Tsujimoto, M.; Sakaki, S.; Horike, S.; Otake, K.; Kitagawa, S., A Dual-Ligand Porous Coordination Polymer Chemiresistor with Modulated Conductivity and Porosity. *Angew Chem International Edition in English* **2020,** *59* (1), 172-176.

113. Carpenter, J. H.; Ghasemi, M.; Gann, E.; Angunawela, I.; Stuard, S. J.; Rech, J. J.; Ritchie, E.; O'Connor, B. T.; Atkin, J.; You, W.; DeLongchamp, D. M.; Ade, H., Competition between Exceptionally Long-Range Alkyl Sidechain Ordering and Backbone Ordering in Semiconducting Polymers and Its Impact on Electronic and Optoelectronic Properties. *Advanced Functional Materials* **2018,** *29*, 1806977.

114. Kondoh, A.; Yorimitsu, H.; Oshima, K., Nucleophilic aromatic substitution reaction of nitroarenes with alkyl- or arylthio groups in dimethyl sulfoxide by means of cesium carbonate. *Tetrahedron* **2006,** *62* (10), 2357-2360.

115. Biesinger, M. C., Advanced Analysis of Copper X-ray Photoelectron (XPS) Spectra. *Surface and Interface Analysis* **2017,** *49*, 1325-1334.

116. Sheng, P.; Sun, Y.; Jiao, F.; Liu, C.; Xu, W.; Zhu, D., Optimization of the thermoelectric properties of poly[Cu_x(Cu-ethylenetetrathiolate)]. *Synthetic Metals* **2014,** *188*, 111-115.

117. Alvarez, S.; Vicente, R.; Hoffmann, R., Dimerization and Stacking in Transition-Metal

Bisdithiolenes and Tetrathiolates. *Journal of the American Chemical Society* **1985,** *107* (22), 6253-6277.

118. Pinkas, J.; Huffman, J. C.; Baxter, D. V.; Chisholm, M. H.; Caulton, K. G., Mechanistic Role of H_2O and the Ligand in the Chemical-Vapor-Deposition of Cu, Cu_2O, CuO, and Cu_3N from Bis(1,1,1,5,5,5-Hexafluoropentane-2,4-Dionato) Copper(II). *Chemistry of Materials* **1995,** *7* (8), 1589-1596.

119. Davide Barreca, A. G., Chiara Maccato, Eugenio Tondello, Oleg I. Lebedev, and Gustaaf Van Tendeloo, CVD of Copper Oxides from a-Diketonate Diamine Precursor: Tailoring the Nano-Organization. *Crystal Growth & Design* **2009,** *9* (5), 2470-2480.

120. Barreca, D.; Fois, E.; Gasparotto, A.; Seraglia, R.; Tondello, E.; Tabacchi, G., How does Cu(II) convert into Cu(I)? An unexpected ring-mediated single-electron reduction. *Chemistry* **2011,** *17* (39), 10864-70.

121. Maiti, B. K.; Pal, K.; Sarkar, S., Selective inclusion of DMF molecules within non-covalent cavity. *Inorganica Chimica Acta* **2011,** *372* (1), 213-219.

122. Sheng, P.; Sun, Y.; Jiao, F.; Di, C.; Xu, W.; Zhu, D., A novel cuprous ethylenetetrathiolate coordination polymer: Structure characterization, thermoelectric property optimization and a bulk thermogenerator demonstration. *Synthetic Metals* **2014,** *193*, 1-7.

123. Alves, H.; Simão, D.; Cordeiro Santos, I.; Gama, V.; Teives Henriques, R.; Novais, H.; Almeida, M., A Series of Transition Metal Bis(dicyanobenzenedithiolate) Complexes $[M(dcbdt)_2]$ (M = Fe, Co, Ni, Pd, Pt, Cu, Au and Zn). *European Journal of Inorganic Chemistry* **2004,** *2004* (6), 1318-1329.

124. Reynolds, J. R.; Lillya, C. P.; Chien, J. C. W., Intrinsically Electrically Conducting Poly(Metal Tetrathiooxalates). *Macromolecules* **1987,** *20* (6), 1184-1191.

125. Cerdeira, A. C.; Afonso, M. L.; Santos, I. C.; Pereira, L. C. J.; Coutinho, J. T.; Rabaça, S.; Simão, D.; Henriques, R. T.; Almeida, M., Synthesis, structure and physical properties of transition metal bis 4-cyanobenzene-1,2-dithiolate complexes $[M(cbdt)_2]^{z-}$ (M=Zn, Co, Cu, Au, Ni, Pd, z=0, 1, 2). *Polyhedron* **2012,** *44* (1), 228-237.

126. Waters, T.; Wang, X. B.; Woo, H. K.; Wang, L. S., Photoelectron Spectroscopy of the

bis(dithiolene) anions [M(mnt)(2)](n-)(M = Fe-Zn; n=1, 2): Changes in electronic structure with variation of metal center and with oxidation. *Inorganic Chemistry* **2006,** *45* (15), 5841-5851.

127. V. Bachler, G. O., F. Neese, K. Wieghardt, Theoretical evidence for the singlet diradical character of square planar nickel complexes containing two osemiquinonato type ligands. *Inorganic Chemistry* **2002,** (41), 4179–4193;.

128. S.I. Gorelski, L. B., J. Vura-Weis, R. Sarangi, K.O. Hodgson, B. Hedman, K. Fujisawa, E.I. Solomon, Spectroscopic and DFT Investigation of [M{HB (3,5-^{i}Pr$_2$pz)$_3$}(SC$_6$F$_5$)] (M = Mn, Fe Co, Ni, Cu, and Zn) model complexes: periodic trends in metal–thiolate bonding. *Inorganic Chemistry* **2005,** *44*, 4947–4960.

129. Sahadevan, S. A.; Abherve, A.; Monni, N.; Saenz de Pipaon, C.; Galan-Mascaros, J. R.; Waerenborgh, J. C.; Vieira, B. J. C.; Auban-Senzier, P.; Pillet, S.; Bendeif, E. E.; Alemany, P.; Canadell, E.; Mercuri, M. L.; Avarvari, N., Conducting Anilate-Based Mixed-Valence Fe(II)Fe(III) Coordination Polymer: Small-Polaron Hopping Model for Oxalate-Type Fe(II)Fe(III) 2D Networks. *Journal of the American Chemistry Society* **2018,** *140* (39), 12611-12621.

130. Becke, A. D., A new mixing of Hartree-Fock and local density-functional theories. *The Journal of Chemical Physics* **1993,** *98* (2), 1372-1377.

131. Lee, C.; Yang, W.; Parr, R. G., Development of the Colle-Salvetti correlation-energy formula into a functional of the electron density. *Physical Review B* **1988,** *37* (2), 785-789.

132. Vosko, S. H.; Wilk, L.; Nusair, M., Accurate spin-dependent electron liquid correlation energies for local spin density calculations: a critical analysis. *Canadian Journal of Physics* **1980,** *58* (8), 1200-1211.

133. Stephens, P. J.; Devlin, F. J.; Chabalowski, C. F.; Frisch, M. J., Ab Initio Calculation of Vibrational Absorption and Circular Dichroism Spectra Using Density Functional Force Fields. *The Journal of Physical Chemistry* **1994,** *98* (45), 11623-11627.

134. Grimme, S.; Antony, J.; Ehrlich, S.; Krieg, H., A consistent and accurate ab initio parametrization of density functional dispersion correction (DFT-D) for the 94 elements H-Pu.

The Journal of Chemical Physics **2010,** *132* (15), 154104.

135. Grimme, S.; Ehrlich, S.; Goerigk, L., Effect of the damping function in dispersion corrected density functional theory. *Journal of Computational Chemistry* **2011,** *32* (7), 1456-1465.

136. Weigend, F.; Ahlrichs, R., Balanced basis sets of split valence, triple zeta valence and quadruple zeta valence quality for H to Rn: Design and assessment of accuracy. *Physical Chemistry Chemical Physics* **2005,** *7* (18), 3297-3305.

137. Chai, J.-D.; Head-Gordon, M., Long-range corrected hybrid density functionals with damped atom–atom dispersion corrections. *Physical Chemistry Chemical Physics* **2008,** *10* (44), 6615-6620.

138. Klamt, A.; Schüürmann, G., COSMO: a new approach to dielectric screening in solvents with explicit expressions for the screening energy and its gradient. *Journal of the Chemical Society, Perkin Transactions 2* **1993,** (5), 799-805.

139. Hirata, S.; Head-Gordon, M., Time-dependent density functional theory within the Tamm–Dancoff approximation. *Chemical Physics Letters* **1999,** *314* (3), 291-299.

140. Furche, F.; Ahlrichs, R.; Hättig, C.; Klopper, W.; Sierka, M.; Weigend, F., Turbomole. *WIREs Computational Molecular Science* **2014,** *4* (2), 91-100.

141. Kresse, G.; Hafner, J., Ab initio molecular dynamics for liquid metals. *Physical Review B* **1993,** *47* (1), 558-561.

142. Kresse, G.; Hafner, J., Ab initio molecular-dynamics simulation of the liquid-metal--amorphous-semiconductor transition in germanium. *Physical Review B* **1994,** *49* (20), 14251-14269.

143. Kresse, G.; Furthmüller, J., Efficiency of ab-initio total energy calculations for metals and semiconductors using a plane-wave basis set. *Computational Materials Science* **1996,** *6* (1), 15-50.

144. Kresse, G.; Furthmüller, J., Efficient iterative schemes for ab initio total-energy calculations using a plane-wave basis set. *Physical Review B* **1996,** *54* (16), 11169-11186.

145. Blöchl, P. E., Projector augmented-wave method. *Physical Review B* **1994,** *50* (24), 17953-

17979.

146. Heyd, J.; Scuseria, G. E.; Ernzerhof, M., Hybrid functionals based on a screened Coulomb potential. *The Journal of Chemical Physics* **2003,** *118* (18), 8207-8215.

147. Adamo, C.; Barone, V., Toward reliable density functional methods without adjustable parameters: The PBE0 model. *The Journal of Chemical Physics* **1999,** *110* (13), 6158-6170.

148. Perdew, J. P.; Burke, K.; Ernzerhof, M., Generalized Gradient Approximation Made Simple. *Physical Review Letters* **1996,** *77* (18), 3865-3868.

149. Krukau, A. V.; Vydrov, O. A.; Izmaylov, A. F.; Scuseria, G. E., Influence of the exchange screening parameter on the performance of screened hybrid functionals. *The Journal of Chemical Physics* **2006,** *125* (22), 224106.

150. Ganose, A.; Jackson, A.; Scanlon, D., sumo: Command-line tools for plotting and analysis of periodic *ab initio* calculations. *Journal of Open Source Software* **2018,** *3* (28), 717.

151. Bradley, C. J.; Cracknell, A. P., *Mathematical Theory of Symmetry in Solids*. Oxford University Press: 1972.

152. Schumaker, R. R.; Lee, V. Y.; Engler, E. M., Noncoupling synthesis of tetrathiafulvalenes. *The Journal of Organic Chemistry* **1984,** *49* (3), 564-566.

153. Dieter Sellmann, D. H. u., Falk Knoch, and Matthias Moll, Transition Metal Complexes with Sulfur Ligands. A Reaction Cycle for Nickel Mediated Thioester Formation from Alkyl, CO, and Thiolate Groups Modeling the Acetyl-Coenzyme A Synthase Function of CO Dehydrogenase. **1995**.